

# **Seismic vulnerability assessment of historical masonry building under near-field earthquake**

Teză destinată obținerii  
titlului științific de doctor inginer  
la  
Universitatea Politehnica Timișoara  
în domeniul Inginerie Civilă

**Nicola Chieffo**

Conducător științific:	Prof. Dr Eng. Marius Moșoarca
Referenți științifici:	Prof. Dr Eng. Prof. Dr Eng. Prof. Dr Eng.

Ziua susținerii tezei: .....

Seriile Teze de doctorat ale UPT sunt:

- |   |  |
|---|--|
| 1. Automatică                               | 9. Inginerie Mecanică                      |
| 2. Chimie                                   | 10. Știința Calculatoarelor                |
| 3. Energetică                               | 11. Știința și Ingineria Materialelor      |
| 4. Ingineria Chimică                        | 12. Ingineria sistemelor                   |
| 5. Inginerie Civilă                         | 13. Inginerie energetică                   |
| 6. Inginerie Electrică                      | 14. Calculatoare și tehnologia informației |
| 7. Inginerie Electronică și Telecomunicații | 15. Ingineria materialelor                 |
| 8. Inginerie Industrială                    | 16. Inginerie și Management                |

Universitatea Politehnica Timișoara a inițiat seriile de mai sus în scopul diseminării expertizei, cunoștințelor și rezultatelor cercetărilor întreprinse în cadrul Școlii doctorale a universității. Seriile conțin, potrivit H.B.Ex.S Nr. 14 / 14.07.2006, tezele de doctorat susținute în universitate începând cu 1 octombrie 2006.

Copyright © Editura Politehnica – Timișoara, 2013

Această publicație este supusă prevederilor legii dreptului de autor. Multiplicarea acestei publicații, în mod integral sau în parte, traducerea, tipărirea, reutilizarea ilustrațiilor, expunerea, radiodifuzarea, reproducerea pe microfilme sau în orice altă formă este permisă numai cu respectarea prevederilor Legii române a dreptului de autor în vigoare și permisiunea pentru utilizare obținută în scris din partea Universității Politehnica Timișoara. Toate încălcările acestor drepturi vor fi penalizate potrivit Legii române a drepturilor de autor.

România, 300159 Timișoara, Bd. Republicii 9,  
Tel./fax 0256 403823  
e-mail: editura@edipol.upt.ro

## Acknowledgements

Upon completion of the Ph.D. program, a heartfelt thanks to my coordinator Prof. Eng. Marius Moroarca for his patience and pertinence profuse supporting me in this broad, articulated, and fruitful scientific formation process.

I am deeply grateful to him for directing me into the research program and allowing me to achieve an important flawlessly result, in as good as possible.

His cooperation and demonstrated determination have made possible the development of a complex issue and have provided me with the necessary tools to enrich myself culturally and professionally. Thanks so much for everything.

Special thanks to my colleagues, I. Onescu and A. Keller who have always helped me by making my days pleasant and motivated. I also thank all the Professors that I have met within the Department of Architecture and Urbanism of the Politehnica University of Timisoara which were kind and understandable.

I would also like to thank Prof. Eng. F. M. Mazzonali, Doctor Honoris Causa of the Politehnica University of Timisoara, for allowing me the possibility to continuing important scientific research begun, together with the late Prof. Eng. V. Giouncu, in the field of Seismic Engineering.

I deeply thank Prof. Eng. A. Formisano for his continuous and constant scientific support even in difficult moments. I am grateful for his remarkable patience, enthusiasm, and for all his recommendations that have always pushed me to improve myself and to consciously dare. You have been a strong shoulder, a point of reference, and a present friend.

I would like to send a special thank you to Prof. Eng. P. B. Lourenço for his contribution to the research developed on the assessment of the seismic vulnerability of historic masonry buildings. His availability and great experience were fundamental in my Ph.D. career. Furthermore, I extend my sincere thanks to the research group of the University of Minho, for the support and collaboration through the Erasmus<sup>+</sup> study grant, especially to Dr. Eng. J. Pereira, Dr. Eng. N. Mendes, and Dr. Eng. T.M. Ferreira.

To All of you Thanks,

Timișoara, 2021

Nicola Chieffo

Chieffo, Nicola

**Seismic vulnerability assessment of historical masonry building under near-field earthquake.**

Teze de doctorat ale UPT, Seria X, Nr. YY, Editura Politehnica, 200Z, 337 pagini, 174 figuri, 38 tabele.

Keywords:

Vertical Ground Motion, Near-field effects, Seismic Vulnerability Assessment, Historical Masonry Building, Damage Assessment, Fragility curves, Vulnerability curves.

Summary,

The historic masonry buildings, as known, represent the living testimony of a building heritage characterized by a high artistic and architectural value. However, this class of constructions are the weakest part of an urban system, since, due to structural weaknesses, they are implicitly deficient in relation to seismic actions especially in near-field conditions in which the effects of the ground motion vertical component play an important role concerning the seismic response of the engineering structures.

Despite this, even the seismic regulations are lacking in providing substantial indications regarding the treatment of the vertical component of the ground movement, limiting themselves only to the effects of the horizontal ones.

The doctoral thesis aims to evaluate the effects of the ground motion vertical component on the seismic vulnerability of a historic masonry building located in the Banat Seismic Region (BSR). In particular, the Municipality of Banloc was hit by a significant seismic sequence in 1991 characterized by impulsive vertical accelerations that altered the integrity of the masonry structures in the epicentre and surrounding villages.

In this regard, a non-linear dynamic analysis was performed to identify the seismic response of the case study structure considering two distinct scenarios for contextualizing the seismic effects induced by both, vertical and horizontal components, respectively.

The proposed methodology provides an exhaustive treatment regarding the estimation of the main demand parameters that identify the seismic behaviour of the examined building in the case of impulsive seismic phenomenon. Starting from the studies conducted in Europe, the doctoral thesis makes important contributions about the importance of taking into account the vertical seismic component in the study of global seismic vulnerability.

In conclusion, the research lays the foundations for a broader awareness of the proposed topic by providing technical information useful for the of historic masonry buildings located in other cities of the Banat Region.



## LIST OF CONTENTS

<b>1</b>	<b>INTRODUCTION.....</b>	<b>17</b>
1.1	BACKGROUND OF THE KNOWLEDGE.....	17
1.2	OBJECTIVES OF THE STUDY SUBJECT.....	21
1.3	RELEVANT OBJECTIVES.....	25
<b>2</b>	<b>SEISMIC VULNERABILITY ASSESSMENT METHODS AND GEOTECHNICAL HAZARD CONDITIONS .....</b>	<b>36</b>
2.1	GENERAL OVERVIEW.....	36
2.1.1	<i>Hazard.....</i>	<i>39</i>
2.1.2	<i>Exposure .....</i>	<i>42</i>
2.1.3	<i>Vulnerability .....</i>	<i>44</i>
2.2	ASSESSMENT METHODS FOR SEISMIC VULNERABILITY PROCEDURES 48	
2.2.1	<i>Empirical methods .....</i>	<i>49</i>
2.2.2	<i>Analytical methods.....</i>	<i>53</i>
2.3	GROUND MOTION HAZARD CONDITIONS.....	60
2.3.1	<i>The influence of local site effects.....</i>	<i>60</i>
2.3.2	<i>The main characteristic of a near-field earthquake .....</i>	<i>64</i>
2.3.3	<i>The effect of recent destructive Italian earthquakes .....</i>	<i>68</i>
<b>3</b>	<b>SEISMIC VULNERABILITY ASSESSMENT OF HISTORICAL MASONRY BUILDING UNDER NEAR-FIELD EARTHQUAKE.....</b>	<b>83</b>
3.1	HISTORICAL BACKGROUND.....	83
3.2	THE EVOLUTION OF THE CITY OF BANLOC: FROM PAST TO PRESENT	86
3.3	SEISMICITY OF ROMANIA.....	88
3.4	SEISMIC ACTIVITY IN THE BANAT AREA.....	93
3.5	ROMANIAN DESIGN CODE APPROACH.....	95
3.5.1	<i>Seismic hazard map .....</i>	<i>95</i>
3.5.2	<i>Romanian Code – Horizontal response spectrum .....</i>	<i>98</i>
3.5.3	<i>Romanian Code – Vertical response spectrum.....</i>	<i>102</i>
3.5.4	<i>Typical failure mechanisms in the epicentre area .....</i>	<i>103</i>
3.6	SEISMIC ASSESSMENT OF THE BANLOC CASTLE.....	108
3.6.1	<i>Preliminary analysis of the case study building .....</i>	<i>108</i>
3.7	MECHANICAL ANALYSIS OF THE BANLOC CASTLE.....	118
3.7.1	<i>Methodology approach .....</i>	<i>118</i>
3.7.2	<i>Modelling philosophy.....</i>	<i>120</i>

3.7.3	<i>Mechanical properties of masonry</i> .....	122
3.7.4	<i>FEM model of the case study building</i> .....	136
<b>4</b>	<b>DISCUSSION AND ANALYSIS OF THE RESULTS</b> .....	<b>159</b>
4.1	INTRODUCTION .....	159
4.2	GLOBAL ANALYSIS .....	160
4.2.1	<i>Identification of the structural typology</i> .....	160
4.2.2	<i>Identification of the global seismic response</i> .....	162
4.2.3	<i>Energy-based method for seismic analysis</i> .....	176
4.3	LOCAL ANALYSIS .....	199
4.3.1	<i>Identification of the structural typology of the wall systems</i> ...	200
4.3.2	<i>In-plane mechanisms</i> .....	201
4.3.3	<i>Numerical damage identification</i> .....	226
4.3.4	<i>Strength domain and failure hierarchy</i> .....	235
4.3.5	<i>Out-of-plane mechanisms</i> .....	258
4.3.6	<i>Numerical Vs real damage correlation</i> .....	264
<b>5</b>	<b>DERIVATION OF ANALYTICAL FRAGILITY AND VULNERABILITY FUNCTIONS IN CASE OF A NEAR-FIELD EARTHQUAKE</b> .....	<b>277</b>
5.1	INTRODUCTION .....	277
5.2	DEFINITION OF FRAGILITY CURVES .....	278
5.3	DEFINITION OF VULNERABILITY CURVES.....	285
<b>6</b>	<b>CONCLUSION</b> .....	<b>299</b>
6.1	PERSONAL CONTRIBUTIONS .....	300
6.2	FUTURE DEVELOPMENTS .....	302
6.3	PUBLISHED PAPERS .....	303
	<b>APPENDIX</b> .....	<b>305</b>
	<b>BIBLIOGRAPHY</b> .....	<b>325</b>

## LIST OF FIGURES

<b>Figure 2.1:</b> Concept of seismic risk analysis.....	37
<b>Figure 2.2:</b> Framework of DSHA. ....	40
<b>Figure 2.3:</b> PSHA algorithm.....	41
<b>Figure 2.4:</b> Inventory of the vulnerability typological classes according to EMS-98 scale [60]. ....	45
<b>Figure 2.5:</b> DPM proposed by Whitman et al. (1974) [78]. ....	50
<b>Figure 2.6:</b> Vulnerability form adopted in Benedetti and Petrini et al., (1984) [83]. ....	51
<b>Figure 2.7:</b> Vulnerability form developed by Formisano et al., (2015) [85]. ....	51
<b>Figure 2.8:</b> Vulnerability curves for each building typology according to Lagomarsino et al., (2006) [90]. ....	52
<b>Figure 2.9:</b> Continuous Vulnerability curves according to [91]. ....	53
<b>Figure 2.10:</b> Descriptive layout of the calculation procedure for vulnerability curves and DPM [1]. ....	54
<b>Figure 2.11:</b> Possible collapse mechanisms according to the FaMIVE method [101]. ....	56
<b>Figure 2.12:</b> Framework of HAZUS method [102]. ....	57
<b>Figure 2.13:</b> Example of essential facility damage estimation process [102]. ....	57
<b>Figure 2.14:</b> Example of limit states for masonry building [105]. ....	58
<b>Figure 2.15:</b> Seismic shaking and seismic waves [19]. ....	60
<b>Figure 2.16:</b> Velocity time histories recorded after the 1991 Chi-Chi earthquake [19]. ....	65
<b>Figure 2.17:</b> Near-source velocities of the 1979 Imperial Valley earthquake [123]. ....	66
<b>Figure 2.18:</b> Vertical component effects [19]. ....	67
<b>Figure 2.19:</b> Vertical to horizontal acceleration ratio for different magnitude, $M_w$ , and source distances, $R$ (km) [108]. ....	68
<b>Figure 2.20:</b> USGS ShakeMap of Central Italy earthquake [133]. ....	69
<b>Figure 2.21:</b> Recorded stations and epicentre location [135]. ....	69
<b>Figure 2.22:</b> Pseudo-acceleration spectra of the L'Aquila seismic event mainshock compared to the NTC08 Italian Code [135]. ....	70
<b>Figure 2.23:</b> Vertical pseudo-acceleration spectra of the L'Aquila seismic event mainshock compared to the NTC08 Italian Code [135]. ....	70
<b>Figure 2.24:</b> Damages surveyed after the L'Aquila earthquake [135]. ....	72

<b>Figure 2.25:</b> ShakeMap of the events that occurred on 24th August (a), 26 <sup>th</sup> October (b), and 30 <sup>th</sup> October 2016 (c) [136].	73
<b>Figure 2.26:</b> Maximum PGAs in vertical direction recorded during the seismic event on 30th October 2016 near the City of Amatrice [136].	74
<b>Figure 2.27:</b> Recorded accelerograms after the Central Italy sequence on 30th October 2016 [41].	74
<b>Figure 2.28:</b> Damage detected after the Amatrice's earthquake [137].	76
<b>Figure 2.29:</b> Damage assessment in the City of Accumuli [137].	77
<b>Figure 2.30:</b> ShakeMap according to USGS ( $M_w$ 6.2) for the inspected area [137].	78
<b>Figure 2.31:</b> Damages detected in Arquata del Tronto [137].	79
<b>Figure 2.32:</b> Damage identification in Pescara del Tronto [137].	80
<b>Figure 2.33:</b> Damage achieved in Norcia [137].	81
<b>Figure 2.34:</b> Damage observed in Castelluccio di Norcia [137].	82
<b>Figure 3.1:</b> Geo-localization of the Banat region.	83
<b>Figure 3.2:</b> Political situation in the middle of 17 <sup>th</sup> century [139].	84
<b>Figure 3.3:</b> The surrounding regions in 1683 [139].	85
<b>Figure 3.4:</b> Geolocalization of the City of Banloc and Banloc in the Iosefină Map of Banat, 1769-72 [142].	86
<b>Figure 3.5:</b> Example of the building's typologies present in the urban area of Banloc [142].	87
<b>Figure 3.6:</b> The Castle of Banloc [142].	88
<b>Figure 3.7:</b> Map of tectonic units in Romania [143].	88
<b>Figure 3.8:</b> Distribution of earthquake epicentres and magnitude ( $M_w$ ) [144].	91
<b>Figure 3.9:</b> Romanian's focal mechanisms [145].	92
<b>Figure 3.10:</b> Map of epicentres from 1443 to 2006. Dashed line bounds Banat Seismic Region [53].	94
<b>Figure 3.11:</b> Seismic stations present in the BSR area (a) and epicentres distributions (b) [53].	95
<b>Figure 3.12:</b> Seismic hazard from all source zones: (a) recurrence period of 475 years and (b) recurrence period of 95 years [146].	96
<b>Figure 3.13:</b> Seismic hazard map in terms of PGA with a probability of exceedance of 10% in 50 years [147].	97
<b>Figure 3.14:</b> Romania's zonation in terms of peak ground acceleration values [39].	98
<b>Figure 3.15:</b> Romania in terms of the zoning control period, $T_C$ spectrum [39].	99

<b>Figure 3.16:</b> Normalized elastic response spectra of absolute accelerations for horizontal components of motion, in areas characterized by the control period (corner) $T_C$ equal to 0.7s, 1.0s, and 1.6s [39].....	101
<b>Figure 3.17:</b> Normalized elastic response spectrum for the horizontal components of the ground motion [39].....	101
<b>Figure 3.18:</b> The aftershocks series of the strongest ( $M_w=5.5-5.6$ ) earthquakes occurred in Banloc (12.07.1991 and 02.12.1991) and Mehadia (18.07.1991) in the time domain of 1988-2013 [53]. .....	104
<b>Figure 3.19:</b> ShakeMap of the Banat-Voiteg event (a) and geolocation of the city of Banloc [148]. .....	104
<b>Figure 3.20:</b> Effect of seismic waves [122]. .....	105
<b>Figure 3.21:</b> Main damages detected after the Banloc-Voiteg earthquake in 1991 [150].....	106
<b>Figure 3.22:</b> Damage reconnaissance on the study Castle after 1991 Banloc earthquake: (a, b) external façade; (c) first floor room; (d) second-floor room [150].....	107
<b>Figure 3.23:</b> The Banloc Castle [151]. .....	108
<b>Figure 3.24:</b> Geographical orientation of the main façade.....	109
<b>Figure 3.25:</b> Architectural plan layout of intermediate-floor (a) longitudinal section A-A' (b) and North façade (c).....	110
<b>Figure 3.26:</b> Degradation detected in the North façade. ....	111
<b>Figure 3.27:</b> Degradation detected in (a) East and West façades, (b) South façade. ....	112
<b>Figure 3.28:</b> Degradation of the wooden roof structure.....	113
<b>Figure 3.29:</b> Geographical identification of the event that occurred in Banloc on 02-12-1991 [148]. .....	114
<b>Figure 3.30:</b> Detected damages on the Banloc Castle after the 1991 earthquake: (a-d) external view, (e-l) first floor and (m-p) second floor [150]. .....	117
<b>Figure 3.31:</b> Modelling strategies: (a) detailed model; (b) simplified model and (c) macro model [156].....	121
<b>Figure 3.32:</b> Failure models: (a) composite interface; (b) anisotropic continuum [156].....	122
<b>Figure 3.33:</b> Masonry experimental test: (a) uniaxial test; (b) diagonal test and (c) compression and shear test [172].....	123
<b>Figure 3.34:</b> Stress-strain law: (a) generic behaviour [135]; (b) EC8 proposal [38].....	125

<b>Figure 3.35:</b> Quasi-brittle materials under uniaxial loading: (a) compressive behaviour; (b) tensile behaviour [176].	125
<b>Figure 3.36:</b> Masonry structure: (a) structural components; (b) wall configurations [172].	127
<b>Figure 3.37:</b> Different modelling techniques for masonry structures: (a) EFM; (b) FEM [185].	128
<b>Figure 3.38:</b> Different collapse mechanisms: (a-b) I Mode Collapse Mechanisms [186]; (c-d) II Mode Collapse Mechanism [187].	131
<b>Figure 3.39:</b> Strength criteria: (a) action in the wall plane; (b) rocking collapse; (c) diagonal shear and (d) sliding shear [190].	132
<b>Figure 3.40:</b> Mechanisms induced by the asynchrony of the seismic vertical component [192].	134
<b>Figure 3.41:</b> Damage recognition after earthquake: (a-c) Northridge and (c-d) Central Italy [193].	135
<b>Figure 3.42:</b> Framework of the operating scheme.	136
<b>Figure 3.43:</b> Typical FEM element types (a) linear elements, (b) shell elements and (c) solid elements [196].	138
<b>Figure 3.44:</b> FEM model of the Banloc Castle, (a) 3D model, and (b) global shell elements.	139
<b>Figure 3.45:</b> Elements with good (a-c) and bad aspect ratios (d-f) [196].	140
<b>Figure 3.46:</b> Loading-unloading-reloading phases condition for TSC model [194].	141
<b>Figure 3.47:</b> Tensile behaviour in TSC model: (a) constant; (b) linear; (c) exponential and (d) brittle [194].	142
<b>Figure 3.48:</b> Compressive behaviour model: (a) elastic; (b) constant and (c) parabolic [194].	142
<b>Figure 3.49:</b> Calculation scheme adopted for the conversion of loads into mass increments (a) and (b) load areas considered.	146
<b>Figure 3.50:</b> Earthquake occurred near the City of Banloc in 1991 [148].	148
<b>Figure 3.51:</b> Accelerograms of the Banat-Voiteg seismic event in all analysis directions.	151
<b>Figure 3.52:</b> Accelerograms load conditions.	151
<b>Figure 3.53:</b> Ground motion parameters: velocity profile, PGV (a) and displacement profile, PGD (b).	152
<b>Figure 3.54:</b> Fourier spectrum in terms of period.	152
<b>Figure 3.55:</b> Acceleration response spectra.	153
<b>Figure 3.56:</b> Vertical to Horizontal spectral ratio estimated for the Banloc event.	153

<b>Figure 4.1:</b> Calculation models adopted for local analysis, (a-b) first type walls, (c-d) second type walls, and (e-f) third type walls [171].	162
<b>Figure 4.2:</b> The main eigenfrequencies mode.	163
<b>Figure 4.3:</b> Synthetic representation of the modal analysis results in X, Y, Vertical, translation directions.	165
<b>Figure 4.4:</b> Comparison between the total base reaction and the accelerations resulting from the Banat-Voiteg seismic event.	166
<b>Figure 4.5:</b> Time histories of total base reaction for the two analysed scenarios, (H) and ((H+V), respectively.	167
<b>Figure 4.6:</b> Base reactions for Banat-Voiteg earthquake considering (H) Vs (H+V) effects.	168
<b>Figure 4.7:</b> Demand/axial capacity ratio.	169
<b>Figure 4.8:</b> Selected monitoring point (MP) for the case study building.	170
<b>Figure 4.9:</b> Displacement-time history plots for MPs: 7352 (a-d), 36082 (e-h) and 14044 (i-n).	172
<b>Figure 4.10:</b> Influence of VGM on the corner MP 19821.	174
<b>Figure 4.11:</b> Displacement ductility factor.	176
<b>Figure 4.12:</b> Backbone hysteretic loop and corresponding envelope in X and Y direction, respectively.	177
<b>Figure 4.13:</b> Mean capacity curves for the scenario (H+V) in X direction (a) and Y-direction (b).	180
<b>Figure 4.14:</b> Identification of the wall system in the X and Y direction.	181
<b>Figure 4.15:</b> Effective walls resistant area.	182
<b>Figure 4.16:</b> Cyclic stiffness degradation in, (a) X direction and (b) Y direction.	183
<b>Figure 4.17:</b> Stiffness degradation curves in X and Y directions (a) and descriptive power function of the stiffness degradation (b).	183
<b>Figure 4.18:</b> Stiffness percentage degradations.	184
<b>Figure 4.19:</b> Estimation of the mean capacity curves at 67%, 50%, and 100% of the structural capacity.	187
<b>Figure 4.20:</b> Equivalence of the areas for the case study structural system at 67%, 50%, and 100% of the capacity.	188
<b>Figure 4.21:</b> Ductility-q factor law for different capacity variations (a-b) 67%, (b-c) 50% and (d-e) 100%.	191
<b>Figure 4.22:</b> IDR variations associated with the MPs for each time step.	193
<b>Figure 4.23:</b> Acceleration-IDR variations for different MPs.	194
<b>Figure 4.24:</b> Identified wall systems for local analysis in X and Y directions, respectively.	201

<b>Figure 4.25:</b> Identifiers, ID, of masonry walls considered in the two analysis directions, X and Y, respectively. ....	203
<b>Figure 4.26:</b> D/C axial ratio associated with the masonry panels analysed in X-direction. ....	204
<b>Figure 4.27:</b> D/C axial ratio associated with the masonry panels analysed in Y direction. ....	205
<b>Figure 4.28:</b> D/C axial ratio associated with the masonry panels analysed in, (a) X and (b) Y direction. ....	206
<b>Figure 4.29:</b> Normalized axial force in case of impulsive earthquake for the masonry walls in X directions. ....	209
<b>Figure 4.30:</b> Normalized axial forces for the masonry panels in Y direction. ....	210
<b>Figure 4.31:</b> Normalized axial ratio for the masonry panels in (a) X direction and (b) in Y direction. ....	211
<b>Figure 4.32:</b> Stress distribution in the masonry wall panel, and stress state in the geometric centre of gravity, G, of the wall. ....	213
<b>Figure 4.33:</b> Time histories of normalized shear capacity and shear demand/capacity ratios for the masonry walls analysed in X-direction. ....	214
<b>Figure 4.34:</b> Shear stress rates for the analysed masonry panels in X-direction. ....	215
<b>Figure 4.35:</b> N(t)/V(t) ratio for the panels analysed in X-direction. ....	216
<b>Figure 4.36:</b> Time histories of normalized shear capacity and shear demand/capacity ratios for the masonry walls analysed in Y direction. ....	217
<b>Figure 4.37:</b> Shear stress rates for the analysed masonry panels in Y direction. ....	218
<b>Figure 4.38:</b> N(t)/V(t) ratio for the panels analysed in Y direction. ....	219
<b>Figure 4.39:</b> Normalized shear ratio for the masonry panels <i>h</i> and <i>i</i> , in X and Y directions, respectively. ....	220
<b>Figure 4.40:</b> D/C shear ratio and N(t)/V(t) ratio for the panels <i>h</i> and <i>i</i> , respectively. ....	221
<b>Figure 4.41:</b> Identification of rocking failure induced by shear force, V. ....	224
<b>Figure 4.42:</b> Diagonal Vs Rocking shear failure mechanisms reached in X-direction. ....	225
<b>Figure 4.43:</b> Diagonal Vs Rocking shear failure mechanisms reached in Y direction. ....	226
<b>Figure 4.44:</b> Identified structural damage in the time domain. ....	228
<b>Figure 4.45:</b> Numerical damage assessment at each time steps considered. ....	232



<b>Figure 4.46:</b> Vertical shear cracks generated by ground motion vertical component detected after the L'Aquila earthquake [31].	233
<b>Figure 4.47:</b> Damage identification for $t > 3.18$ sec, (a)-(e) global overview, (f)-(l) North façade.	235
<b>Figure 4.48:</b> Evolution of the compressive stress state thresholds [171].	237
<b>Figure 4.49:</b> Strength domain in case of (a) flexural conditions and (b) flexural and shear conditions.	238
<b>Figure 4.50:</b> Resistance domains for the selected masonry panels oriented in X-direction.	240
<b>Figure 4.51:</b> Maximum axial (a) and shear force (b) levels reached $t = 3.18$ sec associated with the rocking failure mechanisms.	241
<b>Figure 4.52:</b> Resistance domains for the selected masonry panels oriented in Y direction.	243
<b>Figure 4.53:</b> Characteristic curves for panels <i>a</i> , <i>b</i> , <i>c</i> in X-direction.	246
<b>Figure 4.54:</b> Comparison between capacity and the corresponding seismic demand for the analyzed wall panels in X-direction.	247
<b>Figure 4.55:</b> Comparison between capacity and the corresponding seismic demand for the analysed wall panels in Y direction.	250
<b>Figure 4.56:</b> Comparison between the Cacovic criterion and strength domain in terms of maximum expected shear levels for the considered masonry walls in X and Y directions.	253
<b>Figure 4.57:</b> Correlation between displacements, maximum shear force, and damage index, $DI_{\mu}$ , for panels in X-direction.	256
<b>Figure 4.58:</b> Correlation between displacements, maximum shear force, and damage index, $DI_{\mu}$ , for panels in Y direction.	258
<b>Figure 4.59:</b> Multiplier factor, $a_0$ , $V_s$ mechanisms considering the compressive effects of VGM for the North façade.	263
<b>Figure 4.60:</b> Damage correlation depicted in the South façade of the case study building.	265
<b>Figure 4.61:</b> Vertical displacement profile achieved in the South façade.	266
<b>Figure 4.62:</b> Damage evolution of the masonry vault due to ground motion vertical component of the simulated Banat-Voiteg earthquake.	267
<b>Figure 4.63:</b> Damage influenced by the vertical seismic component for the monitored central vault.	268
<b>Figure 4.64:</b> Damage comparison for masonry vaults at different time steps.	269
<b>Figure 4.65:</b> Damage detected in the East façade.	270

<b>Figure 4.66:</b> Rocking behaviour of the masonry wall panels constituting the East façade. ....	271
<b>Figure 4.67:</b> Damage correlation considering East façade.....	272
<b>Figure 4.68:</b> Damage deducted near the right corner of the West façade. .	273
<b>Figure 4.69:</b> Damage comparison in the North and South façades, respectively. ....	274
<b>Figure 4.70:</b> Evolution of the damage in (a) North façade and (b) South façade, respectively.....	275
<b>Figure 5.1:</b> Capacity curves comparison between (H) and (H+V) scenario, considering (a-b) 33%, (c-d) 50% and (e-f) 100% of the structural capacities. ....	279
<b>Figure 5.2:</b> Fragility curves developed for (H)-(solid line) and (H+V)-(dashed line) scenario for a different level of structural capacity.....	282
<b>Figure 5.3:</b> Banat design spectrum (a) acceleration response spectrum and (b) displacement response spectrum.....	287
<b>Figure 5.4:</b> ADRS spectrum for the Banat Seismic Region.....	287
<b>Figure 5.5:</b> Evaluation of seismic vulnerability index of the MDoF system in the two-analysis direction, X and Y, respectively. ....	288
<b>Figure 5.6:</b> Evaluation of mechanical vulnerability index in absence of VGM. ....	289
<b>Figure 5.7:</b> Structural model elaborated through 3Muri software, (a) solid model, (b) wireframe model., ....	290
<b>Figure 5.8:</b> Non-linear static analysis results, (a-b) capacity curves in X and Y directions, (c-g) damages detected in each façade. ....	291
<b>Figure 5.9:</b> Seismic verification adopting the ADRS spectrum.....	292
<b>Figure 5.10:</b> Vulnerability curves resumed through the empirical formulation proposed in [90]. ....	293
<b>Figure 5.11:</b> Calibrated typological vulnerability curves in the case of VGM. ....	294
<b>Figure 5.12:</b> Correlation between macroseismic intensity $I_{EMS-98}$ and $ag$ . .	295
<b>Figure 5.13:</b> Comparison between typological vulnerability curves for the near-field event. ....	296

## LIST OF TABLES

<b>Table 1:</b> European Macroseismic Scale (EMS-98) [60].	38
<b>Table 2:</b> Exposure classification according to RISK-UE project [72].	43
<b>Table 3:</b> EMS 98 vs HAZUS building typology classification.	46
<b>Table 4:</b> The B.T.M typology classification according to [75].	47
<b>Table 5:</b> Intensity increments $\Delta I$ for different soil conditions [114].	62
<b>Table 6:</b> Amplification factors, $f_{PGA}$ , and corresponding intensities [115].	62
<b>Table 7:</b> Soil classes and range of shear wave velocity ( $V_{s,30}$ ) and corresponding intensity increments ( $\Delta I$ ) [116].	63
<b>Table 8:</b> Crustal earthquakes with $M_w \geq 4.5$ with fault-mechanisms [145].	92
<b>Table 9:</b> Control period $T_B$ , $T_C$ , $T_D$ for the horizontal component of the spectrum [39].	100
<b>Table 10:</b> Mechanical properties adopted for characterizing the masonry [40].	143
<b>Table 11:</b> Design strength adopted for the case study historical building.	144
<b>Table 12:</b> Estimated density material increase.	147
<b>Table 13:</b> Characteristic of the seismic events that occurred in 1991 near the City of Banloc [52].	149
<b>Table 14:</b> Reference event occurred in the Banat seismogenic zone in December 1991 [52].	150
<b>Table 15:</b> Modal characteristics.	164
<b>Table 16:</b> Summary of the results in terms of displacements of the selected MPs.	173
<b>Table 17:</b> Displacements time history of the selected MPs.	173
<b>Table 18:</b> Main capacity parameters in X analysis direction.	178
<b>Table 19:</b> Main capacity parameters in Y analysis direction.	178
<b>Table 20:</b> Yield and maximum forces associated with the capacity variations.	188
<b>Table 21:</b> Yield and maximum displacements associated with the capacity variations.	189
<b>Table 22:</b> Hysteretic energy dissipation at 67%, 50%, and 100% of the structural capacities.	189
<b>Table 23:</b> Estimation of the behaviour factors $q$ .	190
<b>Table 24:</b> IDR-damage correlation according to FEMA-356 [74].	195
<b>Table 25:</b> Characterization of the seismic safety factor, $\alpha_i$ , in the two analysis directions, X and Y, respectively.	198
<b>Table 26:</b> Characteristics of the analysed wall panels in the X-direction.	203

<b>Table 27:</b> Characteristics of the analysed wall panels in Y direction. ....	205
<b>Table 28:</b> Characteristics of the analysed internal wall panels in X and Y directions.....	206
<b>Table 29:</b> Number of propagating cracks during the time history .....	228
<b>Table 30:</b> Input parameters used to estimate the $DI_{\mu}$ for wall panels in the X-direction. ....	255
<b>Table 31:</b> Input parameters used to estimate the $DI_{\mu}$ for wall panels in Y direction. ....	255
<b>Table 32:</b> Evaluation of compressive strength in case of VGM.....	262
<b>Table 33:</b> Results deriving from the kinematic analysis for the North façade..	263
<b>Table 34:</b> EDPs for the simulated scenario (H) and (H+V). ....	279
<b>Table 35:</b> EDPs for the simulated scenario (H) and (H+V). ....	280
<b>Table 36:</b> Results achieved evaluating the mechanical safety index in case of VGM excitation. ....	288
<b>Table 37:</b> Correlation between damage and macroseismic intensity for masonry buildings.....	294
<b>Table 38:</b> Damage comparison for the investigated area. ....	296

# 1 Introduction

## 1.1 Background of the knowledge

Typically, historic masonry buildings represent the weakest part of an urban system, especially when they are subject to the consequences of a seismic phenomenon of a given intensity [1], [2]. In general, masonry constructions have been, over the centuries, the main building assets which have provided economic and functional solutions all over the world. Throughout the various construction eras, masonry buildings have retained the techniques and structural details typical of an implicit approach based on the concept of "perfect workmanship" understood as a set of basic knowledge that allowed the achievement of a specific and organic structural scheme, which globally, it was resistant only to static conditions.

It is quite evident how existing unreinforced masonry buildings (URM) can be considered as "potential risk indicators" since the behaviour of the masonry is very complicated to predict especially in the case of seismic actions [3-7].

When URM buildings are subject to earthquakes, the density of the walls, the presence of reduced light flexible diaphragms, and diffuse material and structural heterogeneity, leads to a rigid-brittle global behaviour that triggers a cascade effect concerning the integrity of the whole building causing physical and economic losses that have reverberated on the entire municipality [8-12].

Generally, such structures, located in an area with medium-high seismicity, are implicitly dependent on aspects related to the basic hazard condition, and, among these, it is possible to mention, the type of earthquake (near or far-field), the type of seismic signal associated with the recorded accelerations (vibratory or impulsive) and the type of fault mechanism that directly affect the behaviour of masonry buildings at a given geographic site [13], [14]. In particular, by focusing on the near-field seismic phenomenon (i.e. seismic events characterized by a reduced site-to-source distance,  $R_{jb} < 25$  km) the ground motion vertical component plays an essential role regarding the global behaviour of buildings [15-19]. From a seismological point of view, the main characteristic of the seismic vertical component, VGM, is to be associated with the propagation of the compressive volume waves (P-waves) that represents the first signal recorded by the seismological station, while, the secondary shear waves (S-waves), are responsible for the arrival of the horizontal components [17-19].

The seismic phenomenon that arises near the source is mainly characterized by the fault rupture dynamics which produces a spectrum of the P-wave with a higher frequency content than the corresponding S-waves. Normally, the ground motion vertical component has a lower energy content which means that all its energy input is concentrated in a very restricted area producing very serious damage to the engineering structures [19].

According to N.A. Abrahamson [20], the effect of the seismic components is generally estimated using the peak acceleration ratio  $V/H$ , between vertical and horizontal spectral accelerations. This ratio, especially near the source, is greater than one and represents an important physical indicator regarding the quantities involved in the scenario. This consideration is in contrast to the study proposed by Newmark and Hall [21] since the  $V/H$  ratio was underestimated suggesting the value of  $2/3$  as the maximum expected threshold.

Consequently, in the research study proposed by V. Gioncu and G. Mateescu [22], the ground motion vertical component has been modelled as a velocity pulse to predict the effect of this component on the steel structure. Thus, the maximum amplification,  $\alpha$ , intended as the ratio between the maximum velocity pulse and the corresponding minimum ones, has provided a clear indication regarding the incidence of the seismic vertical component on the capacity response of the examined steel building. In particular, it has been observed that the global mechanism of the structure was activated for a higher value of the seismic vertical component, which means that the ground motion vertical component did not produce the collapse of the structure (attributable to the horizontal component ones) but reduced the axial force regime in the columns.

This aspect highlights how near the source the velocity is very high, representing the most significant control parameter [17], [18]. As a considerable contribution to the entire scientific community, V. Gioncu and F. M. Mazzolani have analysed the effects of the earthquakes that occurred during the seismic sequences in Northridge and Kobe [19].

During the above-mentioned earthquakes, velocity values of 175 cm/sec were recorded at the soil level [19], demonstrating how the velocity profile in near-field conditions is an important parameter to be taken into consideration for the evaluation of seismic damage. In general, the structures made up of mixed steel-RC were subjected to an impulsive vertical component effect which causing a very destructive scenario. As reported in the study proposed by [23], the RC columns were broken explosively and the steel columns were affected by fragile tensile failure crisis.

Other seismic events occurred in Europe, i.e. Skopje (ex-Yugoslavia, 1963), Managua (Nicaragua, 1972), Thessaloniki (Greece, 1978), El-Asnam (Algeria, 1980), San Salvador (El-Salvador, 1986), and Spitak (Armenia, 1989), are just some of the many earthquakes that have developed their destructive potential due to a short period of recurrence. These events, typically of the intraplate zone type, have caused multiple damages mainly due to the large energy associated with the vertical acceleration field [24-28].

As reported in [18], several buildings suffered damage on the lower floors (a soft-floor mechanism). The columns had reported damages induced by flexural and shear failures since the seismic vertical component had produced a variation in terms of axial stress regime compared to the condition for which they were designed. Concerning the steel structures, severe fragile cracks were also observed not only in the beam-column connections but also in box-column members with a fracture, involved as a horizontal detachment plane, of 20 mm.

More recently, after the disastrous events that took place in Central Italy, the scientific community started to point out the causes induced by the ground motion vertical component on the global seismic response of URM structures [29].

As previously stated, these types of structures maintain their imperturbable condition of equilibrium when subjected to static loads. In the case of seismic action, this imperturbability is altered and damage (or collapses) occur. Mainly, the effect of the vertical component on this class of buildings is disastrous since it alters the axial behaviour in the masonry wall panels, causing a reduction of the shear strength (in-plane response) [12]. This loss of compression triggers a series of harmful consequences that are the cause of many collapses. The field evidence observed after the Central Italy earthquake has shown many collapses. The vertical continuity of the wall panel has been completely disrupted by a variation of the axial stress regime induced by the ground motion vertical component. The most devastating consequence was observed when the masonry structures were subjected to a reduction of the load-bearing capacity induced by tensile stress.

Many studies [30-34] have affirmed that different classes of buildings, such as R.C frame, masonry and steel structure, subjected to vertical ground motion, VGM, had a high propensity of damage induced by shear and/or combined actions due to compression and bending moment derived by the seismic vertical component. In fact, in some cases, the VGM has generated tensile forces in the structural elements altering the conditions of equilibrium and consequently reducing both, axial and shear capacities, respectively.

Among the damage caused by earthquakes, several masonry buildings have shown widespread cracks typically induced by the shear failure with clear detachment among the mortar bed joints.

Another type of cracks that have been found have a pseudo-vertical trend and they are located near the openings. This phenomenology is due to the vertical asynchronous movement between the construction and the ground surface. In these circumstances, each part of the structure is subject to a relative displacement concerning the adjacent portion, constituting a vertical sliding plane (generally between the mortar bed joints or in more serious cases by sectioning the masonry brick). These types of failures usually appear given the variations of the vertical continuity or due to the presence of in-elevation structural discontinuities [19].

A classic example, discussed in [35], highlights the damage that occurred to the Clock Tower of Finale Emilia (Italy). According to this study, the tower collapsed due to the formation of a combined shear-bending plastic hinge in the lower part of the tower induced by the concomitance of both vertical and horizontal seismic actions, respectively. By extending these considerations on structures of historical interest, analogous outcomes were detected following the study proposed in [36].

Despite this, even the seismic code (see for example §4.3.3.5.2 in Eurocode 8, §7.2.1 and §7.3.5 in both NTC08 and the newest version NTC18, Romanian Code, P-100, [37-39]) fails to provide substantial indications regarding the treatment of the ground vertical component, limiting itself only to the horizontal ones. This lack of specific rules implies a limited knowledge of the problem which does not allow to preserve the structures in case of near-field conditions. However, a step forward is offered by the new Italian Code (NTC18) which establishes general design criteria for structural systems accounting for the vertical seismic action [40].

In general, the vertical seismic action is considered as a reduction (or increase) of the specific weight of the masonry by combining them with horizontal actions. This aspect is assumed concerning non-linear static analyses, which, as is known, are very often less exhaustive than a non-linear dynamic analysis [41]. In some circumstances, relying on pushover analysis, it is clear how applying this procedure could be difficult and would tend to overestimate the real capacity of the structure.

In this sense, a specific sector study would be indispensable to better predict the seismic response of a class of buildings (ordinary or of historical ones) through systematic design calculation procedures which would offer a higher



level of detail regarding the intrinsic vulnerability factors of a generic structural system. This aspect would allow for better distribution of direct economic resources to prepare buildings for a hypothetical earthquake scenario, protect the historical structures of intrinsic cultural value, and, the lives of the people who could be involved.

## **1.2 Objectives of the study subject**

The historic masonry buildings represent the living testimony of the historical and artistic heritage of a specific area [42]. These buildings faithfully reflect the aesthetic, architectural, and functional peculiarities characterized by a basic construction technique that did not contemplate an interaction between the structure and seismic actions [43-45].

In these specific conditions, the structures were generally designed to guarantee a high-performance level only concerning the vertical actions (static load), which favour the stability of the structure through the compressive forces that were generated in the vertical structures. However, it is quite evident that in seismic conditions, the lack of adequate construction details and limited technological knowledge used make these structures highly vulnerable to seismic actions. The reduced ductility, together with a low load-bearing capacity makes these class structures particularly complex toward the seismic actions. This phenomenon is accentuated when these typological classes are located near seismogenic sources. In this sense, the susceptibility to seismic inertial forces considerably increases the damage and makes the knowledge process onerous concerning a post-seismic event [46-47].

Scientific sensitivity has conducted very articulated and complex studies for the prediction of structural behaviour in case of a seismic event, focusing attention on the possibility of activating collapse mechanisms that could affect more or less extensive parts of a generic structural system [48]. Multiple methodologies, recognized worldwide, are used for the evaluation of seismic vulnerability, based on diversified approaches such as empirical, mechanical, and hybrid ones, which take into consideration the technological and structural aspects characterizing the peculiarities and/or deficiencies managing to grasp the seismic behaviour of these classes of structures with a satisfactory level of accuracy [49], [50].

Nevertheless, in the circumstance of a near-field (or near-source) phenomenon, the response of the structures is completely different since it is altered by the preponderance, for short periods, of the vertical seismic action,

which, in particularly exceptional cases (see the case of L'Aquila) was comparable to the horizontal component. However, the question is, Does such methodological approaches properly take into account all the effects deriving from a near-field seismic phenomenon?. The study proposed in [51] has focused on understanding the near-field phenomenology, emphasizing the main peculiarities necessary to prepare suitable numerical simulations to potentially predict the possible expected damage deriving from the simulated scenario event.

Researches conducted on both, RC frame buildings and symmetrical masonry buildings, have shown a significant reduction in terms of the axial capacity of the vertical structural elements, which, subject to cyclic action in compression and tension, degrade, reducing the load-bearing capacity [30].

It is extremely significant to consider that the type of event, impulsive or vibratory, produces different effects on the structural seismic response [17], [19].

Generally, impulsive phenomena (compatible with the crustal systems present in the seismic region of Banat, Romania) are characterized by high vertical accelerations in short periods, releasing all the energy content [52], [53].

However, there are some limitations criteria regarding the structural assessment (identification of the typological class, analysis of the main stress states, ductility, the predisposition of strength domains, and fragility and/or vulnerability curves) conjunctly to preliminary estimation of the behaviour factor,  $q$ , which is indispensable for the reduction of the design elastic forces, to take into account, in a simplified way, the inelastic dissipative capacity of the structure. Thus, following the intuition of Professors V. Gioncu and F.M. Mazzolani [19], this thesis aims to provide an exhaustive overview of the seismic vulnerability of historic masonry buildings subject to near-field events, making a significant contribution both nationally and internationally since it is preparatory to other studies conducted. In this perspective, this research topic, presented at various international conferences (such as ICNAAM20, EUROLYN20, SAHC20) and important international peer-reviewed journals with impact factors has allowed to raise awareness and address the scientific community on the importance of the proposed topic. The thesis is articulated in VI Chapters.

- **Chapter 1** provides an organic introduction to the proposed theme, describing its peculiarities and main objectives. Furthermore, the starting point and the opportunity of the subject have been highlighted based on the studies conducted.

- **Chapter 2** consists of two sub-sections. The first part, presented the general context relating to the state of the art, referring to the introduction of the characteristics related to hazard, exposure and vulnerability. Subsequently, the main seismic vulnerability methods have been discussed, offering an exhaustive overview of empirical, mechanical, and hybrid procedures. The second part of the chapter focuses on two basic aspects such as the local effects, which are responsible for the soil amplification and subsequently on the introduction of the phenomenological characteristics of near-field events: rupture directivity; amplification of horizontal and vertical components; peak ground velocities; velocity pulse period; the number of significant pulses; ground motion vertical component.  
Furthermore, a complete overview is provided focusing on the destructive effects induced by the vertical component of the ground motion in Central Italy after the event that occurred in 2009.
- **Chapter 3** has been divided into two parts, diversifying the historical and seismological aspects, relating to the Banat Region (focusing attention on the municipality of Banloc). In particular, the first part of the chapter highlights the typological and structural aspects of the city of Banloc, focusing on its historical evolution. In this sense, the Banloc Castle, a historic masonry building, located in the homonymous municipality is introduced and described, considering its architectural-functional characteristics. Besides, an overview is offered regarding the main typical failure mechanisms deduced after the impulsive shallow-seismic event that occurred in December 1991 in the region. Subsequently, the main aspects concerning the historical seismicity of Romania and the Banat Seismic Region (BSR) were analysed, providing an overview of the significant events that occurred at the site of interest. These events have been classified as near-field since the epicentral distance, concerning the Banloc site, is less than 25 km. In this perspective, the Romanian Design Code was analysed to understand, from the design point of view, the evaluation of the induced effects of both, vertical and horizontal ground motion components, respectively.  
The second part has the main objective to point out the treatment of the mechanical properties of the masonry structure, describing the constitutive laws, particularly by introducing the fracture energy, a fundamental parameter for the implementation of the calculation model.

Subsequently, the main characteristics of the masonry structures were analysed both towards, vertical and horizontal physical actions, highlighting the peculiarities and deficiencies of the design activity framework.

These steps were preparatory to address the calculation model of the Banloc Castle according to the finite element modelling technique. Particular attention was given to the structural analysis procedure, offering a wide and comprehensive explanation regarding the use of non-linear dynamic analysis. This simulation was carried out taking into account the natural accelerograms (in the three analysis directions, two horizontal and one vertical, respectively) of the seismic event that occurred in December 1991, namely Banat-Voiteg with the epicentre located at 7 km far from the reference site.

- **Chapter 4** analyses two aspects concerning the global and local analysis of the building examined. In particular, referring to the global analysis, the concept of typological characterization is introduced by assuming the building as first-class such as masonry buildings with deformable floors. Secondly, two different scenarios, (H) and (H+V) were analysed according to which the vertical component of the ground motion was neglected (scenario H) and considered (scenario H+V) to better understand its potential effects on the case study building. Consequently, through the global analysis, all the Engineering Demand Parameters (EDPs) were considered, focusing the attention on displacements, base reactions, ductility, stiffness degradation, behaviour factor and energy dissipation, IDR, and seismic safety index, offering a complete and comprehensive overview.

Subsequently, the local analysis was implemented considering the in-plane behaviour of the masonry panels oriented in the two analysis directions, X and Y, respectively. In the first part, the capacity of the panels was examined referring to both conditions, static and dynamic, respectively. In particular, the in-plane failure mechanisms have been estimated using the literature formulation and, consequently, by the adoption of strength domains. A failure hierarchy is proposed to identify the type of expected mechanism in the case of vertical excitation. Besides, the damage index was examined for each mechanism detected.

In the second part of the work, the out-of-plane behaviour of the wall panels was analysed, proposing a simplified procedure regarding the

influence of the ground motion vertical component on the activation of the main failure mechanisms. Finally, a comparison of the damages achieved between the simulated numerical model and the real ones detected after the reference earthquake has been proposed.

- **Chapter 5** this chapter analyses the analytical derivation of both, fragility and vulnerability curves relating to the examined building in case of a near-field earthquake. The main objective was to propose a systematic methodology to take into account the effects of the vertical component of the ground motion on the probability of exceeding a specific damage threshold. Therefore, concerning the fragility curves, they have been elaborated according to the formulations proposed in the literature, comparing the scenarios (H) and (H+V) and capturing the main differences in terms of expected performance levels. Subsequently, the typological vulnerability curves were analysed using both, non-linear static and dynamic analysis, respectively. In compliance with this aspect, a new formulation has been proposed for the evaluation of the mean damage grade, based on two significant parameters as the structural damage that occurred in the examined area (evaluated according to the indication of EMS-98 scale) and the hazard of the site considering the seismic intensity recorded in the epicentral area. This formulation, appropriately calibrated, provided a satisfactory forecast regarding the seismic behaviour of buildings placed in near-field conditions.
- **Chapter 6** concerns the conclusions in which the results pursued in the proposed work are discussed. Also, the published articles and the future direction of research are pointed out.

### 1.3 Relevant objectives

The scientific research has set out to achieve the following purposes:

- I. Realising the state of the art concerning the common seismic vulnerability assessment procedures and introducing a suitable overview regarding the characterization of the ground motion vertical component and its effects on masonry buildings;

- II. Identifying the seismic peculiarities of the Banat Seismic Region (BSR), considering an appropriate classification of the major seismic events that have characterized the area;
- III. Methodological interpretation of the earthquake-based design approach about of the Romanian Code for the evaluation of the ground motion vertical component;
- IV. Critical analysis of the main failure mechanisms detected in the epicentral area after the 1991 Banat-Voiteg earthquake;
- V. Structural modelling of the Banloc Castle using FEM approach;
- VI. Evaluation of the main Engineering Demand Parameters, EDPs, by proposing a differentiation between the scenarios analysed in which the vertical seismic excitation was considered and neglected, respectively;
- VII. Proposing the estimation of the behaviour factor in the case of a near-field phenomenon;
- VIII. Critical analysis of both, stress and displacement regime in the case of vertical seismic action;
- IX. Behavioural analysis of the building in dynamic conditions;
- X. Interpretation of the results regarding the in-plane failure mechanisms considering the effects of the ground motion vertical component;
- XI. Defining the strength domains for the masonry panels to identify an appropriate failure hierarchy in case of near-field condition;
- XII. Evaluating a damage index concerning the main in-plane failure conditions in case of near-field excitation;
- XIII. Evaluating the out-of-plane mechanisms considering the ground motion vertical seismic component, proposing a simplified calculation procedure;
- XIV. Calibration of the numerical damage based on the real ones detected after the post-earthquake survey activity in the municipality of Banloc;
- XV. Deriving the fragility and vulnerability curves in case of a near-field condition proposing a new formulation for estimating the mean damage grade;

## **2 Seismic vulnerability assessment methods and geotechnical hazard conditions**

### **2.1 General overview**

Nowadays, the recurrence of very disastrous natural phenomena such as hurricanes, floods, desertification, earthquakes, is significantly increased.

Focusing attention on the seismic phenomenon, the term seismicity defines the occurrence of earthquakes, and it is a physical characteristic of the territory.

Generally, the seismic risk indicates the probability of having an event (E) of a specific intensity of measurement (IMs) in a determined period (T) which cause a loss in a given area [54].

The notion of expected losses could be extended, without distinction, to the whole impacted environment. Essentially, the losses are the consequence of a nefarious event that directly or indirectly harms the entire economic-social community. It is therefore clear that the formulation of a model capable of estimating losses as the results of an earthquake is indispensable to predict the impact of future events and, therefore, to prepare and implement risk mitigation measures through territorial and urban planning able to guarantee and safeguard the security of the whole community [55].

Ideally, a loss model should take into consideration several possible phenomena that can trigger the damage caused by an earthquake such as seismic amplification, possible landslides, liquefaction phenomena.

Therefore, the creation of a loss model related to a city, a region, or a country requires the creation of a database, which contains information on the prevailing socio-economic activities, historical data of the earthquakes, types, and several infrastructures, vulnerabilities of the site to characterize the considered area [56].

From an anthropic and social point of view, the perception of risk is a determining factor since it allows, through knowledge, to recognize and therefore identify the problem. The problem linked to seismic risk is felt even more where the phenomenon occurs with a certain frequency in a given area. This consideration, therefore, makes it possible to assert that the memory of significant events affects and influences the community and the urban context.

On the other hand, in areas where the return period is broad from a cyclical point of view of natural phenomena, the perception of risk tends to doze off, fuelling the sensation of a total absence of risk.



In this circumstance, the principle of risk is understood as an extraordinary manifestation and not as an ordinary condition of a specific territory.

Specifically, the seismic risk is conceived and quantified as a multifactorial combination of three random variables, such as *hazard* (H), *exposure* (E), and *vulnerability* (V), interconnected one to the other, according to Equation (2.1):

$$R = H \otimes E \otimes V \quad (2.1)$$

This formulation measures the expected risk in a given time interval, based on the seismicity of the area, the resistance of the buildings, and anthropization i.e. nature, quality, and quantity of the exhibited heritage. The summary scheme concerning the risk analysis is depicted in Figure 2.1

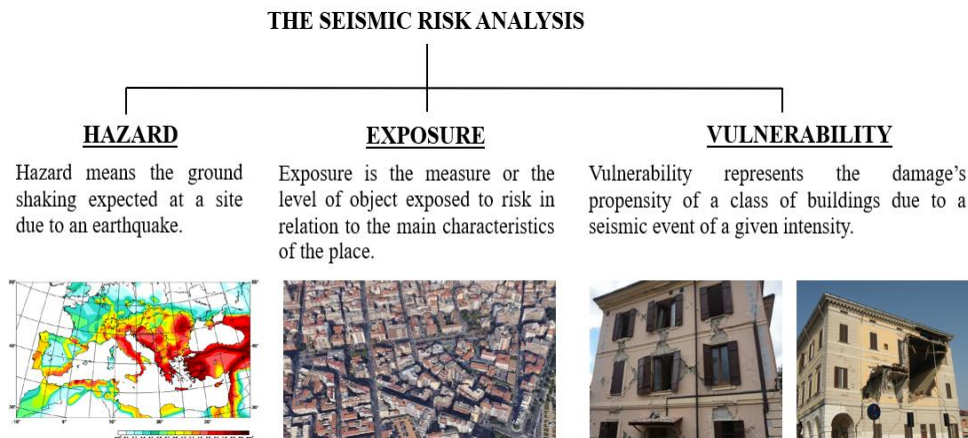


**Figure 2.1:** Concept of seismic risk analysis.

To measure and classify the impact of an earthquake, seismologists have developed various measurement scales that establish a direct correlation between the event that occurred and its perception in the surrounding environment. The first seismic scale adopted, refers to the last century. Henceforth, several intensity measurement scales have been widely used worldwide.

Generally, the Modified Mercalli scale, MMI, is accepted in the USA and it is based on the original draft devised in 1902 by Giuseppe Mercalli [57] and consequently updated by Frank Neumann [58].

The MMI scale is characterized by ten grades that measure seismic severity utilizing the classification of earthquake effects at different sites of the Earth surface.



In Europe, instead, two different scales have been adopted, Mercalli-Cancani-Sieberg (MCS) [59] and European Macroseismic Scale (EMS-98) [60], respectively. These scales are formally equivalent in terms of the perception of the effects produced and they are based on twelve grade ratings as Roman numerals from I (lower grade) to XII (higher grade).

The Shindo (JMA) [61] is used in Japan. The aforementioned scale measures the degree of perception associated with the ground shaking induced by an earthquake. The associated numerical scale is different from that generally used to describe the potential of an earthquake magnitude which reflects the source energy released. The shaking and effects become greater as the number increases, with Shindo 5 and 6 further divided into lower and upper levels.

Other seismic scales are also based on the energy released in the hypocentre area. An example of such a measurement scale is the one conceived and developed according to the study available in [62]. This classification varies from country to country concerning the built environment, the quality of buildings, and human perception. Moreover, other intensity scales are reported in [60] and [63] which describes accurately the damage suffered by buildings under earthquakes.

So, the correlation between the recorded intensity and the corresponding perception threshold has been reported in Table 1 [60].

**Table 1:** European Macroseismic Scale (EMS-98) [60].

<b>Intensity</b>	<b>Description</b>
<b>I.</b>	No perception
<b>II.</b>	Scarcely perception
<b>III.</b>	Weak
<b>IV.</b>	Largely observed
<b>V.</b>	Strong
<b>VI.</b>	Slightly damaging
<b>VII.</b>	Damaging
<b>VIII.</b>	Heavily damaging
<b>IX.</b>	Destructive
<b>X.</b>	Very destructive
<b>XI.</b>	Devastating
<b>XII.</b>	Completely devastating

### **2.1.1 Hazard**

Seismic hazard is intended as the probability that in a given area and in a certain interval of time an earthquake could occur exceeding an intensity threshold,  $I$ , magnitude,  $M_w$ , or peak acceleration, PGA, of interest.

Conceptually, based on the definition provided, it seems clear that to evaluate the possible risk, induced from the earthquake shaking, it is necessary to determine the annual probability (or rate) of exceeding a certain level of the earthquake ground shaking at the site, for a range of intensity levels [64].

Two mathematical approaches have been defined to assess seismic hazards such as Deterministic (DSHA) and Probabilistic (PSHA), respectively [65], [66].

Essentially, DSHA considers the unfavourable scenario in terms of the size and location of the earthquake. Specifically, given a generic site surrounded by different seismogenic sources, the DSHA procedure aims to first calculate the maximum shaking of each source and the minimum distance from the site. Next, the maximum contribution in terms of motion effects produced by the generic source is considered for estimating the expected level of seismic hazard [67].

Thus, the hazard model allows to identify and characterize all the seismogenic sources by finding these pieces of information from exhaustive documentation of the seismic history i.e. faults, the magnitude of the maximum earthquakes that occurred, distance from the site, of the area. For each seismogenic source, the maximum magnitude observed in the epicentre area and the distance to the site are fixed.

Secondly, the identification of the site-source distance is essential to define the worst scenario [68].

Finally, the third step is the selection of a controlled earthquake, calculate using an attenuation law that allows estimating the ground motion within the area of interest. Figure 2.2 shows a schematic framework of the DSHA's algorithm.

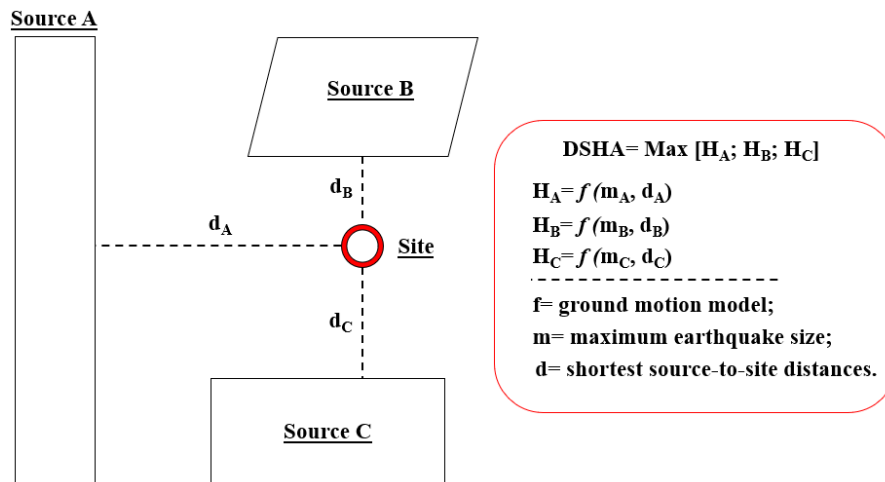


**Figure 2.2:** Framework of DSHA.

Furthermore, the method proposed in [65] evaluates the impact of a ground-shaking scenario in a given area. The PSHA procedure is composed of four steps:

- i. Identifying all earthquake sources capable of producing damaging ground motions;
- ii. Characterizing the distribution of earthquake magnitudes according to the rate of exceeding a certain completeness threshold,  $M_w^*$ ;
- iii. Characterizing the seismic sources;
- iv. Predicting the effects caused by the release of seismic energy in a given place;

Thus, the above-mentioned steps are summarized in Figure 2.3.

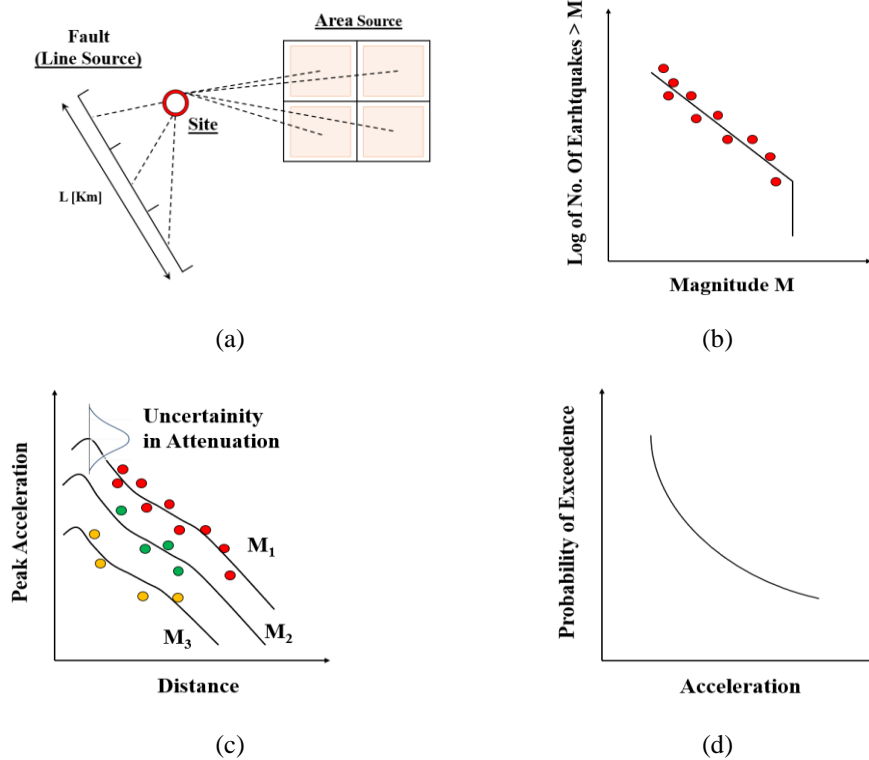


Figure 2.3: PSHA algorithm.

The probabilistic methodology is conceived according to the procedures proposed in [69], [70] and represents the most used approach to the problem of determining the characteristic of strong ground motion for engineering design.

The analysis of the seismicity of a given area is carried out through the Homogeneous Poisson Process. The basis of the method is to determine the number of earthquakes that occur in the time interval,  $t$ . In fact, given a seismogenic source, the number of earthquakes to consider are all those that have a magnitude,  $M_w$ , below the completeness threshold ( $M_w^* > M_w$ ).

It is a stationary process since the sample average of earthquakes does not depend on the period. Mathematically, the formulation governing the problem is defined according to Equation (2.2) [69]:

$$P(N_{im}(\Delta t) = n) = \frac{(\lambda_{im} \cdot \Delta t)^n}{n!} \cdot e^{-(\lambda_{im} \cdot \Delta t)} \quad (2.2)$$

where,  $\lambda_{im}$  is the rate of exceedance in the unit of time,  $\Delta t$ .

Subsequently, the seismicity of an area can be examined in terms of expected magnitude,  $M_w$ .

In fact, by resorting to the historical seismicity database of the study area, it is possible to define the seismic frequency through the given Equation (2.3)

$$\log n = a - b \cdot M \quad (2.3)$$

where  $a$  and  $b$  are the parameters depending on the Gutenberg–Richter law [71].

Finally, combining all the information described previously, the *total* probability theorem is used to defining the hazard integral [69] as reported in Equation (2.4)

$$P(IM > x) = \int_{m_{\min}}^{m_{\max}} \int_{r_{\min}}^{r_{\max}} P(IM > x | m, r) \cdot f_M(m) \cdot f_R(r) \cdot d_r \cdot d_m \quad (2.4)$$

where,  $P(IM > x | m, r)$  is the probability of exceeding an intensity measurement (IM) given a magnitude,  $m$ , and epicentre distance,  $r$ ;  $f_M(m)$  and  $f_R(r)$  are probability density functions, PDFs, for magnitude and distance, respectively.

Introducing a small simplification, the previous formulation can be expressed as a function of the rate of exceedance of a given seismic event ( $\lambda$ ). Therefore, generalizing the problem, Equation (2.5) assumes mathematical significance [69]:

$$\lambda(IM > x) = \lambda(M > m_{\min}) \cdot \int_{m_{\min}}^{m_{\max}} \int_{r_{\min}}^{r_{\max}} P(IM > x | m, r) \cdot f_M(m) \cdot f_R(r) \cdot d_r \cdot d_m \quad (2.5)$$

where  $\lambda(M > m_{\min})$  represents the exceeding occurrence probability of earthquakes higher than  $m_{\min}$ , and  $\lambda(IM > x)$  is the overcoming level related to  $IM > x$ .

In general, a probabilistic method can be considered, for all purposes, inclusive of all the uncertainties of the calculation model and allow to determine a finite probability of occurrence.

On the other hand, deterministic methods are easily implemented and are properly focused on a single event that would produce the most unfavourable case.

### 2.1.2 Exposure

The exposure (E) of an area, refers to the nature, quality, and quantity of the assets exposed to risk. Therefore, the estimation of the exposure results in the quantification of the artefacts present in an urban context such as buildings,

infrastructures as well as the number of people who will presumably be involved in the seismic event, and the evaluation of their reaction capacity.

The exposure is therefore composed of a functional component and a user component. Besides, with the development of the territory, many urban contexts present a high demographic concentration which, together with the socio-economical activities present, are hypothetically "exposed" to the seismic phenomenon and therefore the capacity to react, is drastically reduced.

Therefore, a simplified approach is generally used to define priority criteria for future urban mitigation and resilience interventions.

This procedure evaluates the exposure by determining a factor, defined exposure index  $I_e$ , obtained as the product of two further indices which are the user index,  $I_U$ , and the function index,  $I_f$ , considering the Equation (2.6) achieved below [70]:

$$I_e = I_U \cdot I_f \quad (2.6)$$

Referring to the category of buildings, the classification criterion groups the buildings that one would expect to have similar seismic behaviour.

According to the vulnerability assessment, the buildings were generally classified into vulnerability classes based on the adopted vulnerability model.

Therefore, a professional classification system is used proposed by the RISK-EU project [72] according to which the influence of occupancy related to the architectural organization of the building is taken into consideration as shown in Table 2:

**Table 2:** Exposure classification according to RISK-UE project [72].

<b>Building stock</b>	<b>Essential facilities</b>
Residential	Government functions and civil defence
Commercial	Health and medical cure
Cultural	Emergency response
Multiple-use	Education facilities
Monuments and historical Heritage	
Religion	
Industrial	
Temporary buildings	

Thus, from these considerations, it emerges that in a given urban sector, such as historical centre, the distribution of the elements exposed to risk is not uniform, therefore, high concentrations of exposed assets, would result in a proportional "sensitivity" to the risk and, therefore, both a lower capacity to react and urban resilience.

### **2.1.3 Vulnerability**

The vulnerability denotes the propensity to damage a certain class of services (buildings, infrastructures, urban services, etc.) or people, due to a seismic event.

Generally, the concept of vulnerability is directly connected to the socio-economic structure of the territory and to its capacity to absorb the seismic impact.

The drastic and inappropriate urbanization has produced, over the years, a significant reduction in the capacity to absorb the seismic impact since entire urban centres are characterized by old buildings conjunctly with limited urban spaces. Rapid urbanization and population growth in heavily populated areas have greatly increased risk perception.

In this perspective, it seems evident that the high concentration of housing churches, monuments and historic buildings, is symptomatic of an intrinsic vulnerability of the urban centre [14], [45].

First of all, it seems clear that it is necessary to investigate and then classify the urban fabric to identify its typological class. Indeed, the typological classification of a structural system is an important procedure to be implemented since it depends on the geometric and structural characterization of a given urban context. **The classification systems proposed in [73] and [74], introduce a specific construction subdivision based on the structural characteristics of buildings.**

On the other hand, building classification has been evolved starting from macroseismic intensity scales, such as the MSK–64 scale [63]. By adopting this scale, the buildings were classified based on their basic material and the type of structural system in three distinct vulnerability classes A, B, and C. Subsequently the classification scheme of the MSK-64 was updated by the European Macroseismic Scale, EMS-98 [60], in which they have been supplemented by three other classes D, E and F to take into account several structural types (i.e. steel system) as well as buildings designed with anti-seismic design levels (ERD).

A classic example of the European Macroseismic Scale (EMS-98) [60] which associates the vulnerability class to a sample of buildings, establishing a certain margin of uncertainty, is shown in Figure 2.4.

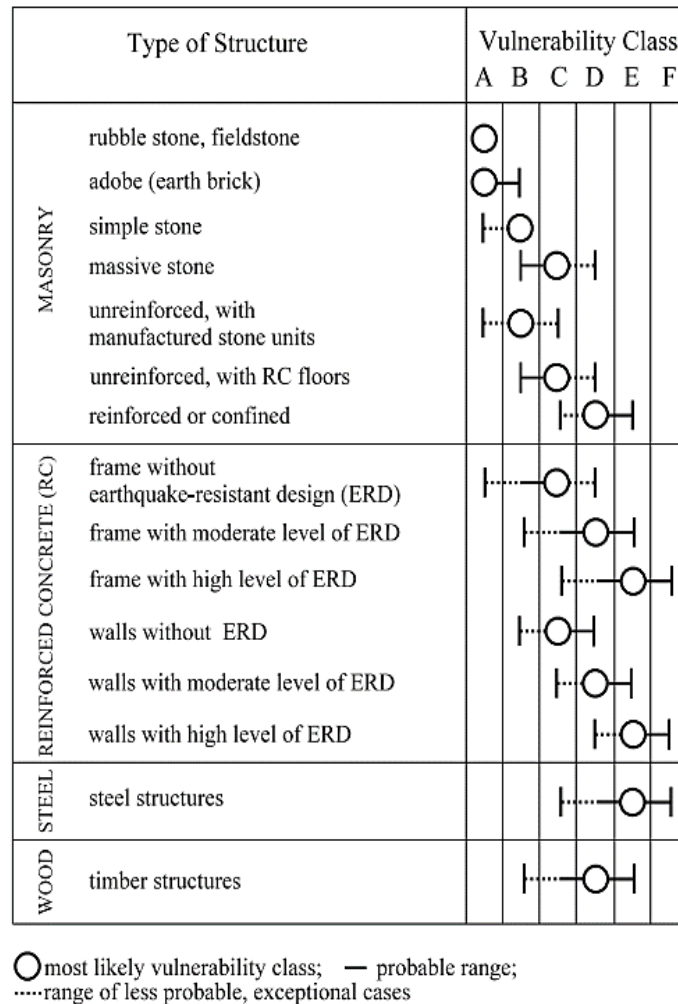


**Figure 2.4:** Inventory of the vulnerability typological classes according to EMS-98 scale [60].

Later on, a comparison between the HAZUS method [74] and EMS-98 scale [60] is depicted in Table 3.



**Table 3:** EMS 98 vs HAZUS building typology classification.

<b>EMS-98, [60]</b>	<b>HAZUS, [74]</b>
<b>Unreinforced masonry</b>	<b>Masonry typologies</b>
Rubble stone	Unreinforced Masonry Bearing Walls
Adobe (earth brick)	
Simple stone	
Massive stone	
U Masonry (old brick)	
U Masonry – r.c. floors	
<b>Reinforced/confined masonry</b>	<b>Reinforced/ confined masonry</b>
Reinforced/ confined masonry	RM Bearing walls with wood or metal deck diaphragms
	RM Bearing walls with precast concrete diaphragms
<b>Reinforced concrete</b>	<b>Reinforced concrete</b>
Frame in reinforced concrete	Concrete Moment Frame
Shear wall	Concrete Shear Walls
	Concrete Frame with U. Masonry Infill Walls
<b>Steel typologies</b>	<b>Steel typologies</b>
Steel structures	Steel Moment Frame Low-Rise
	Steel Braced Frame
	Steel Light Frame
	Steel Frame with Cast-in-Place Concrete Shear Walls
	Steel Frame with Unreinforced Masonry Infill Walls
<b>EMS-98</b>	<b>HAZUS</b>
<b>Timber typologies</b>	<b>Timber typologies</b>
Timber structures	Wood, Light frame
	Wood, Commercial and Industrial
	<b>Pre-Cast typologies</b>
	Precast Concrete Tilt-Up Walls
	Precast Concrete Frames with Concrete Shear Walls
	<b>Mobile Homes</b>

Another innovative classification was also suggested by [75]. The proposed classification, defined as *Building Typology Matrix* (B.T.M), aims to update the classification adopted by the EMS-98 method and also catalogues the structures starting from the awareness that the HAZUS method is representative of the American construction technique.

The proposal for the European classification of the sample of buildings is presented in Table 4 [75].

**Table 4:** The B.T.M typology classification according to [75].

Class	Building Typology
	Unreinforced Masonry
M1	Rubble Stone
M2	Adobe (earth brick)
M3	Simple stone
M4	Massive stone
M5	U Masonry (old brick)
M6	U Masonry – RC. floors
M7	Reinforced/ confined masonry Reinforced concrete
RC1	Concrete Moment Frame
RC2	Concrete Shear Walls
RC3	Dual System
S	<b>Steel</b>
W	<b>Timber</b>

Thus, based on this classification method, focusing on ordinary buildings, the seismic vulnerability can be understood as the probability of reaching different damage thresholds until collapse, evaluated according to the intensity of the earthquake and conditioned by its occurrence [75], [76].

From these basic concepts, it can be deduced that the reduction of the vulnerability of the built can be carried out through an opportune organization of the urban context which can be implemented only through the planning of appropriate risk mitigation procedures.

However, a vulnerability model aims to provide a measure of the possible level of damage of a class of buildings due to a calamitous event of a given intensity, defining in most cases the so-called vulnerability index, i.e. a synthetic parameter that provides important indications about the global physical vulnerability of the sample. Several methods for vulnerability assessment have been developed and proposed over the years, to evaluate and reduce the propensity to damage buildings based on an appropriate classification system [1].

Generally, these procedures can be classified into three main orders [77] to investigate and therefore mitigate the expected risk:

- i. Empirical methods;
- ii. Analytical or mechanical procedures;
- iii. Hybrid methods.

However, empirical methods evaluate the vulnerability of building aggregates based on the definition of typological classes: construction type; plano-altimetric distribution; the age of construction; functional aspects depending on the intended use. In particular, it is a semiotic approach according to which the level of detail of the analysis is adaptable to the degree and quality of the information available. Essentially, these methods allow establishing a uniqueness between the vulnerability index and damage caused by earthquakes. The quantification of the damage can be carried out through the definition of the typological vulnerability curves or, more commonly, through the damage probability matrices (DPM) for a determined class of vulnerability, based on the statistical processing of the damages caused by events that occurred (a posteriori analysis).

Mechanical methods are more sophisticated procedures than the previous ones as they require a level of detail such as to be able to perform numerical simulations using a mechanical-analytical approach. In this circumstance, non-linear analyses are performed to evaluate the seismic response of a given structure. The associated damage can be assessed by reaching a limit state identifiable by the achievement of a limit tensional state or a collapse mechanism of the structure. Finally, hybrid methods are derived from the combination of previously defined methods. This macroseismic approach is based on the definition of the European Macroseismic Scale EMS-98 [60], which implicitly defines a model of vulnerability and is applicable also in the European context.

## **2.2 Assessment methods for seismic vulnerability procedures**

In this framework, the structural vulnerability can be analysed using different methodologies to guarantee a satisfactory level of detail, depending on the availability of the data collected, and the time needed to perform the required analyses.

Diversification of the vulnerability models have been provided: empirical procedures which are related to the damage effects observed from past earthquakes; numerical assessments, based on a computational analysis which univocally establishes the correlation between both, the cause intended as the damage occurred and the effect related to the specific reference seismic event.

Therefore, a literature overview is provided among the main seismic vulnerability assessment procedures.

### 2.2.1 Empirical methods

One of the first to have systematically elaborated statistically the damage to buildings induced by real earthquakes was Whitman et al., (1974) [78].

He collected the data on the damage caused by the San Ferdinando earthquake of 9 February 1971. The analysed sample was vast and assorted, with around 1600 buildings. These buildings were catalogued diversifying the number of floors and by type of damage.

Therefore, different empirical methods for seismic vulnerability assessment are counted:

- i. Damage Probability Matrix (DPM): which expresses the conditional probability of having a level of damage,  $d$ , due to a given seismic intensity,  $I$ .  $P(D=d|I)$ ;
- ii. Vulnerability index method: indirect method because it establishes the relationship between the seismic action and the structural response through a Vulnerability Index.
- iii. Continuous vulnerability functions: expressing in a continuous form the conditional probability function,  $P(D=d|I)$ ;

#### 2.2.1.1 Damage Probability Matrix - DPM

The first damage matrices, DPMs, were developed after the earthquake occurred in San Francisco [78], for a given typological class (Figure 2.5). These matrices provide the probability of having a given state of structural damage conditioned by a seismic intensity,  $I$ .

In Europe, the first version was developed by [79] after the disastrous earthquake that happened in Irpinia in 1980. The probability model is based on the continuous binomial function to describe the distribution of the damage for the various typological vulnerability classes (A, B, and C) and different macroseismic intensities based on the MSK scale. The DPMs proposed by [80] introduced a new measure of the seismic intensity scale, replacing the MSK with the Mercalli-Cancani-Sieberg scale (MCS) [59].

Furthermore, vulnerability class C has been subdivided into two sub-categories, C1, for masonry in good condition and class C2, for RC buildings, respectively.

Damage State	Structural Damage	Non-structural Damage	Damage Ratio (%)	Intensity of Earthquake				
				V	VI	VII	VIII	IX
0	None	None	0-0.05	10.4	-	-	-	-
1	None	Minor	0.05-0.3	16.4	0.5	-	-	-
2	None	Localised	0.3-1.25	40.0	22.5	-	-	-
3	Not noticeable	Widespread	1.25-3.5	20.0	30.0	2.7	-	-
4	Minor	Substantial	3.5-4.5	13.2	47.1	92.3	58.8	14.7
5	Substantial	Extensive	7.5-20	-	0.2	5.0	41.2	83.0
6	Major	Nearly total	20-65	-	-	-	-	2.3
7	Building condemned		100	-	-	-	-	-
8	Collapse		100	-	-	-	-	-

**Figure 2.5:** DPM proposed by Whitman et al. (1974) [78].

Subsequently, the DPMs proposed by [79] has been adapted for the city of Potenza (Italy) according to [81], adding the vulnerability class D, which represents buildings constructed since 1980 and expressing seismic intensity according to the European Macroseismic Scale (EMS-98) [60].

The newest is the work proposed by [82] which leads to the definition of damage probability matrices based on the EMS-98 macroseismic scale. The peculiarity of this EMS-98 scale is the direct quantification ("few", "many", "very many") between 5 levels of damage and the levels of macroseismic intensity in the range 5-12 with 6 different classes of vulnerability (from A to F) as achieved in the § 2.3.3. The problem related to the incompleteness of the matrices was solved by the authors themselves [82] using la *Fuzzy-Set Theory*. This theory is based on the degree of membership function, according to which a class of generic elements is associated with a continuous real interval [0; 1]. The value 0 (zero) indicates that the element is not at all included in the specified set, the value 1 (one) indicates that the element is certainly included in the set.

Thus, the DPMs produced for each vulnerability class have been related to the whole population of buildings surveyed through a vulnerability index that depends on the structural type and the characteristics of the buildings such as the number of floors, irregularities, and many other vulnerability factors.

#### 2.2.1.2 Vulnerability Index Method – V.I.M

The Vulnerability Index Method [83] firstly developed for isolated buildings (not in continuity with adjacent structural units), consists of a specific form composed of 10 parameters that, to a lesser or greater extent affect the physical vulnerability of a building. An example of the vulnerability form is reported in Figure 2.6.

Parameters	Class Score, $S_i$				Weight, $W_i$
	A	B	C	D	
1. Organization of vertical structures	0	5	20	45	1,00
2. Nature of vertical structures	0	5	25	45	0,25
3. Location of the building and type of foundation	0	5	25	45	0,75
4. Distribution of plan resisting elements	0	5	25	45	1,50
5. In-plane regularity	0	5	25	45	0,50
6. Vertical regularity	0	5	25	45	0,50÷1,00
7. Type of floor	0	5	15	45	0,75÷1,00
8. Roofing	0	15	25	45	0,75
9. Details	0	0	25	45	0,25
10. Physical conditions	0	5	25	45	1,00

Figure 2.6: Vulnerability form adopted in Benedetti and Petrini et al., (1984) [83].

The vulnerability index can be evaluated according to Equation (2.7):

$$I_V = \sum_{i=1}^{10} S_i \cdot W_i \quad (2.7)$$

Finally, the vulnerability index is in the range [0-382.5] but is normalized in the range 0-100. Where 0 indicates a condition of lower vulnerability whereas, 100 is the most vulnerable building. Subsequently, according to [84], has developed two distinct vulnerability forms for the characterization of both, the façades of masonry buildings and, historical aggregates, respectively.

In Formisano et al., 2015 [85], the vulnerability form proposed (see in Figure 2.7), is based on Benedetti and Petrini's form properly updated for aggregate buildings.

Parameters	Class Score, $S_i$				Weight, $W_i$
	A	B	C	D	
1. Organization of vertical structures	0	5	20	45	1,00
2. Nature of vertical structures	0	5	25	45	0,25
3. Location of the building and type of foundation	0	5	25	45	0,75
4. Distribution of plan resisting elements	0	5	25	45	1,50
5. In-plane regularity	0	5	25	45	0,50
6. Vertical regularity	0	5	25	45	0,50÷1,00
7. Type of floor	0	5	15	45	0,75÷1,00
8. Roofing	0	15	25	45	0,75
9. Details	0	0	25	45	0,25
10. Physical conditions	0	5	25	45	1,00
11. Presence of adjacent building with different height	-20	0	15	45	1,00
12. Position of the building in the aggregate	-45	-25	-15	0	1,50
13. Number of staggered floors	0	15	25	45	0,50
14. Structural or typological heterogeneity among adjacent S.U.	-15	-10	0	45	1,20
15. Percentage difference of opening areas among adjacent facades	-20	0	25	45	1,00

Figure 2.7: Vulnerability form developed by Formisano et al., (2015) [85].

The new parameters are defined according to [85] and extensively discussed in [86-89].

Furthermore, the expected structural damage was appropriately expressed as a function of the vulnerability indicator,  $I_V$ , and the macroseismic scale (EMS-98, [60]) to correlate the seismic hazard with the mean damage grade as reported in the following Equation (2.8) [90]:

$$\mu_D = 2.5 \cdot \left[ 1 + \tanh \left( \frac{I + 6.25 \cdot V - 13.1}{Q} \right) \right] \quad (2.8)$$

having identified as  $I$ , the hazard level related to the intensity of the site,  $V$ , is the expected vulnerability threshold and finally the ductility  $Q$ -factor, ranging in the range 2.3-3.4, defined according to the building typology (Figure 2.8) [90]. The representation of the typological vulnerability curves is the derivation of the DPMs, in which, varying the macroseismic intensity, the value assumed by the distribution of the average damage,  $\mu_D$ , is univocally determined. In this way, the DPMs have been parameterized concerning a single parameter,  $V$  (normalized vulnerability index, conventionally between 0 and 1) independent of macroseismic intensity and it has been associated with each vulnerability class.

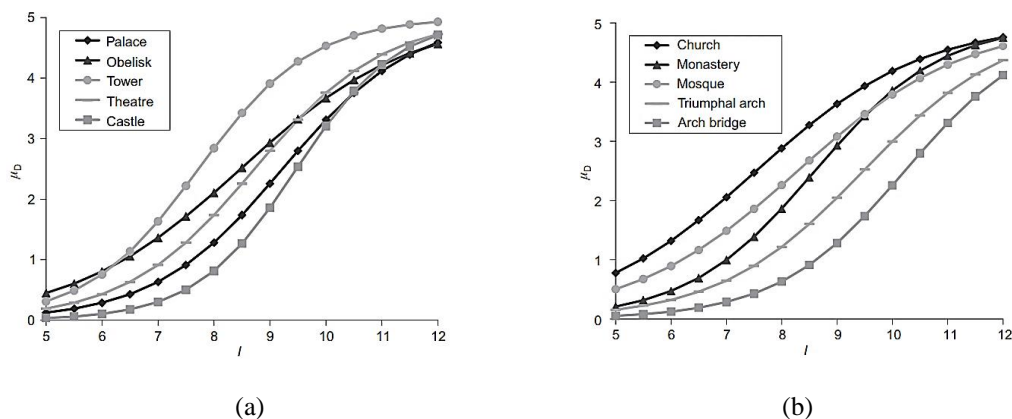


**Figure 2.8:** Vulnerability curves for each building typology according to Lagomarsino et al., (2006) [90].

### 2.2.1.3 Continuous vulnerability function

The continuous vulnerability curves are based on the damage suffered by the structures after an earthquake and were introduced slightly after the DPM. A substantial limitation concerns their derivation since Macroseismic Intensity is

not a continuous variable. This problem has been overcome by [91] through the use of the Parameterless Scale Of Intensity (PSI) to derive the vulnerability functions based on the observed damage to structures using the MSK damage scale (Figure 2.9).

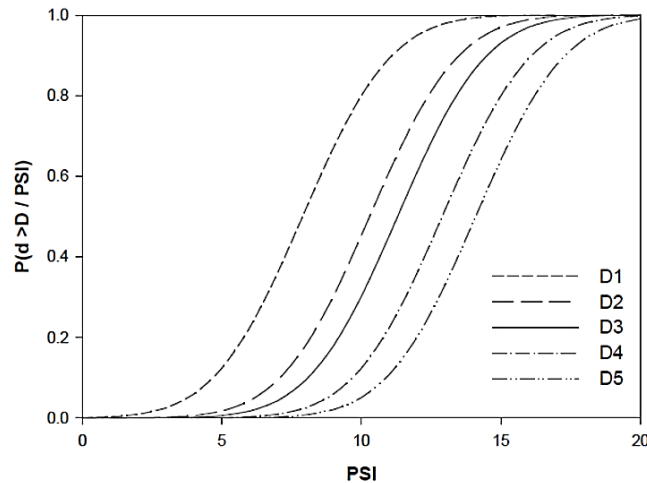


Figure 2.9: Continuous Vulnerability curves according to [91].

A study proposed by [92], converted the PSI values into PGA using empirical correlation functions. Sabetta (1987) [93] used post-seismic damage data for around 50.000 buildings to derive vulnerability curves assuming the model proposed in [94] considering a bad-rock soil condition.

## 2.2.2 Analytical methods

### 2.2.2.1 Analytical vulnerability curves and Damage Probability Matrix

Singhal and Kiremidjian [95], have developed fragility curves and damage probability matrices for three categories of reinforced concrete buildings, using the Monte Carlo simulation.

This method uses computational algorithms based on random sampling to obtain numerical results. It, therefore, represents a useful tool for overcoming computational problems related to exact tests (for example, methods based on the binomial distribution and combinatorics, which for large samples generate an excessive number of permutations).

In detail, the authors have implemented several non-linear dynamic analyses considering the contribution of different ground motions. Non-linear dynamic analyses were performed using a set of time histories for many buildings with



random structural characteristics. The output of each analysis allowed an evaluation of the global damage index based on the method proposed by [96] which has been further calibrated on a set of various structures damaged by past earthquakes.

Furthermore, based on this consideration, the derivation of both vulnerability curves and damage probability matrices has been developed by simulation analysis to overcome the limits of empirical methods. In Figure 2.10, it is possible to summarize the basic components that are needed to analytically derive vulnerability curves or damage probability matrices.

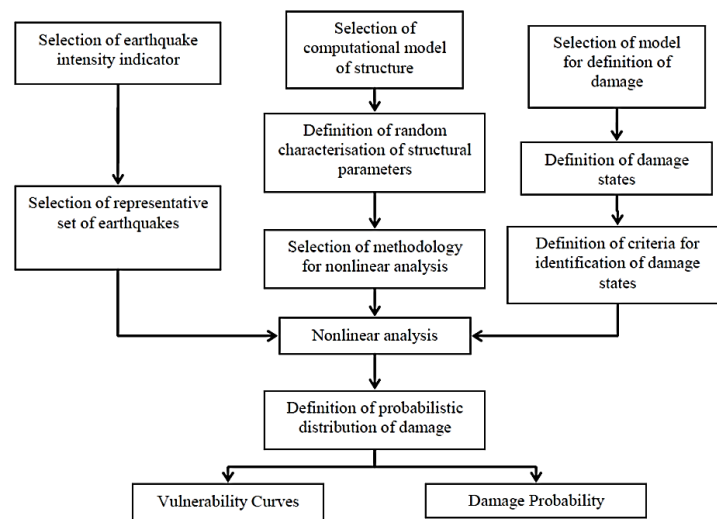


**Figure 2.10:** Descriptive layout of the calculation procedure for vulnerability curves and DPM [1].

Rossetto and Elnashai [97] have been proposed a methodology for defining vulnerability curves, applying a non-linear static analysis, and using the Capacity Spectrum Method, defined the performance point (P.P). Once the PP was determined, it was subsequently correlated to the damage calibrated on experimental data. This procedure was then repeated using different acceleration spectra related to seismic records that occurred and calibrating the vulnerability curves based on the displacement parameter.

However, the analytical vulnerability curves were frequently used as a support for vulnerability curves and empirical DPMs, thus leading to the emergence of so-called hybrid methods.

### 2.2.2.2 Hybrid methods for vulnerability estimation

Hybrid methods allow the definition of DPM and vulnerability curves, through a combination of empirical analysis and analytical methods.

This solution is particularly advantageous when there is a high degree of incompleteness about damage for certain levels of intensity for a given geographical area.

As deduced from [98] the DPM derived from the damage data observed for earthquakes occurred through the procedure of the vulnerability index method and was partially obtained from non-linear dynamic analyses performed on buildings whose models are representative of different typological classes.

The difficulties in using hybrid methods are mainly related to the calibration of the analytical results. For this reason, to eliminate or at least reduce the uncertainties associated with empirical models, it is appropriate to calibrate the empirical vulnerability curves considering the median values (50<sup>th</sup>-percentile).

#### 2.2.2.2.1 Models based on collapse mechanisms

The Vulnus Method [99], is based on the fuzzy set theory for estimation of collapse multipliers [100] and the definition of fragility curves.

Operatively, the vulnerability is studied using three indexes:

- i.  $I_1$ : which takes into account the probable in-plane mechanisms. It is defined as the ratio between the in-plane shear strength of walls in the weakest building direction and the total building weight (W) [99];
- ii.  $I_2$ : takes into account the probable out-of-plane mechanisms. It is defined as the ratio between the average acceleration related to out-of-plane mechanisms of perimeter walls and the gravity acceleration [99];
- iii.  $I_3$ : considers the intrinsic vulnerability parameters that influence the behaviour of the building [99].

The probability of exceeding the damage level (EMS-98 damage scale, [60]) for a group of buildings depends on the parameters mentioned above is given by Equation (2.9):

$$V_g = f(I_1; I_2; I_3; A) \quad (2.9)$$

where  $A$  is the mean absolute acceleration that activates the mechanisms.

The FaMIVE method [101], derives from the acronym of *Failure Mechanisms Identification for Vulnerability Evaluation* is another procedure adopted for the estimation of collapse multipliers of buildings located in historical centres. The

method is based on the identification of the probable collapse mechanisms (Figure 2.11) through the load factor deriving from an equivalent static analysis according to which, having calculated the equivalent shear capacity, the most probable mechanism is activated for the portion of the building that has the lower shear-capacity.

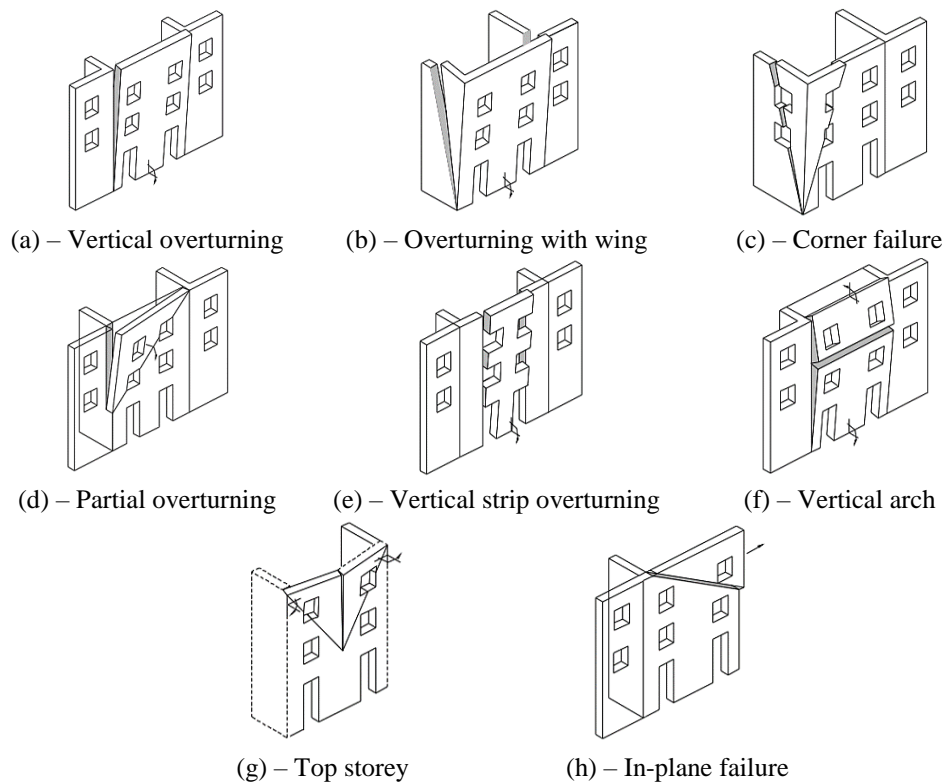


**Figure 2.11:** Possible collapse mechanisms according to the FaMIVE method [101].

#### 2.2.2.2.2 Capacity spectrum method

The HAZUS method (HAZard-US) deriving from the project carried out by the *National Institute of Building Science* (NIBS) as part of a cooperation agreement with the Federal Emergency Management Agency (FEMA), has developed a methodology applicable to the national level for estimating of potential earthquake losses [102]. The schematization of the analysis procedure is deduced in Figure 2.12

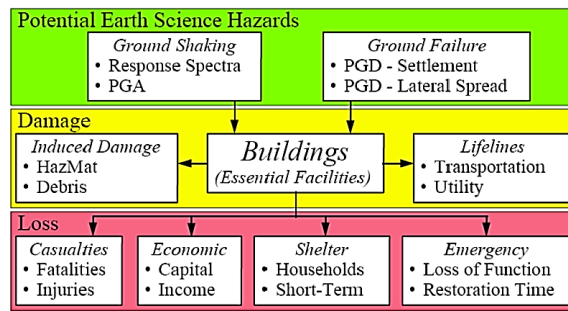


Figure 2.12: Framework of HAZUS method [102].

The vulnerability assessment procedure is based on the capacity spectrum method according to ATC-40 [103].

In this way, the performance point (P.P) of a building is given by the intersection of the ADRS (acceleration-displacement response spectra) spectrum and the respective capacity curve of the building deriving from pushover analysis [104].

However, the reduction of the demand spectrum is applied to account for the hysteretic damping that occurs when the structure has an inelastic behaviour in which the damping is based on the area enclosed by the hysteretic cycle at the acceleration and displacement response peak. Furthermore, a reduction factor is applied to the hysteretic damping to simulate, during the earthquake, the degradation of the capacity of the structure during the cyclic response.

Finally, the capacity spectrum has been developed for each typological class, to determine the vulnerability index and consequently, the various expected damage thresholds for the definition of the vulnerability curves. The framework of the mentioned procedure is shown in Figure 2.13 [102].

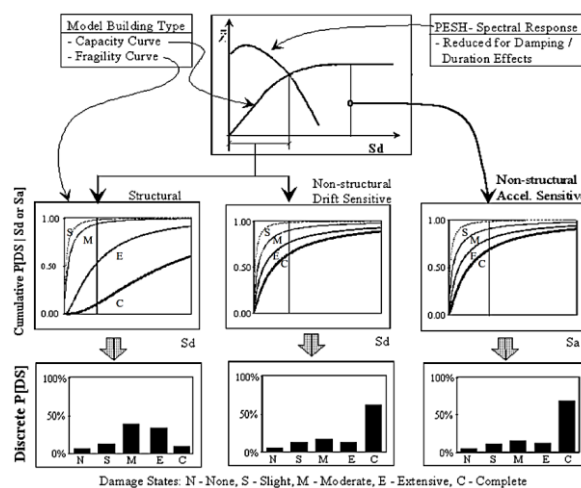
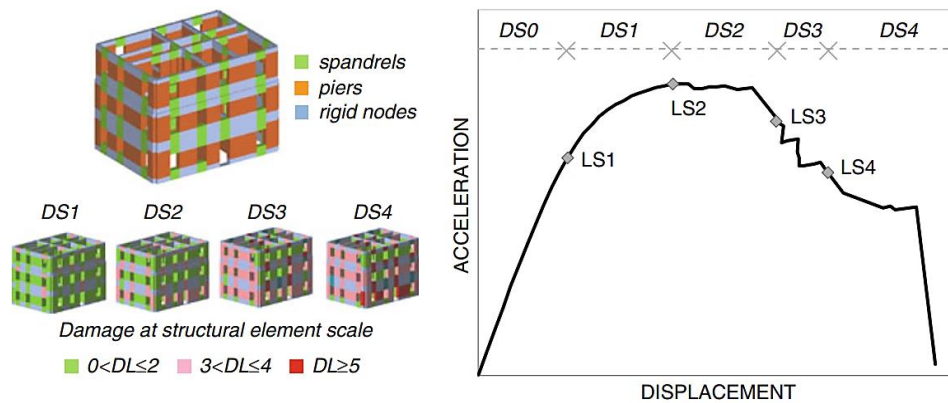


Figure 2.13: Example of essential facility damage estimation process [102].

According to [82], an analytical-mechanical procedure was presented to assess the vulnerability of masonry and reinforced concrete buildings, adopting the simplified bilinear capacity spectra according to which the basic shear coefficient is generally a function of a series of parameters such as, geographic area, seismic soil conditions, dynamic response of the structure, structural typology and the importance of the construction.

For example, as reported in [105] have proposed a multi-scale approach for masonry buildings for the definition of limit states (LS) directly on the capacity curve of an SDoF system. Nevertheless, to reduce the related uncertainties, the mean values of the damage thresholds are functions of the capacity of the structural system. In particular, four different progressive limit states (LS) are included, from LS1 (slight damage) up to LS4 (collapse), as shown in Figure 2.14



**Figure 2.14:** Example of limit states for masonry building [105].

Furthermore, the damage thresholds are based on expert judgment and have been verified based on the results of push-over analyses carried out on prototype buildings even if the details of these analyses have not been reported. The mathematical formulation is reported in Equation (2.10):

$$\begin{aligned}
 LS_1 &= 0.7 \cdot d_y \\
 LS_2 &= 1.5 \cdot d_y \\
 LS_3 &= 0.5 \cdot (d_y + d_u) \\
 LS_4 &= d_u
 \end{aligned}
 \tag{2.10}$$

where  $d_y$  and  $d_u$ , are the yielding and ultimate displacements, respectively.

However, these vulnerability curves are defined by a lognormal distribution function, expressed in terms of a given intensity measure such as PGA, PGV,

spectral displacements [105]. A classical formulation is reported according to Equation (2.11) expressed in terms of spectral displacement [105].

$$P(D = d_k) = \Phi \cdot \left[ \frac{1}{\beta} \cdot \left( \frac{S_d}{S_{Lk}} \right) \right] \quad (2.11)$$

Generally, the parameters that make up the proposed mathematical formula assume this meaning,  $\Phi$  is the standard deviation of the lognormal distribution,  $S_d$  represents the median displacement of the structural system and the denominator is representative of the previously defined damage thresholds.

The fundamental parameter for graphing the vulnerability curves is the standard deviation. In general, it is defined by Equation (2.12):

$$\beta_{ds} = \sqrt{(COV[\beta_C, \beta_D])^2 + (\beta_{T, ds})^2} \quad (2.12)$$

where the  $\beta_C$ ,  $\beta_D$  and  $\beta_{T, ds}$  are evaluated according to [105].

In particular, the variability of the uncertainties mainly concerns the definition of the capacity curve, the thresholds of the states of damage, and the population of the building, e.g. individual buildings or groups of buildings.

However, according to [106], a simplified formulation of the standard deviation has been proposed, based on the ductility of the structure, as reported in Equation (2.13):

$$\beta_{ds} = \log(\mu) \quad (2.13)$$

Instead, according to [107], the estimation of uncertainties is achieved as reported in Equation (2.14).

$$\begin{aligned} \beta_1 &= 0.25 + 0.07 \cdot \ln(\mu) \\ \beta_2 &= 0.20 + 0.18 \cdot \ln(\mu) \\ \beta_3 &= 0.10 + 0.40 \cdot \ln(\mu) \\ \beta_4 &= 0.15 + 0.50 \cdot \ln(\mu) \end{aligned} \quad (2.14)$$

## 2.3 Ground motion hazard conditions

### 2.3.1 The influence of local site effects

Over the last few years, there has been a progressive and marked development of systematic methodologies that have introduced the problem of site effects into the analysis of vulnerability procedures. A fundamental and non-negligible component in seismic vulnerability analyses, e.g., local or large-scale, is the local seismic response (LSR). This phenomenon is understood as the variability of the seismic motion on the crustal surface, as a function of the mechanical properties of the ground deposits traversed [19].

More in detail, the vibrational phenomenon induced by a seismic event in a generic site is characterized by the propagation, at a certain distance from the seismogenic source, of elastic volume waves (P-waves). These waves crossing deep rock masses parallel to the direction of the seismic wave until they reach the ground surface [108]. This dynamic condition involves a regime of compression and expansion of the soil. Similarly, the waves connected to phenomena of distortional type (S-waves) are directed orthogonally to the direction of the earthquake. The schematic representation of the site effects phenomenon is shown in Figure 2.15.

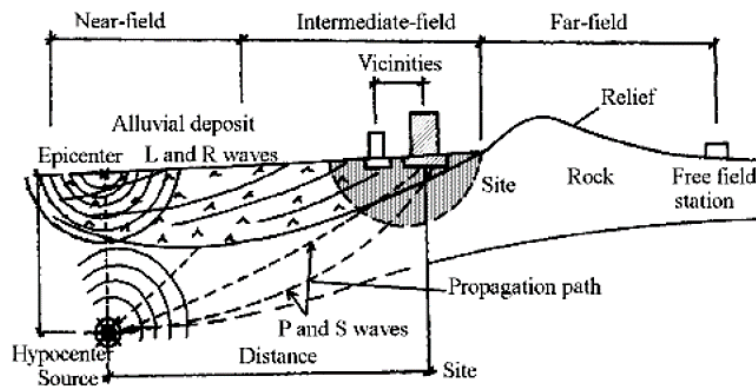


Figure 2.15: Seismic shaking and seismic waves [19].

From a physical point of view, it is clear from the previous Figure 2.15, how the site effects represent a set of changes in terms of amplitude, duration, and frequency content that the seismic motion undergoes to the bedrock up to the ground surface. In general, the seismic phenomenon is the bearer of different effects if it is located near or far from the seismogenic source.

In this circumstance, earthquakes are divided into two main categories: *far-field* and *near-field*.

In the first case, which is placed at a certain distance from the source ( $>150$  km), the vibrational amplitude of the phenomenon decreases with the distance from the hypocentre, and the frequencies associated with the signal are low. In the second case, near-field earthquakes are located in an area near the seismogenic source ( $<25$  km). These earthquakes are characterized by the type of fault rupture (strike-slip, dip-slip), the fault mechanism (dislocation instead of crack-like rupture), high-frequency content, and magnitude ( $5.0 < M_w < 6.5$ ) [19].

Furthermore, in agreement [108], earthquakes can also differ according to the Joyner and Boore distance,  $R_{JB}$  [109]. This quantity represents the horizontal projection of the minimum distance between the site and the fault rupture plane between 0 and 90 km. Thus, earthquakes are classified in *near-field* when  $R_{JB} < 25$  km and *far-fields* for  $R_{JB} > 150$  km. In this regard, greater attention is paid to near-field earthquakes which are very dangerous and devastating phenomena.

Indeed, by examining the existing literature [110-113] the effects of ground motion in case of near-field, closely related to the fault mechanism and its characteristics, are: (i) relevant vertical seismic component; (ii) directivity; (iii) velocity pulse; (iv) rotational seismic components. In this context, it is evident that the analysis of the LRS induced by the local seismic hazard represents an important element for a more effective and refined forecast of the probable damage scenarios for a given area. It is known that site and conditions can significantly influence the ground motion and consequently exert a substantial increase in terms of damage caused by the earthquake on the building stocks. From this, it can be highlighted that risk analyses, regardless of the methodology used, the influence of site conditions cannot be neglected. Therefore, this type of problem allows the implementation of accurate seismic risk mitigation plans.

According to the study conducted by [114], when the hazard is conceived in terms of macroseismic intensity, empirical correlations have been defined (based on post-event statistical analysis) to provide the increase of macroseismic intensity depending on the type of soil conditions as reported in Table 5. As can be seen from the aforementioned table 5, the seismic intensities tend to increase from granites ( $\Delta I=0$ ) to moist fill ( $\Delta I=3.3-3.9$ ).



**Table 5:** Intensity increments  $\Delta I$  for different soil conditions [114].

Soil condition	$\Delta I_M$
Granites	0
Limestone, Sandstone, Shale	0.2-1.3
Gypsum, Marl	0.6-1.4
Coarse-material ground	1.0-1.6
Sandy Ground	1.2-1.8
Clayey Ground	1.2-2.1
Fill	2.3-3.0
Moist ground	1.7-2.8
Moist fill	3.3-3.9

Alternatively, [115] proposes that, when the seismic hazard is expressed in terms of peak ground acceleration (PGA), the local amplification factor,  $f_{PGA}$ , has been evaluated as the ratio between the site spectral acceleration and the corresponding soft-rock outcrop spectral acceleration at the same time. Subsequently, the increment in terms of macroseismic intensity for different geological conditions was evaluated based on the soil factor as reported in Table 6.

**Table 6:** Amplification factors,  $f_{PGA}$ , and corresponding intensities [115].

Soil condition	$f_{PGA}$	$\Delta I_M$
Holocene	3.0	2.3
Pleistocene	2.1	1.6
Quaternary volcanic rocks	1.6	1.0
Miocene	1.5	0.9
Pre-Tertiary	1.0	0

Faccioli, (2006) [116], within the European project RISK-UE [72], [107], has distinguished two different methodologies namely: levels I and II, respectively. to take into account the site effects for scenario analyses. The level I approach is obtained from the interpretation of the local seismic response measurements or using the geological map of a determined site. The second approach, level II, takes into account the data obtained employing detailed analysis from a geotechnical point of view. The substantial difference between the two approaches lies in the quantity and quality of pieces of information retrieved to exhaustively characterize the morphology and stratigraphy of a bank of soil.

Depending on the type of level considered, without distinction, the data collected must be scrupulously analysed and processed allowing the tracing of the shear wave profile in the 30 m ( $V_{s,30}$ ) of the analysed area.

Based on these studies, the same authors proposed a one-to-one correspondence between the type of soil bank (classifying it based on the geomorphology and propagation of shear waves,  $V_{s,30}$ , respectively) and the increase in macroseismic intensity in agreement on the EMS-98 scale [60], as shown in Table 7.

**Table 7:** Soil classes and range of shear wave velocity ( $V_{s,30}$ ) and corresponding intensity increments ( $\Delta I$ ) [116].

Soil Class	Stratigraphic profile	$V_{s,30}$	$\Delta I_{EMS-98}$
A	Rock geological formation	>800	0
B	Deposits of very dense sand	360-800	0
C	Deep deposit of dense or medium dense sand	180-360	0.5
D	Deposits of loose-to-medium cohesionless soil	<180	1.0

Consequently, Giovinazzi, (2009) [117], proposes a methodology of evaluation of the seismic vulnerability that implicitly takes into account the effects of local amplification based on a macroseismic approach. In this case, the increases of macro-seismic intensity are derived based on the class of buildings and soil conditions. In particular, the local amplification coefficient,  $f_{PGA}$ , is evaluated as a function of the elastic response spectrum,  $S_{ae}$ , for a given vibration period,  $T$ .

This coefficient has been evaluated as the ratio between the elastic spectral acceleration of a generic type of soil,  $k$ ,  $S_{ae, k}(T)$ , evaluated for the fundamental period,  $T$ , and the corresponding spectral acceleration  $S_{ae, A}(T)$  in case of bedrock. The increase in macroseismic intensity is obtained by applying Equation (22):

$$\Delta I = \frac{\ln(f_{PGA})}{\ln(c_2)} \quad (2.15)$$

where,  $f_{PGA}$  referred to the spectral form EC8 for a magnitude,  $M_w$ , greater than 5.5, and the coefficient  $c_2=1.6$  according to the intensities-acceleration correlation law. Similarly, according to [118], have shown how the influence of local effects plays a fundamental role in risk analyses at a territorial scale. The proposed methodology, for building aggregates, has shown that the expected damage increases significantly.

This treatment has allowed us to identify the local amplification factor,  $f_{PGA}$ , through a mechanical-parametric approach, according to which  $n$ -damage scenarios have been contextualized varying the seismogenic site-source distance, depending on the soil class and the topographic category [119].

### 2.3.2 The main characteristic of a near-field earthquake

Nowadays, a remarkable scientific sensitivity was shown concerning the effects induced by near-field earthquakes. Within the area near the source, the induced effects are influenced by the rupture mechanism, the direction of propagation of the rupture concerning the site location, and the possible ground displacements due to the fault mechanism. Furthermore, the characteristics of near-source ground motion result in a long period and a high-velocity pulse.

According to [120], near field earthquakes are characterized by specific peculiarities that they preserve due to their reduced site-source distance. They would mainly be:

- i. rupture directivity;
- ii. amplification of horizontal and vertical components;
- iii. peak ground velocities;
- iv. velocity pulse period;
- v. number of significant pulses;
- vi. vertical component.

In detail, *rupture directivity* is an effect influenced by the rupture of the fault system according to which the in the direction of rupture propagation the effects are more severe than in other directions distant from the source of the earthquake.

Most of the seismic energy generated near the rupture, arrives in a very short time interval, resulting in a single and large long-period pulse of motion.

As an example, the 1999 Chi-Chi earthquake [19], is the result of slipping of a thrust fault (Figure 2.16). As can be seen, the normal velocities generated by ground motions are higher than the parallel ones since the largest dynamic ground velocities are coincident with the ground displacement and occur in a very short time interval.

Thus, comparing the effects of directivity, the rupture is similar, except for the fling slip displacements, which are not present in the case of thrust earthquakes.

Therefore, the main parameters that characterize the near-field trumps are: amplification of horizontal and vertical components, peak ground speed, pulse period, and the number of significant pulses as indicated in [121].

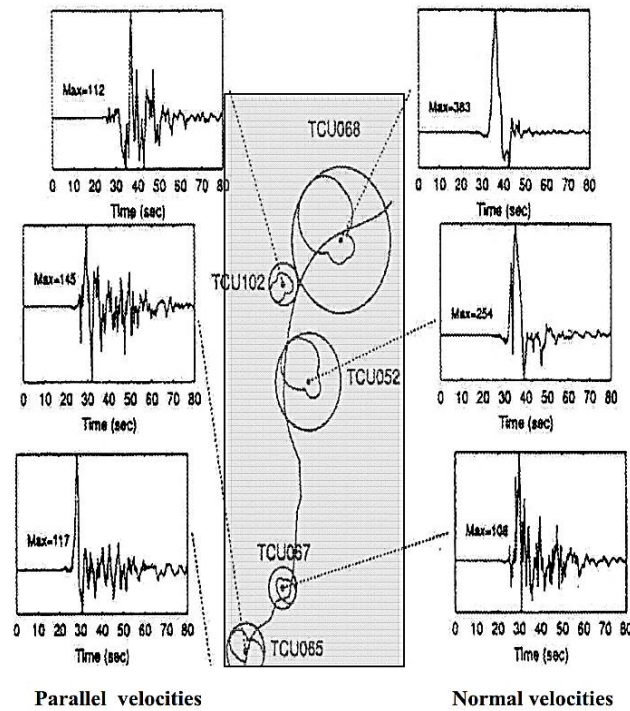


**Figure 2.16:** Velocity time histories recorded after the 1991 Chi-Chi earthquake [19].

Regarding the *amplification of horizontal and vertical components*, it has been observed that the horizontal accelerations, in the case of near-field, undergo a considerable increase, and tend to decrease for distances greater than 30 km from the seismogenic fault [19].

Consequently, the *peak ground velocity* is the most important parameter for characterizing the ground motions near-source areas. This factor significantly influences the induced potential damage due to the high effect on the material properties (strain rate) as reported in [19], [122].

After the Imperial Valley earthquake of 1979, the velocity records associated with the seismic phenomenon showed that the maximum peak velocity reached, in the case of forwarding directivity (recording stations near El Centro Arrey), was 120 m/sec, while in case of backward directivity was around 40 m/sec [123] as reported in Figure 2.17.

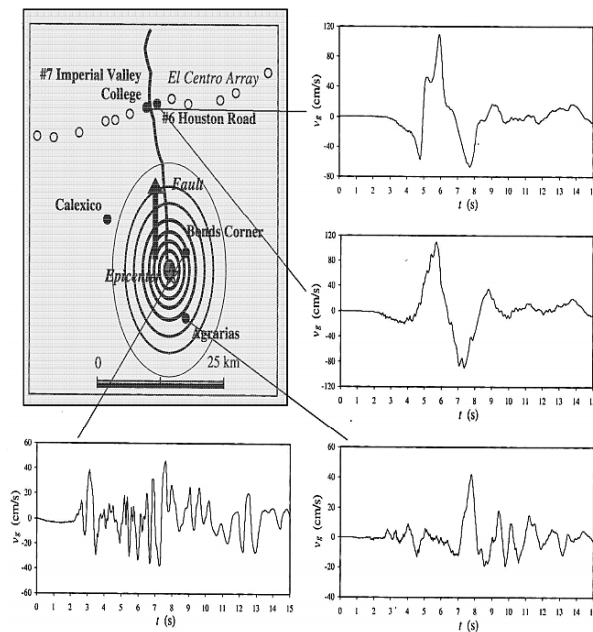


**Figure 2.17:** Near-source velocities of the 1979 Imperial Valley earthquake [123].

Another important feature is the *velocity pulse period*. Near the source, the velocities recorded, produced long and significant impulses of about 1-2 seconds.

According to [124], [125], [121] a direct dependence was observed between the pulse period and magnitude [19].

They have noticed that structures characterized by short vibration periods are subject to significant amplification. Conversely, velocities increase proportionally with increasing magnitudes and pulse periods [126].

The number of significant pulses denotes the number of velocity pulses whose amplitudes are at least 50% of the peak velocity of the ground motion [19].

From what has been specified, it has been observed that the main characteristic of near-field earthquakes is the number of reduced cycles of velocity pulses that satisfy these criteria. Generally, according to what is filed in Figure 2.17, the Imperial Valley earthquake is a classic example of cyclical pulses three or a maximum of four pulses have been generated [19].

Finally, the *ground motion vertical component*, near the seismogenic source, is associated with the vertically propagating compressive P-waves. As it knows, the wavelength of P-waves is shorter compared to the S-waves (shear waves), and it is characterized by very high frequencies pulse (velocity and displacement) and relatively long period [127], [19].

Normally, the vertical component has a lower energy content than the horizontal one but it tends to have all its energy concentrated in a restricted area producing very devastating effects on the engineering structures (Figure 2.18).

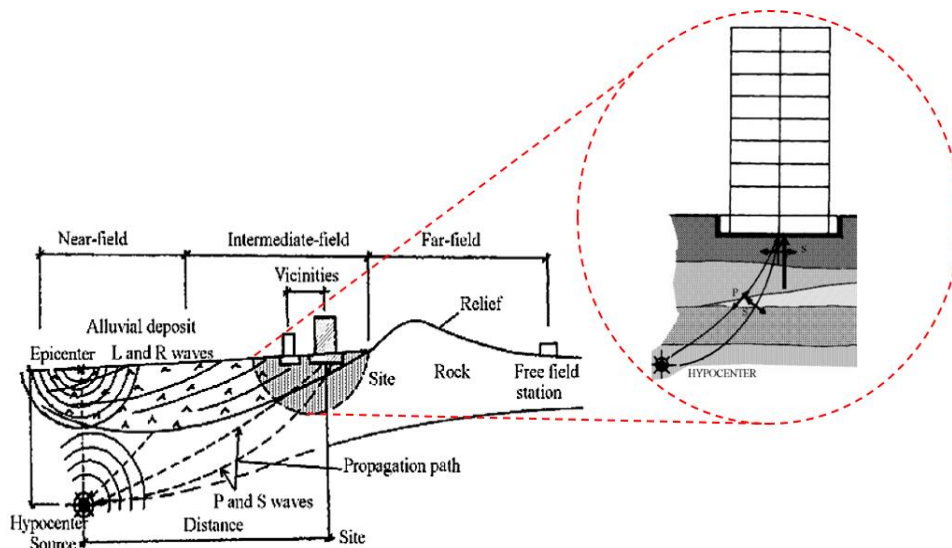


**Figure 2.18:** Vertical component effects [19].

The behaviour of these components is related to the vertical to horizontal peak ground acceleration ratio (V/H).

This ratio provides the influence of the vertical component concerning the horizontal one in a given area, for a given event of magnitude,  $M_w$ .

Currently, the design codes suggest adopting the vertical component in the seismic calculation only for some types of structures (main structures with very large overhangs). However, the vertical component is still derived directly from the horizontal components.

This procedure was originally proposed by [128] according to which the ratio between the vertical and horizontal mean accelerations should be equal to 2/3.

Furthermore, this condition has been strongly denied as recent earthquakes have shown how the V/H ratio, in the epicentre area, exceeds unity [17]. The first studies conducted by N.A. Abrahamson [20], and later on by N.N. Ambraseys [129], confirmed that the value of 2/3 is rather unreasonable, especially in epicentre areas. The confirmation of what has been asserted is represented by the earthquakes that occurred in the 1994 Northridge earthquake in California, which has produced a V/H ratio of 1.79, and the 1995 Hybu-ken Nanbu earthquake which has provided a V/H ratio up to 1.63 [17], [19].

To take into account, the vertical component, [18] proposed, starting from the data deriving from the Imperial College database, a graph showing that the ratio

V/H tends to decrease to increase in epicentre distance varying the magnitude,  $M_w$  (Figure 2.19).

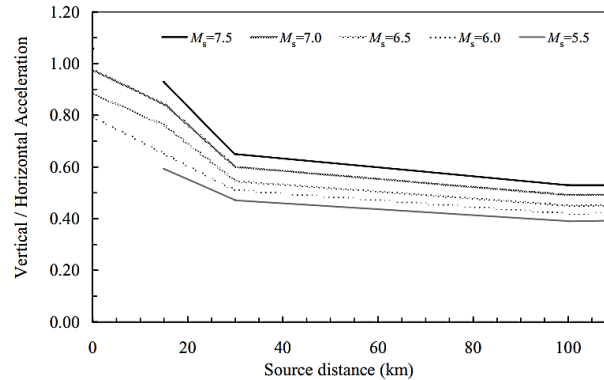


**Figure 2.19:** Vertical to horizontal acceleration ratio for different magnitude,  $M_w$ , and source distances,  $R$  (km) [108].

Alternatively, the vertical acceleration can be considered employing seismic attenuation laws according to the suggestions proposed by [130], [129], [131] and [132]. Recently, earthquakes occurred in Italy (L'Aquila, Amatrice, Accumoli, Norcia, Arquata del Tronto, Pescara del Tronto, Norcia, and Castelluccio di Norcia) have shown how the influence of the vertical component in epicentral areas has a primordial aspect due to the high level of damages observed. With this awareness, in the next paragraph, are shown the drastic effects that the vertical component has indiscriminately caused on built-up areas.

### 2.3.3 The effect of recent destructive Italian earthquakes

#### 2.3.3.1 L'Aquila earthquake

On 6 April 2009 (3:32:12 GMT), a seismic event of magnitude  $M_w=6.3$  ( $M_s=6.3$ ,  $M_L=6.2$ ), according to the Italian Institute of Geophysics and Volcanology (INGV, [133], [134]) have hit the Abruzzo Region (Central Italy), with the epicentre circumscribed at 10 km (coordinates 42.348 N, 13.380 E) located near the City of L'Aquila (about 7 km south-west), a city of 73.000 inhabitants (Figure 2.20). The death toll has been enormously high. Approximately 305 people died and over 1500 wounded.

A vast area, including the historic centre of L'Aquila, the suburbs, and many neighbouring villages, was hit by the seismic event.

The damage inherent to the structures was considerable, affecting both old and recently constructed buildings.



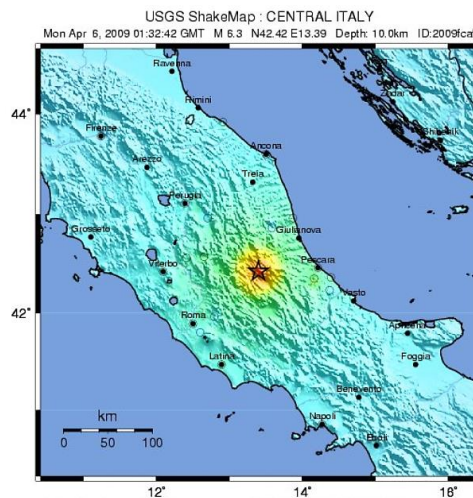


**Figure 2.20:** USGS ShakeMap of Central Italy earthquake [133].

The focal mechanism was of an extensive type with fault planes oriented in the NW and SE directions.

The rupture segment has a depth between 2 and 10 km and a length between 15 and 18 km, respectively. The event is intended as a near-field phenomenon that has produced devastating effects and high vertical PGAs.

The recordings' mainshock has been obtained from the most relevant four stations, indicated as AQQ, AQA, AQV, and AQK, are depicted in Figure 2.21.

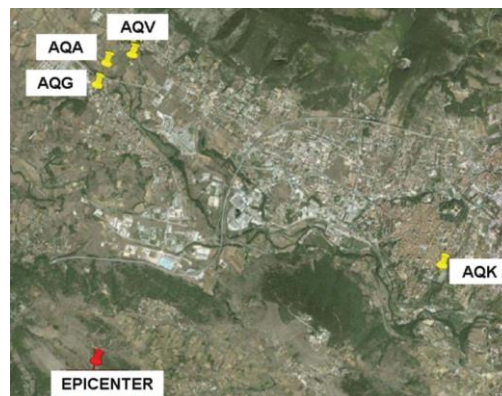


**Figure 2.21:** Recorded stations and epicentre location [135].

The elaborated elastic spectra, horizontal and vertical components, have a 5% damping and were compared with the current Italian Code NTC 2008 [37] as reported in Figure 2.22 [135].



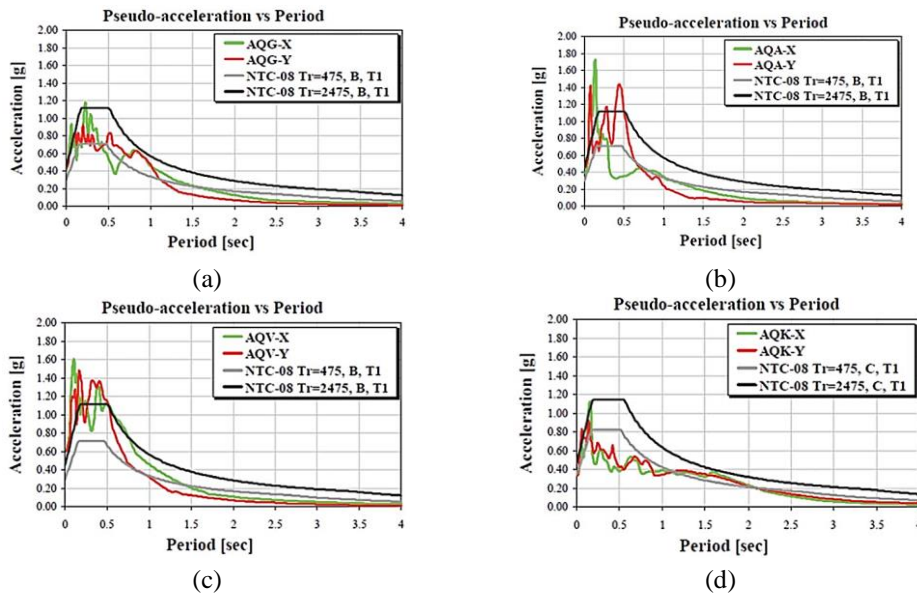


**Figure 2.22:** Pseudo-acceleration spectra of the L’Aquila seismic event mainshock compared to the NTC08 Italian Code [135].

Similarly, since it is an event classified as near-source, the spectra were also processed in the vertical direction and compared with the reference Italian Code [37] for a return period,  $T_r=475$  years and  $T_r=2475$  years, respectively, considering a soil category T1 (Figure 2.23).

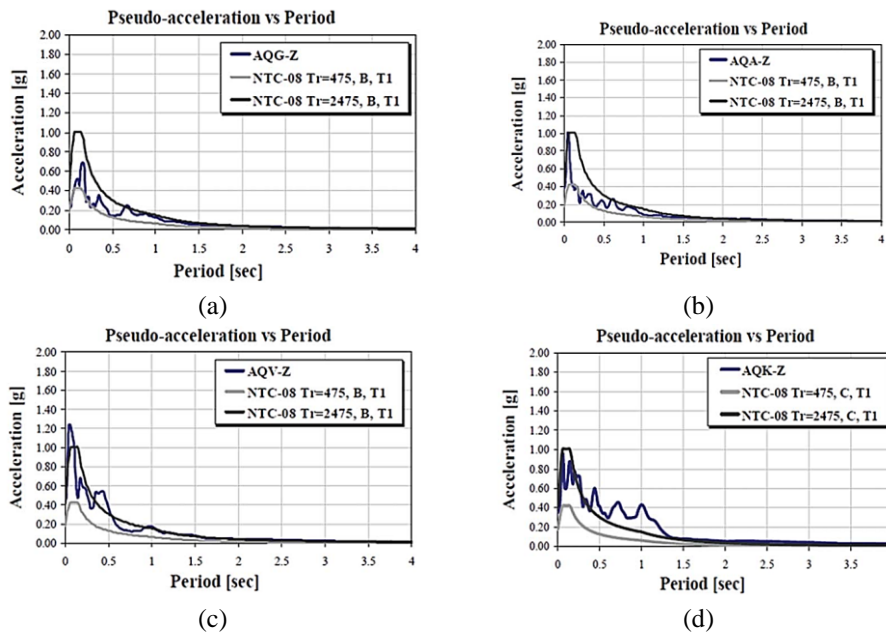


**Figure 2.23:** Vertical pseudo-acceleration spectra of the L’Aquila seismic event mainshock compared to the NTC08 Italian Code [135].

As can be seen from the analysis of the spectral accelerations that occurred, for the AQV station, the maximum PGA value recorded for the horizontal direction X is 0.63 g and the maximum vertical component recorded is 0.42 g.

Similarly, for the AQK station, the vertical component takes on higher values (0.35 g) and is comparable to the horizontal one (0.34 g) with an increase of 3%. Furthermore, the values of the vertical acceleration observed were enclosed in the range from 0.22 g to 0.42 g, respectively, and are responsible for considerable damage to the structures.

### 2.3.3.1.1 General overview on damage assessment

In general, the affected area was devastated by a significant seismic event. All the buildings have suffered considerable damage, especially masonry buildings (URM). The building stock has suffered considerable losses from a historical point of view [135].

Monumental buildings, historic buildings in Romanesque and Renaissance style were significantly damaged and declared uninhabitable.

It has been estimated that over 50% of the buildings in the towns of Onna and Paganica (small district within the City of L'Aquila) have been almost destroyed.

The damages detected after the seismic event are shown below (Figure 2.24).



(a)



(b)



(c)



(d)



(e)



(f)

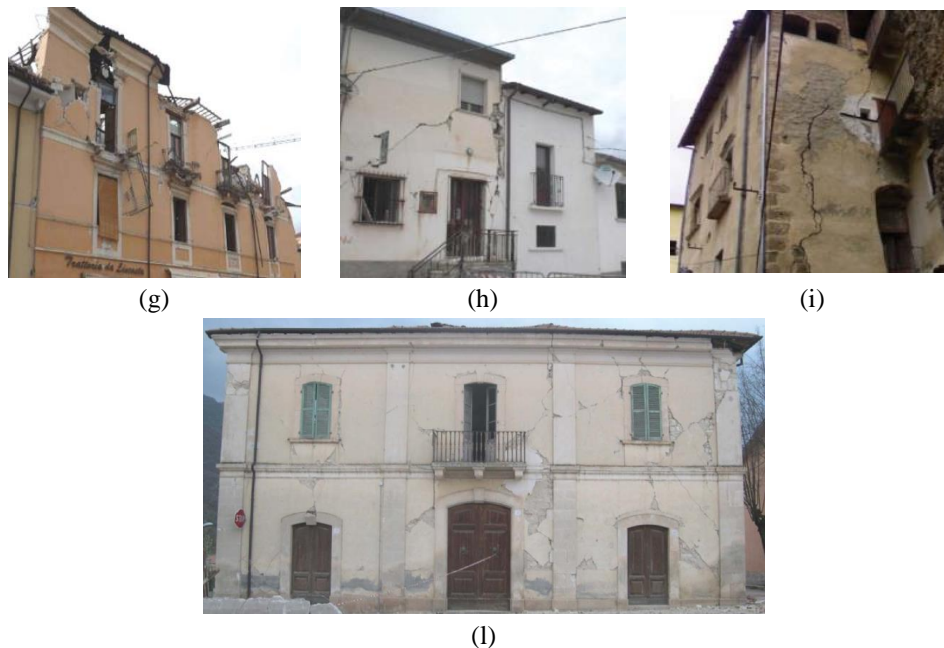


**Figure 2.24:** Damages surveyed after the L'Aquila earthquake [135].

Thus, it can be seen that the free field effects, due to the reduced site-source distance (near-field earthquake), have generated a high vertical PGA which, in combination with the soil amplification, has caused a reduction of shear capacity of the load-bearing elements with the consequent disaggregation of the walls. In particular, there are widespread diagonal cracks mainly induced by the horizontal components in the two main directions X and Y, respectively. Moreover, the vertical cracks detected have propagated in correspondence of the spandrel beams and near to the openings (Figures 2.24 (c), (e), (g), (h), (l)). This field evidence is suitable to comply with the damage found in Banloc after the earthquake of 1991, highlighting how the ground motion vertical component is not negligible but essential to consider in the seismic assessment.

### 2.3.3.2 Central Italy earthquakes

On August 24<sup>th</sup> and later on October 30<sup>th</sup>, two strong earthquakes struck Central Italy (near the border along with Lazio, Abruzzo, Umbria, and Marche Regions). In particular, the epicentre has been localized in the Apennines range, near the City of Accumoli, with a fault rupture length of approximately 25km. The main shock occurred on 24 August 2016, had a magnitude,  $M_w$ , equal to 6.0 on the Richter scale, with its epicentre located between the municipalities of Accumoli (RI) and Arquata del Tronto (AP), Pescara del Tronto (AP), Norcia (PG), Castelluccio di Norcia (PG).

Subsequently, two replicas (with a moment magnitude of 5.4 and 5.9, respectively) took place on 26 October 2016 with epicentres on the Umbrian-Marche border, between the municipalities of the province of Macerata di Visso, Ussita, and Castelsantangelo Sul Nera.

Consequently, in a territory already affected by the seismic sequence that took place on August 24<sup>th</sup>, on October 30<sup>th</sup> 2016 the strongest magnitude 6.5 was recorded with its epicentre between the municipalities of Norcia and Preci, in the province of Perugia (Figure 2.25).

The rupture mechanism that gave rise to the three main shocks was obtained by the Time Domain Moment Tensor technique and implemented at the INGV National Seismic Center [136]. This type of mechanism presents a normal fault rupture, following the extensional regime of the Central Apennines which caused the earthquakes in Colfiorito ( $M_w$  6.0 in 1997) and the City of L’Aquila in 2009, with a magnitude,  $M_w$  equal to 6.1 [135]. These events are of considerable importance but also on a global scale since they increase towards near-source phenomena which are usually poorly represented in global strong-motion databases [136].

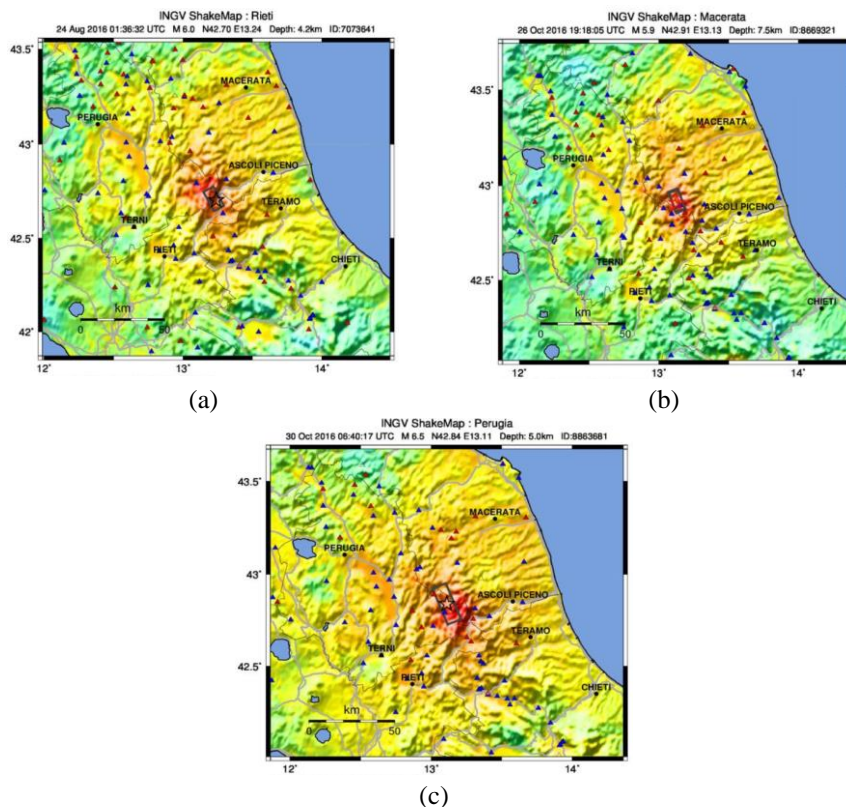


**Figure 2.25:** ShakeMap of the events that occurred on 24<sup>th</sup> August (a), 26<sup>th</sup> October (b), and 30<sup>th</sup> October 2016 (c) [136].



Referring to the event that occurred on 24<sup>th</sup> August, the peak ground acceleration of 0.45 g has been recorded, with a maximum peak of 0.86 g recorded only in Amatrice (which amplified the violence of the earthquake and aggravated the damage to the building heritage due to the very closed site-source distance, <30 km). As for the event of October 30<sup>th</sup>, the ground acceleration values recorded were 0.48 g, with a maximum PGA= 0.76 g in Arquata del Tronto. Moreover, considering the maximum PGA recorded in the vertical direction in the City of Amatrice, was 0.54g, as reported in Figure 2.26 considering the recording station MZ12.

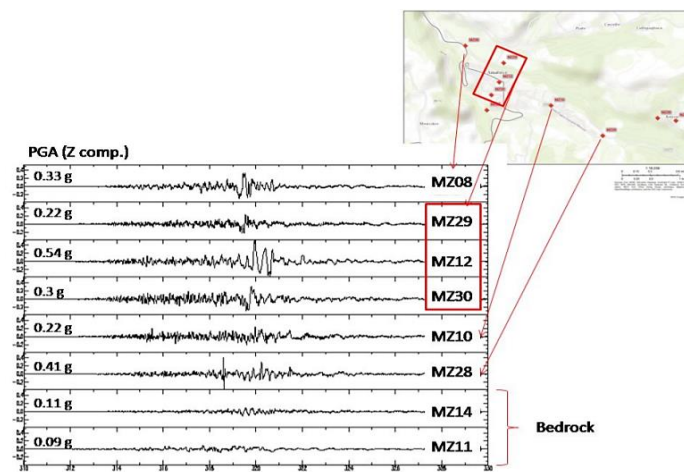


**Figure 2.26:** Maximum PGAs in vertical direction recorded during the seismic event on 30th October 2016 near the City of Amatrice [136].

According to the study conducted by Mariani et al., 2019 [41] on the effects induced by the vertical component, the superimposed accelerograms referred to the Accumuli station located at 18.6 km from the epicentre, are shown.

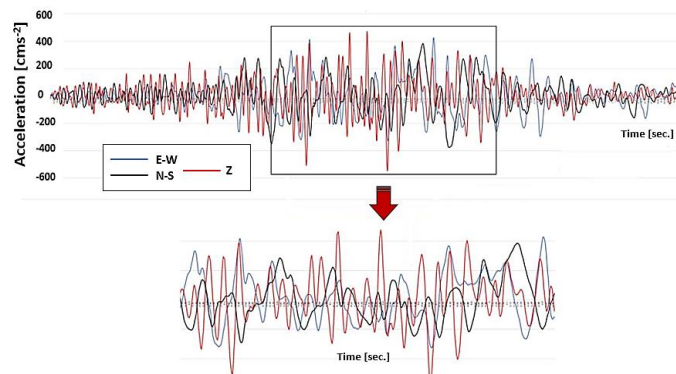


**Figure 2.27:** Recorded accelerograms after the Central Italy sequence on 30th October 2016 [41].

As can be seen, the vertical accelerations (Z) are characterized by a high frequency concerning the horizontal components (N-S and E-W).

In particular, it is noted that the vertical component reaches a maximum peak acceleration of 0.54 g at 4.44 seconds.

In general, this cyclic effect causes a reduction in terms of compressive strength of the masonry which will be subject to disaggregation caused by the horizontal components. This phenomenon is typical for near-field events and it is the cause of extensive damage and collapse of the entire urban centre.

#### 2.3.3.2.1 Damage recognition

The majority of the present building heritage was built in non-reinforced masonry structures (URMs). The masonry buildings surveyed have a high degree of seismic vulnerability due to obsolete construction techniques about seismic action. The lack of connection between floors and perimeter walls together with a planimetric irregularity due to restructuring works has considerably compromised the capacity of the structures against seismic action.

The walls present are often made up of pebbles and rounded river boulders, with a poor internal connection, merged with a sandy or mud-based mortar [137].

Furthermore, the advent of an "extraordinary" event has strongly influenced the building with countless deaths and destroyed cities. In this circumstance, the simultaneous occurrence of PGAs (horizontal and vertical) almost equal to the gravity acceleration, has produced a devastating scenario. The damages detected after the seismic events that characterized Central Italy have been shown below.

##### i. Amatrice



(a)



(b)



(c)

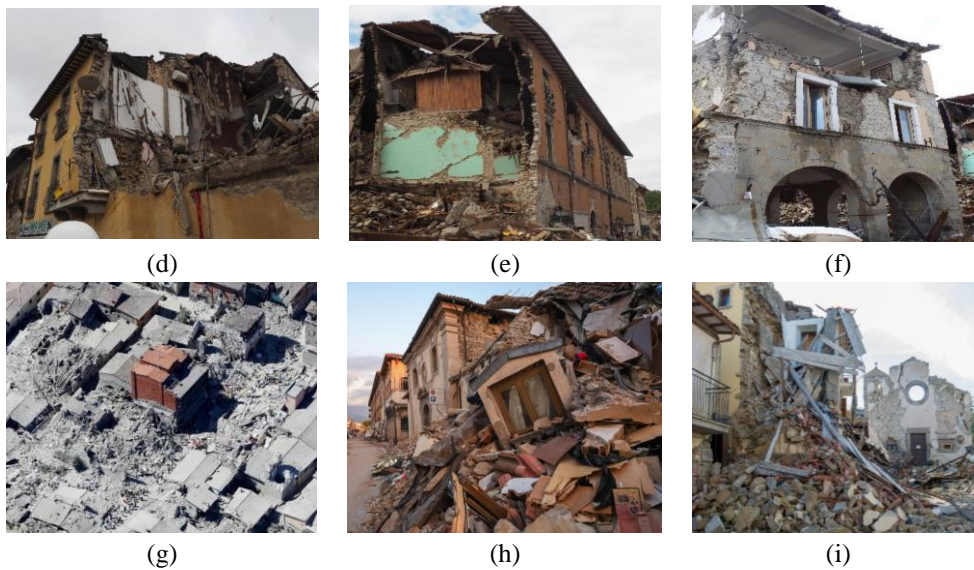


**Figure 2.28:** Damage detected after the Amatrice's earthquake [137].

In particular, from the analysis of the damages observed, the vertical component caused a variation of the stress regime in the walls. Two different conditions are to be considered fundamental: (i) the vertical component is concordant with the gravity loads; (ii) the vertical component is in opposition to the direction of gravitational loads.

In the first case, there is an increase in the capacity of the structure since the compression in the wall panels increases, and consequently, the shear strength increases as well.

Conversely, in the second case, the vertical component causes the raises of the macro elements constituting the wall panel. In this condition, cohesion and friction are lost between the faces of the elements placed in contact with each other and, therefore, compression and shear strengths are reduced and the panel manifests its vulnerability. From this consideration, it appears that these effects strongly depend on the frequency content of each record and tend to cause the activation of collapse mechanisms, in-plane, and out-of-plane, respectively (Figure 2.28) [137].

ii. Accumuli

The conditions of the city after the seismic sequence that began on August 24<sup>th</sup> and ended on October 30<sup>th</sup> are irreversibly catastrophic. In the city of Accumuli, although located near the epicentre of the August 24<sup>th</sup> event, most of the buildings collapsed due to the events that occurred in October. The main reason is due to fatigue i.e., the cumulative damage following the seismic sequence occurred.

In this case, the buildings, characterized by a clear technological deficiency (masonry walls and timber horizontal structures), showed all their fragility towards remarkable seismic actions (Figure 2.29) [137].

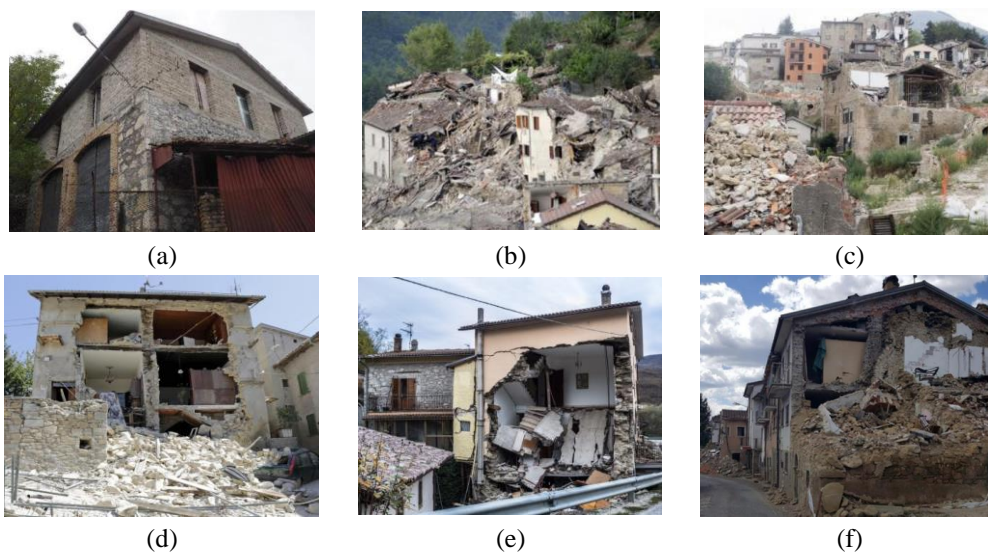


**Figure 2.29:** Damage assessment in the City of Accumuli [137].

In particular, it has been observed that the vertical component favours the overcoming of the seismic capacity of the buildings causing, consequently, a significant variation of the axial stress in the external walls.

This variation affects the entire structural body since the walls do not support the shear actions and favour the activation of overturning mechanisms.

iii. Arquata del Tronto

Arquata del Tronto is a town in the province of Ascoli Piceno with 1300 inhabitants. The historic centre is typically characterized by load-bearing masonry buildings with relatively poor mechanical characteristics erected around the main square [137].



From a seismological point of view, Arquata del Tronto falls within the seismic crater with PGA occurred, about the event of 24<sup>th</sup> August 2016, very high in the epicentral area. The magnitude event,  $M_w = 6.2$  produced peak ground accelerations (PGA) greater than 0.3 g. In particular, the violence of the earthquake was related to the Joyner-Boore distance ( $R_{jb}$ ), that is the minimum distance between the site and the rupture surface projection, highlighting high PGA which for the city of Arquata del Tronto were between 0.56-0.68 g (Figure 2.30) [137].

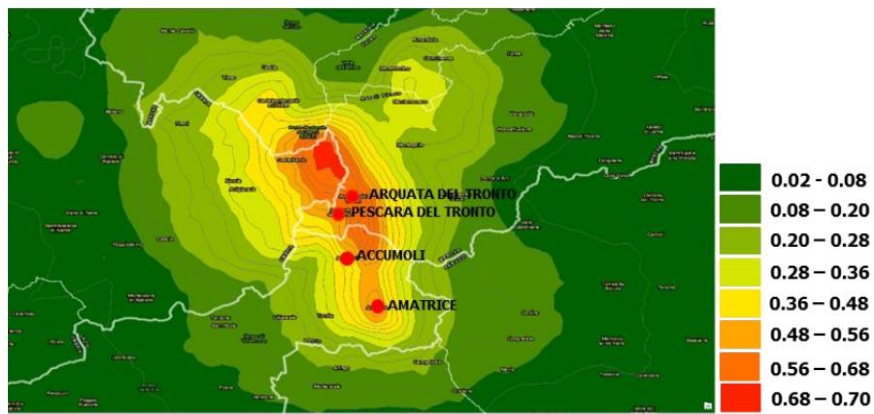


**Figure 2.30:** ShakeMap according to USGS ( $M_w$  6.2) for the inspected area [137].

Many of the observed collapses (partial or total) show a high level of damage produced by a level of macroseismic intensity varying between the VIII-XI degree of the EMS-98 scale [60] as reported in Figure 2.31 [137].



(a)



(b)



(c)



(d)

**Figure 2.31:** Damages detected in Arquata del Tronto [137].

iv. Pescara del Tronto

The construction context that characterized the small centre was mainly made up of brick buildings whose technological qualities were scarce and inadequate (brick elements or travertine stones). The quality of the mortar is poor, consisting of sand and hydraulic lime. No building had reinforcement devices as metal tie-rods. As for the horizontal structures, they are mainly wood and steel, as well as the presence of vaults poorly connected to the vertical structures and mainly located on the ground floor [137].

The high level of destruction observed has been interpreted as partly due to landslides and the collapse of the geological structure on which the city was built, influencing the foundation of many of these buildings. This aspect denotes the presence of high vertical accelerations which due to their impulsive effect caused the uplift of the ground. Many buildings have suffered vertical cracks at the main facades which highlight the influence of the vertical component (Figure 2.32).



(a)



(b)



**Figure 2.32:** Damage identification in Pescara del Tronto [137].

v. Norcia

The proximity of the epicentre to the location of the city has caused moderate damage to the buildings since they have been strengthened. During the seismic sequence of Central Italy in 2016, several earthquakes of significant magnitude occurred over a couple of months [137].

The first earthquake of 24 August of magnitude 6.0 (epicentre located in the municipality of Accumoli (RI)), followed by two earthquakes of 26 October, of magnitude 5.4 and 5.9 respectively located in Visso (MC). The fault models, based on seismometric, accelerometric, and geodetic data (GPS and SAR - satellite radar interferometry) provided indications regarding the geomorphology of the structure. It is characterized by superficial faults of overall length in the order of 20-30 km, consisting of minor segments of length equal to 5-10 km. According to the damage observed, most of the buildings were not damaged because of the efficient retrofitting interventions used [137]. A minority of buildings showed mild-moderate damage and the level of macroseismic intensity reached in the examined area was equal to the VII degree according to the European Macroseismic Scale (EMS-98, [60]). The damage has been presented in Figure 2.33.





(a)



(b)



(c)



(d)

**Figure 2.33:** Damage achieved in Norcia [137].

vi. Castelluccio di Norcia

From a constructive point of view, the buildings present on site are mainly in traditional masonry with wooden horizontal structures. The quality of the stone used and the degree of internal connection between the masonry leaves are very poor. Some buildings have retrofitting elements that could improve the behaviour of the structure towards off-plane stresses. However, some devices are also in deficit [137]. The damage observed, due to local amplification phenomena, caused significant collapses (partial or total) as reported in Figure 2.34.



(a)



(b)



**Figure 2.34:** Damage observed in Castelluccio di Norcia [137].

From the data acquired, it has been shown that the vertical component is markedly influential in the case of near-field earthquakes producing impulsive effects with a consequent increase of the damages. Generally, the panorama of design codes, NTC18 [40] and EC8 [38], neglect the effects of the ground motion vertical component, providing indications regarding only the horizontal actions deriving from probabilistic seismic risk analysis (PSHA) in the hypothesis of far-field conditions and soil category A.

These considerations demonstrate the lack of a systematic methodology such as empirical and numerical methods, that takes into account the effects induced by the vertical earthquake in areas located near the seismic source.

The variation in axial stress caused by the vertical earthquake and the reduction of the shear capacity of the masonry demonstrated a reduced level of seismic capacity with the consequent disaggregation of the walls. In this perspective, in the following chapters, the thesis work aims to evaluate the seismic response of a historic masonry building subject to vertical seismic action to propose appropriate structural design indications for masonry buildings placed in the epicentre area.

### 3 Seismic vulnerability assessment of historical masonry building under near-field earthquake

#### 3.1 Historical background

Banat is a Romanian region (Figure 3.1), geolocated in Central Europe, bordering on Serbia, Romania, and Hungary, respectively. The historical capital of Banat is the city of Timisoara, the biggest commercial and bureaucratic pole in the Banat Region. The territory of the Banat is presently part of the Romanian jurisdiction the City of Timiș, Caraș-Severin, Arad and Mehedinți; the Serbian autonomous province of Vojvodina and Belgrade City District; and the Hungarian Csongrád County.



**Figure 3.1:** Geo-localization of the Banat region.

The region is delimited on three sides by important rivers: the Mureș /Maros to the North, the Tisza to the West, and the Danube to the South. On the Eastern side, the Banat borders with the Carpathians, which give to the Romanian Banat a hilly aspect, unlike the Serbian Banat which is part of the Pannonian lowland [138].

From a historical point of view, archaeologists have found Stone Age peoples who lived in the Banat region. An ethnic multiplicity has lived in the Banat Region such as the Celts who settled down there about 2400 years ago, followed by Romans, Goths, Huns, Gepids, and Avars, respectively. The first known population of today's Banat were the Neolithic inhabitants. In the 4<sup>th</sup> century B.C., Celtic groups settled in this area forming real productive systems by minting coins to manage the prosperous local economy.

In a first instance, in this area, the population of the Scordisci, and also the other tribes present, submitted themselves to the Dacian Empire under the direction of the sovereign Burebist until the first century B.C., but later on, the power of Burebist began to decline gradually with the arrival of the military legions conducted by Augustus [139].

Consequently, Banat was administered by the First Bulgarian Empire from the 9<sup>th</sup> to the 11<sup>th</sup> century, but this control gradually declined by annexing into the Kingdom of Hungary which was administered from the 11<sup>th</sup> century until 1552, when the Temesvár region (now Timișoara) was captured by the Ottoman Empire incorporating the Banat Region in 1552.

The Banat region was populated mainly by the Serbs in the West and Vlachs (Romanians) in the East. Numerous Ottoman Muslims settled in the area, living mainly in the cities practising commercial and administrative exchanges.

However, not all the vast territory of the Banat was subjected to Turkish rule.

The eastern regions of Lugoj and Caransebeș passed under the rule of the Transylvanian princes forming a new Banato. In the mid of 17<sup>th</sup> century, the territories of Lugoj and Caransebeș fell under the Turkish empire and have been incorporated into Temeșvar's Eyalet (Figure 3.2) [139].

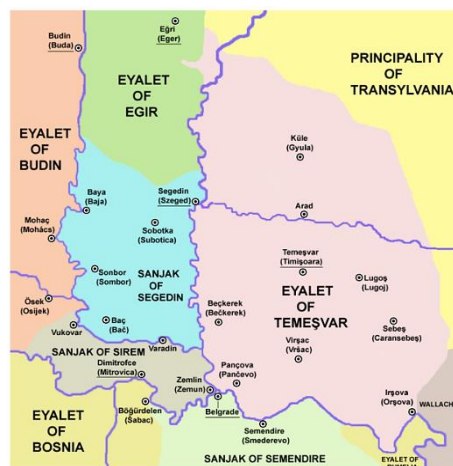
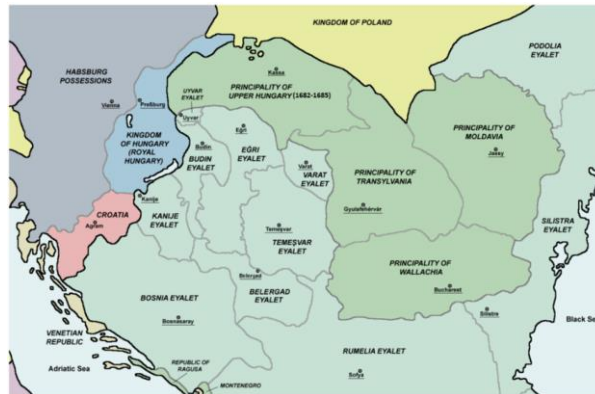


Figure 3.2: Political situation in the middle of 17<sup>th</sup> century [139].



During the Austro-Turkish war (1683-1699), the revolts of local Serb was disseminated in various parts of dell'Eyalet Temešvár (Figure 3.3).



**Figure 3.3:** The surrounding regions in 1683 [139].

The Austrian armies and the Serbian militia tried to drive the army of sultans out of the province, but the Turks managed to keep the Temesvár fort [139].

Farmers took their families and belongings on rafts along the Danube River and were encouraged to restore agriculture in the area. Moreover, as a programmatic activity induced by the governor, the marshes were reclaimed near the Danube and Tisa rivers, and began to build roads and canals and restored agriculture and favoured commercial exchanges [140], [141].

After the First World War, the Trianon Treaty of 4 June 1920 has sanctioned the division of the Banat Region between Romania (18.945 km<sup>2</sup>), the Kingdom of Yugoslavia (9.307 km<sup>2</sup>) and Hungary (217 km<sup>2</sup>), respectively. It was then that the exodus of the German population of Banat began, after the ephemeral existence of the Republic of Banat. Etymologically, the term "Banat" referred to a border province governed by a ban. In the Middle Ages, in the Kingdom of Hungary, there were numerous banati, such as the banati from Dalmatia, Slavonia, Bosnia, and Croatia as well, which disappeared with the conquests of the Venetians and the advance of the Ottoman Empire. The Banat of Temesvár (Timișoara) acquired this title after the Treaty of Passarowitz, although it was never ruled by a ban. Today, without any specification, the term Banat refers mainly to the Timișoara, which still occupies the same area in the present region.

### 3.2 The evolution of the City of Banloc: from past to present

At present, little pieces of information have been found about the urban evolution of the city of Banloc however, the name Banloc derives, originally, from the fusion of two words such as: Pan, from the name of the Greek God who in Greek mythology was connected to the forests and nature, and loc or place, where the god resided. Only later, the term *Pan* was replaced with *ban* to indicate the noble title used in various states of central and South-Eastern Europe between the seventh and twentieth centuries (Figure 3.3) [142].

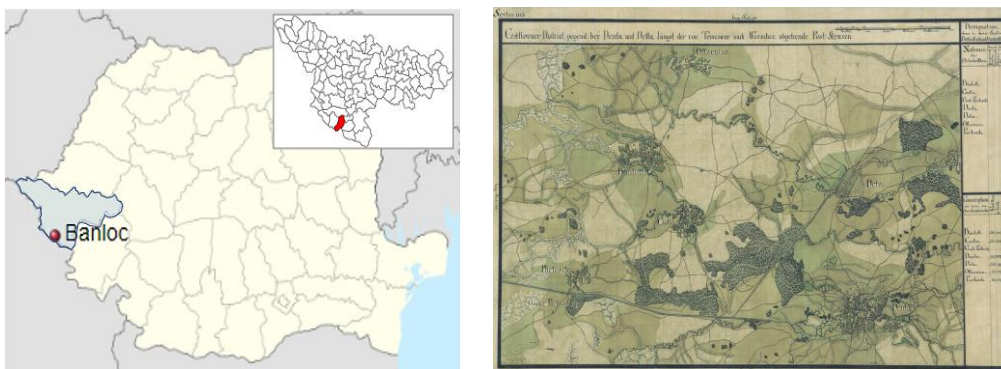


**Figure 3.4:** Geolocalization of the City of Banloc and Banloc in the Iosefină Map of Banat, 1769-72 [142].

However, Banloc's history is closely tied to the history of Karátsonyi rule and its economic performance.

The vastness of the domain included rich forests, agricultural land the majority of which were rice fields of Topolea. The presence of large fishing lakes, tobacco plantations, and farm animals favoured commercial development facilitated by the presence of rail locomotion systems.

Today the city of Banloc has about 2805 inhabitants, located in the district of Timiș, in the historical region of Banat. The municipality is characterized by the union of 4 villages: Banloc, Ofsenița, Partoș, Soca [142].

From an urban point of view, the city is constituted by wide roads that connect the inhabited centre with the neighbouring cities. Furthermore, from a structural point of view, the buildings present in the area are mostly made of solid brick or adobe masonry walls with wooden or vaulted floors systems (90% of the cases), and only 10% are built in a random position within the urban sector. Generally, these buildings are mainly single-story and were built near the main roads.

The buildings have a typical and regular plano-altimetric configuration creating a linear layout, and many of them have been built in an isolated position (Figure 3.5).



**Figure 3.5:** Example of the building's typologies present in the urban area of Banloc [142].

Besides, the city of Banloc is renowned for the Banloc Castle, a historic building at a crossroads of remote eras selected as a reference case study in the present thesis. It represents the most important monument in the municipality, it is a massive U-shaped building erected in the early 19<sup>th</sup> century. The main façade is oriented to the South, while on the opposite side the two wings delimit a courtyard. Along the main façade, two portals recall the style of ancient Egypt and give access to the area on the sides of the two wings.

In the past, the façade was surmounted by a central elevation bearing the coat of arms of the Karátsonyi family, who had the castle built.

The Banloc Castle was built between 1759 and 1793 (Figure 3.6). Currently, the Banloc Castle is undergoing restoration and consolidation since it suffered extensive damage following the earthquakes that occurred in the area after the seismic event in 1991 [142].



(a) – North façade, 1914



(b) – South façade, 1936



(c) – North-East façade

(d) – North façade

**Figure 3.6:** The Castle of Banloc [142].

### 3.3 Seismicity of Romania

The Romanian tectonic system is made up of pre-Alpine orogenic units (i.e. deriving from an orogenic process, in which the predominant reliefs consist of rocky masses that have undergone a tectonic deformation due to lateral thrust) characterized by the presence of Moldavian plates, from the Eastern Carpathians (Apuseni Mountains) and in the Eastern sector from the Transylvanian depression. Thus, the complex tectonic system has generated important crustal earthquakes due to the presence of faults identified along the contact lines of the tectonic plates themselves. Other faults have been identified in the transverse direction of the Carpathians area which has generated medium seismicity of the entire area as reported in Figure 3.7 [143].

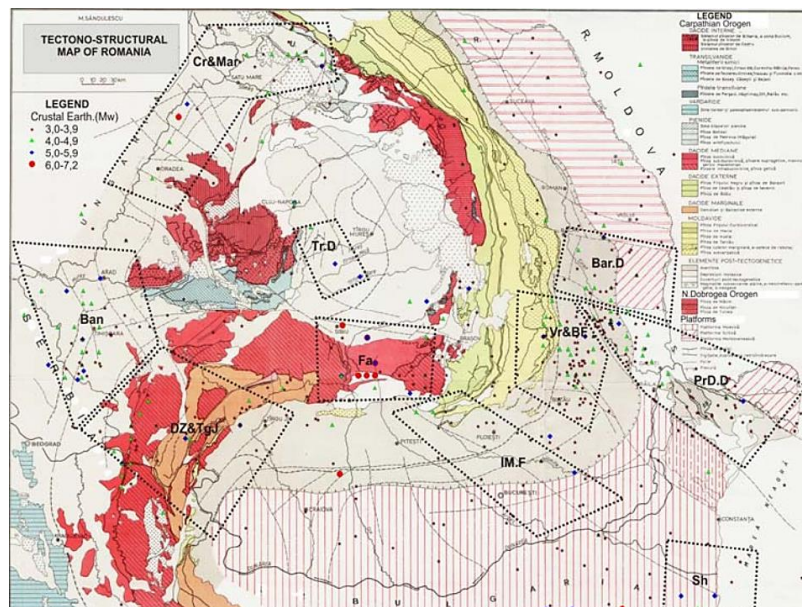


**Figure 3.7:** Map of tectonic units in Romania [143].



As shown in Figure 3.7, different areas with variable crustal seismicity are identified [143]. In particular in the Southern part:

- i. *Pontic earthquakes*: that occurred along and near the shore of the Black Sea, in the area of Constance-Mangalia-Cavarna-Balcic. They include historical events that occurred in 1869-1901, such as the devastating earthquake of March 31, 1901, from Shabla (Bulgaria) with  $M_w = 7.2$ . Instead, moderate seismic activity was recorded in the central Dobrogea in two directions parallel to the Capidava-Ovidiu fault;
- ii. *Romanian plain* (in Fig. 3.7 it is denoted with the acronym of *Vr&BF*, that is Vrancea and Focşani basin): in the period between 1872 and 2005, approximately 300 events were recorded characterized by a magnitude between 3.0 and 5.4.  
Many of these events were located near the Arges River. Subsequently, a series of medium-low seismicity events were generated around Bucharest. The Vrancea sub-crustal earthquake (March 4, 1977), has produced a magnitude of 7.4, which is relevant. It is worth mentioning other significant earthquakes that occurred in 1967 such as Cazanesti with an  $M_w = 5.0$  and Radulesti event with an  $M_w = 5.4$  dated 1960;
- iii. *Fagaras-Campulung area* (Fig. 3.7, in the central part of the map indicated with the acronym of "*Fa*"): has seen the strongest Romanian crustal earthquake occurred, with a magnitude of 6.5. Chronologically, the area underwent a similar event in 1916 with a magnitude of 6.4. More recently in 1969, an event of a magnitude 5.2 followed by an important series of aftershocks, approximately 500. The historical seismicity of the area was characterized by 271 events known between 1550 and 2001. Furthermore, 5% of them, verified before 1900, had a magnitude between 6.2 and 6.5, the remaining series, between 1900 and 1980, were characterized by a modest magnitude.

The South-West part of the Romanian territory was characterized by moderate seismicity. In particular, seismic events with a magnitude between 3.0 and 4.9 were recorded in the Western part, near the Olt river. However, events with a magnitude greater than 5.0 have been defined as exceptional events since, due to the geomorphological conformation of the area, have a very low probability of occurrence considering a return period,  $T_r$ , of 275-year as confirmed in [143]. Consequently:

- i. *Danube area* (indicated in Fig. 3.7 with the acronym of DZ&TgJ): located in the western part of Oltenia, was characterized by events with a maximum magnitude of 5.6 occurred in the area near Mehadia-Baile Herculane in 1991, Moldavia Noua ( $M_w= 5.3$ , in 1879) and nearby Tismana ( $M_w= 5.2$  in 1943). Other minor seismic events, of a lower magnitude (less than 4.0) have been followed, between 1879 to 1984, in Moldova Noua, Oravita, Targu-Jiu, Anina, Sasca Montana, Baile Herculane, Resita, Bozovici;
- ii. *Banat region* (identified with the acronym of Ban): in its seismic history, it presents a high dispersion and variability of the epicentres concerning the events observed. The most significant earthquakes were recorded in Banloc ( $M_w= 5.6$  and  $M_w= 5.5$  in 1991).  
The Banat earthquakes are triggered by contact with the plate system of the Carpathians and Pannonia and affecting also the city of Timisoara. Moreover, the contact between the deeper tectonic blocks between Sannicolau Mare, Nadlag-Jimbolia, Arad- Vinga-Calacea, and on the Timis valley in Faget have generated other earthquakes with lower energy.
- iii. In the North-Western part of Romania, precisely near the areas of Crisana, Satu Mare, and Maramures (see Fig. 3.7, the area namely Cr&Mar) have been observed events that have produced earthquakes of moderate magnitude. However, historically, only one event with a magnitude greater than 5.0 was recorded, i.e in 1829 an event with a magnitude  $M_w$  approximately of 6.2 was found, the other earthquakes, which occurred in the last century, showed a moment magnitude equal to 5.0 [143].
- iv. Finally, the Transylvanian depression (see Fig. 3.7 called Tr.D) is considered an area with low historical seismicity. Events of the maximum magnitude of 5.3, occurred in 1880, between the two Tarnava rivers have been verified and, only in 1975, a weak earthquake of magnitude 3.3 was found.

The Western part of Romania is one of the most seismically active areas characterized by medium local seismicity, mainly in the Pannonian Basin. A map of the distribution of epicentres was provided by the ROMPLUS catalogue [144] as shown in Figure 3.8. Seismogenic areas are represented by rectangles. The magnitudes associated with the events that occurred did not exceed  $M_w= 5.6$  in Banat and  $M_w= 6.2$  in Crisana-Maramures.

The analysis of the distribution of the magnitude and therefore of the epicentres, has shown that most of the earthquakes had a magnitude,  $M_w$  equal to 2.0 and 3.0 (about 90% of the cases), while the remaining events have had a magnitude between 3.0 and 4.0 (about 5% of the sample), 2% of cases having a magnitude between 4.0 and 5.0 (2% of the cases) and only 1% with  $M_w > 5.0$  as depicted in Figure 3.8.

However, the majority of earthquakes have been recorded in Banat, in the Southern Transylvania and Crişana areas, respectively [144].

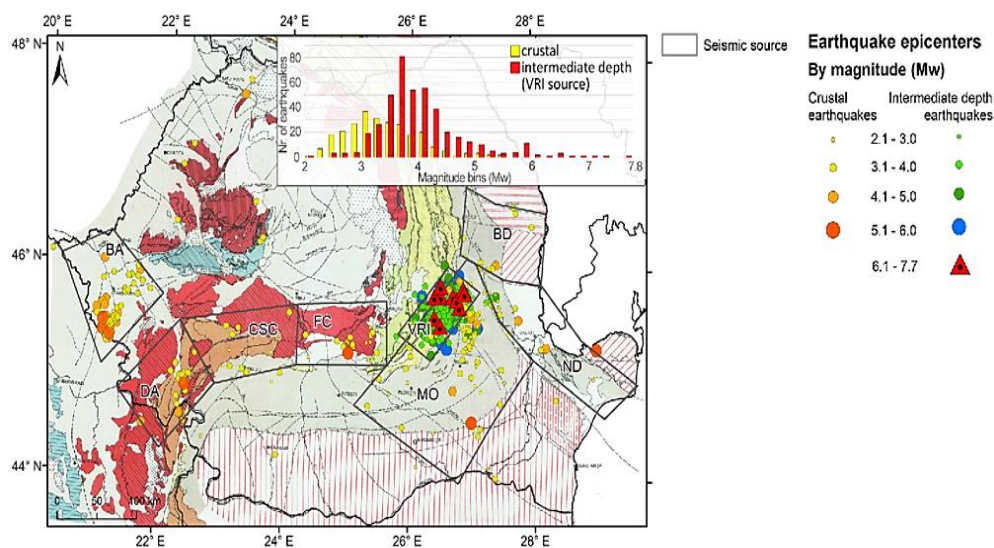


**Figure 3.8:** Distribution of earthquake epicentres and magnitude ( $M_w$ ) [144].

Focusing on the Banat region, subsequently assumed as a study area, it consists of a dense capillary network of faults that branch out [144]:

- i. one oriented north-west, towards Lugoj-Zarand, Sacoşul Mare-Arad and Nădlag Jimbolia which separates the Caransebes and Sânnicolau Mare;
- ii. a fault system in a transverse direction (Lucareţ faults) involving Timisoara and Calacea;
- iii. an E-W-oriented system, present in the southern Pannonia basin.

The hypocenters in the Banat area have been estimated at 5 km and 33 km (Figure 3.9) [145]. The historical crustal earthquakes with fault-plane mechanisms presented in Figure 3.9 have been synthesized in Table 8 [145].



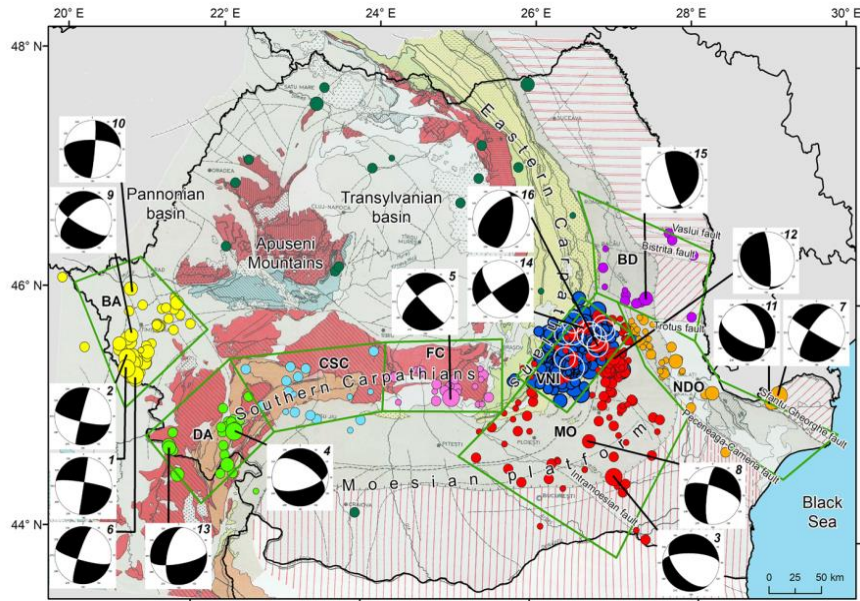


Figure 3.9: Romanian's focal mechanisms [145].

Table 8: Crustal earthquakes with  $M_w \geq 4.5$  with fault-mechanisms [145].

ID	Year	Month	Day	Latitude [°N]	Longitude [°E]	Depth [km]	$M_w$
1	1991	7	12	45.36	21.06	11	5.6
2	1991	12	2	45.45	21.06	9	5.5
3	1960	1	4	44.60	27.00	41	5.4
4	1991	7	18	44.89	22.41	12	5.3
5	1969	4	12	45.25	25.02	8	5.2
6	1991	7	19	45.31	21.17	10	5.1
7	1981	11	13	45.27	29.01	8	5.1
8	1967	2	27	44.90	26.70	42	5.0
9	1959	5	27	45.64	21.09	9	5.0
10	1974	4	17	46.03	21.04	16	4.9
11	2004	10	3	45.21	28.92	4	4.9
12	1969	12	21	45.60	27.00	38	4.6
13	2002	5	24	44.72	21.64	9	4.6
14	1975	3	7	45.56	26.63	21	4.5
15	1956	4	18	46.10	27.40	20	4.5
16	1952	6	3	5.70	26.80	22	4.5

### **3.4 Seismic activity in the Banat area**

As proposed by [53], the Seismological Database for Banat Seismic Region, SDBSR, is a useful tool for quantifying the seismic hazard of the area to guarantee accurate forecasting of seismic risk mitigation plans.

In particular, the SDBSR database has been developed in detail since Romania is a border territory, the local seismic risk is influenced by earthquakes generated in neighbouring areas such as Hungary, Serbia, and Bulgaria, and also in the Romanian provinces, i. e Transylvania and Western Muntenia as well. Thus, the database consists mainly of two main parts, the first, essentially related to the number of earthquakes generated in the Banat region according to the Parametric Earthquakes Catalogue for BSR, PECBSR, the second one, take into consideration the extent of the focal mechanisms that generated the reference events in a given period referred to the Catalogue of Focal Mechanism Solutions for BSR, CFMSBSR [53].

Concerning the parametric catalogue of earthquakes, it considers each earthquake as a uniform set of standard parameters such as time of origin (GMT), geographical coordinates of the epicentres and their distribution (latitude and longitude), focal depth, and epicentral macroseismic intensity, expressed according to the EMS-98 scale, [60]. To establish the implementation boundaries of the parametric catalogue, two areas were defined: one in the longitudinal direction and one in the transverse direction, respectively. The area of interest, therefore, has an area of 25000 km<sup>2</sup> and is bounded by Serbia and Hungary.

The catalogue includes approximately 7783 earthquakes from 1443 to 2006. The magnitudes occurring in the area vary between 0.2 to 5.6 with epicentral intensity intended as the maximum recorded intensity,  $I_i$ , between 2 and 9. Also, Figure 3.10 shows the map of the distribution of the epicentres [53].

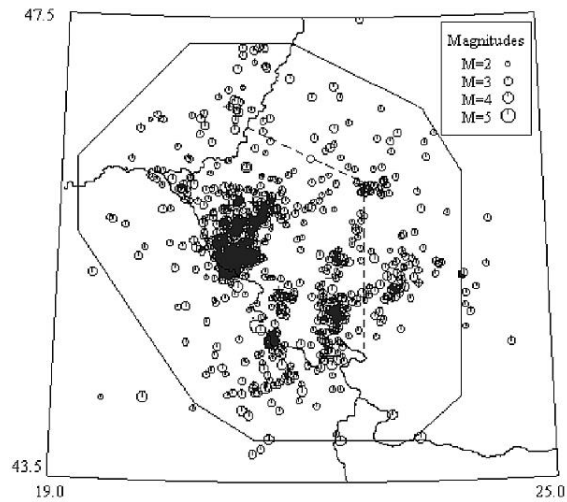
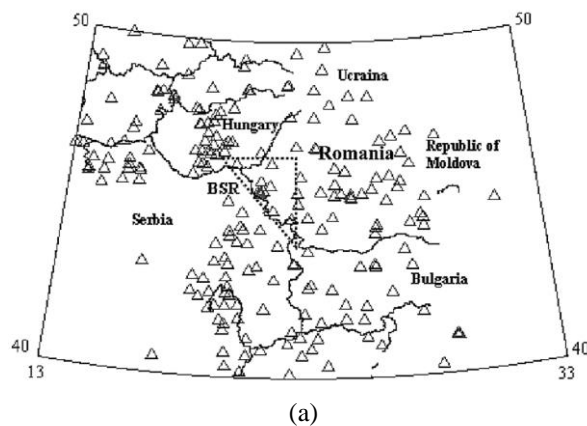


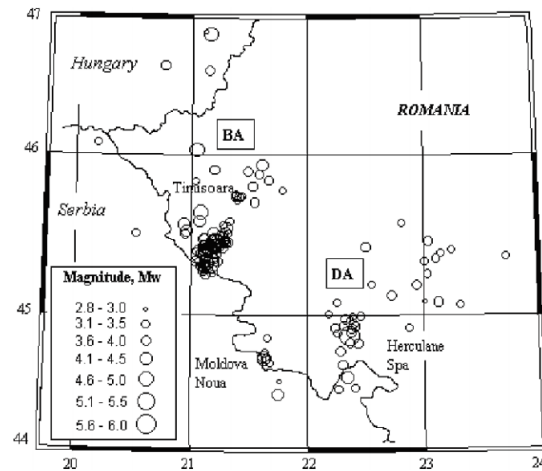
**Figure 3.10:** Map of epicentres from 1443 to 2006. Dashed line bounds Banat Seismic Region [53].

The distribution of the magnitudes refers to the duration magnitude,  $M_D$ , evaluated according to the duration of the seismogram. However, systematic studies of focal mechanisms, FMS, have provided fundamental data regarding the origin of the seismic phenomenon, such as the stress field and the types of fault present as well as their geometry.

In this perspective, the focal mechanisms evaluated for the region have been carefully selected and archived based on the coverage of the recording station concerning the position of the epicentres.

Furthermore, given the short distances between the location of the epicentre and the seismic station it has estimated also the focal depths concerning the earthquakes that occurred in the area (Figure 3.11) [53].





(b)

**Figure 3.11:** Seismic stations present in the BSR area (a) and epicentres distributions (b) [53].

From these considerations, it can be highlighted how the Banat area have generated small earthquakes from a seismic point of view. However, what makes such events dangerous is the reduced focal depth. From what has been acquired, it is possible to highlight that the damage caused to the structures was conditioned by the combination of the magnitudes that occurred,  $M_w$ , and the reduced focal depths.

### 3.5 Romanian Design Code approach

#### 3.5.1 Seismic hazard map

In Romania, there are multiple areas with different and significant seismicity that have generated earthquakes of varying depths.

A seismic hazard map [146] has been proposed as an integral part of the Romanian Code based on the EC8 [38], as reported in Figure 3.12.

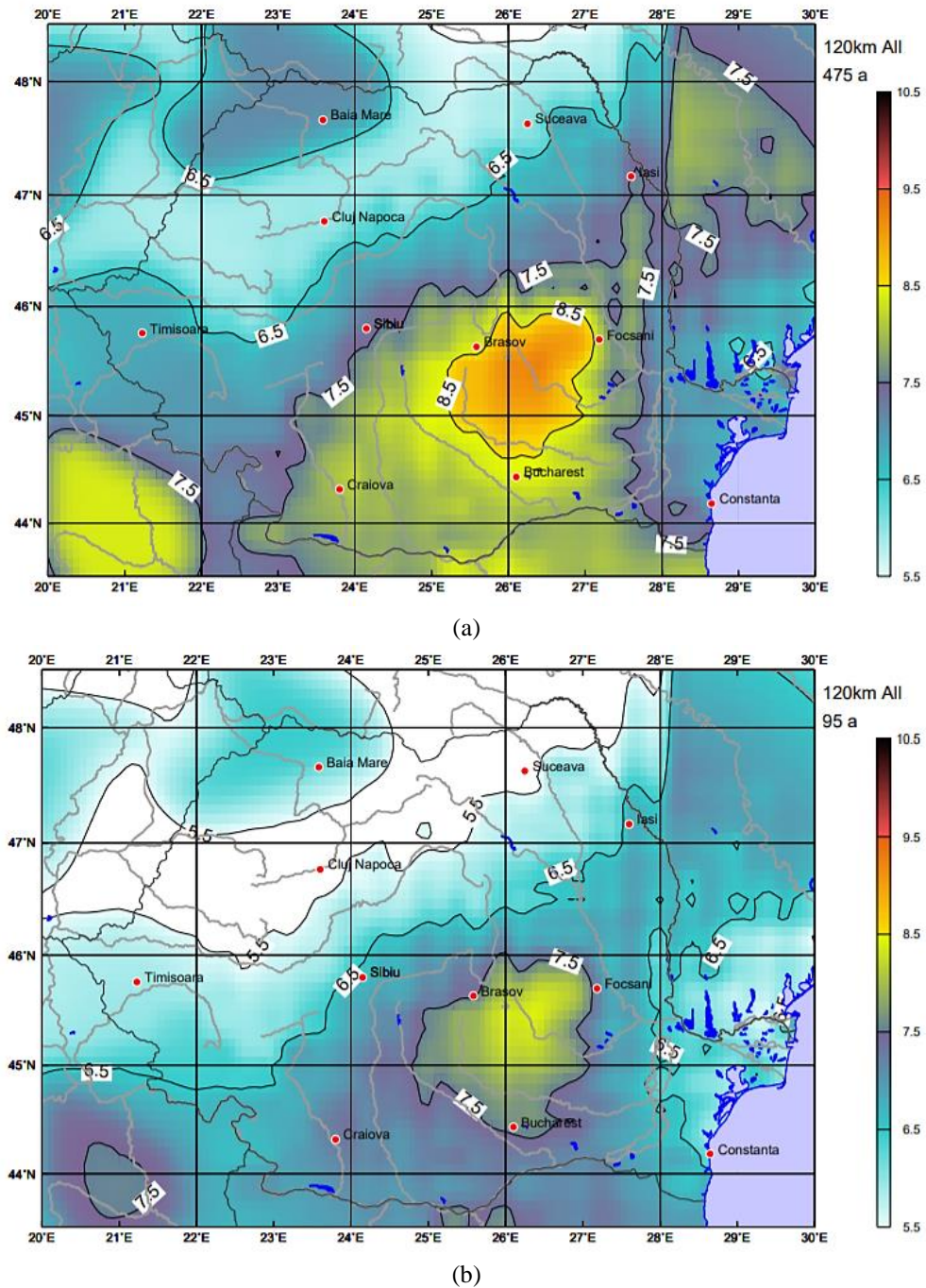


**Figure 3.12:** Seismic hazard from all source zones: (a) recurrence period of 475 years and (b) recurrence period of 95 years [146].

The final maps of the seismic hazard are drawn up for a recurrence period of 95 and 475 years and they are a combination of the maps for areas characterized by normal depth and those for an intermediate depth such as the Vrancea region.



Besides, according to EC8 [38], the hazard map with a recurrence period of 95 years has been elaborated since it takes into consideration the buildings that can suffer damage from not very consistent earthquakes, characterized by higher occurrence but with reduced magnitude.

As can be seen from Figure 3.12, the expected level of hazard is very high for the Vrancea Region for which major earthquakes with a macroseismic input intensity of 6.5 and 7.5 can occur considering return periods of 475 years and 95 years, respectively. On the other hand, in the Banat Region, the expected macroseismic intensities are lower, from 5.5 until 6.5 for return periods of 475 and 95 years.

Alternatively, for an exhaustive and immediate interpretation of the expected level of hazard in Romania, the hazard map has been expressed in terms of PGA [147] with a probability of exceeding 10% in 50 years. As can be seen, this hazard map allows defining the expected acceleration level for the entire national territory.

In particular, for the Vrancea Region, a maximum PGA of  $600 \text{ cm/sec}^2$  is associated, while for the Banat Region, a maximum expected PGA is equal to  $200 \text{ cm/sec}^2$  (Figure 3.13).

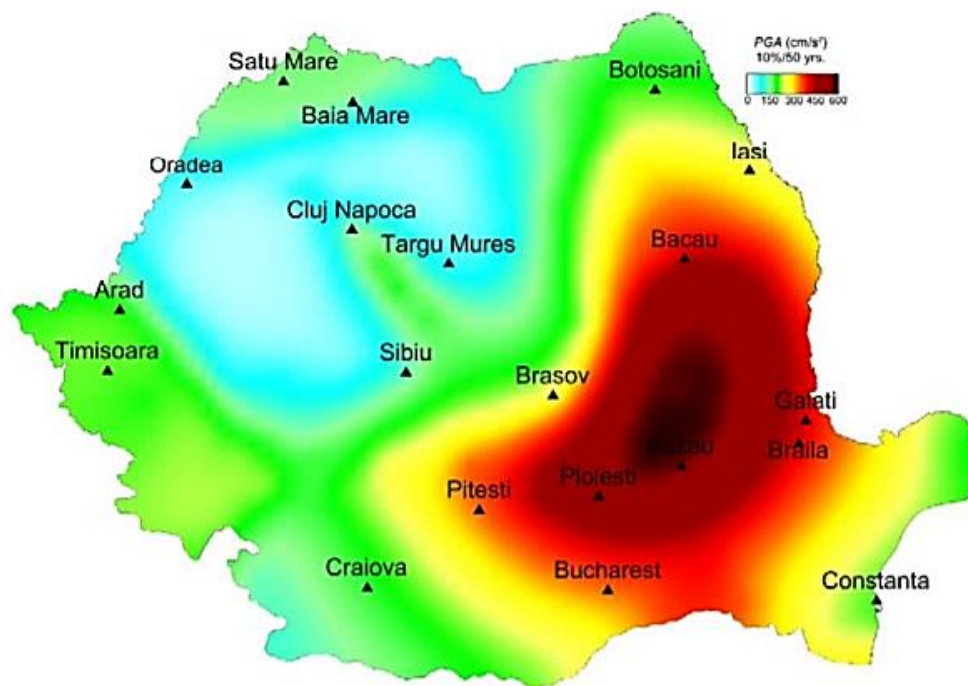


**Figure 3.13:** Seismic hazard map in terms of PGA with a probability of exceedance of 10% in 50 years [147].



### 3.5.2 Romanian Code – Horizontal response spectrum

The Romanian Code [39] subdivides the national territory into seismic zones, with different hazard levels. The hazard seismic design is described by the horizontal peak ground acceleration  $a_g$ , determined by the average return period, IMR.

The design value of seismic action,  $A_{Ed}$ , is evaluated as the multiplication of the characteristic value of the seismic action,  $A_{Ek}$ , and exposure factor,  $\gamma_{1,e}$ , of the construction (see Equation 3.1):

$$A_{Ed} = A_{Ek} \cdot \gamma_{1,e} \quad (3.1)$$

The values of  $a_g$  are given in Figure 3.23 which corresponds to IMR= 225 years with a 20% probability of exceedance in 50 years. For the city of Timisoara, the estimated value is 0.20g (Figure 3.14).

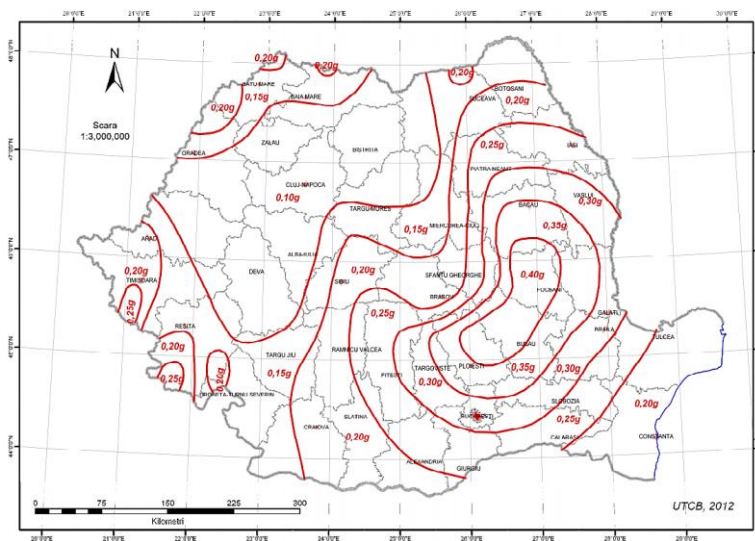


**Figure 3.14:** Romania’s zonation in terms of peak ground acceleration values [39].

The horizontal component of the elastic response spectrum  $S_{ve}(T)$ , expressed in  $ms^{-2}$ , is defined as:

$$S_{ve}(T) = \gamma_{1,e} \cdot a_g \cdot \beta(T) \quad (3.2)$$

where  $\gamma_{1,e}$  is the earthquake exposure importance factor,  $a_g$  represents the acceleration and  $\beta(T)$  identified the design spectrum [39].

The design spectrum  $\beta(T)$ , is generally related to damping,  $\xi$ , equal to 0.05, and mathematically defined according to the following relations [39]:

$$0 \leq T \leq T_B \quad \beta(T) = 1 + \frac{(\beta_0 - 1)}{T_B} \cdot T \quad (3.3)$$

$$T_B \leq T \leq T_C \quad \beta(T) = \beta_0 \quad (3.4)$$

$$T_C \leq T \leq T_D \quad \beta(T) = \beta_0 \cdot \frac{T_C}{T} \quad (3.5)$$

$$T_D \leq T \leq 5 \text{sec} \quad \beta(T) = \beta_0 \cdot \frac{T_C \cdot T_D}{T^2} \quad (3.6)$$

Furthermore,  $T_B$ ,  $T_C$ , and  $T_D$  define the spectrum shape and the  $T_C$  value is given in Figure 3.15 [39].

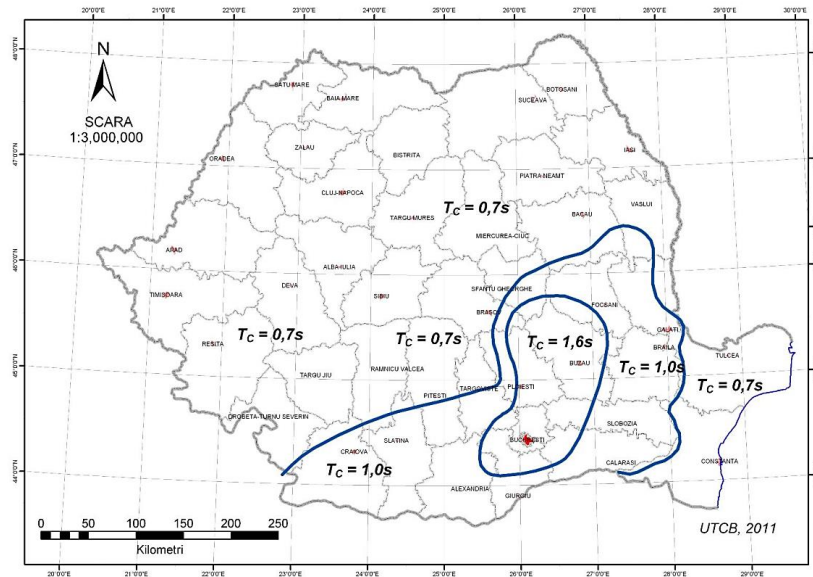


Figure 3.15: Romania in terms of the zoning control period,  $T_c$  spectrum [39].

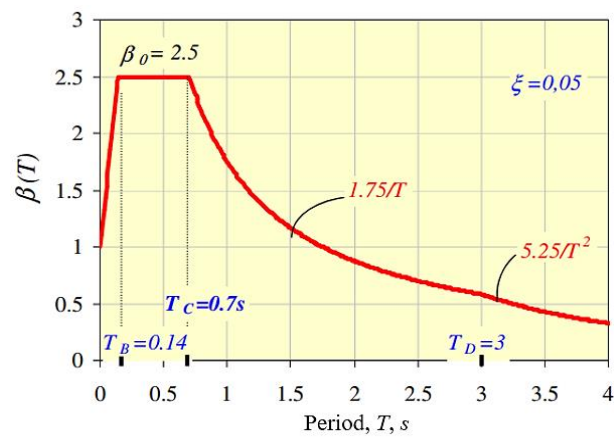
The values of  $T_B$  and  $T_D$  are given in Table 8 [39]:

**Table 9:** Control period  $T_B$ ,  $T_C$ ,  $T_D$  for the horizontal component of the spectrum [39].

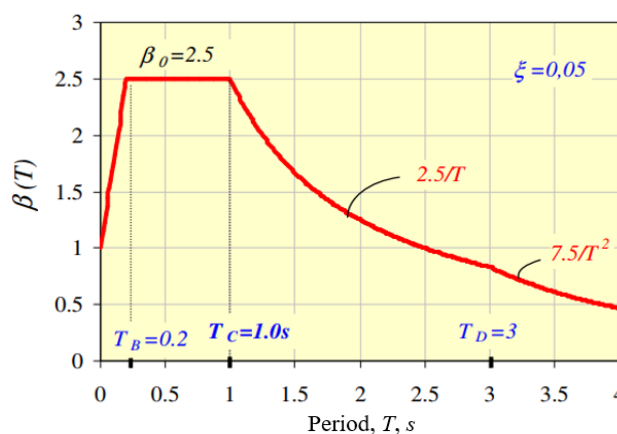
Period [sec]			
$T_B$	0.70	1.00	1.60
$T_C$	0.14	0.20	0.32
$T_D$	3.00	3.00	2.00

Furthermore, based on the different levels of seismicity of the areas belonging to the Banat Region, it is possible to distinguish:

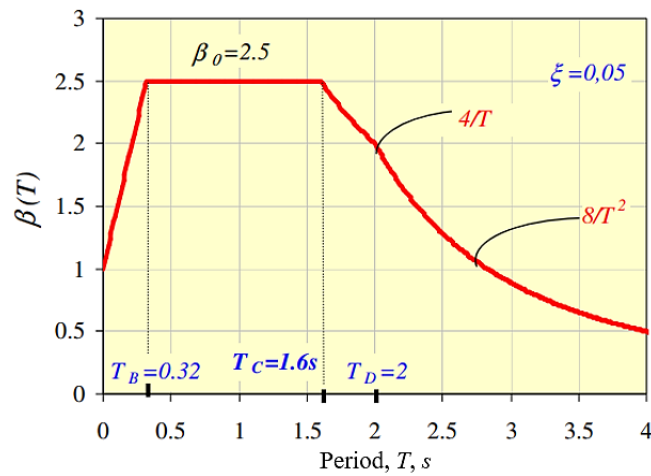
- i. seismic areas where the expected PGA is equal to 0.08g and 0.12g, the normalized spectrum, presented in Figure 3.16, is adopted for  $T_C \leq 0.7s$  and damping,  $\xi$ , equal to 5%.



(a)



(b)



(c)

**Figure 3.16:** Normalized elastic response spectra of absolute accelerations for horizontal components of motion, in areas characterized by the control period (corner)  $T_C$  equal to 0.7s, 1.0s, and 1.6s [39].

- ii. seismic zones characterized by the acceleration  $a_g=0.16g$  and  $a_g=0.20g$ , the normalized elastic response spectrum depicted in the Figure 3.17 is used:

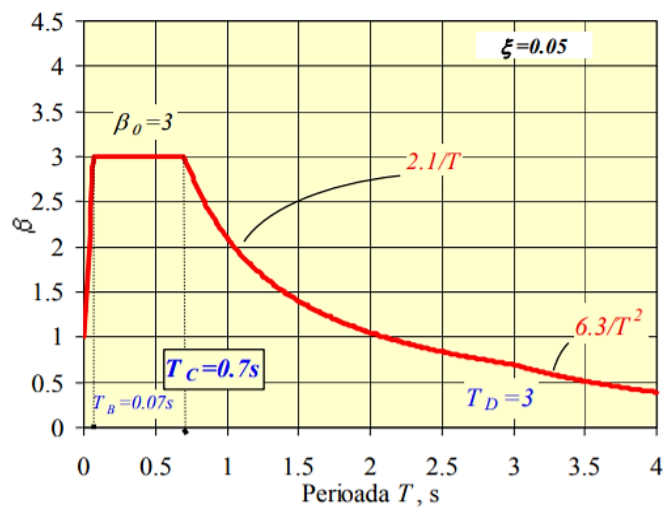


**Figure 3.17:** Normalized elastic response spectrum for the horizontal components of the ground motion [39].

### 3.5.3 Romanian Code – Vertical response spectrum

The seismic vertical action used for the design of buildings is represented by the elastic response spectrum of the absolute accelerations for the vertical component of the ground motion,  $S_{ve}$  expresses in  $\text{ms}^{-2}$  [39], defined the following relation:

$$S_{ve}(T) = \gamma_{l,e} \cdot a_{vg} \cdot \beta_v(T) \quad (3.7)$$

where:

- $a_{vg}$  is the peak value of the acceleration for the vertical component of the ground motion, in  $\text{ms}^{-2}$ ;
- $\gamma_{l,e}$  is the earthquake exposure importance factor;
- $\beta_v(T)$  is the normalized elastic response spectrum of the absolute accelerations for the vertical component of the ground motion.

Moreover, the peak value of vertical acceleration is evaluated as a function of the horizontal ones, according to Equation 3.8:

$$a_{vg} = 0.7 \cdot a_g \quad (3.8)$$

The normalized elastic response spectrum of absolute accelerations for the vertical component of the ground motion,  $\beta_v(T)$  is given by the following relations:

$$0 \leq T \leq T_{Bv} \quad \beta_v(T) = 1 + \frac{(\beta_{0v} - 1)}{T_{Bv}} \cdot T \quad (3.9)$$

$$T_{Bv} \leq T \leq T_{Cv} \quad \beta_v(T) = \beta_{0v} \quad (3.10)$$

$$T_{Cv} \leq T \leq T_{Dv} \quad \beta_v(T) = \beta_{0v} \cdot \frac{T_{Cv}}{T} \quad (3.11)$$

$$T_{Dv} \leq T \leq 5 \text{ sec} \quad \beta_v(T) = \beta_{0v} \cdot \frac{T_{Cv} \cdot T_{Dv}}{T^2} \quad (3.12)$$

where  $\beta_{0v} = 2.75$  is the maximum dynamic amplification factor of the vertical acceleration for the conventional value of the fraction of the critical damping,  $\xi$ , equal to 0.05, and  $T_{Bv}$ ,  $T_{Cv}$ ,  $T_{Dv}$  are the control periods of the response spectrum of the vertical component [39].

Finally, the control periods of the normalized spectrum for the vertical component have been defined according to the simplified relationships [39]:

$$T_{BV} = 0.1 \cdot T_{CV} \quad (3.13)$$

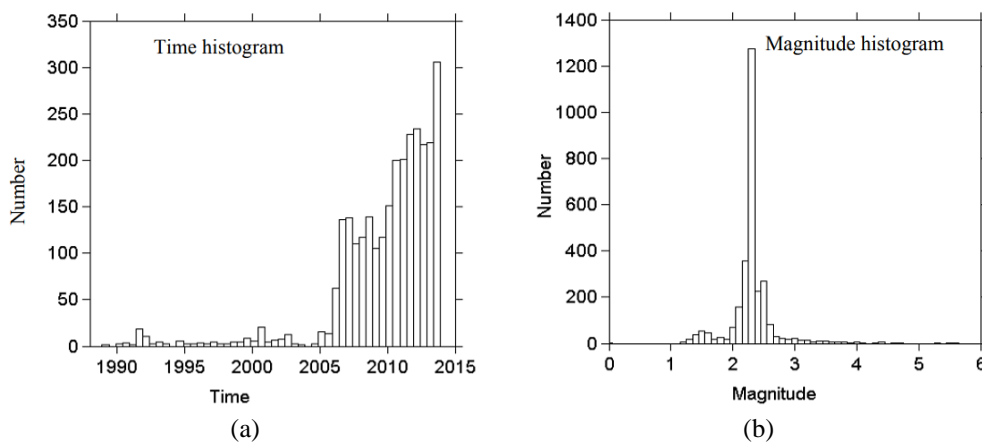
$$T_{CV} = 0.45 \cdot T_C \quad (3.14)$$

$$T_{DV} = T_D \quad (3.15)$$

### 3.5.4 Typical failure mechanisms in the epicentre area

The seismicity of the western part of Romania has generated, over the years, crustal earthquakes mainly in the Banat Region (or Banat Seismic Region, BSR) and in the North of the Danube (Danube Seismogenic Zone, DSZ). The epicentres located in these regions are characterized by seismicity controlled by different fault systems which, in particular stress conditions, have generated a medium-high magnitude earthquake that caused substantial damage to the buildings present in the epicentral area.

Recently, the earthquake catalogue concerning the entire Banat area was updated, using a complete set of condensed and processed data regarding geology, geophysics. In particular, three zones with different seismicity have been defined, i.e. Sinnicolau Mare-Arad, Timisoara and Banloc-Voiteg, Oravita, based on the distribution of the earthquakes that occurred with a moment magnitude  $M_w > 5.3$ . These data were elaborated according to the study proposed by Oros, 2008 [53]. The results are shown in Figure 3.18.





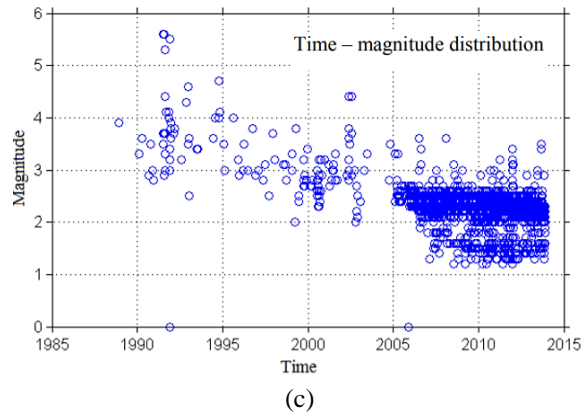


**Figure 3.18:** The aftershocks series of the strongest ( $M_w=5.5-5.6$ ) earthquakes occurred in Banloc (12.07.1991 and 02.12.1991) and Mehadia (18.07.1991) in the time domain of 1988-2013 [53].

As can be seen, only two significant events of magnitude  $M_w > 5.0$  occurred in 1991 (Banloc-Voiteg). Subsequently, a large number of earthquakes with  $M_w = 2.3$  occurred between 2006 and 2013 with a high frequency of magnitude earthquakes,  $M_w = 2.3-2.5$  since 2006.

#### 3.5.4.1 Field evidence after the 1991 Banloc-Voiteg seismic event

The seismic phenomenon can be defined as near-source type since the city of Banloc has located approximately 7 km from the epicentre (Figure 3.19) [148].

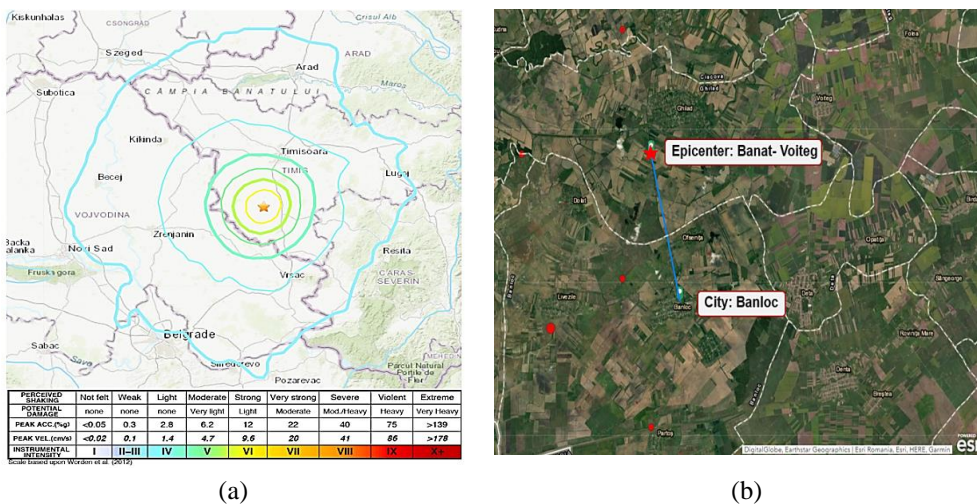


**Figure 3.19:** ShakeMap of the Banat-Voiteg event (a) and geolocation of the city of Banloc [148].

In detail, the occurrence of the vertical component of the earthquake is associated with the arrival of vertical propagating compressive P-waves and, secondary, S-waves (shear) which are the cause of the horizontal component [19].

Generally, P-waves are shorter than the other ones, which means that vertical ground motion is associated with higher frequencies compared to the horizontal ones. In fact, near the source, the vertical component is characterized by higher frequency content that attenuates faster. Normally, the ground motion vertical component has a lower energy content than the horizontal one and they tend to have all the accumulated energy concentrated in a very restricted area producing damage to the structures. Another important aspect to be considered is the spatial variation of ground motions.

Gioncu and Mazzolani [19] have been reported the effect of the spatial variation of ground motion due to the differences in amplitude and phase of seismic motions recorded over extended areas.

These variations produce differential motions of building foundations and in the soft soils, the effects can be significant (Figure 3.20). These effects, according to [149] may depend on:

- i. *Incoherence effect*: loss of coherency of seismic waves due to scattering in heterogeneous ground and superposition of the waves arriving from a different point of the source;
- ii. *Wave-passage effect*: differences in the arrival time of waves;
- iii. *Attenuation effect*: gradual decay of wave amplitude with the distance due to the energy dissipation;
- iv. *Site-response effect*: spatially varying local soil profiles and they influence both amplitude and frequency content of the ground motion.

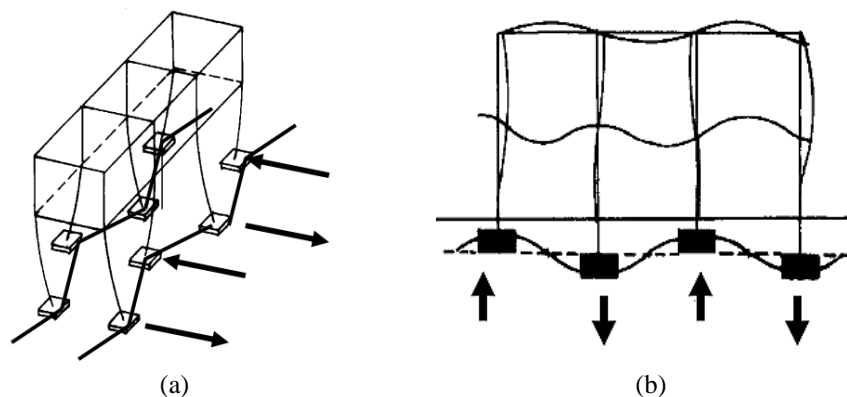


**Figure 3.20:** Effect of seismic waves [122].

Moreover, the seismic history that occurred in the Banat Region, has caused multiple damages in the areas surrounding the epicentres. In particular, the damages induced as a result of the seismic phenomenon have generated partial or total collapses of extensive portions of buildings. These damages are presumably due to the cumulative effect of the seismic sequences.

In other words, the buildings surrounding the areas affected by earthquakes have been subject to the fatigue phenomenon. They showed a sudden and gradual deficit of the resistance (up to the partial collapse) of the material mainly induced by a varying load during the time (earthquake) repeated for a certain number of cycles.

Nonetheless, even if the material retains its elastic limit, during the cyclic action, the loads generate a tensional state which remains close to the value of the ultimate tensile strength or yield stress of the basic material, causing the formation of in-plane or out-of-plane collapse mechanisms.

Most of the buildings located in the epicentre area are made of brick or adobe.

These materials are susceptible to seismic actions, offering, therefore, a low resistance against horizontal actions. Some examples of collapses that occurred in the City of Banloc, following the events of 1991 are shown in Figure 3.21.

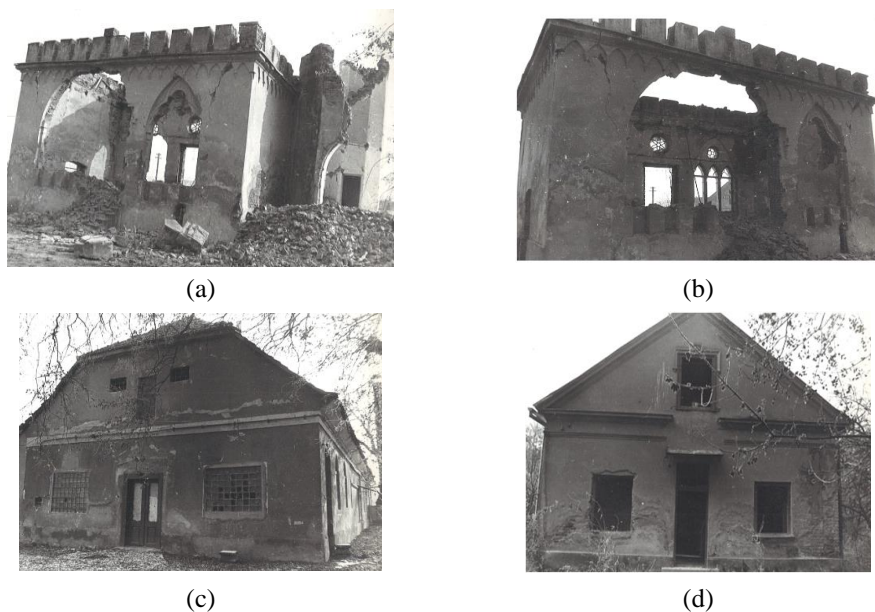


**Figure 3.21:** Main damages detected after the Banloc-Voiteg earthquake in 1991 [150].

As can be seen from the previous figure, the damage is manifested by the presence of widespread cracks. In particular, in Figure 3.21 (a)-(b), pseudo-

vertical cracks are denoted in the upper part of the wall panels near the openings which could be attributable to the effects of ground motion vertical component. Moreover, as reported in Figure 3.21 (c) it is possible to observe diagonal cracks near the opening located on the left side of the building and an extended horizontal crack that affects the entire spandrel beam. Finally, in Figure 3.21 (d) are noted a detachment of plaster is localized in the wall panels adjacent to the windows and, in the upper part of the door.

Another example is the Banloc Castle, intended as a case study building in the following paragraphs. The damage was detected through on-site inspections after the earthquake occurred. The achieved post-earthquake damages are presented in Figure 3.22 [150].

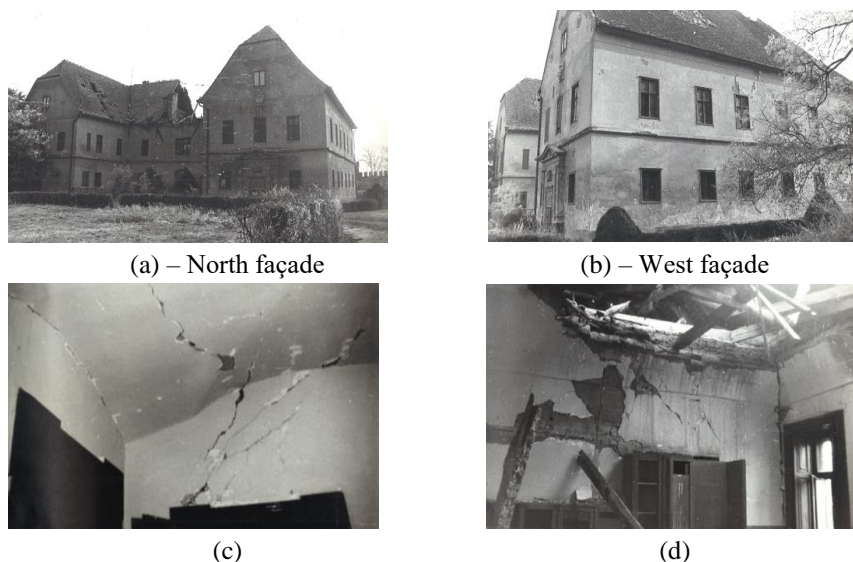


**Figure 3.22:** Damage reconnaissance on the study Castle after 1991 Banloc earthquake: (a, b) external façade; (c) first floor room; (d) second-floor room [150].

Generally, these types of damage occur for two main reasons: (i) a reduced focal depth (hypocentre); (ii) a reduced seismogenic site-source distance. In such circumstances of near-field effects, the ground vertical accelerations are significantly higher than horizontal ones, consequently causing significant damage to structures. These damages are characterized by vertical cracks, typical for buildings located in the epicentre area.

### 3.6 Seismic assessment of the Banloc Castle

#### 3.6.1 Preliminary analysis of the case study building

The Banloc Castle is the most important monument of the municipality and it has been completed in 1759. It is located in the centre of the homonymous city of Banloc and it is a massive building with a "U" shape-plan built at the beginning of the 19<sup>th</sup> century (Figure 3.23) [151].



**Figure 3.23:** The Banloc Castle [151].

The main facade is oriented to the South, while on the opposite side the two wings delimit a terraced courtyard (Figure 3.24). On the sides of the main façade, two portals recall the style of ancient Egypt and give access to the area on both sides of the two wings. From an architectural-functional point of view, the spatial configuration consists of a dominant room in the centre of the building, perpendicular to the south-façade, which crosses the whole building;

on the left and right side of the main room, there are two other rooms, for a total of five rooms, respectively. Along with the western wings of the building, there are three rooms, served by a corridor for each wing. In the dead corners are respectively the stairs and in the northern corridors, the bathrooms and the toilets. The castle has two main entrances in correspondence with the courtyard (north side) equipped with three double doors with external shutters. Most of the windows and doors in some cases have a 19<sup>th</sup>-century brass frame. The windows have two rows of fixtures, which open inwards, with external shutters. The doors, mostly double (internal-external and partly with parapets) have two moving parts.



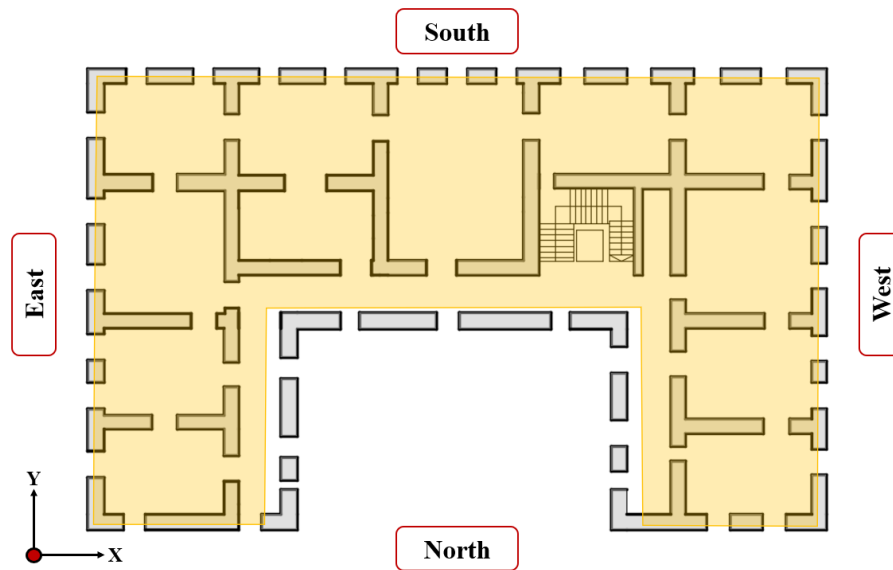


**Figure 3.24:** Geographical orientation of the main façade.

Internally, the castle was very rich in friezes, there is a "Kehleim" natural stone plate. The main staircase was made of richly decorated oak wood, in the neo-Renaissance style, according to the second part of the 19<sup>th</sup> century.

Several rooms are paved with oak floors of different ages and sizes, with large tables (18<sup>th</sup> century) and medium and small tables (19<sup>th</sup> century), and some rooms are paved with simple, painted, and unpainted. The party room had red marble floors. In some outbuildings and partly in the cellar there are concrete floors and tiled bathrooms. The building is plastered both inside and outside, except for parts of the cellar.

Structurally, the castle (Figure 3.25) is an imposing building with very thick and heavy solid brick walls with maximum plan dimensions are 38.80 m x 24.20 m. It is consisting of a ground floor, intermediate floor, and massive wooden roof. They have a thickness of 1.30 m on the ground floor, the external walls on the first floor, made of the same material, are 0.90 m thick while the internal walls have a thickness of 0.80 m.

On the upper part, there are vaulted ceilings with a thickness of 0.25 m. The roof is solid and robust, with a wooden supporting structure whose construction technique was used in the Banat region. The heights between the floors are 4.0 m and 5.70 m, respectively.



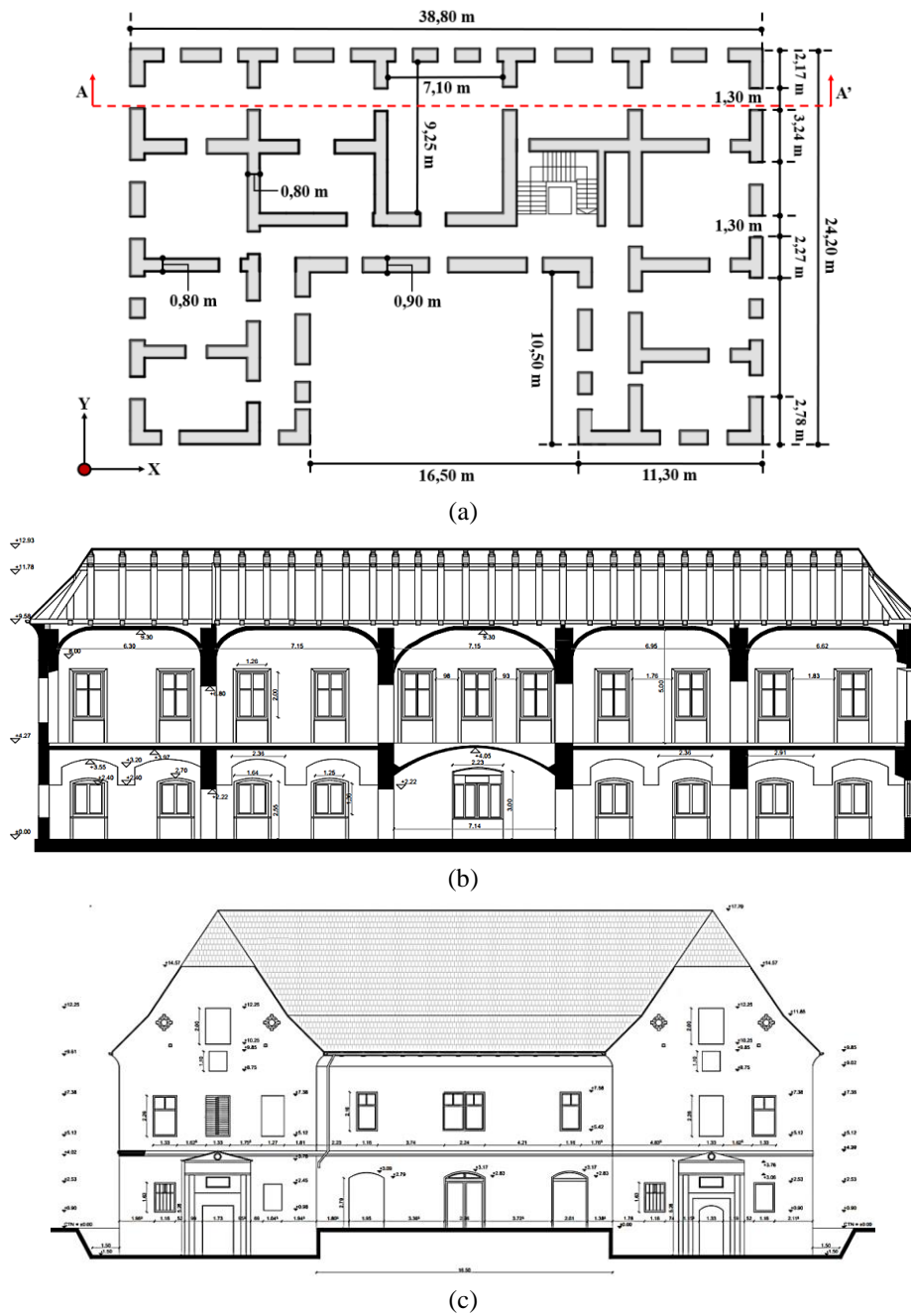


**Figure 3.25:** Architectural plan layout of intermediate-floor (a) longitudinal section A-A' (b) and North façade (c).

### 3.6.1.1 Physical conservation state condition

The causes of the deterioration of the external walls are difficult to avoid since they are related to the nature of the materials and their exposure to degradation agents (natural degradation). Generally, the main degrading agent of the exposed surfaces is the water which directly or indirectly, and in different forms (liquid, solid, gaseous), comes into contact with the wall surface structures causing (more or less) a rapid deterioration.

In particular, contextualizing the case study, the façades are characterized by plaster detachments due to the action of low temperatures (increase in volume/disintegration of the surfaces) which develop interstitial pressures which, together with the internal stresses, interrupt the weaving of the material. These phenomena have allowed the development of diffuse efflorescence and moulds which negatively affect the mechanical resistance of masonry (Figure 3.26).

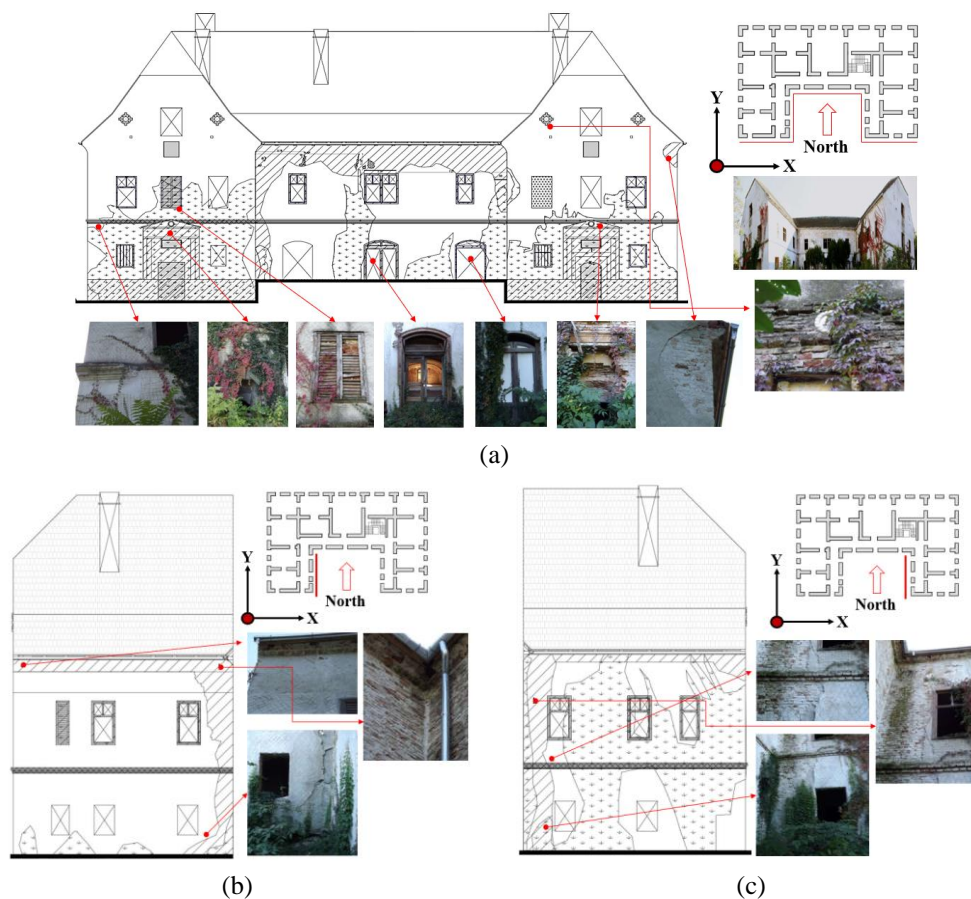
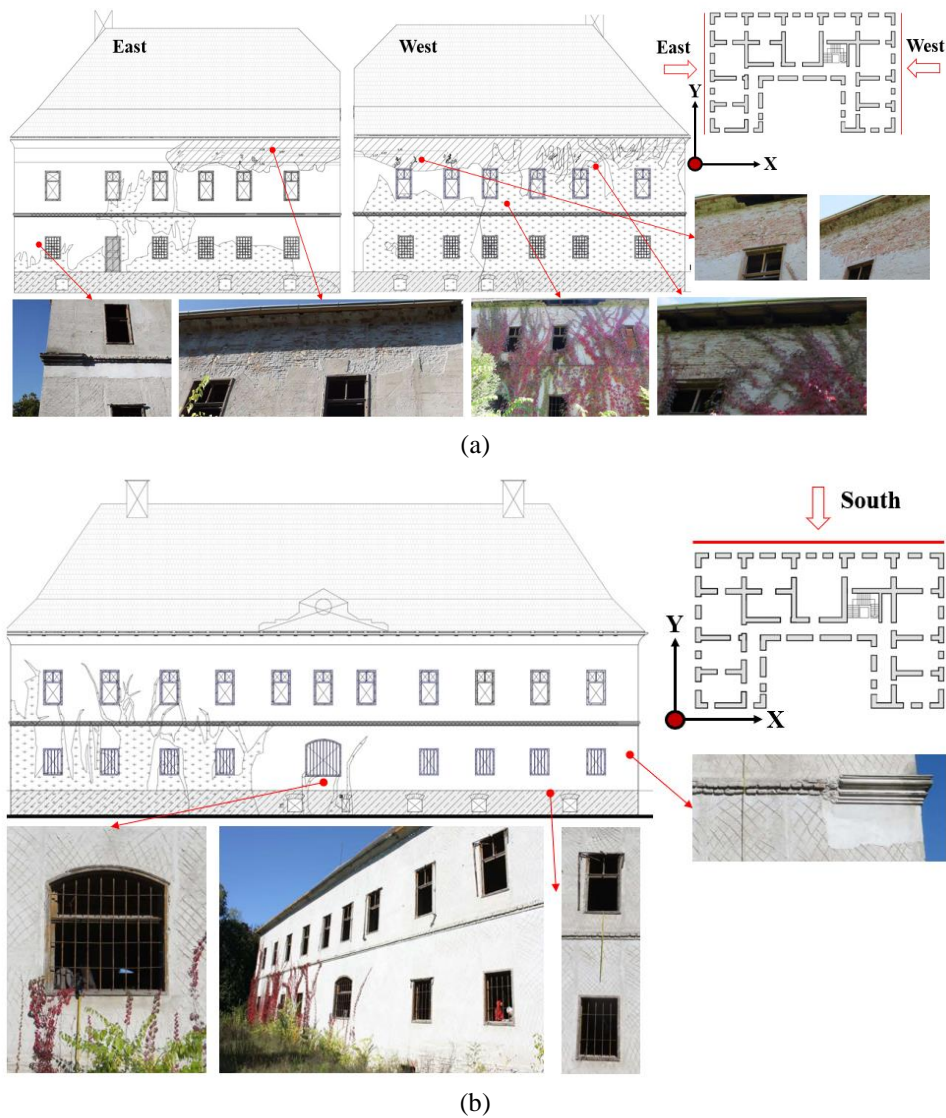


Figure 3.26: Degradation detected in the North façade.

Similarly, a degradation state is reported for the other main façades of the case study building as well (Figure 3.27).



**Figure 3.27:** Degradation detected in (a) East and West façades, (b) South façade.

As for the massive wooden roof structure, it is characterized by a widespread degradation that affects the dense system of support beams and the connections present. Generally, being a multifunctional material, wood is also vulnerable to several factors, such as exposure to bad weather (which causes rotting), attacks by plant organisms (molds, fungi, and lichens) or xylophagous insects

(woodworms and termites), or is also weakened by some wood defects (knots, cracks, and chives) or by the action of prolonged loads.

In particular, the state of conservation (even if partially collapsed following the earthquake of 1991 due to the overturning of the chimney flue) of the wooden structure is quite neglected. Excluding the presence of nodes and cracks due to the age of the wood material, other contributing factors have led to degradation over the years. In this sense, Figure 2.38 shows the plan layout with some of the inspected areas.

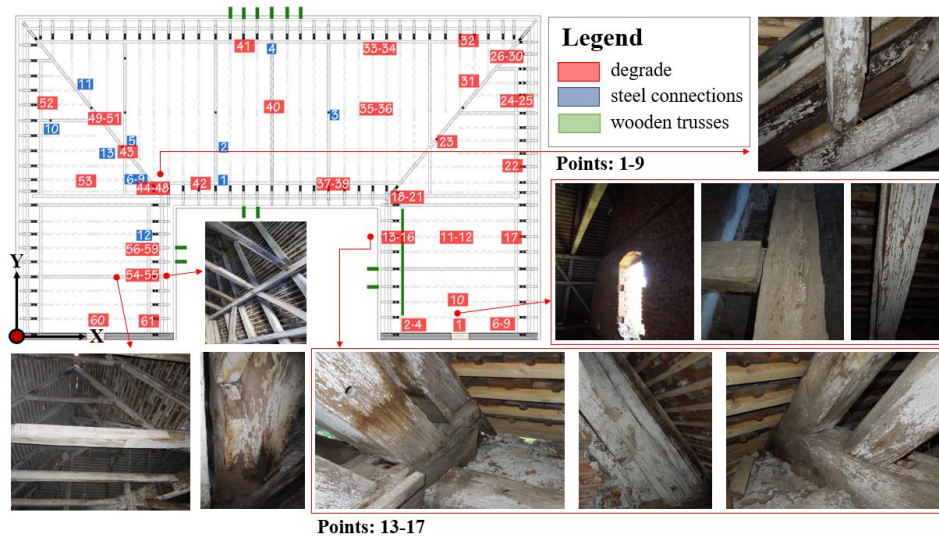


Figure 3.28: Degradation of the wooden roof structure.

As can be seen from the previous figure, there is a widespread presence of rotting of the wood. It is one of the most common pathologies and above all concerns the heads of the beams and trusses that are clamped in a wall subject to frequent infiltration of water. The presence of water that soaks the wood leads to the proliferation of mould, fungi, and lichens, capable of decomposing the wood (and therefore making it rot). Rotten wood is easily recognized, both for the possible presence of mould and its typical soft consistency. Furthermore, the presence of caries in the wood is a disease due to the presence of insidious pathogenic elements which, especially in the structural elements, cause the progressive degeneration of the physical and mechanical characteristics of the wood, obviously compromising its resistance. Finally, viscous deformation is a phenomenon that occurs when an elastic material (such as wood) remains subjected to loads for a very long period: in this case, the bending deformation of the stressed element continues to grow constantly.



### 3.6.1.2 Post-earthquake damage assessment

The Banloc earthquake was recorded on 02-12-1991 at a focal depth of 9 Km. The seismic energy released produced a magnitude ( $M_w$ ) of 5.5 according to the Richter scale. Considering the reduced focal depth, this event is best classified as a medium-depth geological event. Moreover, it is characterized by a reduced site-source distance (7.01 km far from the epicentre), which makes it a near-field event. The earthquake intensity (epicentral intensity) associated with the event that occurred was VII-VIII according to Mercalli Intensity Scale (MCS) as reported in Figure 3.29 [148].

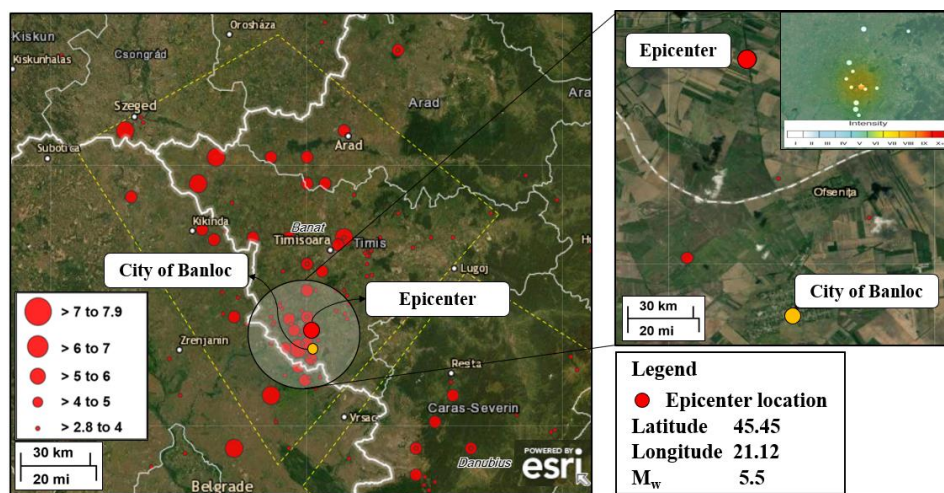


Figure 3.29: Geographical identification of the event that occurred in Banloc on 02-12-1991 [148].

This seismic event, even though of moderate magnitude, caused extensive damage to numerous unreinforced masonry buildings (URM) present in the Banloc seismic area. It caused slight damages to newly designed structures, but several masonry buildings in the area were characterized by very serious damages, also with partial collapses. As introduced in paragraph § 3.5.4.1, the damages observed after the seismic phenomenon are numerous and have produced partial or total collapses of large portions of buildings in the epicentral area. Presumably, these damages are due to the cumulative effect of the seismic sequences that occurred in the seismic area of Banloc characterized by crustal earthquakes.

Referring to the case study building, the damage was detected through on-site inspections after the earthquake occurred in December 1991.

The achieved post-earthquake damages is presented in Figure 3.30 [150].



(a) - North façade



(b) - South façade



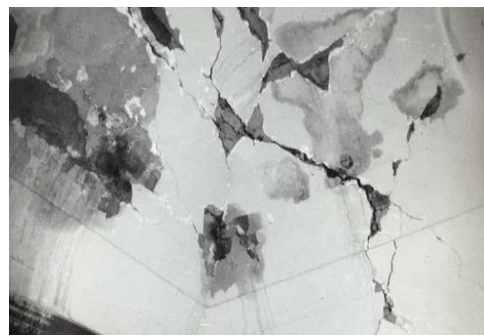
(c) – North-West façade



(d) – North façade (internal court)



(e) first floor



(f) first floor





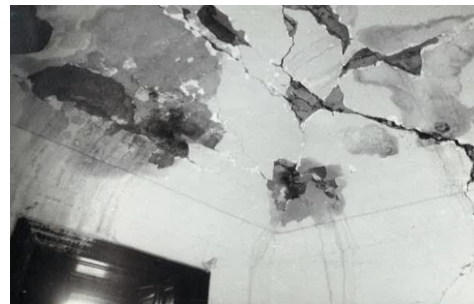
(g) first floor



(h) first floor



(i) first floor



(l) first floor



(m) second floor



(n) second floor

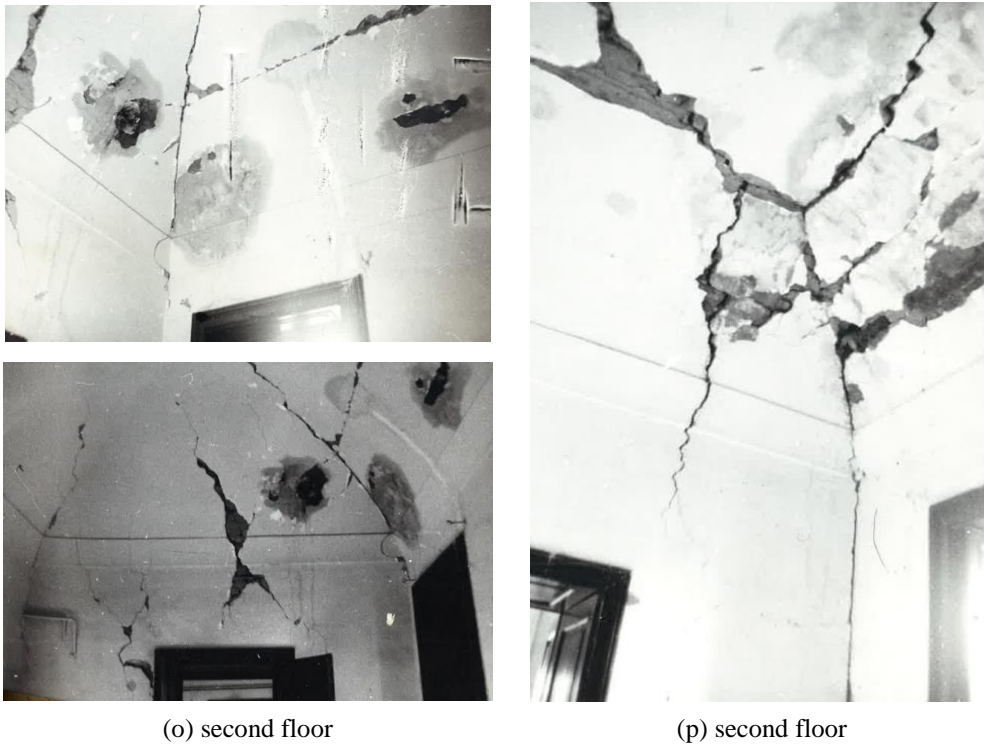


**Figure 3.30:** Detected damages on the Banloc Castle after the 1991 earthquake: (a-d) external view, (e-l) first floor and (m-p) second floor [150].

As can be seen from the previous figures, the seismic event has produced a considerable level of damages. In general, two distinct time steps can be considered to characterize the damage achieved.

Being a near-field event, in the first seconds of the time domain, the seismic vertical component induces an initial impulse effect which produces a consistent level of damage, especially in the horizontal structures and, subsequently, with the arrival of the horizontal components, the damage extends to vertical structures mainly in the spandrel beams due to the formation of shear failures.

Finally, it is worth noting the partial collapse of the wooden roof structure. In this case, the collapse is attributable to the overturning of the chimney due to the seismic action as depicted in Figures 3.30 (m-n), respectively.

### **3.7 Mechanical analysis of the Banloc Castle**

#### **3.7.1 Methodology approach**

As part of non-linear mechanical procedures for assessing the vulnerability of a building, it is possible to include non-linear static analysis (commonly called pushover) and non-linear dynamic analysis (called non-linear time-history), respectively. Basically, in the first methodology, the pushover analysis provides a useful and reliable tool for assessing the seismic vulnerability of existing buildings, since it allows, through an iterative procedure, to characterize the seismic capacity, (C), of a structural system and to compare it with the respective seismic demand (D).

The procedure described, therefore, leads to represent the structural system (MDoF) through the capacity curve. This curve uniquely represents the force-displacement law, which exhibits the structural system until it reaches its ultimate condition. Being a non-linear methodology, the non-linearities associated with the structural model are modelled through a set of plastic hinges which represent the energy dissipated during the progressive increase of the load (applied statically to the structure) and the corresponding decay of the resistance.

Therefore, the structure reaches its ultimate displacement when the decay of 20% of the maximum shear force is reached. Generally, this methodology is widely used since it guarantees quick and easy implementation and reduced post-processing computational time.

The second method, more sophisticated and refined, is implemented employing non-linear dynamics also named non-linear time history analysis. In particular time history analysis provides an assessment of the dynamic structural response under variable load based on the specified time-domain, i.e ground motion accelerograms.

Although these analyses can be linear or non-linear, depending on the considerations made on the mechanical properties of the material, which are, generally, considered the most representative parameters for studying the seismic behaviour of the structures. However, there are some disadvantages associated with this type of analysis: (i) these analyses take a long computational time since they depend on the duration of the ground motion; (ii) these analyses may depend on the selection of the applied ground motion accelerograms; (iii) complexity of execution and interpretation of results. However, although allowed in the design regulation codes [152], the analysis of the time history seems to be used mainly for academic and research purposes, is occasionally used in case of high impact

structures such as complex or historical-cultural heritage structures. To adequately take into account the variability of the seismic action, the seismic design codes require the execution of numerous analyses with different earthquake motions. For this reason, the selection and the elaboration process of the ground motion accelerograms as well as the number of analyses required, make this approach extremely laborious in design practice.

However, the starting point for performing time history analysis is the definition of the input accelerogram representative of the event being analysed. In general, the possible solutions are contemplated in [38], [40], [153]: (i) using artificial accelerograms compatible with the response spectrum; (ii) using synthetic accelerograms generated by seismological source models; (iii) using real accelerograms recorded during earthquakes.

The first types of accelerograms (compatible with the artificial spectrum) are obtained according to the response spectrum derived from seismic codes. In general, this accelerogram is defined by the power spectral density function from the response spectrum and, subsequently, by deriving signals compatible with that spectrum [153], [154].

The second type of accelerogram is defined as synthetic since it can be generated by seismogenic source models.

Finally, the third type of accelerogram is derived directly from seismic recordings and contains several pieces of information regarding the nature of ground motions. Given the vast database of events that have taken place, this approach is undoubtedly the most used [153]. In seismic design codes, a guideline concerning the use of accelerograms for nonlinear dynamic analysis is not explicitly defined. Generally, the information is not exhaustive and fragmented [152].

Based on these considerations, in the present thesis, the non-linear dynamic analysis has been performed using the third type of accelerograms, representative of the event that occurred in Banloc in December 1991.

### 3.7.2 Modelling philosophy

The modelling represents a relevant and very complex aspect since, as far as analysed, it highlights how masonry is a heterogeneous material whose mechanical characteristics differ according to the disposition of the mortar (which represents the weak points). This task is of fundamental importance since, in the modelling phase, these masonry properties must be taken into account to calibrate numerical models in the best way.

In the 1960s, Pauley et al., (1974) [155] has been introduced two distinct cracking models: discrete cracking and smeared crack, respectively. The first numerical simulation was developed for the analysis of concrete fractures using non-linear constitutive models.

The modelling alternatives depend mainly on how detailed the numerical model is and how accurately it can describe different types of failures [156], [157].

In general, three distinct approaches have been used for the numerical calculation of masonry. These techniques depend on the level of accuracy of the models and differ as follows [156]:

- i. *Detailed macro model* (Figure 3.31a): bricks and mortar are considered continuous interacting elements with specific failure criteria. This approach faithfully reproduces the geometry of the wall and taking into account the level of detail, the interface between bricks and mortar is considered with *interface elements* that represent the discontinuities reproducing the failure of masonry;
- ii. *Simplified micro model* (Figure 3.31b): the bricks are considered continuous elements interconnected to the mortar through suitable contact systems. However, this modeling is deficient in identifying some possible cracks since the mortar and brick interaction is not considered;
- iii. *Macro model* (Figure 3.31c): this method, generally adopted for non-detailed analyses, considers the generic structural element not characterized by a diversification between the constituents elements such as mortar and brick. This modeling approach is unable to reproduce the typical collapse mechanisms in a very refined way.

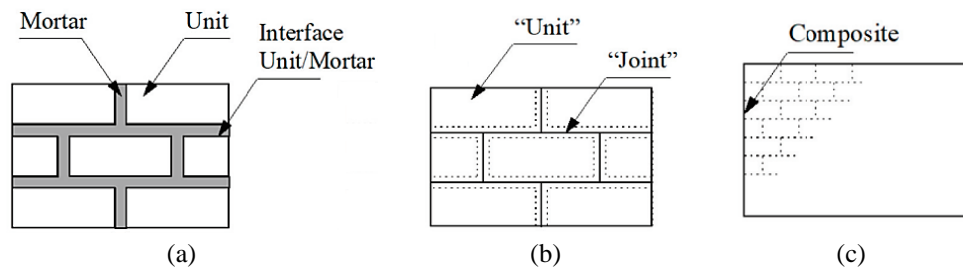


**Figure 3.31:** Modelling strategies: (a) detailed model; (b) simplified model and (c) macro model [156].

In the framework of this thesis, only the macro-modelling technique has been considered in the implementation of the numerical model.

However, it is worth considering the non-linear behaviour of masonry. One of the precursors regarding the study of non-linear masonry behaviour was [158].

The study proposed to consider masonry as an equivalent two-phase material (bricks and mortar) interacting with each other. The brick has been identified as finite quadrilateral elements with plane stress, whereas the mortar joints are represented by connecting elements, capable of deforming only in the normal and tangential direction concerning the applied load.

Subsequently, in the 80s, Page et al., (1985) [159] an experimental campaign was carried out conducted on half-scale brick masonry samples. The data collected from the tests allowed to development of the first reports regarding the non-linear constitutive law (inelastic behaviour) of masonry.

According to [156], two different non-linear models for masonry were defined:

- i. composite interface model;
- ii. an anisotropic continuum model.

The first model is defined by structural boundaries condition representative of the inelastic behaviour of the masonry. The model of the coupling plasticity can reproduce three different types of failure mechanisms, i.e, shear tension, Coulomb friction, and elliptical domain (Figure 3.32a).

In the second one, the continuous anisotropic model is based on two main criteria, as reported in [156], to identify the proper tensile and compressive behavior, respectively (Figure 3.32b).



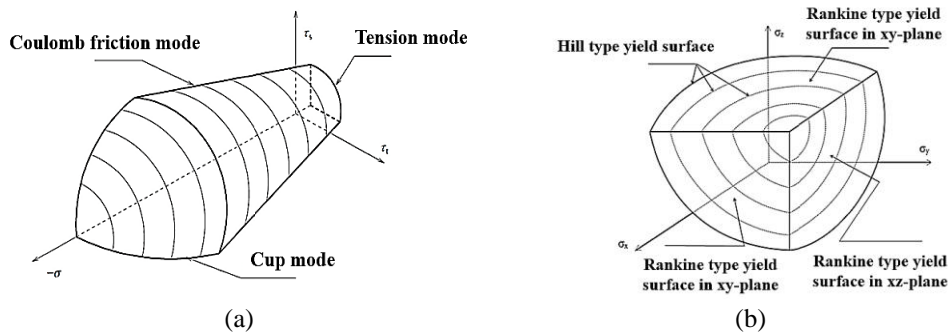


**Figure 3.32:** Failure models: (a) composite interface; (b) anisotropic continuum [156].

However, the experiments conducted over the years have developed many other constitutive models with the aim of best representing the non-linear behaviour of different types of masonry [160-163].

### 3.7.3 Mechanical properties of masonry

Masonry is a very complex composite material, based on the interaction between stone elements and mortar. However, although considerable and reliable calculation procedures have been achieved, the evaluation of the properties of the masonry still represents a significant problem, due to the different uncertainties of the material. In particular, the most influential mechanical parameters for structural analysis are mainly related to compressive strength, bending and shear, modulus of elasticity, and friction coefficient [164-169]. For this reason, it is necessary to study the behaviour of masonry using appropriate experimental tests [170]. The main experimental tests carried out on masonry samples are [171], [172]:

- *Uniaxial compression test* (Figure 3.33a): performed on a masonry sample using flat jacks. This procedure shows the vertical fissures that are triggered in the stone units along the median line of the sample and as the deformation increases there are further vertical crack increases located on the smaller side of the sample that lead to failure by splitting the prism;
- *Diagonal test* (Figure 3.33b): consists of applying an external compressive force along the diagonal on the panel. Generally, the failure is related to the overcoming of the compressive strength of the masonry in the direction of the applied load;

- *Compression and shear test* (Figure 3.33c): performed on a sample subjected simultaneously to a constant vertical compression load and gradually increased horizontal load.

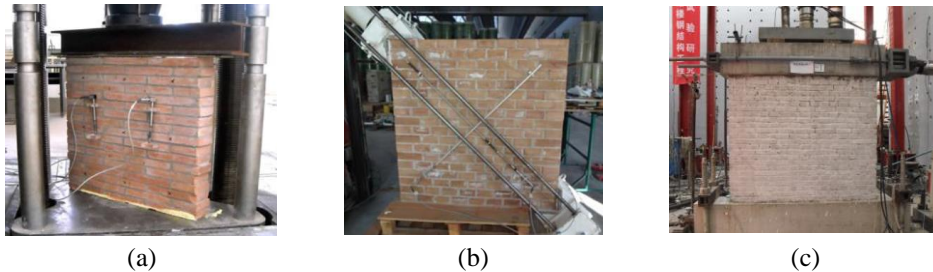


**Figure 3.33:** Masonry experimental test: (a) Uniaxial test; (b) Diagonal test and (c) Compression and shear test [172].

However, if experimental data are not available, the characteristic compressive strength of the masonry,  $f_k$ , can be determined starting from the normalized compressive strength ( $f_b$ ) defined previously, according to [171]:

- for masonry made with a general-purpose mortar and lightweight mortar (Equation 3.16):

$$f_k = K \cdot f_b^{0.7} \cdot f_m^{0.3} \quad (3.16)$$

- for masonry made with thin layer mortar, in bed joints of thickness 0.5 mm to 3 mm (Equation 3.17):

$$f_k = K \cdot f_b^{0.85} \quad (3.17)$$

- for masonry units made with thin layer mortar, in bed joints of thickness 0.5 mm to 3 mm, and clay units (Equation 3.18):

$$f_k = K \cdot f_b^{0.7} \quad (3.18)$$

where  $K$  is a constant depending on the classification of the masonry unit.

Another important property for masonry is the ability to withstand lateral forces. Therefore, shear strength is defined as the combination of the initial shear strength in the absence of vertical load and an increase in strength due to the compressive stress perpendicular to shear in the element at the examined level [173]. The masonry shear strength is established by specific experimental tests

according to EN 1052-3 [174] so that only shear stresses develop in the mortar. The characteristic shear strength  $f_{vk0}$  must not be greater than a limit value specified in the codes and can be taken from the following Equation:

$$f_{vk} = f_{vk0} + 0.4 \cdot \sigma_d \quad (3.19)$$

where  $\sigma_d$  is the design compression stress perpendicular to the shear direction. However, masonry is characterized by weak tensile strength with brittle fracture. This resistance is assumed to equal 10% of the compressive strength. Finally, the elastic modulus,  $E$ , secant modulus of elasticity, and  $G$ , tangential elasticity modulus, can be experimentally evaluated by adopting the Equations prescribed by Italian Code, NTC08 [135]:

$$E = 1000 \cdot f_k \quad (3.20)$$

$$G = 0.4 \cdot E \quad (3.21)$$

### 3.7.3.1 Constitutive model

Masonry is influenced by its morphological properties such as heterogeneity and anisotropy which significantly influence its mechanical behaviour.

The stress-strain law about uniaxial and biaxial loading conditions presents a variable behaviour depending on whether the behaviour of only stone, mortar, or composite such as stone element + mortar is analysed, the latter has intermediate characteristics concerning the resistance offered by individual elements.

Although the behaviour of the materials (stone and mortar) is characterized by high resistance to compression, regarding the tensile behaviour, there is a decay of resistance due to the fragile nature of the base materials.

Substantially, the masonry material, when subjected to tensile forces, presents a reduction of the resistance since the contribution of the tensile stresses is guaranteed only by the mortar. The NTC08 [135] and EC8 [38] also proposes a stress-strain relationship to be used in the design phase. This law represents a non-linear relationship and can be considered linear, parabolic, rectangular, or simply rectangular (Figure 3.34).

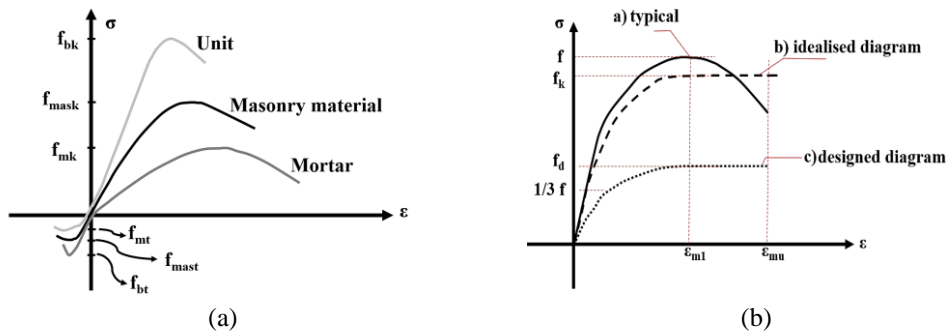


**Figure 3.34:** Stress-strain law: (a) generic behaviour [135]; (b) EC8 proposal [38].

The study proposed by Lourenço, 1996 [175] has highlighted how masonry manifests a strongly non-linear behaviour characterized by a post-peak softening trend, which consists of a gradual reduction of the resistance of the material under a continuous increase of the deformation. This characteristic is typical of quasi-brittle materials.

According to [175], the material is characterized by compressive,  $G_c$ , and tensile,  $G_t$ , fracture energy. The fracture energy can be defined as the amount of energy required to propagate a unitary area of the crack, intended as the projected on the plane parallel to the direction of the main fracture.

Figures 3.35 (a) and 3.35 (b) have shown the characteristic stress-strain diagrams related to the uniaxial behaviour of masonry in compression and tensile, respectively [176].

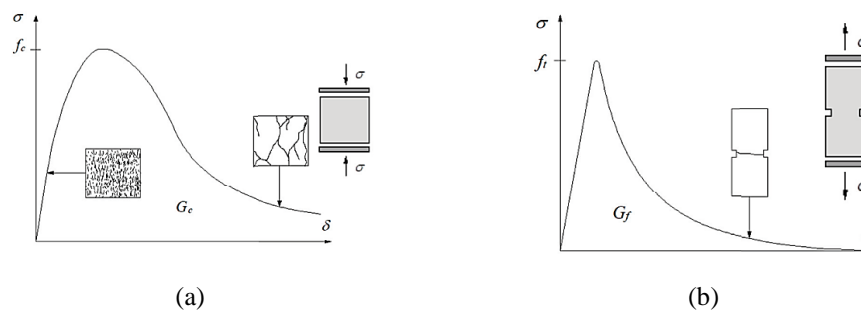


**Figure 3.35:** Quasi-brittle materials under uniaxial loading: (a) compressive behaviour; (b) tensile behaviour [176].

Therefore,  $f_t$  and  $G_f$  are the tensile strength and fracture energy, and  $f_c$  and  $G_c$  refer to the compressive strength and fracture energy, respectively.

Jansen and Shah [177] proposed a qualitative and quantitative evaluation of fracture energy using the *ductility index*, according to Equation 3.22:

$$d = \frac{G_f}{f} \quad (3.22)$$

The ductility index ( $d$ ), is defined as the ratio between the energy of the fracture  $G_f$  and the corresponding maximum strength  $f$ . As proposed by [178] various experimental campaigns have been developed for the definition of the aforementioned index about the type of masonry [179], [180].

The authors specify that the diversity of values is due to the different procedures used in the calculation of fracture energy. However, the recommended ductility index, in absence of further information is the average, 0.029 mm.

Model Code 90, [181], recommends the following Equation 3.23:

$$G_f = 0.025 \cdot \left( \frac{f_c}{10} \right)^{0.7} \quad (3.23)$$

with  $G_f$  in N/mm and the compressive strength,  $f_c$ , in N/mm<sup>2</sup>.

Furthermore, according to [182], the tensile fracture energy is defined by Equation 3.24:

$$G_f = 0.025 \cdot (2 \cdot f_t)^{0.7} \quad (3.26)$$

### 3.7.3.2 Modelling techniques

Masonry structure can be considered as the assembly of different elements such as piers, spandrels, and nodal panels, all configurable as bi-dimensional plate-type elements that are subject to an in-plane stress state.

The pier elements can be defined as the wall element of finite dimensions that has the task of transferring the loads to the foundation system. The spandrel is that part of the building that lies between two openings in a vertical direction. It plays the role of taking matched masonry piers and transferring to them the stresses induced by external loads. Finally, the nodal panels are finishing elements between piers and spandrels (Figure 3.36a) [172].

Moreover, a wall system can be defined as regular, if the openings are vertically and horizontally aligned (Figure 3.36b) [172].

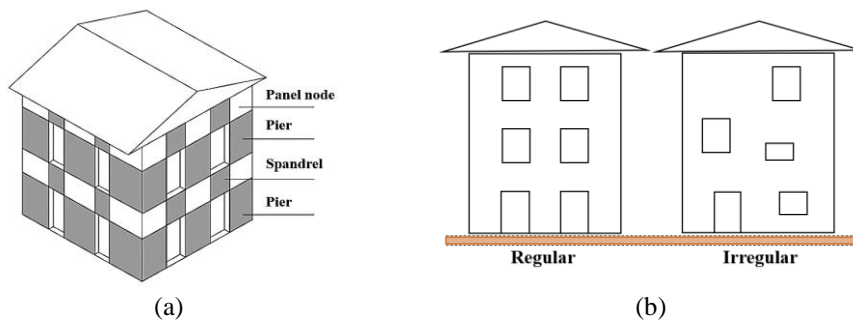


**Figure 3.36:** Masonry structure: (a) structural components; (b) wall configurations [172].

According to what has been introduced in § 3.7.2 concerning the third modeling criterion (macro elements), the proposed methods can be distinguished in [183-185]:

- *Simplified structural models;*
- *Refined structural Model (FEM).*

In the first case, it is possible to consider:

- i. *Equivalent Frame Model (EFM):* the structure is represented as an assembly of vertical and horizontal elements that schematize the behaviour of piers and spandrels. The nodal panels are connected by rigid nodes. Usually, only the in-plane mechanisms are considered. By concentrating damage, slides, and rotations in predefined sections of the structural elements, these models allow performing non-linear incremental collapse analysis of entire buildings [183];
- ii. *Macro element model:* which considers the structure as an assembly of two-dimensional cut walls connected through a flexible diaphragm floor. Each wall is assumed as constituted by deformable panels, called macro-elements, connected using rigid elements (nodal panels).

In this scheme, all the deformations and damages are concentrated in the macro elements while the rigid parts rarely suffer structural damage [184].

The FEM technique is much more detailed and exhaustive than what has been explained by the previous methodologies. Mainly, there are two types of finite elements to be defined [185]:



- *Two-dimensional elements (EFM)*: which allow you to generate faster models from a computational point of view and more controllable due to the presence of fewer joints than brick elements (Fig. 3.37a);
- *Three-dimensional elements (brick)*: generated by very refined models allow controlling the stresses evolution within the structure (Fig. 3.37b).

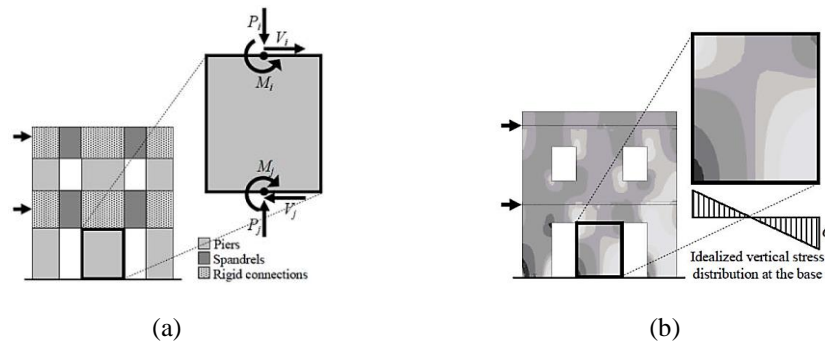


**Figure 3.37:** Different modelling techniques for masonry structures: (a) EFM; (b) FEM [185].

### 3.7.3.3 The behaviour of masonry structure under gravitational load

First of all, a numerical model means a mathematical tool that allows the analysis of the behaviour of the structural system to determine the state of stress.

The main analysis types under vertical loading conditions are summarized in two main groups:

- i. **Elastic analysis:** according to which there is a direct proportionality between cause (external load) and effect (deformation). In this case, the structural system is assembled as a series of two-dimensional panels interconnected with each other (macro-elements or EFM methods). The analysis is based on an elastic-linear constitutive model that allows guaranteeing the global equilibrium between forces and deformations;
- ii. *Non-linear analysis:* this type of calculation takes into account the non-linear behaviour of the material, according to the previous explanations mentioned in § 3.7.2 paragraph.

For masonry, typically conceived as a material with reduced tensile strength, the parzialization of the section occurs for low load levels compared to the design ones. This condition consists of a reduction of the resistant area of the masonry elements.

Generally, according to EC6, [164] to perform structural analysis, the following combination of actions can be taken into consideration (Equation 3.27):

$$F_d = \gamma_{G_1} \cdot G_{k1} + \gamma_{G_2} \cdot G_{k2} + \gamma_{Qk} \cdot Q_{ki} \quad (3.27)$$

where:

- $G_{k1}$  e  $G_{k2}$  express the characteristic value of the permanent loads;
- $Q_{ki}$  express the characteristic value of variable load;
- $\gamma_G$  represents the partial safety factor for the ultimate limit state;

Furthermore, the EC6 [164] defines the safety checks relating to unreinforced masonry walls **in a static regime:**

**Gravitational load:** the verification is satisfied when the condition reported in Equation 3.28 is guaranteed. In particular, the axial stress regime provided by the gravitational loads, namely  $N_{Ed}$ , is less than the corresponding structural resistance, identified as  $N_{Rd}$ , offered by the masonry panel [164]:

$$N_{ED} \leq N_{RD} = \Phi \cdot t \cdot f_d \quad (3.28)$$

in which  $\Phi$  is the capacity reduction factor, associated with both, the slenderness of the panel and load eccentricity;  $t$  and  $f_d$  refer to the thickness and the design strength of the wall panels, respectively.

**Bending moment:** the verification is satisfied when the bending action generated by the applied load ( $M_{Ed}$ ) is less than or equal to the bending resistant moment of the wall ( $M_{Rd}$ ) according to Equation 3.29 [164]:

$$M_{ED} \leq M_{RD} = f_{bd} \cdot Z \quad (3.29)$$

where the corresponding mechanical parameters are derived according to [164].

**Horizontal forces:** is satisfied when Equation 3.30 is mathematically arisen [164]:

$$V_{ED} \leq V_{RD} = f_{vd} \cdot t \cdot l_c \quad (3.30)$$

having assumed as  $f_{vd}$  the shear design resistance of the masonry panel and  $t$  and  $l_c$  are the thickness and the extension compressive area of the masonry, respectively.

**Concentrated actions:** defined according to Equation 3.31 [164]:

$$N_{Edc} \leq N_{Rdc} = \beta \cdot A_b \cdot f_d \quad (3.31)$$

where  $\beta$  is the strengthening factor for concentrated loads,  $A_b$  is the loaded area,  $f_d$  is the design compressive strength of masonry.

#### 3.7.3.4 The behaviour of masonry structure subject to ground motion horizontal components

In seismic conditions, the global analysis of a masonry building is always necessary and unavoidable.

The cyclical nature of the increasingly devastating seismic events has demonstrated the high vulnerability of the existing building heritage. In general, the seismic vulnerability of masonry buildings derives from several factors, recognized in modern design regulations.

The main vulnerability factor is associated with the building's capacity to absorb the function of uniformly distributed, based on the rigidity of the walls, the seismic load, and, therefore, assuming a "global" behaviour.

Generally, masonry buildings are designed to fulfil the function of transferring vertical loads to foundations, however, in seismic conditions, obvious critical aspects of the construction techniques used are evident. Substantially, different structural models that characterize the behaviour of a masonry building can be taken into consideration:

- i. *analysis of the individual walls* (considered independent): in this case, the connection capacity of the floor is neglected, and its function of distributing the loads. In this case, the walls are exposed to out-of-plane mechanisms that are triggered by the seismic load;
- ii. *three-dimensional analysis of the building*: in which the walls are well connected but the floor does not absorb the connection's function. In this hypothesis, the possible out-of-plane mechanisms are reduced;
- iii. *three-dimensional analysis of the building as a frame*: in which the building is considered as a space-frame model with deformable floors;
- iv. *analysis of the building with box behaviour*: in this case, the building has rigid floors with impeded nodal rotations. The walls are well connected, avoiding the problem of out-of-plane mechanisms.

To the grade of connection, more or less effective, between orthogonal walls influence the capacity of the buildings that are subject to different types of failure [186], [187]:

- i. **I Mode Collapse Mechanisms** (Figs. 3.38a-3.38b): generally involve out-of-plane damage and can be considered local mechanisms, since they are associated with portions of macroelements;
- ii. **II Mode Collapse Mechanisms** (Figs. 3.38c-3.38d): related to the in-plane mechanisms of structural elements.

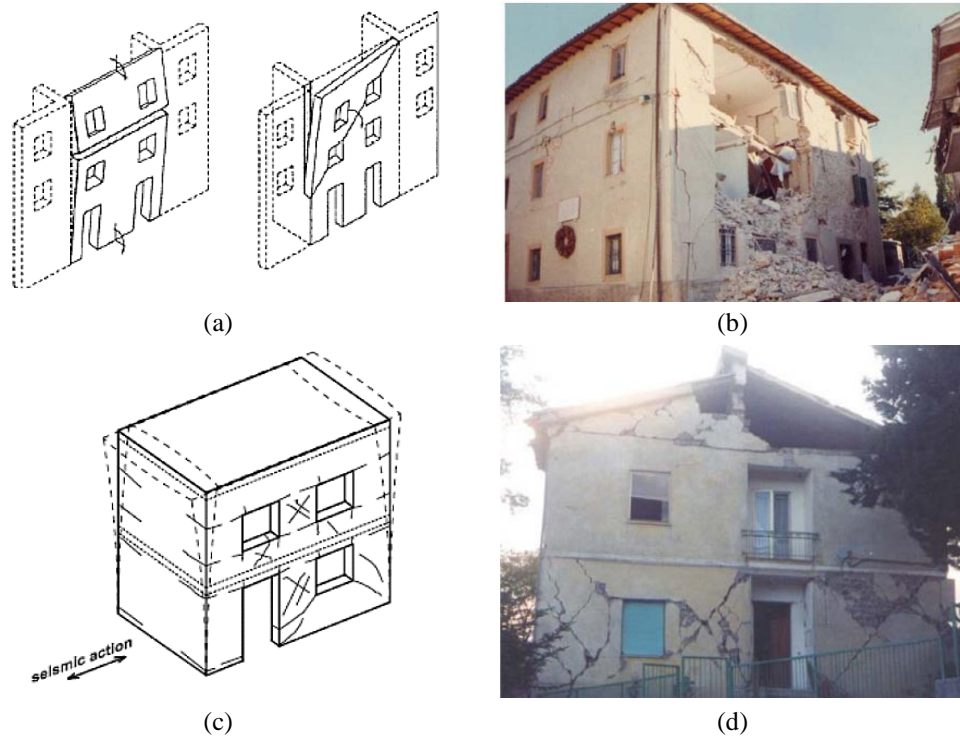


**Figure 3.38:** Different collapse mechanisms: (a-b) I Mode Collapse Mechanisms [186]; (c-d) II Mode Collapse Mechanism [187].

Accordingly, the actions that characterize the seismic condition (EC8, part. 1, 2004, [188]) are provided by the following Equation 3.32:

$$F_d = \gamma_{G_1} \cdot G_{k1} + \gamma_{G_2} \cdot G_{k2} + \sum_i \Psi_{0i} \cdot Q_{ki} + E \quad (3.32)$$

as can be seen, the seismic action (E) is added to the vertical loads of the quasi-permanent combination. In this case,  $\psi_i$  is generally assumed to be 0.3 for ordinary buildings. The general principle of considering an accidental eccentricity,  $e$ , to take into account the spatial variability of seismic motion to consider the torsional contribution to the global seismic response of the building is assumed to equal to  $\pm 5\%$  of the size of the building orthogonal to the earthquake's direction.

Other vulnerability factors are related to the building's configuration (e.g. dimensions, building form, geometric proportions, location of structural components).

To verify the safety of masonry construction, a simplified formulation is adopted. The main strength criteria are related to the following state: (i) compressive-bending; (ii) diagonal shear; (iii) sliding shear (Figure 3.39), [188-190].

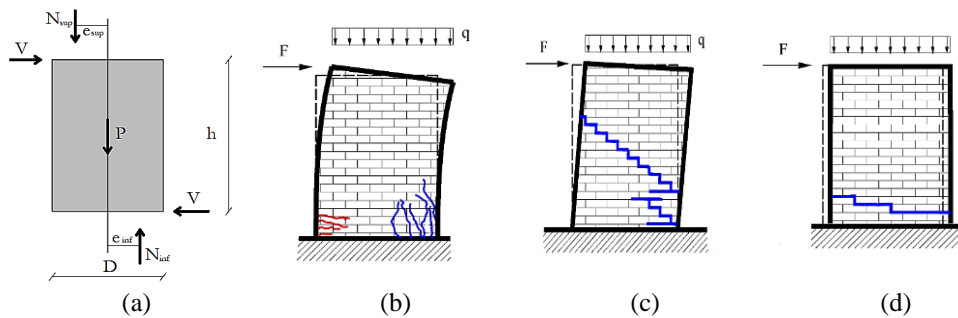


**Figure 3.39:** Strength criteria: (a) action in the wall plane; (b) rocking collapse; (c) diagonal shear and (d) sliding shear [190].

Concerning the rocking failure mode (Figure 3.39b), a proper stress distribution has been introduced in Equation 3.33 [188]:

$$M_u = \left( \frac{N \cdot l}{2} \right) \cdot \left( 1 - \frac{N}{\chi \cdot f_d \cdot D \cdot t} \right) = \left( \frac{\sigma_0 \cdot D^2 \cdot t}{2} \right) \cdot \left( 1 - \frac{\sigma_0}{k \cdot f_d} \right) \quad (3.33)$$

where  $N$  represents the applied axial load;  $\sigma_0$  is the mean compressive stress;  $D$  and  $t$  are related to the geometry of the panel (width and thickness);  $k$  correlated to the stress block assumed equal to 0.85 and,  $f_d$  is the design compressive stress [188]. About the diagonal cracking (Figure 3.39c), failure is achieved with the formation of a diagonal crack, which develops from the centre of the pier and propagates towards the corners. This failure criterion is very complex and is influenced by many factors such as the heterogeneity of the masonry and the quality of the basic components that play a predominant role.

A simplified approach has been formulated by [189] as reported in Equation 3.34:

$$V_u = \frac{1.5 \cdot f_{v0d} \cdot D \cdot t}{\xi} \cdot \sqrt{1 + \frac{\sigma_0}{1.5 \cdot f_{v0d}}} \quad (3.34)$$

where  $f_{v0d}$  represents the design conventional strength of masonry and  $\zeta$  is a coefficient based on the geometry of piers;

Finally, the sliding shear failure (Figure 3.39d), developing as a result of flexural cracking, in the tensile regime, at the corners of the wall panel, is attained with sliding on a horizontal bed joint plane, usually located at one of the extremities of the wall providing a reduction of the masonry resisting section.

The simplified relation for the sliding shear generally concerns the verification of the spandrel's elements. It is regulated by the following Equation 3.35.

$$V_u = h \cdot t \cdot f_{v0d} \quad (3.35)$$

where  $h$ , is the spandrel depth;  $t$  is the spandrel thickness;  $f_{v0d}$  is the design shear strength with no axial force [188].

### 3.7.3.5 The behaviour of masonry structure subject to ground motion vertical component

Typically, the vertical component of earthquake ground motion has been ignored in structural earthquake engineering. The seismic design of Unreinforced Masonry (URM) structures is limited to the effects of the horizontal acceleration, neglecting the vertical component of the design ground motion (i.e. § 4.3.3.5.2 in Eurocode 8 [38] and §7.2.1 in NTC2018 [40]). The damage caused by disastrous earthquakes that occurred highlights a fragile structural system concerning seismic action.

Field evidence has shown that the vertical component of ground motion is more significant than previously thought, especially for near-field events.

The study proposed by Campbell [191] has shown how the V/H ratio in the near-source region of large earthquakes was considerably different than the expected value derived at a smaller magnitude and higher distances, suggesting that the empirical limit of V/H=2/3 could be re-evaluated to better foresee the effects of ground motion vertical component for design purposes. These ratios near the seismogenic source exceed the 2/3 limit, exceeding unity.

Generally, earthquakes that occur close to the source are characterized by impulsive phenomena [126]. These pulses release very high energy accumulated during the dislocation of the faults systems transmitting it directly to the buildings located above the ground surface[122].



The effects produced by the ground motion vertical component significantly influence the dynamic response of the structures.

As reported in [32] the influence of vertical excitation consists in a progressive reduction of the bearing capacity of a generic structural element since in the time domain, the continuous variation of compression and decompression actions gradually reduce the strength of the masonry, altering its susceptibility to the damage [122].

Two main aspects that characterize the induced effects can be identified. The first aspect, in the case of compression peak, leads to an improvement in terms of strength of the masonry since, being more compressed, enhanced the load-bearing capacity towards vertical and shear loads. Conversely, the second aspect concerns the peak decompression phase. In this circumstance, the masonry suffers a reduction of the load-bearing capacity induced by the axial forces, providing a lower resistance concerning the shear forces with the consequent formation of collapse mechanisms or pseudo-vertical cracks. The identification of possible asynchronous failures mechanisms induced simultaneously by the ground motion components (vertical and horizontal) can be interpreted as shown in Figures 3.40 [15], [192].

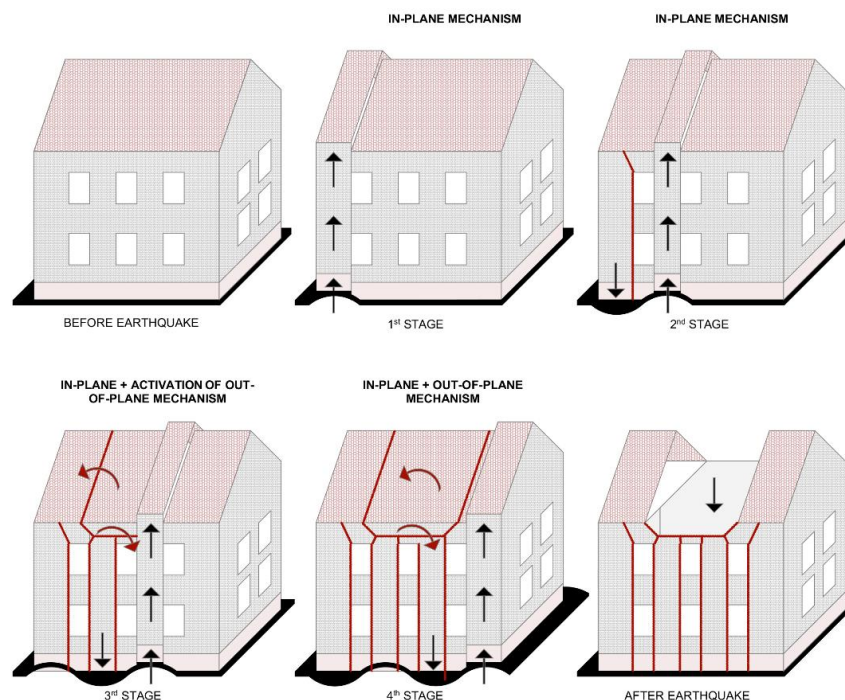


**Figure 3.40:** Mechanisms induced by the asynchrony of the seismic vertical component [192].

As can easily guess, the previous figure shows how the arrival of the vertical seismic component induces in the first instance vertical cracks induced by the asynchrony of the seismic wave. As evidenced by the damage found after the 1991 earthquake in Banloc, many buildings suffered vertical cracks to vertical and/or horizontal structures in the first seconds of the time history.

This happens since the vertical main-shock releases all its energy content impulsively when the structure can still be considered in the elastic regime.

Subsequently, after the energy dissipation of the vertical component, the horizontal seismic actions trigger the local or global mechanisms as in-plane or out-of-plane failures [15], [192].

Many structural damages that occurred after strong earthquakes (Northridge in 1994, L'Aquila in 2009, Kobe in 1995, [193]) consistently showed a progressive reduction in shear strength and ductility due to the variations of axial force regime deriving from the vertical component of ground motion (Figure 3.41) [122].

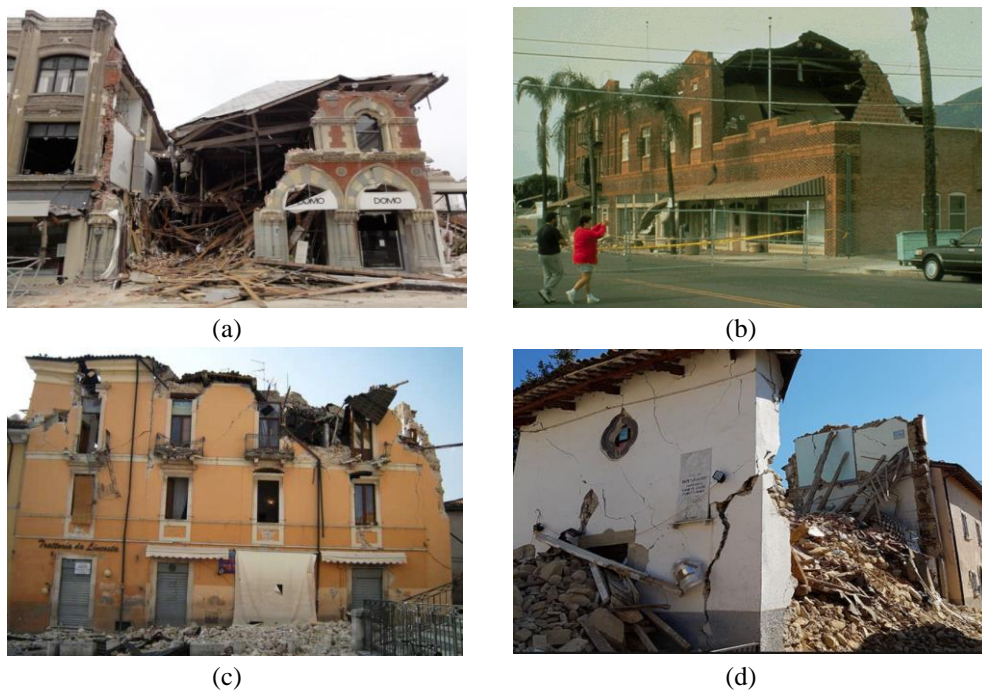


**Figure 3.41:** Damage recognition after earthquake: (a-c) Northridge and (c-d) Central Italy [193].

As supported by the studies developed by [32] and [30], in terms of forces regime, it has been shown how the influence of the vertical component induces an axial load variation of about 400% and 460% in the masonry and R.C

buildings compared to the case in which the vertical component is neglected. This aspect is strongly influenced by the selection of the accelerograms representative of the studied event since the vertical acceleration peaks depend on the type of fault mechanisms, the distance  $R_{jb}$ , the site conditions, and finally, the energy content released.

### 3.7.4 FEM model of the case study building

#### 3.7.4.1 Calculation procedure

The TNO DIANA FEA calculation software package has been used to analyse the building, selected as a case study [194].

Such software is the acronym of DIsplacement ANAlyzer, it is a large multi-purpose finite element software package dedicated, but not exclusively, to Earthquake Engineering.

The robust functionality of the program includes extensive material models, element libraries, and analysis procedures, which are based on the latest and most advanced finite element analysis techniques.

The software is also equipped with powerful solvers to optimize the solution procedures for all types of complex linear and nonlinear models with accurate results and quick and reliable calculations. FEM is a refined computational numerical technique most commonly used to solve complex engineering problems. Therefore, it should be taken into consideration that a finite element analysis (FEA) does not generate a closed formulation as an output but an approximate result (taking into account the intrinsic errors deriving from the modelling). However, to analyse the structure, the software idealizes it by dividing the structural elements into a finite number of regions and/or parts (elements) interconnected by nodes. This assembly is called a mesh. The operating principle of the software is based on the scheme presented in Figure 3.42:

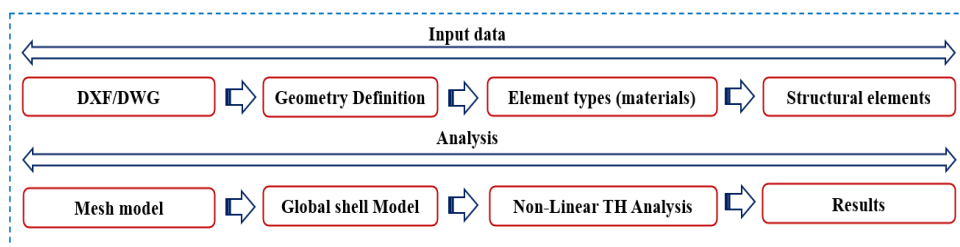


Figure 3.42: Framework of the operating scheme.

To reduce the time processing is necessary to minimize the number of errors in the building model process. However, some basic aspects must be taken into account to maximize the goodness of the expected results: (i) physically understand the problem and the behaviour of the elements that are assembled and set the basic hypotheses, (ii) correctly arrange the elements to do not generate structural lability, (iii) critically evaluate the results and possibly make changes to the model to improve its accuracy.

So, based on these requirements, before performing the analysis, it is important to plan concretely the approach to be used to and circumscribe the problem (structural model). For this reason, it is important to have a clear understanding of (i) what the goals are to be archived; (ii) which criteria will be used to evaluate the set objectives; (iii) what is the expected output based on the objectives (iv) how much part of the structure must be modelled to simplify and streamline the problem; (v) what are the boundary conditions and the loads to be considered [194].

#### 3.7.4.2 FEM Model

The analysis of historic masonry buildings represents a very complex task that depends on numerous factors that can significantly influence the expected output. In general terms, this problem can be addressed by considering two main aspects, such as (i) simplification of the geometric model and (ii) idealization of materials. It is evident that these two steps are important and influence the global seismic response of the structure. From a geometric point of view (idealization of the structural model), the completeness of the information is indispensable to reduce the uncertainties related to the modelling phase and the assumption of simplifications (the geometric model must comply with the real case but at the same time it must be as simple as possible).

Secondary, focusing on the idealization of the materials, as is known, masonry structures are characterized by low tensile strength values, which produces important cracks in the structure, with opening, closing, and reopening of the cracks during the analysis process. This the mechanical behaviour present in masonry introduces in the numerical calculations the so-called "numerical noise", due to the rapid transition from linear elastic behaviour to a complete cracking (post-elastic phase) state involving almost zero rigidity [195].

In general, with the adoption of the FEM calculation models, different types of elements are available (linear elements, 2D elements such as shells, and 3D

elements such as solids) to idealize and contextualize the real problem. Some of them are more suitable for general applications, while others have limited adaptability. In the specific case of historical masonry structures, geometry can usually be idealized in different ways, in particular by using:

- i. *linear elements*: idealize truss elements, beam, steel tie rods or seam bars, lintels, columns and are generally used to represent linear structural components;
- ii. *two-dimensional elements (2D shell)*: typically used for walls, slabs, vaults, domes being flat or curved components;
- iii. *three-dimensional elements (solid)*: used to define the basic conditions to best represent the geometry appropriately.

The representation of the type elements is presented in Figure 3.43 [196]:

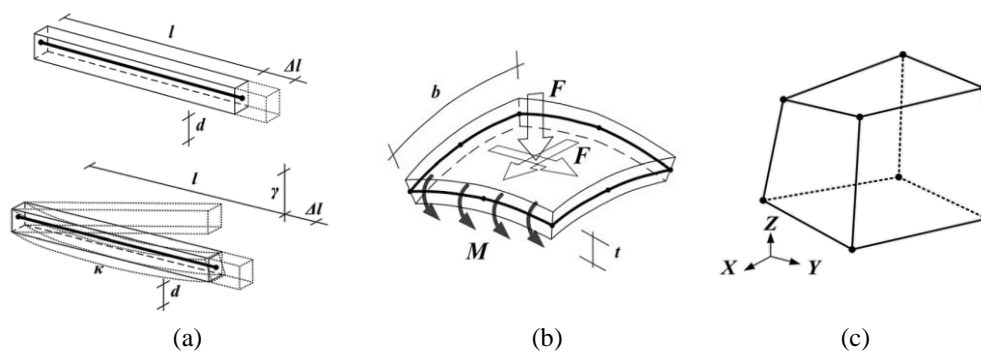


**Figure 3.43:** Typical FEM element types (a) linear elements, (b) shell elements and (c) solid elements [196].

For completeness, the linear elements are characterized by deformations due only to the axial elongation ( $\Delta l$  or  $\theta$ ) or may be subject to axial elongation ( $\Delta l$ ), shear deformation ( $g$ ), curvature ( $k$ ), and torsion ( $f$ ) (typical for beams). The two-dimensional elements (shell) present a deformation which can only be the translation in the three main directions ( $u_x$ ,  $u_y$ , and  $u_z$ ) and the rotations in the directions of the element plane ( $\Phi_x$  and  $\Phi_y$ ). Finally, the solid elements, generally, for what has been explained, are three-dimensional elements of general use in which the deformation can be the translation in the three main directions ( $u_x$ ,  $u_y$ , and  $u_z$ ) [196].

Furthermore, another relevant aspect concerns the discretization of the geometric model to define, among the various elements, a univocal solution in terms of equilibrium and congruence.



In this circumstance, the order of the element refers to the polynomial representation of the shape functions of the element itself.

This form function is a mathematical law that can be linear or quadratic and allows the solution to be interpolated between the discrete values (i.e. displacements or rotations) obtained at the nodes of the mesh.

Consequently, the choice of the order of the elements directly influences the precision of the expected solution [197].

Based on these assumptions, the FEM model of the Banloc Castle is presented in Figure 3.44.

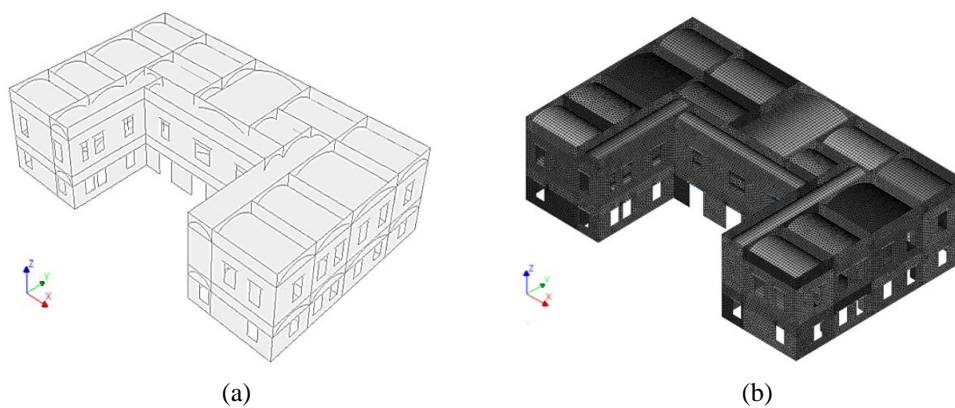


**Figure 3.44:** FEM model of the Banloc Castle, (a) 3D model, and (b) global shell elements.

In particular, the case study geometric model consists of a set of shell elements suitably interconnected with 255000 nodes, appropriately named DOF, the acronym for a degree of freedom.

DOFs depend on the number of nodes that discretize the structural elements, therefore it is clear that the discretization of the mesh is directly proportional to the number of nodes generated.

Too dense mesh can produce inaccurate solutions, while a too fine mesh will be excessive about computation time, especially for non-linear dynamics. Another relevant condition concerns the *aspect ratio* between elements of the mesh. In Figure 3.45 the examples of elements with good and bad aspect ratios have been presented [196].



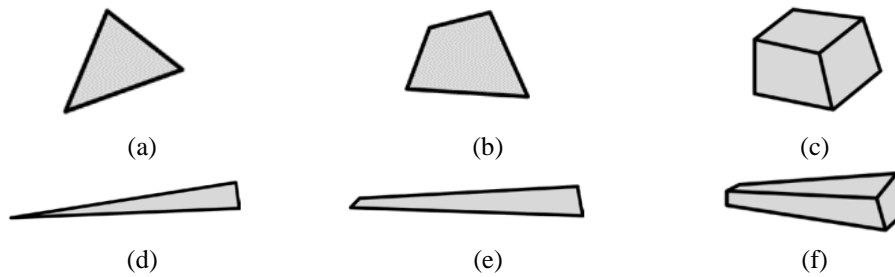


**Figure 3.45:** Elements with good (a-c) and bad aspect ratios (d-f) [196].

From the previous figure it is clear that the adoption of elements of bad shape will not produce wrong results, but probably, create convergence problems in non-linear analysis.

Moreover, according to [198], suggest using a mesh size varying between 10 and 30 cm for historic masonry buildings to have an adequate level of detail of the mesh. However, to reduce calculation time, in the current case a 40 cm of mesh size has been assumed to have reliable output results both in terms of stress and expected damage, respectively.

Afterwards, two different types of mesh have been used to characterize the geometric model of the Banloc Castle based on the aspect ratios. The first type, adopted for vertical structures, has a triangular mesh while the second type, adopted for horizontal structures (vaults), has a quadrangular mesh.

This choice is justified by the fact that the vertical structures have openings and for this reason, to guarantee geometrical continuity in terms of equilibrium and local congruence, a triangular mesh has been adopted, which is properly suited for the representation of the stress state and damage as well.

Furthermore, for horizontal structures, the quadrangular mesh discretizes the surface of the structural element in the best way and, therefore, favours a clear and direct representation of the stresses, deformations, and damages.

Finally, the boundary conditions or supports have been assigned to the geometric model. They have a great influence on the calculated results. In the specific case, all the nodes at the base of the model have been constrained by fixed supports and kinematically prevent rotations ( $\Phi_x$ ,  $\Phi_y$ , and  $\Phi_z$ ) and translations ( $u_x$ ,  $u_y$ , and  $u_z$ ) in the three main directions X, Y, and Z, respectively.

As regards the mechanical characterization of the masonry, DIANA FEA [194] software allows to model the non-linear behaviour of the masonry through two different approaches:



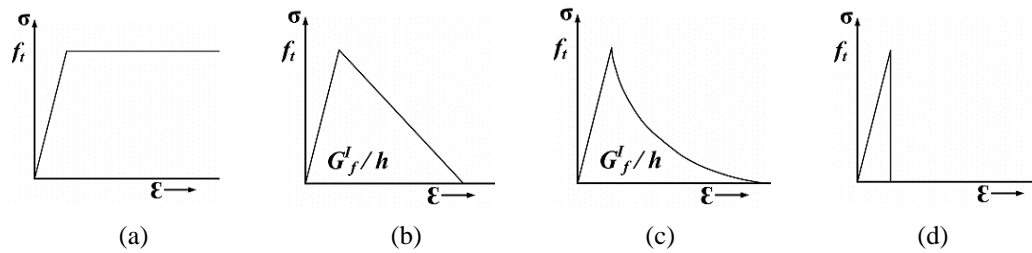


**Figure 3.47:** Tensile behaviour in TSC model: (a) constant; (b) linear; (c) exponential and (d) brittle [194].

Analogously, the compressive behaviour can be schematized, like elastic, constant, and parabolic (Figure 3.48).

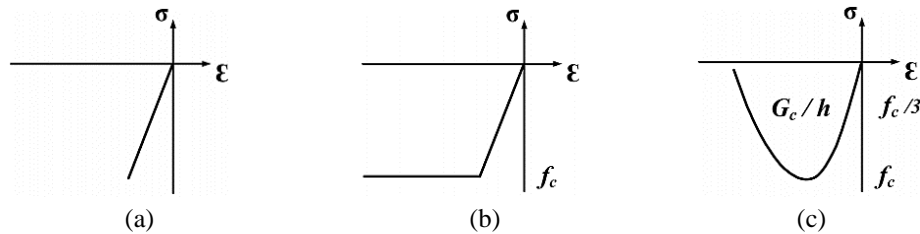


**Figure 3.48:** Compressive behaviour model: (a) elastic; (b) constant and (c) parabolic [194].

However, based on these considerations, the constitutive model requires some input parameters to be implemented, such as (a) density ( $\rho$ ); (b) Young's modulus ( $E$ ); (c) compressive strength ( $f_c$ ); (d) compression fracture energy ( $G_c$ ); (e) tensile strength ( $f_t$ ) and (f) mode-I fracture energy ( $G_f$ ). Besides, to make the results independent of the type of mesh adopted, the fracture energy has been divided (implicitly by the software) by the volume factor of the mesh element,  $h$ . This factor is called the *characteristic length*.

Focusing on the case study model, the building is composed of solid bricks and lime mortar joints, resulting the widest masonry typology in Romania. In particular, an experimental campaign was conducted on the characterization of the mechanical properties of the masonry as reported in the technical report developed by the authorized laboratory of the Politehnica University of Timisoara [200]. These experimental tests were performed using both, a 200-ton hydraulic press and a sclerometer, as explained in [200]. Moreover, the data obtained have been compared with other experimental tests performed on similar historical masonry buildings, characterized by the same geometric, structural, and typological characteristics [200] resulting in line with the indications provided with the Romanian Code [39].

Furthermore, the Romanian historical heritage has similar construction and material characteristics of the buildings located in the Northern part of Italy and for this reason, the mechanical characteristics of the masonry were adopted about the experimental data used by the Italian Code [40].

The Italian Code [40] provides a vast and varied morphological assortment of historic masonry, providing for each type the maximum and minimum values of the mechanical parameters, such as the average value of compressive strength ( $f_m$ ), average value of shear strength ( $\tau_0$ ), normal and tangential elasticity modules (E and G) and weight per volume unit (density, W).

In particular, the first 6 lines of the typological classification of masonry, are related exclusively to the historical masonry, in the hypothesis of not particularly thin joints, absence of masonry chases, and, in a global view of the structure, lacking connections between orthogonal walls.

Based on these considerations, the mechanical properties of the masonry, adopted in this study, are summarized in Table 10.

**Table 10:** Mechanical properties adopted for characterizing the masonry [40].

<b>Mechanical Properties</b>		
Modulus of elasticity	E [N/mm <sup>2</sup> ]	1500
Shear modulus	G [N/mm <sup>2</sup> ]	500
Compressive strength	$f_m$ [N/mm <sup>2</sup> ]	2.40
Tensile strength	$f_t$ [N/mm <sup>2</sup> ]	0.24
Tangential strength	$\tau_0$ [N/mm <sup>2</sup> ]	0.06
Specific weight	w [KN/m <sup>3</sup> ]	18
Poisson ratio	$\nu$ [-]	0.20
Fracture energy (compression)	$G_{fc}$ [N/mm]	4.64
Fracture energy – Mode I (tensile)	$G_{ft}$ [N/mm]	0.012

As regards the elasticity modules, normal, E and tangential, G, the average values have been used, while, for normal,  $f_m$ , and tangential strength,  $\tau_0$ , the minimum values were used. As known, the mechanical characterization of the existing masonry must also take into account the expected level of knowledge (LC) which subsequently determines the confidence factor (CF) to be adopted for the reduction of the value of the mechanical strength of the materials.

This factor is intended as a partial safety factor that prudently takes into account the uncertainties related to partial knowledge and the generally non-exhaustive level of investigation.

The application criteria can be inferred following the Romanian Code [39] as well as by the Italian [40] and European (EC8) Codes [38], respectively.

Therefore, the expected level of knowledge assumed is LC1 which corresponds to a confidence factor, CF, equal to 1.35. The values of the design resistances are determined based on the ratio between the characteristic values of the resistances,  $f_k$  (see Table 10), and the partial safety factor,  $\gamma_M$ , multiplied for the confidence factor, CF, as well. However, in the case of non-linear analyses, the partial safety factor is assumed to equal to 1, according to the Design codes, [39], [38] and [40]. Thus, the design strengths are evaluated based on Equation 3.36:

$$f_d = \frac{f_k}{\gamma_M \cdot CF} \quad (3.36)$$

The masonry design parameters are shown in Table 11.

**Table 11:** Design strength adopted for the case study historical building.

	CF	$\gamma_M$	$f_k$ [N/mm <sup>2</sup> ]	$f_d$ [N/mm <sup>2</sup> ]
LC1	1.35	1.00	Compressive strength - $f_m$	2.4
			Tangential strength - $\tau_0$	0.06
			Tensile strength - $f_t$	0.24

Moreover, for the characterization of the constitutive model, the TSC model was used according to § 3.7.4.2. In this case, the non-linear behaviour of the masonry was diversified in compression and tension. Specifically, a parabolic constitutive law was assumed in compression (see Figure 3.48c), while an exponential law has been assumed in tension (see Figure 3.48c). Mathematically, the formulations adopted for the definition of tensile fracture energy,  $G_{ft}$ , are reported in section § 3.7.3.3, referring to Equation 3.26. This formulation is a function of the design tensile strength,  $f_{t,d}$  (see Table 11).

The compressive fracture energy,  $G_{fc}$ , assumed equal to 4.62 N/mm (see Table 17) was defined employing the inverse formulation as proposed previously (see §3.7.3.3), considering the design strength,  $f_{m,d}$ , as follows:

$$G_{fc} = d \cdot f_{m,d} \quad (3.37)$$

where,  $d$ , is the *ductility index*, assuming equal to 2.62 mm, for lower-strength materials, defined as following [196]:

$$d = 2.8 - (0.1 \cdot f_{m,d}) \quad (3.38)$$

It is worth highlighting, how the data processed for the mechanical characterization of the masonry in terms of tensile and compressive fracture energies are comparable with the study proposed in [201] and [202] developed on the same typological class of masonry.

The gravitational load condition applied to the structure takes into account the effect of the weight of the structural and non-structural elements combined through the incremental partial coefficients,  $\gamma_i$ .

The vertical loads, as known, are divided into three categories,  $G_1$ ,  $G_2$ ,  $Q_k$  which represent the permanent structural loads (induced by the own weight of the primary structural elements), the permanent non-structural loads (due to the additional elements such as plaster or floors) and variable loads (defined according to the intended use of the building), respectively. These values refer to characteristic values, i.e. corresponding to the 95% fractal (i.e. 95% of values higher than the characteristic value equal to 5%). The partial safety factors,  $\gamma_i$ , are associated with the previously defined loads and are equal to  $\gamma_{G1}=1.3$ ,  $\gamma_{G2}=\gamma_Q=1.5$ , respectively. The fundamental load combination is reported in section § 3.7.3.4 and it has been defined according to Equation 3.39

$$F_d = \gamma_{G_1} \cdot G_{k1} + \gamma_{G_2} \cdot G_{k2} + \gamma_{Qk} \cdot Q_{ki} \quad (3.39)$$

Furthermore, in the case of seismic combinations, Equation 3.39 is particularized, as reported in Equation 3.40 (see § 3.7.3.4):

$$F_d = \gamma_{G_1} \cdot G_{k1} + \gamma_{G_2} \cdot G_{k2} + \sum_i \Psi_{oi} \cdot Q_{ki} \quad (3.40)$$

where the partial safety factors,  $\gamma_i$ , are equal to 1 and  $\psi$  is equal to 0.3.

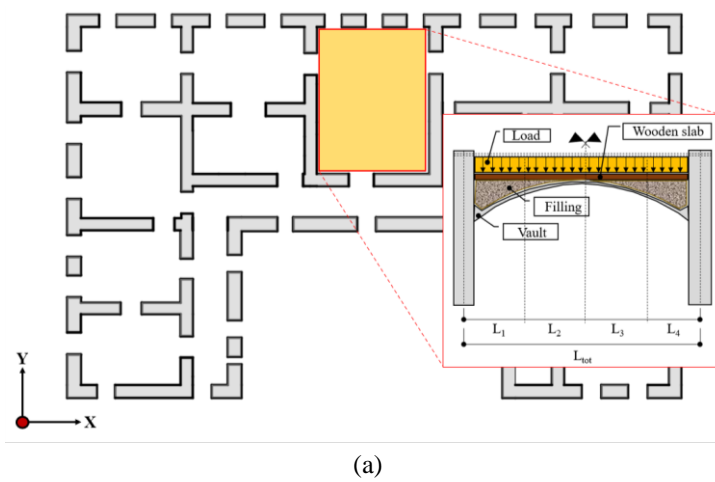
In the DIANA FEA environment [194], the arrangement of the load conditions depends mainly on the type of analysis to be performed. In particular, for static linear analysis, the loads are generally applied to employ nodal loads or distributed loads, however, for non-linear analyses (such as time-history) the loads are applied through appropriate accelerograms together with the existing external loads. So, a recurring problem in the modelling of loads for complex buildings is the application of the same to the various structural elements that differ in shape and volume. For this reason, a refined but simplified procedure is to consider the floor loads converted into mass successively added to the density of the base material (masonry) as specified in [196].

In this perspective, the loads applied to the case study structure were converted in terms of mass and appropriately added to the material density,  $W$ .

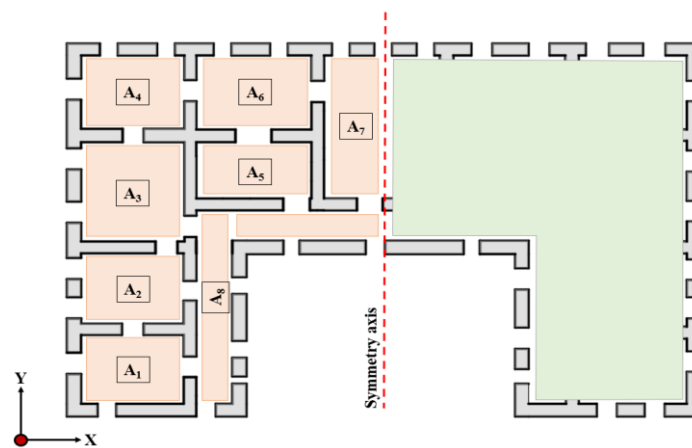


This choice was supported by the fact that in this way the computational errors are reduced due to the variation of the load pressure on curved surface elements and the calculation time for the post-processing phase is reduced.

Operatively, each horizontal element (masonry vaults), of length  $L_{tot}$ , was discretized in portions of semi-length  $L_i$ . Subsequently, for each load area of semi-length  $L_i$ , the load contributions induced by the filling sand, wooden slab, and non-structural loads have been considered. These load areas, based on their occupied volume portion, were converted into density,  $\rho_i$ , and subsequently added to the basic density of the masonry vault ( $W = 18 \text{ KNm}^{-3}$ ), as briefly presented in Figure 3.49 a.



(a)



(b)

**Figure 3.49:** Calculation scheme adopted for the conversion of loads into mass increments (a) and (b) load areas considered.

Subsequently, for each structural load area,  $A_i$ , (see Figure 3.49 b), the mean density,  $\rho_m^*$ , calculated as the weighted average of the individual load areas of semi-length,  $L_i$ , has been evaluated according to Equation 3.41:

$$\rho_m^* = \frac{\sum_{i=1}^n (\rho_i \cdot L_i)}{\sum_{i=1}^n L_i} \quad (3.41)$$

The summary of the results obtained taking into account the structural symmetry is shown in Table 12:

**Table 12:** Estimated density material increase.

Level	Element ID Area, $A_i$	Surface Area [m <sup>2</sup> ]	W [KNm <sup>-3</sup> ]	$\rho_m^*$ [KNm <sup>-3</sup> ]
I	A1	37.80	18	25.46
	A2	37.52		25.46
	A3	52.56		25.47
	A4	40.32		25.46
	A5	33.55		25.39
	A6	44.24		25.43
	A7	40.14		13.23
	A8	37.52		25.34
<b>Mean</b>		<b>40.45</b>		<b>23.90</b>
II	A1	37.80	18	18.84
	A2	37.52		18.84
	A3	52.56		18.85
	A4	40.32		18.84
	A5	33.55		18.79
	A6	44.24		18.82
	A7	40.14		9.79
	A8	37.52		18.75
<b>Mean</b>		<b>40.45</b>		<b>17.96</b>

As shown in the previous table, the calculated density takes into account a mean reduction of 26% between the two levels. This density reduction takes into account that at the second level there is no sand filling but the induced load (per linear meter) of the wooden roof structure applied on both, perimeter and internal walls that do not cover directly into the calculation of the surface loads.

Also, it is worth noting that for the element ID: A7, the calculated density refers to half part of the horizontal area (geometric symmetry) for both levels, respectively.

### 3.7.4.3 Ground motion characterization

The Banat Seismic Region (BSR) is characterized by an important tectonic activity mainly thickened in two areas such as the Banat Seismogenic Zone (BSZ) and Danube Seismogenic Zone (DSZ), respectively. In particular, focusing on the BSZ, it has been observed important crustal events generated by tectonic blocks that move along different surrounding fault systems. During the seismic history of the Banat Region, these earthquakes caused medium-high events. The City of Banloc, belongs to the Banat Seismic Region (BSR) and it has been susceptible to a series of seismic events, especially occurred in 1991, that has substantially influenced the behaviour of URM buildings located in the City [52]. The open-source Web-GIS “*BigSees Earthquake Selection*” [148] was used to identify the events that occurred in 1991 near the City of Banloc to have a global overview of the seismic phenomena that affected the Banloc area as reported in Figure 3.50.

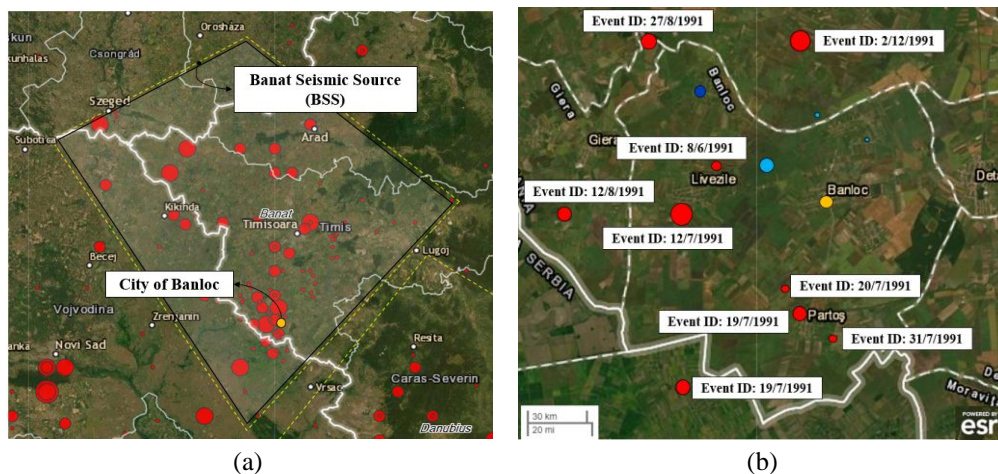


**Figure 3.50:** Earthquake occurred near the City of Banloc in 1991 [148].

In Figure 3.50 (a), the seismogenic area of the Banat has been marked with the yellow dashed line while the red points identify the history of the seismic that occurred in the whole Region. Moreover, the yellow point indicates the location of the City of Banloc. In Figure 3.50 (b), an enlargement of the Banloc area is shown considering the seismic events that occurred in that zone in 1991. In particular, these events are indicated by red points whose size identifies the magnitude that occurred. The cyan dots are identifying the events that occurred in 1915 and, finally, the blue point identifies the event that occurred in 2001 only.

These events are excluded from the context of the discussion since the damages caused to the Banloc Castle are attributable to the seismic sequence that occurred in 1991.

The events that occurred in 1991 [52], differ in terms of magnitude,  $M_w$ , epicentral distance,  $R$  (assessed concerning the City of Banloc), and focal depth,  $h$ . The parameters are summarized in Table 13.

**Table 13:** Characteristic of the seismic events that occurred in 1991 near the City of Banloc [52].

Event ID	Magnitude, $M_w$	Epicentral distance, $R$ [km]	Depth, $h$ [km]
08/06/1991	3.8	5.3	11
12/07/1991	5.6	6.7	11
19/07/1991	4.5	5.0	10
19/07/1991	5.0	11.0	10
20/07/1991	3.8	4.60	10
31/07/1991	4.0	6.28	30
12/08/1991	4.2	12.0	10
27/08/1991	4.5	10.0	10
07/12/1991	5.5	7.0	9

As can be seen from the previous Table, the events are characterized by a moment magnitude,  $M_w$ , ranging from 3.8 up to a maximum of 5.6, a focal depths variable between 9 and 30 km, and epicentral distances from 4.60 km up to 12 km. The selected earthquakes (see Table 13) are characterized by an epicentral distance,  $R$ , between 4.60 and 12 km, where precisely  $R$  denotes the areal distance between the site and the physical location of the epicentre. Following the definition provided in [108] the selected ground motion events are to be considered as near-field (NF) since they have an epicentral distance,  $R < 25$  km [19]. In particular, near-field events are typically dependent on-site to source distance and are independent of the extension of the fault systems (such as near-source events characterized by a dependence due to seismic directivity).

Based on these considerations, the event ID of 7/12/1991 was selected as a reference case. The main reasons that influenced this choice are substantially three: (i) shorter focal depth than other events that occurred in the area; (ii) the accelerograms of the event have been elaborated and supported by scientific validation as reported in [52]; (iii) no other events have been found in literature or Strong Motion Database. Moreover, Abrahamson and Litehiser (1989) [20] have reported that the vertical seismic component is particularly important for NF seismic events characterized by medium-high magnitude.

To this purpose, it seems evident that only seismic events with a moment of magnitude  $M_w \geq 5.0$  needs to be taken into consideration.

So, the main records were recorded at ground level and they have been processed by the INCERC (part of the *National Institute for Research and Development URBAN-INCERC*) seismic network during the seismic sequence that occurred in Banloc in 1991 [52].

The processed records have highlighted important peculiarities concerning the selected case study event. In particular, a reduced time history duration has been observed (maximum of 24 sec) and the values of maximum spectral amplification were correlated to short periods, varying between 0.1 sec  $< T < 0.3$  sec [52].

Furthermore, the impulsive event presents a vertical amplitude of  $1.3 \text{ ms}^{-2}$  at 1.68 sec, generated at 9 km of depth which corresponds to a moment magnitude,  $M_w=5.5$ . The associated level of macroseismic intensity recorded at the epicentre,  $I_0$ , was equal to VII-VIII degree [52].

Thus, the above-introduced recorded accelerograms are representative of the event that occurred in Banloc in December 1991 considering the BNL1 seismometric station (Tawn-Hall) located at 7 km from the epicentre [52]. The seismic station (geographical coordinates and station code) was contemplated following the SM-ROM-GL [52].

The characteristics of the event are reported in Table 14.

**Table 14:** Reference event occurred in the Banat seismogenic zone in December 1991 [52].

Earthquake	Date	LatN°	LongE°	Depth- <i>h</i> (km)	$M_w$	Station
Banat-Voiteg	1991/12/07	45.45	21.12	9.0	5.5	BNL1

For engineering purposes, the information useful to characterize and contextualize the seismic motion at the site essentially concerns: (i) the amplitude, associated with the maximum peak, in absolute value, of acceleration; (ii) frequency content, referring to how seismic motion amplitudes are distributed over time; (iii) the duration, intended as the time concerning which all the seismic input is released. However, this information must be associated with registration.

Thus, the accelerograms of the Banloc event, have been processed using the SeismoSignal software [203], and they are characterized by maximum peak amplitude in X direction (Longitudinal) of  $0.80 \text{ ms}^{-2}$ , in Y direction (Transversal) of  $1.30 \text{ ms}^{-2}$ , and Vertical direction of  $1.30 \text{ ms}^{-2}$  (Figure 3.51). Considering the time domain, a time history of 10 seconds has been plotted since all the energy content has been released.

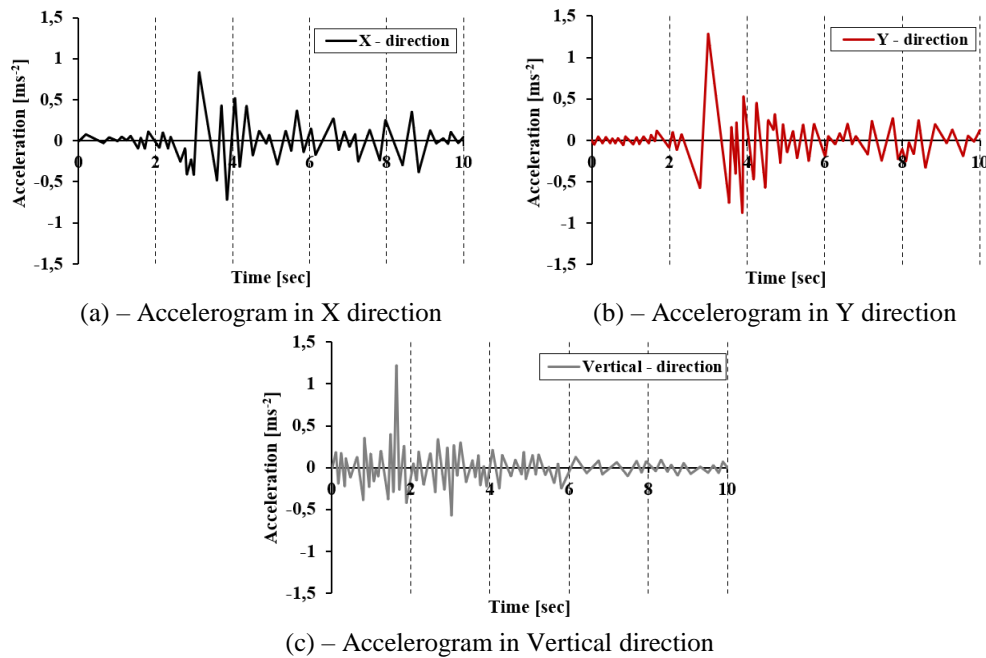


**Figure 3.51:** Accelerograms of the Banat-Voiteg seismic event in all analysis directions.

It is possible to consider two fundamental loading conditions were considered regarding the analysis of ground motion accelerograms. In particular, from the direct comparison of ground motions, in the first step, it is possible to notice how the vertical component assumes a maximum amplitude in the first two seconds of the time domain, releasing all its energy content, while in a second step, the vertical component has lost its energy input and the maximum horizontal components have been achieved. The two horizontal components have a maximum amplitude between 2 and 4 seconds until up to 6 seconds, as shown in Figure 3.52.

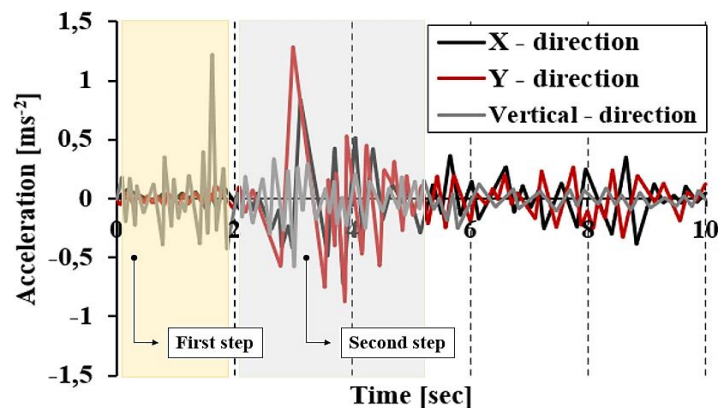


**Figure 3.52:** Accelerograms load conditions.



As can be seen from the previous figure, it is denoted that the presence of ground motion vertical component is mainly associated with the arrival of compressive P-waves with vertical propagation, while, only subsequently, the secondary shear S-waves are the main cause of horizontal components (as explained in the § 2.3.2) [19]. Besides, seismic motion is also characterized by other parameters that affect the seismic response of a structure, such as velocity and displacements, respectively. In particular, the velocity profile (PGV) is generally used to characterize the amplitude of the seismic motion for intermediate frequencies while the displacement profile (PGD) is useful for the characterization of the motion at low frequencies (Figure 3.53) [19].

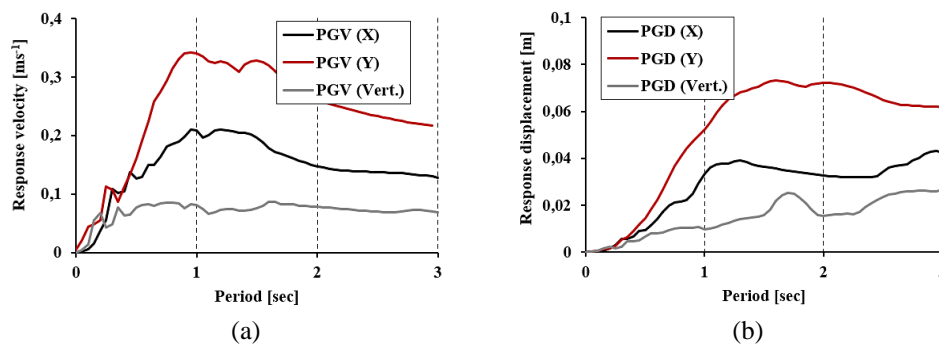


**Figure 3.53:** Ground motion parameters: velocity profile, PGV (a) and displacement profile, PGD (b).

Another fundamental aspect concerns the wavelength of the P-waves, which is generally shorter than the corresponding S-waves. This aspect justifies how the vertical component is associated with higher frequencies (frequency content) than its source parameters [30], [32], [122].

Thus, Figure 3.54 shows the Fourier spectrum in terms of the natural period concerning the selected seismic event.

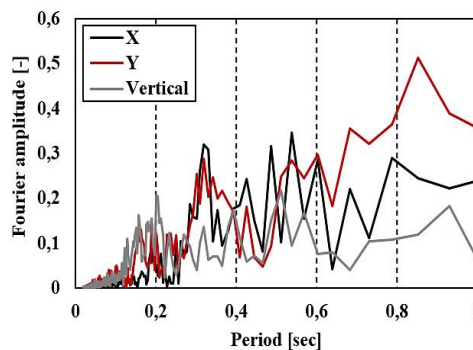


**Figure 3.54:** Fourier spectrum in terms of period.

As can be observed, in the above-mentioned Figure 3.56, the high frequencies content of the ground motion vertical component are reached for a predominant period,  $T_p$ , of 0.2 sec denoting, once again, the impulsiveness of the vertical action which occurred in a short period.

Subsequently, the response spectrum associated with the events analysed has been processed by SeismoSignal software [203] and placed in comparison with the Romanian design spectrum [39] as shown in Figure 3.55.

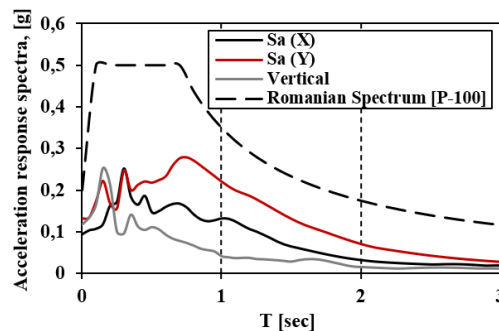


Figure 3.55: Acceleration response spectra.

Even in this case, supporting what has been affirmed previously, it is noted that the vertical component has a maximum acceleration peak for  $T=0.2$  sec.

Furthermore, to characterize the influence of the vertical component, the ratio between vertical spectral acceleration,  $V$ , and the corresponding horizontal spectral ones,  $H$ , are shown below. In particular, in Figure 3.56, the  $V/H$  PGA spectral ratios in the two directions  $X$  and  $Y$ , is plotted. Thus, for NF phenomena, the  $V/H$  PGA ratio is generally greater than 1 exceeding the  $2/3$  limit imposed by Newmark and Hall [21]. These results are conforming with the studies proposed in [33], [32], which showed that the effects of the vertical component are more influential for seismic events characterized by a reduced site to source distance.

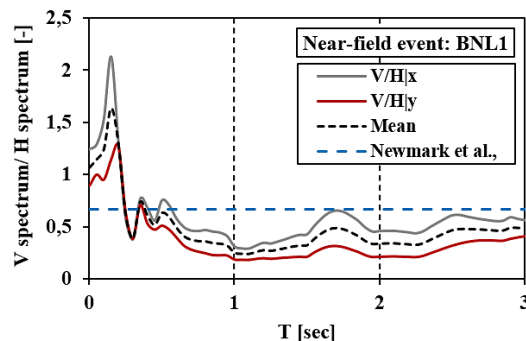


Figure 3.56: Vertical to Horizontal spectral ratio estimated for the Banloc event.

### 3.7.4.4 Non-linear dynamic analysis

In general, the problem of the dynamic equilibrium of an MDoF system is solved by integrating the equations of motion that characterize the seismic response of a generic structure in the time domain. In particular, the dynamic equilibrium of a structural system, subject to a certain seismic input (earthquake), is particularized utilizing the dynamic function as reported in Equation 3.42 [107]108:

$$F_I + F_D + F_R = F_E \quad (3.42)$$

where  $F_I$  is the inertia force vector,  $F_D$  is the damping force vector,  $F_R$  is the restoring force vector and  $F_E$  is the earthquake loads vector.

Particularizing the previous equation of motion, it can also be expressed in terms of mass as follow:

$$\underline{M} \cdot \ddot{x} + \underline{C} \cdot \dot{x} + \underline{K} \cdot x = -\underline{M} \cdot I \cdot \ddot{x}_g \quad (3.43)$$

where:

$$F_I = \underline{M} \cdot \ddot{x} \quad (3.44)$$

$$F_D = \underline{C} \cdot \dot{x} \quad (3.45)$$

$$F_R = \underline{K} \cdot x \quad (3.46)$$

$$F_E = -\underline{M} \cdot I \cdot \ddot{x}_g \quad (3.47)$$

in which the terms  $\underline{M}$  and  $\underline{C}$  denotes the mass and the damping matrices and  $\ddot{x}$  is the vector of absolute acceleration of the masses,  $\dot{x}$  is the vector of the velocity relative to the base of the structure and  $\ddot{x}_g$  represents the ground acceleration. Moreover,  $\underline{K}$  is the stiffness matrix and  $x$  represents the vector of the displacement. Finally,  $I$  is the influence vector, intended as the unity vector associated with the unitary matrix.

In particular, in the transient dynamic analysis, it is necessary to apply Rayleigh damping associated to the damping matrices  $\underline{C}$  according to the following Equation 3.48:

$$\underline{C} = a \cdot \underline{M} + b \cdot \underline{K} \quad (3.48)$$

where the coefficients  $a$  and  $b$  are derived from two main eigenvalue frequencies associated with the first vibration modes,  $\omega_1$  and  $\omega_2$ , respectively. Therefore, it is important to establish how to determine the coefficients  $a$  and  $b$  for a given structural damping ratio,  $\xi_i$  [204].

So, in this circumstance, the previously mentioned coefficients,  $a$  and  $b$ , are reported in the following Equations:

$$a = 2 \cdot \omega_1 \cdot \omega_2 \cdot \beta \quad (3.49)$$

$$b = 2 \cdot \beta \quad (3.50)$$

in which,  $\beta$  is equal to:

$$\beta = \frac{(1 - \alpha) \cdot \xi}{\omega_2 - \alpha \cdot \omega_1} \quad (3.51)$$

The parameter  $\alpha$  represents the eigenvalue frequencies ratio defined according to Equation 3.52:

$$\alpha = \frac{\omega_1}{\omega_2} \quad (3.52)$$

In the non-linear context, the equations of motion remain the same and the non-linearities (geometric and mechanical) applied to the structural elements are considered. Thus, the time history analysis provides the evaluation of the dynamic structural response as a function of the time domain considering as exciting input the representative accelerograms of a set of seismic motions.

As previously mentioned, these types of analyses can be linear or non-linear, depending on the assumptions made on the mechanical properties of the material.

However, as reported in [196] there are some limitational aspects regarding this type of procedure: (i) these analyses required a very long-time process; (ii) these analyses may depend on the selection of the ground motion accelerograms; (iii) complexity of execution concerning the interpretation of results.

Regarding the selection of the seismic input (accelerograms), is not clearly defined in the European seismic building codes (e.g. [38], [40] and [39]), for this reason, [153], specify the possible alternatives procedure to selecting the ground motion accelerograms: (i) using artificial spectrum-compatible accelerograms; (ii) using synthetic accelerograms generated from seismological source models; (iii) using real accelerograms recorded during earthquakes. In particular:

- i. *Artificial accelerograms*: proposed by [205] are generated employing the "random vibration theory" mathematical function according to which the generated accelerogram corresponds, mathematically, to what would have been characterized by a spectrum compatible with the reference one. Although they are commonly used to determine the structural dynamic response, these accelerograms do not exhibit the same physical characteristics as real recordings. Therefore, they can simulate the frequency content of a real earthquake only during the "strong motion" phase to which the acceleration peaks are associated. The characteristics of the time history of these artificial earthquakes differ, for this reason, considerably from those of real earthquakes;
- ii. *Synthetic accelerograms*: allows the combination of natural accelerograms compatible with the spectra proposed according to NTC2018 and Eurocode 8 and reflect the characteristics of the genetic seismic source in terms of magnitude,  $M_w$ , and epicentral distance,  $R$ . Thus, it is possible to determine the reference spectrum and then select the real accelerograms belonging to intervals of magnitude and distance. These accelerograms will be used to create combinations of seven recordings that, on average, respect the previously defined target spectrum [206];
- iii. *Real accelerograms*: are recordings of natural events readily available at the common databases of recognized research institutions. Since the design earthquake is generally defined only in terms of a few parameters, it is difficult to guarantee in the selected records a model capable of representing all the characteristics of the earthquake and the site.

However, since there is no clear identification of the earthquakes to be selected, the difficulty in identifying an earthquake scenario that best lends itself to representing the effects of the site, is evident.

So, as mentioned in the previous paragraph § 3.7.4.3, the real accelerograms derived from the records during the Banloc earthquake that occurred in December 1991, have been used.

Non-linear time history analysis of masonry structures is very complex. As is known, masonry structures have low tensile strength which allows the evolution of damage with cracks in the structure (opening, closing, and reopening). This cyclic behaviour introduces a certain complexity into the numerical calculations due to the rapid transition from the linear-elastic behaviour to the fully cracked state with almost zero stiffness [48]. To this purpose, in the DIANA FEA environment, it is important to use an appropriate time-integration method to introduce numerical dissipation without degrading the accuracy [194].

The integration procedures are essentially two: the Newmark method and the Hilber-Hughes-Taylor integration method [194]. The first one is used for simple and fast non-linear time history analysis, while the second one, is generally used, for very time-consuming time history. So, the Newmark method or “method of decomposition” is a step-by-step integration method that belongs to the group of algorithms that are unconditionally convergent for obtaining a response of the MDoF system under base ground motion excitation.

The integration formulas adopted for calculating velocity,  $\dot{x}$ , and displacements,  $x$ , are presented in the following Equations 3.53 and 3.54:

$$\dot{x}^{t+\Delta t} = \dot{x}^t + ((1-\gamma) \cdot \dot{x}^t + \gamma \cdot \dot{x}^{t+\Delta t}) \cdot \Delta t \quad (3.53)$$

$$x^{t+\Delta t} = x^t + \dot{x}^t \cdot \Delta t + ((\frac{1}{2} - \beta) \cdot \dot{x}^t + \beta \cdot \dot{x}^{t+\Delta t}) \cdot \Delta t^2 \quad (3.54)$$

The Hughes-Taylor integration method [194] is used in the case in which the calculations process has to be performed for a large number of time steps with the required precision. This method implements numerical damping of higher frequencies without the loss of solution accuracy according to the following Equation 3.55:

$$M \cdot \ddot{x}^{t+\Delta t} + (1+\alpha) \cdot C \cdot \dot{x}^{t+\Delta t} - \alpha \cdot C \cdot \dot{x}^t + (1+\alpha) \cdot f_{int}^{t+\Delta t} - \alpha \cdot f_{int}^t = f_{ext}^{t+(1+\alpha)\Delta t} \quad (3.55)$$

where the parameters  $\beta$  and  $\gamma$  control the convergence and precision of the results obtained through the method. Thus, the convergence parameters are assumed as follow:



$$\gamma = \frac{1}{2} \cdot (1 - 2^\alpha) \quad (3.56)$$

$$\beta = \frac{1}{4} \cdot (1 - \alpha)^2 \quad (3.57)$$

in which the parameter  $\alpha$  is associated with the numerical damping. Thus, the  $\alpha$  parameter, which represents the dynamic transient coefficient adopted in non-linear analysis, varies between [-1/3-0]. In particular, assuming  $\alpha=0$  the method reduces to the Newmark method, instead of for  $-1.3 < \alpha < 0$  the formulas 3.56 and 3.57 provide an accurate and unconditionally stable solution. Another important aspect to take into consideration for the correct execution/definition of the time history is the characterization of the time increment at each step of the analysis. In this perspective, the commonly used approach is to explicitly define the time-step,  $\Delta t$ , as suggested in DIANA (2017) [194] according to Equation 3.58:

$$\Delta t = \frac{1}{20} \cdot T_i \quad (3.58)$$

where  $T_i$  is the lowest period characterizing the structural behaviour.

## 4 Discussion and analysis of the results

### 4.1 Introduction

In this Chapter, the results deriving from the non-linear dynamic analysis were presented and discussed taking into account the influence of the ground motion vertical component on the global behaviour of the case-study building. In particular, two procedures were analysed. The first takes into account the global behaviour of the structure, the second, on the other hand, focuses on the local behaviour. Thus, the results achieved for the global behaviour, analyse two distinct scenarios named (H+V) and (H), respectively, to simulate the seismic effects in which the vertical component of ground motion has been considered (scenario H+V) and neglected (scenario H).

To this purpose, specific comparisons have been done providing interesting insights in terms of energy dissipation capacity, secant stiffness, ductility, and behaviour factor,  $q$ , which was suitably compared with the provisions of the EC8 [38].

Furthermore, the variation of the inter-story-drift during the time-history domain has been analysed and compared to the damage thresholds proposed to the EMS-98 scale [60]. Besides, the seismic safety index was proposed taking into account the ratio between the capacity PGA ( $PGA_C$ ) and the corresponding demand PGA ( $PGA_D$ ).

Subsequently, through a local analysis, the behaviour of the individual wall panels in the two main directions, X and Y was investigated appropriately, through the use of the strength domains to obtain a rigorous solution that can provide important considerations regarding the effects of the seismic vertical component.

In this framework, the failure hierarchies were defined which allowed developing a clear identification of the possible collapse mechanisms and the capacity curves of the individual wall panels have been done.

The results obtained, therefore, can interpret the global and local behaviour of the structure providing interesting preliminary conclusions comparing the numerical damage with the experimental ones derived after the Banat-Voiteg seismic event.

## 4.2 Global analysis

### 4.2.1 Identification of the structural typology

Preliminarily, it was appropriate to resort to a typological classification regarding the case-study building. As widely defined in [207], the historical building can be classified based on specific geometric-functional characteristics (such as dimensions and heights) which intrinsically provide a clear and essential typological classification. Generally, it is worth considering what can be the necessary criteria may be to carry out an accurate classification, whether the possible classes must necessarily correspond to a rigorous historical succession or must refer to construction techniques or different structural behaviour. In this overall view, an important classifying factor is certainly the global behaviour of the structure under vertical and horizontal loads, respectively.

According to [171] and [208], a classification based on the global behaviour of the building, allows highlighting, for each typological class, the specific criticalities towards the vulnerability factors that influence the seismic response. Therefore, an adequate typological classification must take these factors into account, classifying buildings as follows:

- i. *The first type of buildings:* are masonry buildings made up of deformable floors (vaulted or wooden floors). The vertical walls are continuous from the foundations to the roof which are subject to the pushing actions induced by the presence of masonry vaults. The presence of the vaults affects the overall behaviour of the structure under loads (vertical and horizontal). the horizontal actions generated by the vaults are balanced in the internal nodes of the "wall box" while they exert an out-of-plane action of the perimeter walls. The combination of these effects causes the overturning failure of the perimeter walls. The transverse walls are opposed to this kinematic system as long as they are adequately connected to the perimeter ones;
- ii. *The second type of buildings:* they are characterized by masonry walls with decks consisting of isostatic floors characterized by beams located in special slots in the masonry. The presence of a floor slab eliminates the problem of the "pushing effect" of the vaults and consequently, it is possible to have a lower thickness of the walls than in first-class buildings. Global behaviour is characterized by the tendency of the walls to overturning since the "box-behaviour" is not guaranteed. These effects are generally caused by the action of the

eccentricities of the vertical loads concerning the wall plane. These pushing actions are generated by the offset of the walls that are defined from one floor to another and therefore there is the onset of local bending moments;

- iii. *The third type of buildings*: these buildings are characterized by reinforced concrete floors that interrupt the vertical continuity of the walls favouring the correct "box behaviour". The presence of reinforced concrete elements gives the building a very performing structural behaviour by eliminating the pushing forces present in the first and second classes defined previously. The presence of ring beams gives a better distribution of compression in the walls, also performing a tie-rod function. Referring to seismic actions, the distribution of the horizontal actions is entrusted to the rigid floors and the walls mainly in the direction of the earthquake, eliminating or at least reducing the incidence of out-of-plane mechanisms.

Accordingly to what has been introduced, [171] also appropriately differentiates the behaviour of the individual walls to classify the masonry walls typologically for local analysis:

- i. *The first type of walls*: the spandrel elements have no tensile strength (guaranteed by steel tie rod or reinforced concrete ring beam) and they are excluded from the seismic calculation/verification. In this sense, the spandrel has no flexural and shear resistance and the wall is characterized as a system of isostatic cantilevers. This behaviour is typical of first-class buildings where there is the presence of vaulted or wooden floors (historical building); The main failure mechanism is due to rocking (Figs. (a-b));
- ii. *The second type of walls*: the spandrel beams have an extensional stiffness guaranteed by steel tie rod or concrete ring-beam. In this model, the spandrel under horizontal and vertical loads exhibit shear cracks. The collapse of the wall occurs when the pier panel reaches the rocking failure (Figs. (c-d));
- iii. *The third type of walls*: the spandrel elements are equipped with a double system of horizontal elements resistant to traction such as steel tie-rod or reinforced concrete ring-beam (rigid floor). The spandrels have flexural stiffness and the wall can be considered as a hyperstatic frame in which it is possible to individuate piers, spandrels, and rigid nodes (Figs. (e-f)).

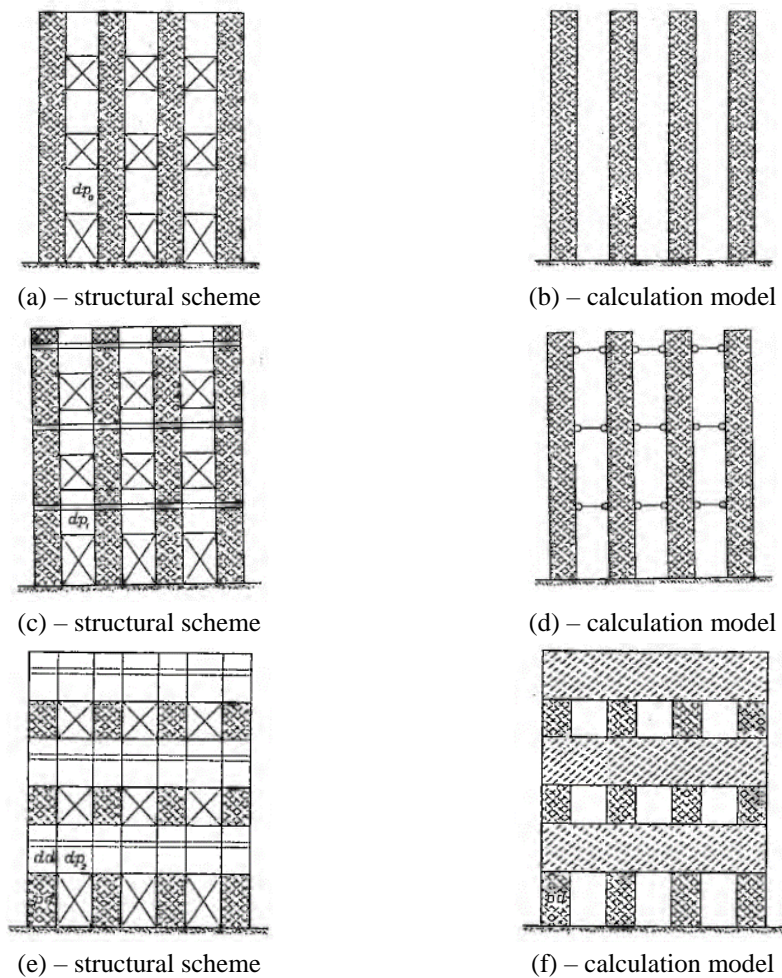


**Figure 4.1:** Calculation models adopted for local analysis, (a-b) first type walls, (c-d) second type walls, and (e-f) third type walls [171].

Based on these indications, referring to the case study building, it was assumed to be classified as the "*first type of building*".

## 4.2.2 Identification of the global seismic response

### 4.2.2.1 Modal analysis

Real structures are continuous and inhomogeneous systems, which have an infinite number of degrees of freedom and are characterized by a certain number of natural resonance frequencies that allow the energy induced by the external forcing to be dissipated. The interaction of the properties of mass and stiffness, therefore, determines frequencies of free oscillation that allow describing the behaviour of the structure employing  $n$ -vibration modes.

The numerical procedure for evaluating the vibration modes was analysed using an eigenproblem equation according to the mode superposition method as reported in Equation 4.1 [194]:

$$K \cdot \phi = \omega^2 \cdot M \cdot \phi \quad (4.1)$$

where  $K$  is the symmetric stiffness matrix,  $M$  is the mass matrix of the FEM model,  $\omega$  is the natural frequency and  $\Phi$  is the shape unitary vector.

It is worth underlining that since these are buildings of historical interest, the coupling of the vibration modes does not always systematically identify the main modal forms (translational and rotational) associated with the first vibration modes. In fact, in some cases, the presence of local modes greatly influences the identification of the predominant modal forms. For this reason, a conspicuous number of vibration modes should be considered to excite at least 85% of the participating mass. However, in the specific case, only the first 10 modes were considered, too: (i) reduce the calculation time process, (ii) estimate the modes that provide a vibration period close to the predominant period evaluated in paragraph §3.7.4.3 [32].

The main eigenfrequencies have been shown in Figure 4.2

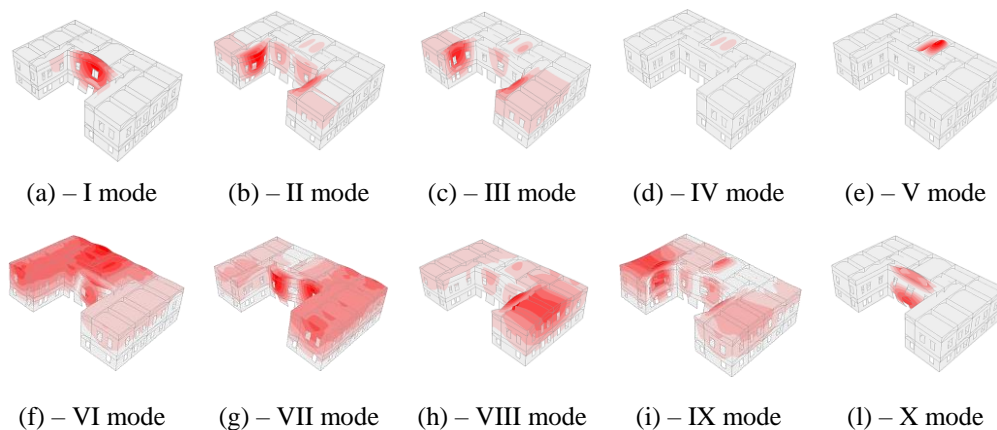


**Figure 4.2:** The main eigenfrequencies mode.

It was possible to observe how the structure is characterized by many independent areas that vibrate autonomously without involving the entire structure. Generally, this happens for articulated structural systems that have plan-shapes that are not very compact and have only one axis of symmetry and local analysis is required.



In this sense, it was evident that the mass percentage activated did not satisfy the 85% (and consider all frequencies that activate at least 5% mass) as required by the seismic code. In general, for historic buildings, to reach 85% of the participating mass, a very high number of vibration frequencies should be considered to have a complete view of global behaviour. Furthermore, in Figures (d) and (e) it was possible to identify the vibration frequencies, which denote a local behaviour of the vault located at the second and first levels. The results achieved have been presented in Table 15.

**Table 15:** Modal characteristics.

Mode	$f$ [Hz]	T [sec]	Part. Fact. Y	Mass, X [%]	Mass, Y [%]	Mass, Vert. [%]
I	2.8	0.36	1.8	0.000	3.068	0.003
II	4.3	0.23	3.3	11.56	0.012	0.000
III	4.6	0.22	1.3	0.114	0.674	0.001
IV	4.7	0.21	2.1	0.055	0.001	0.001
V	4.8	0.21	1.1	0.002	0.027	0.002
VI	4.9	0.20	4.2	0.263	23.07	0.003
VII	5.0	0.20	3.9	2.740	5.190	0.002
VIII	5.2	0.19	2.7	22.06	0.103	0.009
IX	5.4	0.19	1.5	3.140	0.164	0.015
X	5.6	0.18	6.5	0.026	0.686	0.000
Sum				33.62	28.26	-

The results presented in Table 15 highlight the main modal characteristics of the case-study building. It has been possible to note that for frequency,  $f$ , enclosed in the range  $4.7 \text{ Hz} < f < 5.0 \text{ Hz}$  there are associated vibration periods very close to the predominant period of the structure,  $T_p$ , ( $T_p=0.20 \text{ sec}$ ) due to the vertical spectrum (see §3.7.4.3). In this view, the seismic scenario event, characterized by a reduced site to source distance, provides frequency values equal to 5Hz which could cause the local resonance phenomenon and the consequent amplification of the structural demand due to the ground motion vertical component. However, the translational masses,  $M_i$ , associated with the vibration modes in the three analysis directions (X, Y, and Vertical), provide a small percentage of participating mass, this is because the structure is mainly characterized by local-frequency modes. The modal analysis, therefore, appears to be a quickly operational methodology to solve the long-standing problem of eigenvalues. In this case, the dynamic variables of the problem are decoupled since the structure is not characterized by predominant frequencies in the main directions of analysis, X and Y, respectively. Consequently, a synthetic representation of the data shown in Table 15 has been provided in Figure 4.3.

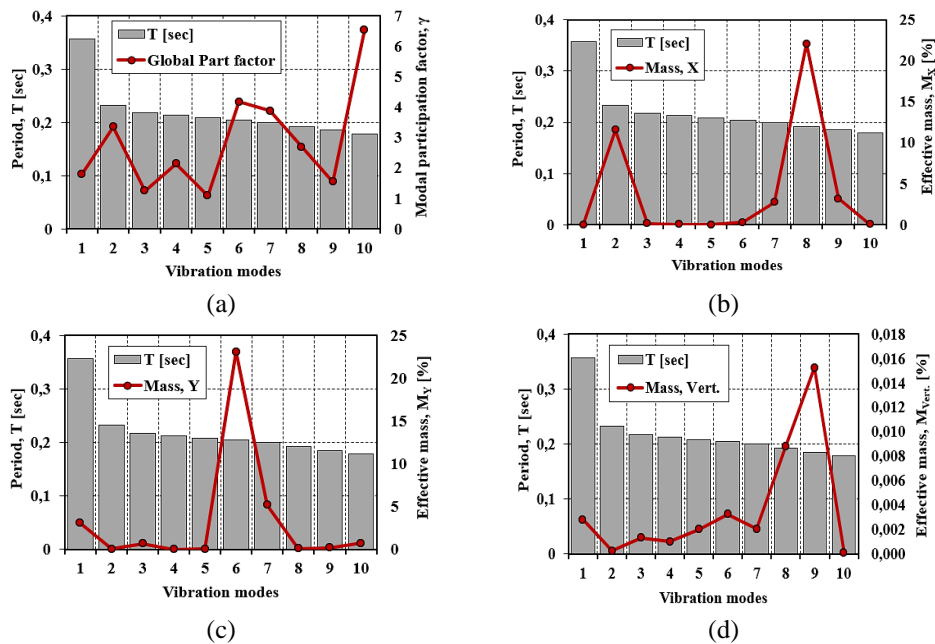


**Figure 4.3:** Synthetic representation of the modal analysis results in X, Y, Vertical, translation directions.

Thus, from the above results, it is apparent that:

- i. the local frequencies have identified the structural parts in which the damage is mainly concentrated;
- ii. the structure is mainly characterized by vibration frequencies that identify local modes. A greater number of frequencies should be investigated to excite at least 85% of the participating mass as prescribed by the European Seismic Design Code [38-40];
- iii. globally, the modal analysis has allowed identifying which vibration frequencies could cause resonance phenomena induced by the vertical component of the seismic motion. It has been shown that for frequencies between 4.7 Hz and 5.0 Hz, resulting very close to the predominant period due to the vertical component of the earthquake;
- iv. the highest contribution of participating mass, equal to 22.06% of the total mass (11600 ton-mass) was reached in X direction which corresponds to a frequency,  $f=5.2$  Hz. Similarly, in Y direction, the participating mass was 23.07% which corresponds to a frequency,  $f$ , of 5 Hz. The vertical seismic action has provided a greater contribution in the two directions X and Y, respectively causing an increase in terms of seismic demand.

4.2.2.2 Analysis of engineering demand parameters (EDPs)

The analysis of the EDPs was conducted considering two distinct scenarios, namely (H) and (H+V) to better highlight the influence of the vertical ground motion (VGM). In particular, scenario (H) neglects the vertical component of the ground motion while the corresponding (H+V) takes into consideration the vertical seismic action. In the first instance, the comparison between the newly adopted mentioned scenarios provides a clear indication about the incidence of the seismic vertical component as suggested in [32], [33], and [108].

In this framework, these scenarios were compared in terms of total base reactions, proving to be particularly sensitive to VGM in the first seconds of the time history (in which the vertical component provides the maximum acceleration peak). In particular, the variation of the shear components ( $V_i$ ) in the two analysis directions, X and Y, respectively, and the axial force regime (N) that globally characterize the dynamic response of the structure. So, to ensure the congruence of the archived results, in Figure 4.4 the total base reactions were compared with the accelerations induced by the Banat-Voiteg seismic event.

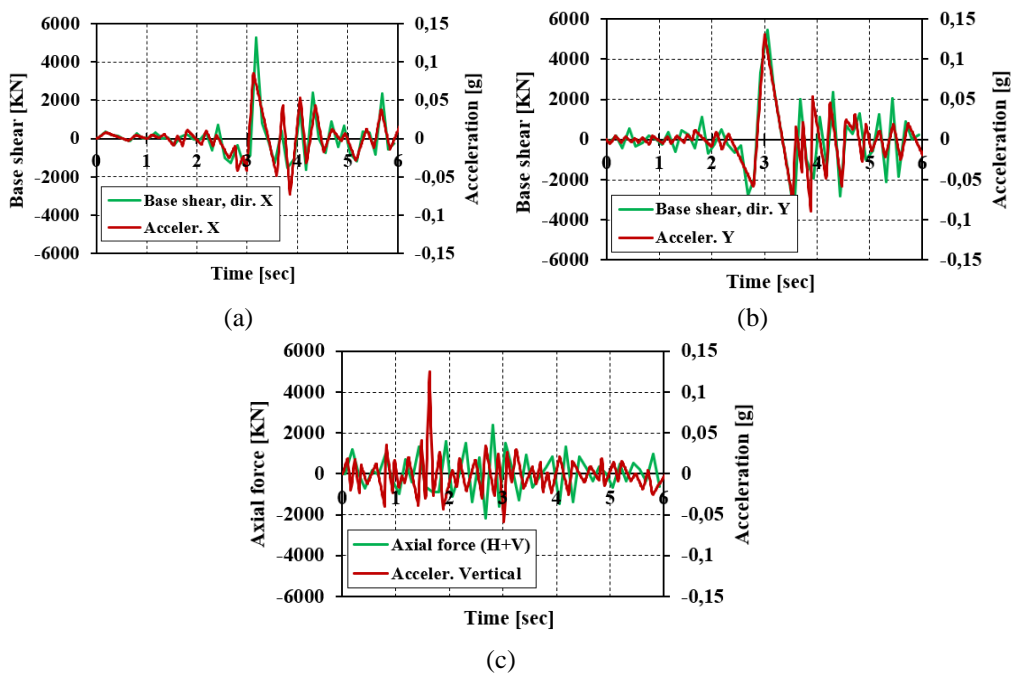


**Figure 4.4:** Comparison between the total base reaction and the accelerations resulting from the Banat-Voiteg seismic event.

Subsequently, the scenarios (H) and (H+V) were suitably shown in Figure 4.5

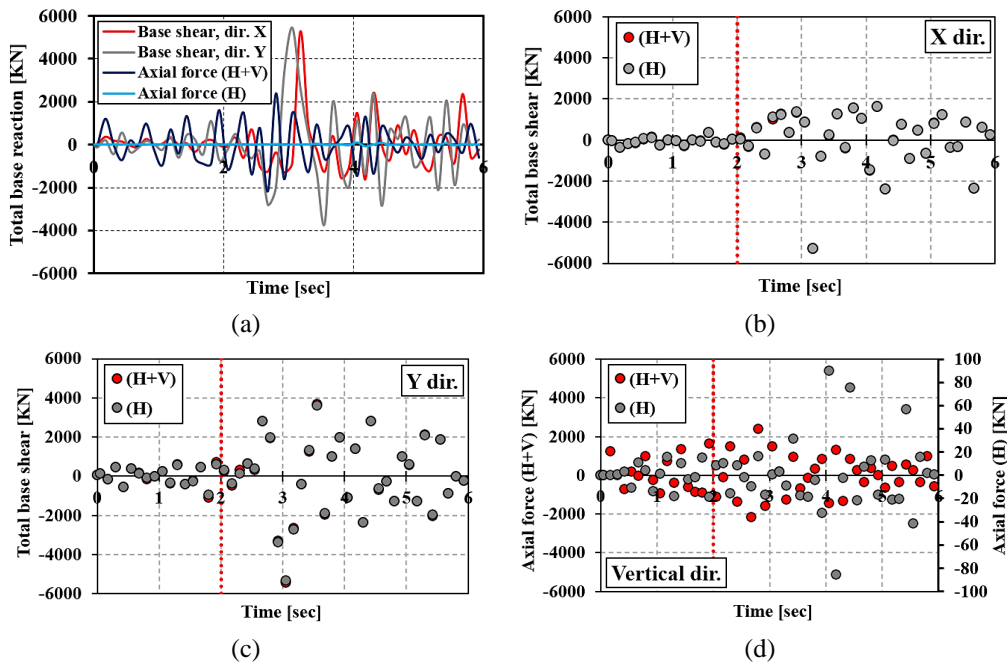


**Figure 4.5:** Time histories of total base reaction for the two analysed scenarios, (H) and ((H+V), respectively.

First of all, in Figure 4.5 (a), the base reactions in the time domain have been shown. From a first direct comparison, it can be easily seen how the seismic demand in the vertical direction has produced a significant increase in terms of axial forces regime when it is compared to the case in which it was neglected (scenario (H)). However, for a more comprehensive understanding, the base reactions were analysed separately to capture the substantial differences between the proposed scenarios. It is worth noting that at  $t= 2.00$  sec the limit of the maximum effects induced by the VGM was represented by the dashed red line.

In Figure 4.5 (b) and (c), it was observed that there was no variation of the base shear between the two scenarios (H) and (H+V), respectively. Consequently, in Figure 4.5 (d) it was possible to note that globally for the entire time history, the average variation in terms of axial force regime between the two scenarios considered was around 100%. In particular, at  $t=1.68$  sec, which corresponds to the vertical acceleration peak, the axial force's variation for the scenario (H+V) was higher than the corresponding scenario (H). This result is also confirmed in studies proposed by other authors [32], [33], and [108].

More specifically, Figure 4.6 has been plotted the scatter of the base reactions for the (H) and (H+V) analyses at each time step of the Banat-Voiteg ground motion event.

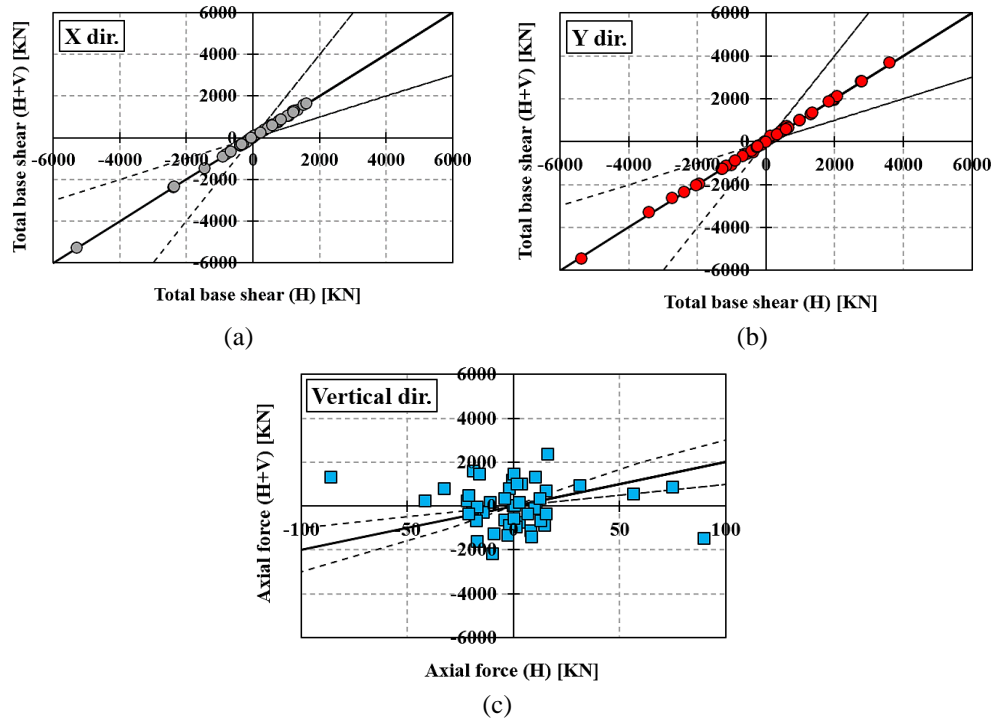


**Figure 4.6:** Base reactions for Banat-Voiteg earthquake considering (H) Vs (H+V) effects.

The graphs presented, have shown the results concerning the bisector  $y=x$  and the upper ( $y=0.5x$ ) and lower ( $y=2x$ ) bounds of the dispersion range.

It was easily understood from the proposed results, how VGM has a greater influence on the variation of axial stress. Indeed, the greater the scatter concerning the bisector, the larger effect of the ground motion vertical component [32], [33], and [108].

Finally, the axial stresses deriving from the scenario (H+V) have been normalized to the gravitational loads, to catch the incidence of the vertical seismic component towards the gravitational action.

At each time step, therefore, the demand/axial capacity ratio was carried out between the gravitational loads and the corresponding axial force,  $N(t)$ , induced by the vertical earthquake as reported in Figure 4.7.

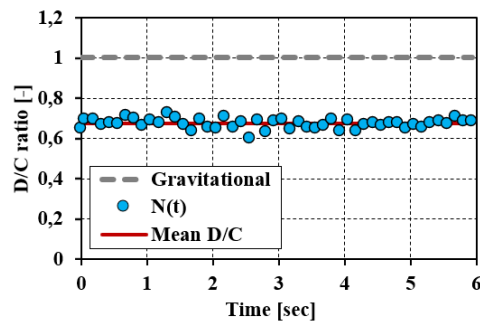


Figure 4.7: Demand/axial capacity ratio.

The gotten result has shown an important consideration regarding the behaviour of the case study building. As can be seen, for each time step, on average the ratio  $D/C$  is equal to 0.67, which means that the axial action produced by the vertical earthquake reaches 67% of the gravitational action. This highlights how the impulsive effect of the vertical acceleration decompression peak has produced a global variation of the axial stress regime but did not cause an incipient collapse of the masonry panels since, as stated above, the gravitational loads are greater than the corresponding seismic demand.

Thus, it was possible to provide the first important indications regarding the total base reactions as a contribution effect of the ground motion vertical component:

- i. congruently to accelerograms, the total base reactions,  $V_X(t)$ ,  $V_Y(t)$ , and  $N(t)$ , were to be considered compatible with the seismic event of Banat-Voiteg;
- ii. comparing the scenarios (H) and (H+V) it was possible to note that the shear stresses in the two analysis directions, X and Y, were not affected by the vertical ground motion, VGM;
- iii. by comparing the axial stresses regime between the scenarios (H) and (H+V), it has been observed how the maximum impulsive contribution of the vertical seismic action at  $t=1.68$  sec (maximum vertical decompression acceleration peak), was 100 times higher compared to the scenario (H);
- iv. by considering the scenario (H+V), the effective incidence of the VGM, was estimated through the  $D/C$  ratio, normalized to gravitational loads. It has been observed that the VGM did not produce a significant structural deficiency.

Subsequently, it was possible to analyse the effects of the vertical seismic component in terms of displacements. In the first instance, to have an exhaustive interpretation of the results deriving from the global analysis,  $n$ -control nodes were appropriately selected to have a uniform dynamic characterization induced



by the scenario earthquake. Furthermore, it should be noted that the choice of monitoring points (hereinafter referred to as MP) is an important step to be taken into consideration since the behaviour of the structure during seismic excitation is derived from them. With this intent, a conspicuous number of control nodes were selected to better identify the structural behaviour based on two main reasons:

- i. since the case study structure is a historical building with deformable floors (vaulted floors) it is clear that a single monitoring point would be too reductive and disadvantageous to fully understand, globally, the dynamic behaviour of the structure since it was affected by local frequencies;
- ii. given the asymmetry conditions in X direction.

Therefore, as stated, 38 monitoring points have been selected, that is 19 for each floor. For a clearer and more accurate overview, Figure 4.8 shows the MP relating to the second level, specifying that the respective control nodes at the first level are placed on the same alignment.

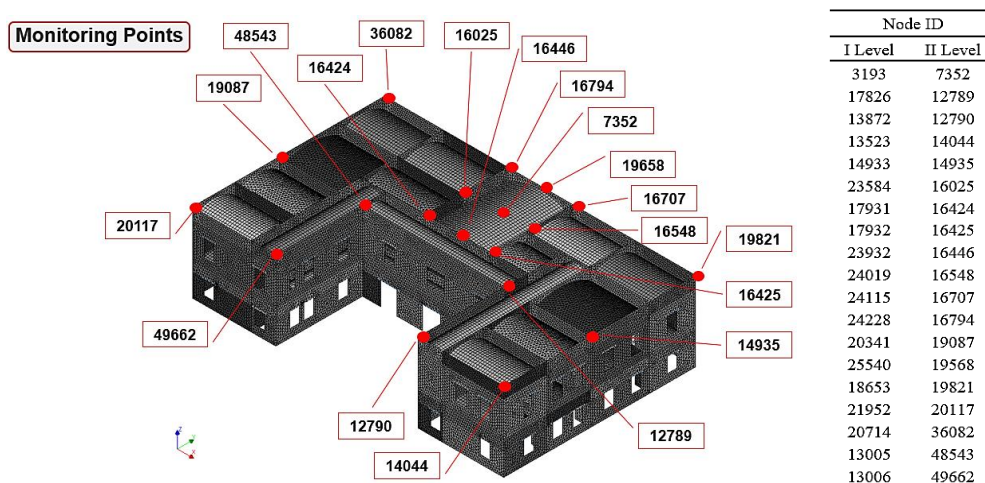
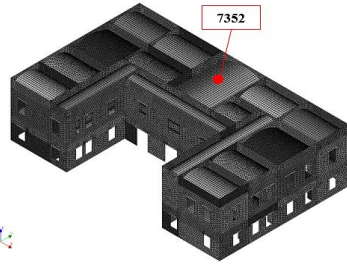


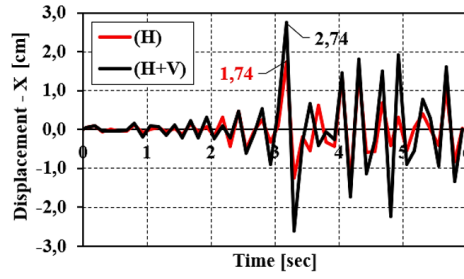
**Figure 4.8:** Selected monitoring point (MP) for the case study building.

Therefore, for all the MPs the displacements in the time domain were analysed, however, by way of example, for a quick interpretation of the results the influence of the vertical component was ascertained for the MPs 7352, 36082, 14044, respectively as reported in Figure 4.9.

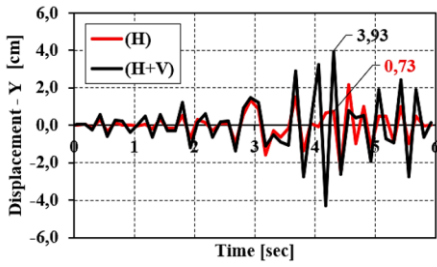
MP: 7352



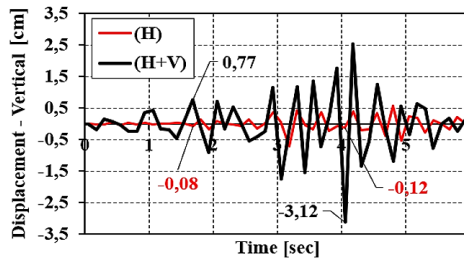
(a)



(b)



(c)

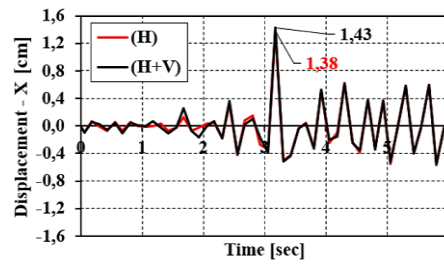


(d)

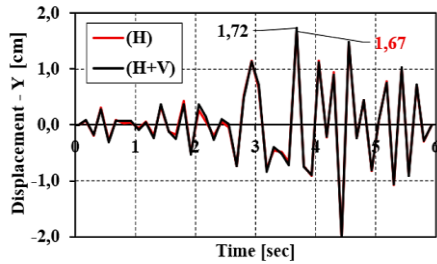
MP: 36082



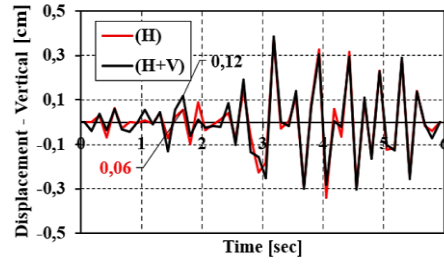
(e)



(f)



(g)



(h)

MP: 14044

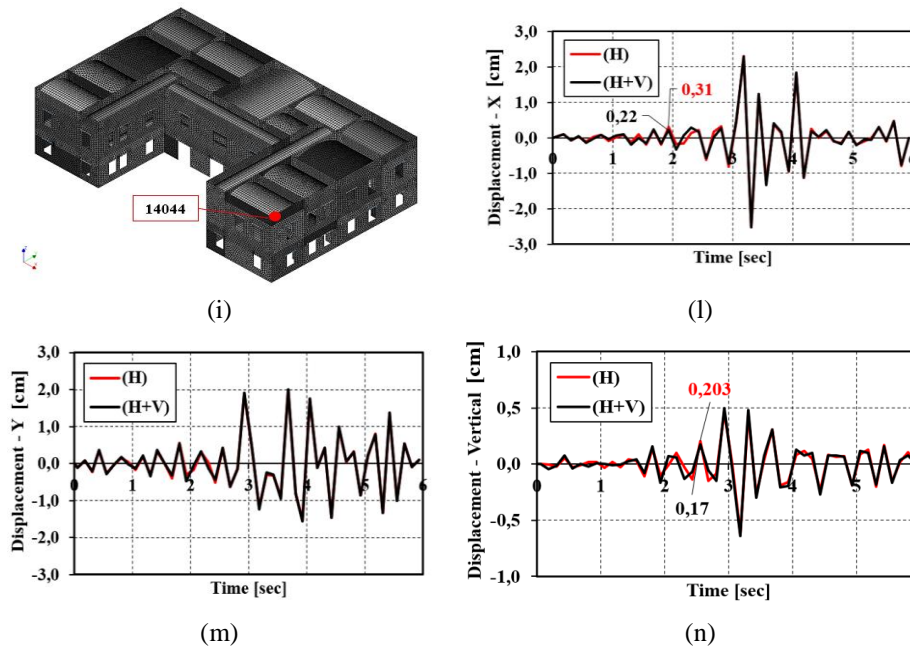


**Figure 4.9:** Displacement-time history plots for MPs: 7352 (a-d), 36082 (e-h) and 14044 (i-n).

As has been noted from the archived time-history displacements, the vertical component of the ground motion affects the position of the selected MP.

Considering the control node placed in the centre of the vault (MP 3752), the displacements in the three analysis directions were increased compared to the case in which the vertical component is neglected (H). In particular, in X-direction there was an increase of 57% compared to scenario (H); in Y direction, by comparing the scenarios, (H) and (H+V) there was an increase of 434% and finally, in the vertical direction, there was an increase of 860% confirming an important aspect deriving from other studies [32], [33], and [108].

Similarly, for the MP 36082, located in the south-east corner of the building, it was noted that in the direction X the displacements induced by the vertical component, (H+V), were increased by 3.62%, instead of in Y direction by 3%, and finally in the vertical direction of 50%. Concerning the control node 14044, it has been observed that in X direction, the displacements decreased by 40%, in Y direction the displacements obtained comparing the two scenarios (H) and (H+V) were the same and in the vertical direction, the displacement's decrease was 17%.

The summary of the results has been shown in Table 16:

**Table 16:** Summary of the results in terms of displacements of the selected MPs.

MP	Displ. (H+V) [cm]			Displ. (H) [cm]			$\Delta_x$ [%]	$\Delta_y$ [%]	$\Delta_{vert.}$ [%]
	X	Y	Vert.	X	Y	Vert.			
7352	2.74	3.93	1.00	1.74	0.73	0.08	57	434	860
36082	1.43	1.72	0.12	1.38	1.67	0.06	3.62	3.00	50
14044	0.22	1.90	0.17	0.31	1.90	0.20	-40	-	17

Therefore, Table 17 have been shown the absolute displacements afferent to all the MPs located on the second floor of the building diversifying the position of the point placed on the vault, V, from those afferent on the wall panels, WP. In particular, as regards the vertical displacements, they were considered at the time step,  $t$ , equal to 1.68 sec in which the maximum vertical acceleration peak is reached, while for both the horizontal displacements, in X and Y, directions, a time step,  $t$ , of 3.18 sec was considered since corresponds to the maximum horizontal acceleration.

**Table 17:** Displacements time history of the selected MPs.

Position	MP	Displ. (H+V) [cm]			Displ. (H) [cm]			$\Delta_x$ [%]	$\Delta_y$ [%]	$\Delta_{vert.}$ [%]
		X	Y	Vert.	X	Y	Vert.			
V	7352	2.74	3.93	0.77	1.74	0.73	0.08	57	438	863
WP	12789	1.79	0.82	0.33	1.74	0.80	0.18	3	2	83
WP	12790	2.31	0.32	0.02	2.31	0.29	0.02	-	10	-
WP	14044	2.31	1.24	0.11	2.29	1.17	0.08	1	6	38
WP	14935	3.24	0.85	0.04	3.12	0.80	0.03	4	6	33
WP	16025	1.78	1.21	0.03	1.75	1.17	0.00	2	3	-
WP	16424	1.73	1.16	0.04	1.71	1.10	0.02	1	5	100
WP	16425	1.71	1.46	0.06	1.68	1.43	0.04	2	2	50
WP	16446	1.58	1.40	0.05	1.57	1.30	0.02	1	8	150
WP	16548	1.86	1.51	0.06	1.87	1.41	0.03	1	7	100
WP	16707	1.11	0.64	0.08	1.12	0.58	0.05	1	10	60
WP	16794	1.16	0.45	0.06	1.16	0.44	0.02	-	2	200
WP	19087	3.22	0.68	0.04	3.14	0.61	0.01	3	11	300
WP	19568	1.08	1.12	0.06	1.08	1.04	0.03	-	8	100
WP	19821	1.26	0.55	0.12	1.22	0.50	0.05	3	10	140
WP	20117	2.65	0.51	0.12	2.60	0.43	0.05	2	19	140
WP	36082	1.43	0.84	0.12	1.31	0.78	0.06	9	8	100
WP	48543	1.43	1.42	0.05	1.43	1.34	0.04	-	6	25
WP	49962	2.78	1.64	0.04	2.74	1.57	0.08	1	4	50

From this comparison, it is evident how the VGM influences the displacements of the control nodes, on the dynamic response of the case study structure for three main aspects:

- i. it produces a global increase of the displacements in horizontal directions as confirmed in the study [32], [33], and [209];
- ii. it favours torsional phenomena in X-direction;
- iii. increases the displacements in Y direction (along the axis of symmetry of the structure).

These aspects are very significant, since, according to the studies proposed by [32], [33] the seismic vertical component increases the displacement demand, however, the planimetric configuration of the case studies analysed by [32], [33], have presented a plan-regularity in the two main directions, X and Y, respectively. However, referring to the case-study building, it has been observed how the VGM increases the displacements mainly in Y direction while in X direction, the displacements were reduced given the structural asymmetry and torsional deformability.

To provide an exhaustive investigation of what was previously mentioned, Figure 4.10 shows the influence of the VGM on the MP 19821 located in the corner in the southwest façade.

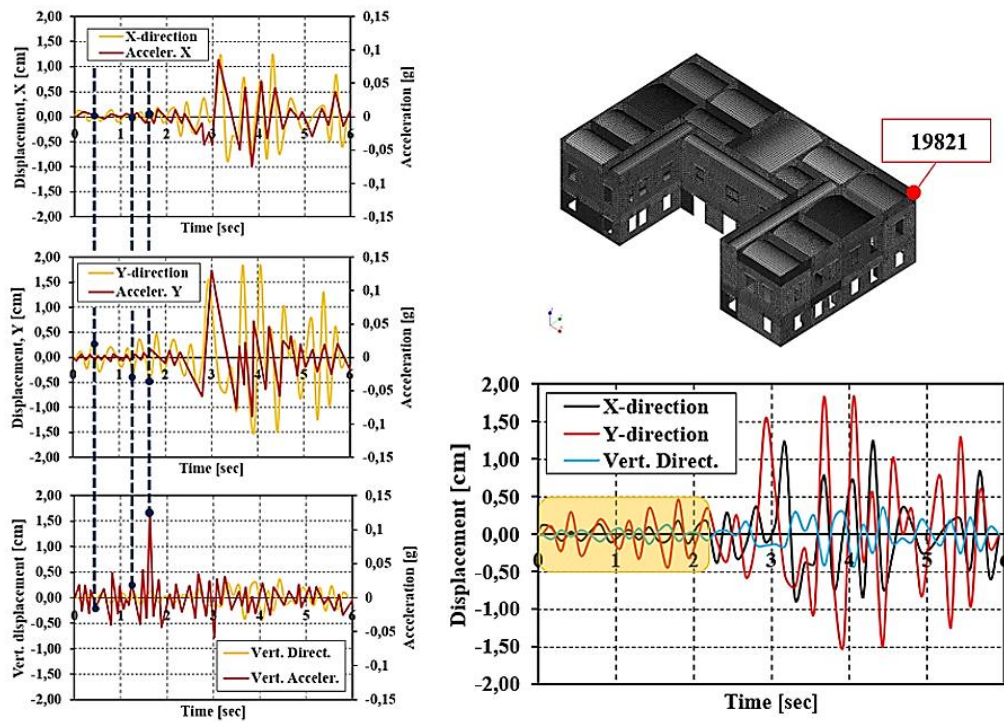


Figure 4.10: Influence of VGM on the corner MP 19821.

First of all, as it can be seen from the previously Figure 4.10, in the first two seconds of the time domain, the vertical component of the ground motion produced increases in terms of displacement in Y direction but not in X direction.

Secondly, from the acceleration-displacements comparison in the three main directions, a congruence condition has been guaranteed. Furthermore, it is worth specifying that in Y direction the displacements, at  $t > 3$  sec, were increased concerning the corresponding acceleration profile since, in the examined direction, the structure dissipates more seismic energy, consequently occurs a reduction of the secant stiffness and, therefore, the displacement profile tends to increase more than those in X direction.

Based on these physical aspects, it was possible to assert:

- i. by comparing the two analysed scenarios (H) and (H+V) it was shown how the seismic vertical component has produced an average percentage displacements increase enclosed in the range [5%-133%] concerning the case in which the vertical component was neglected;
- ii. the VGM has increased the displacements of the building in Y direction more than in X direction, since, given the asymmetry, was subject to torsional phenomena;
- iii. the MP placed on the vault (MP 7352) was subject to a higher influence of the ground motion vertical component with a considerable displacement increase ( $\Delta_{\text{vert.}} = 860\%$ ) compared to the scenario (H);
- iv. control nodes located in the corner positions were much more sensitive to the effects of VGM which influence the seismic demand.



### 4.2.3 Energy-based method for seismic analysis

#### 4.2.3.1 Ideal elastoplastic behaviour

In the non-linear dynamic analysis, it was possible to estimate the effect of the Banat-Voiteg seismic earthquake on the vulnerability assessment of the case-study building. Generally, considering the inelastic behaviour of the building, it was usual to express the maximum occurred deformations in terms of ductility factor as suggested in [210], [122].

As it known, the displacement ductility factor,  $\mu$ , is defined as the maximum deformation reached by the structures during a seismic excitation divided by the corresponding yielding deformation as reported in Equation 4.2:

$$\mu = \frac{\Delta_u - \Delta_y}{\Delta_y} \quad (4.2)$$

where,  $\Delta_{\max}$  is the maximum displacement reached and  $\Delta_y$  is the displacement at yield, generally estimated in non-linear time history analysis. The use of this parameter allowed us to analyse the evolution of plasticity in the structure during seismic motion expressing the maximum deformation in a dimensionless form to obtain, mathematically, a synthetic index parameter in closed form.

Moreover, the  $\mu$ -factor could be expressed in different terms, related to deformations (displacements), rotation ( $\theta_i$ ), and curvature ( $\Phi_i$ ) as reported in [120]. In this context, the displacement ductility factor,  $\mu$ , is shown in Figure 4.11 for ideal elastoplastic behaviour.

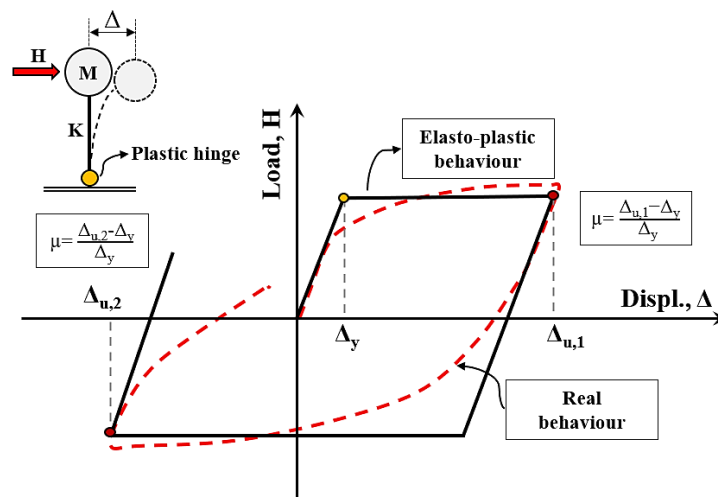
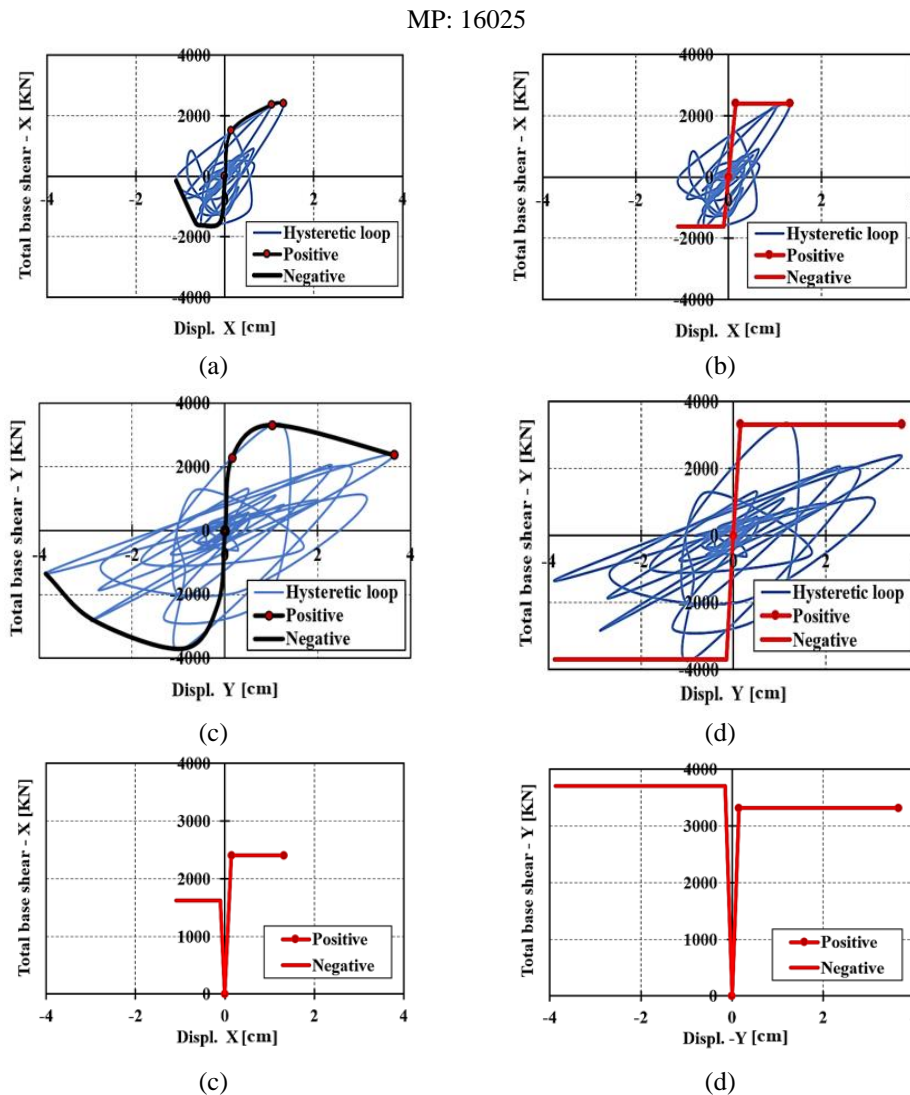


Figure 4.11: Displacement ductility factor.

However, in this research work, the ductility factor has been adopted in terms of displacements. So, to characterize the dynamic behaviour of the case study building,  $n$ -monitoring points were considered (see § 4.2.2.2) to idealize the structural behaviour as an equivalent elastic-plastic system. Besides, only the scenario (H+V) has been examined since it was the most unfavourable condition.

In this perspective,  $n$ -hysteretic cycles were analysed for  $n$ -MPs, and for each of them, the non-linear cyclic behaviour was enveloped, as proposed by [211]. For this purpose, Figure 4.12 has shown an example of the envelope of the hysteretic cycle, regarding the MP 16025



**Figure 4.12:** Backbone hysteretic loop and corresponding envelope in X and Y direction, respectively.

As previously specified, this procedure was applied for all the MPs belonging to the second level of the building to characterize the dynamic behaviour of the structure in the two main directions, X and Y, respectively. Moreover, Tables 18 and 19 have reported the results in terms of the maximum force ( $F_{max}$ ), yield displacement ( $d_y$ ), ultimate displacement ( $d_u$ ), and the evaluated ductility factor,  $\mu$ , in positive and negative directions, diversifying the point located on the vault, V, from those afferent on the wall panels, WP.

**Table 18:** Main capacity parameters in X analysis direction.

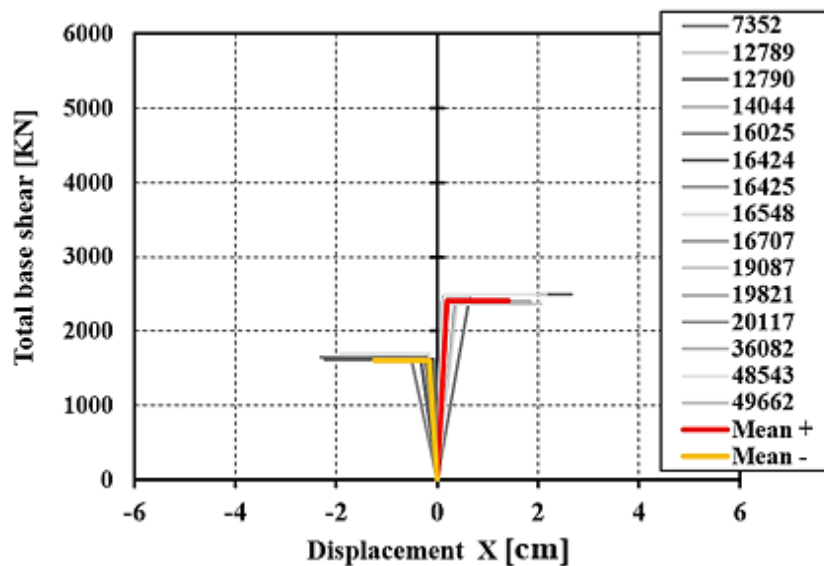
		X-direction							
Pos.	Node ID	Positive direction (X <sup>+</sup> )			$\mu^+$ factor	Negative direction (X <sup>-</sup> )			$\mu^-$ factor
		$d_y$ [cm]	$d_u$ [cm]	$F_{max}$ [KN]		$d_y$ [cm]	$d_u$ [cm]	$F_{max}$ [KN]	
V	7352	0.37	1.46	2401.71	2.95	-0.31	-1.37	1622.06	3.35
WP	12789	0.25	1.33	2362.21	4.32	-0.25	-1.86	1622.10	6.44
WP	12790	0.65	2.65	2501.71	3.05	-0.50	-1.63	1622.06	2.26
WP	14044	0.18	0.96	2401.71	4.30	-0.22	-1.27	1622.06	4.80
WP	14935	0.25	0.64	2362.21	1.56	-0.20	-1.20	1264.49	5.00
WP	16025	0.15	1.32	2401.71	7.83	-0.10	-0.66	1622.06	5.55
WP	16424	0.20	1.14	2362.21	4.70	-0.20	-0.69	1622.06	2.45
WP	16425	0.10	0.87	2401.71	7.70	-0.10	-0.60	1622.00	5.00
WP	16446	0.15	1.01	2362.00	5.73	-0.15	-0.60	1622.00	3.00
WP	16548	0.20	1.01	2401.71	4.05	-0.20	-1.00	1622.00	4.00
WP	16707	0.20	1.01	2401.71	4.05	-0.20	-0.61	1622.00	2.07
WP	16794	0.20	1.01	2401.71	4.05	-0.20	-0.61	1622.00	2.07
WP	19087	0.40	2.15	2501.71	4.38	-0.20	-1.20	1646.94	5.00
WP	19568	0.15	0.87	2401.00	4.80	-0.15	-0.50	1646.94	2.33
WP	19821	0.15	1.24	2401.71	7.30	-0.15	-0.85	1622.06	4.65
WP	20117	0.22	1.83	2401.71	7.32	-0.15	-0.40	1700.00	1.67
WP	36082	0.11	0.62	2462.00	4.64	-0.10	-0.57	1622.00	4.66
WP	48543	0.30	1.56	2501.00	4.20	-0.25	-1.66	1622.06	5.64
WP	49662	0.20	1.55	2362.00	6.75	-0.15	-1.20	1622.06	7.00
Minimum		0.10	0.62	2362.00	1.56	-0.10	-0.50	1264.49	2.07

**Table 19:** Main capacity parameters in Y analysis direction (continue).

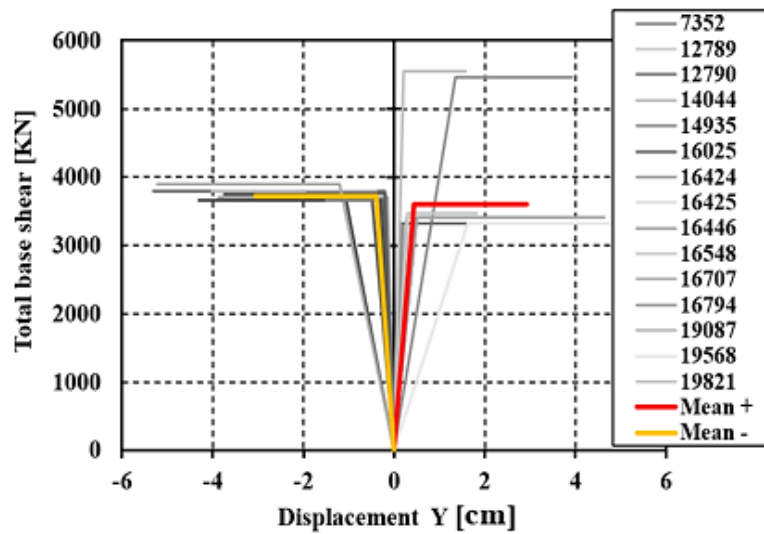
		Y-direction							
Pos.	Node ID	Positive direction (Y <sup>+</sup> )			$\mu^+$ factor	Negative direction (Y <sup>-</sup> )			$\mu^-$ factor
		$d_y$ [cm]	$d_u$ [cm]	$F_{max}$ [KN]		$d_y$ [cm]	$d_u$ [cm]	$F_{max}$ [KN]	
V	7352	1.35	3.93	5456.92	1.68	-1.07	-2.62	3659.85	1.39
WP	12789	0.23	1.78	3316.64	3.53	-0.17	-1.11	3659.85	3.17
WP	12790	0.30	2.25	3316.64	3.46	-0.25	-1.87	3659.85	3.46
WP	14044	0.30	1.97	3316.64	3.18	-0.20	-1.22	3765.85	3.04

		Y-direction								
Pos.	Node ID	Positive direction (Y <sup>+</sup> )				$\mu^+$ factor	Negative direction (Y <sup>-</sup> )			$\mu^-$ factor
		d <sub>y</sub> [cm]	d <sub>u</sub> [cm]	F <sub>max</sub> [KN]	d <sub>y</sub> [cm]		d <sub>u</sub> [cm]	F <sub>max</sub> [KN]		
WP	14935	0.20	1.70	3316.63	7.48	-0.20	-1.41	3765.85	6.05	
WP	16025	0.30	2.40	3316.00	7.00	-0.30	-1.59	3700.00	4.30	
WP	16424	0.50	3.52	3416.64	6.03	-0.50	-2.77	3750.00	4.54	
WP	16425	0.40	3.09	3416.64	6.73	-0.40	-2.34	3800.00	4.86	
WP	16446	0.30	2.09	3416.64	5.97	-0.30	-2.34	3800.00	6.80	
WP	16548	0.30	2.39	3416.64	6.97	-0.30	-1.62	3659.85	4.40	
WP	16707	0.60	3.77	3416.64	5.28	-0.60	-3.28	3800.00	4.47	
WP	16794	0.50	2.83	3416.64	4.66	-0.40	-3.28	3800.00	7.20	
WP	19087	0.22	1.57	5556.92	6.15	-0.20	-1.91	3759.00	8.53	
WP	19568	1.63	5.39	3316.00	2.31	-1.20	-5.22	3900.00	3.35	
WP	19821	0.30	1.83	3466.00	5.11	-0.40	-1.49	3659.85	2.73	
WP	20117	0.20	1.77	3416.64	7.84	-0.30	-2.40	3600.00	7.00	
WP	36082	0.60	1.72	3416.64	1.87	-0.70	-2.02	3600.00	1.89	
WP	48543	0.20	1.72	3316.00	7.61	-0.25	-2.24	3700.00	7.96	
WP	49662	0.25	2.13	3316.00	7.52	-0.28	-2.45	3650.00	7.75	
Minimum		0.10	1.57	3316.00	1.68	-0.17	-1.11	3600.00	1.39	

Therefore, the results were then plotted to identify the mean capacity curves, in positive and negative directions, of the case study building, as reported in Figure 4.13.



(a)



(b)

**Figure 4.13:** Mean capacity curves for the scenario (H+V) in X direction (a) and Y-direction (b)

From the results presented it was possible to highlight some aspects concerning the global behaviour of the structure when it is affected by VGM:

- i. the maximum shear threshold in Y direction ( $F_{\max}^Y = 3600$  KN) is 34% higher than the corresponding threshold in the orthogonal direction ( $F_{\max}^X = 2362$  KN);
- ii. in X direction the structure have resented a geometric asymmetry resulting affected by torsional phenomena, thus, the yielding and ultimate displacements are 55% and 52% lower than those estimated in Y direction;
- iii. the minimum ductility factor estimated for the horizontal structures in the two analysis directions, X and Y, was equal to 1.39;
- iv. by comparing the global behaviour in terms of ductility for the vertical structures, it has been observed that in Y direction, the minimum ductility ( $\mu_{\min}^Y = 1.39$ ) was 10% lower than that in the orthogonal direction,  $\mu_{\min}^X = 1.56$ .

### 4.2.3.2 Stiffness degradation

To analyse the stiffness degradation, the contribution of the wall resistant area in the two main directions X and Y was initially analysed. This view, as provided by [40] suggests to adopted two specific geometric limitations, as reported in Equations 4.3 and 4.4:

$$a' \geq 50\% \cdot a \tag{4.3}$$

$$b' \geq 50\% \cdot b \tag{4.4}$$

having indicated with  $a'$  the sum of the lengths of the elements of each single wall system in X direction,  $a$  is the dimension of the building in the parallel direction to of the wall system being considered,  $b'$  is the distance between the wall systems and  $b$  is the maximum dimension of the building in the orthogonal direction of the wall systems. Therefore, defined with  $a$  and  $b$  the total lengths of the walls in X and Y directions (see Figure 4.14), it was possible to satisfy the two conditions presented by the above equations.

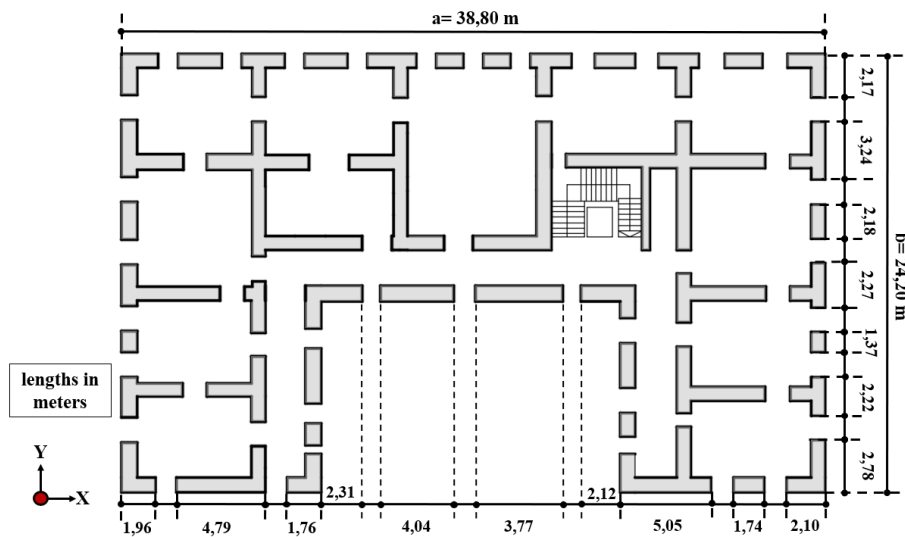


**Figure 4.14:** Identification of the wall system in the X and Y direction.

Calculated  $a' = 29.64$  m, it has been shown that this value is greater than 50% of the length of the total walls in X direction (19.4 m). Similarly, in Y direction,  $b' = 16.23$  m, which is greater than 50% of the length of the total walls in Y direction (12.1 m).

Subsequently, it was possible to identify the effective resistant area in the two analysis directions, as shown in Figure 4.15.



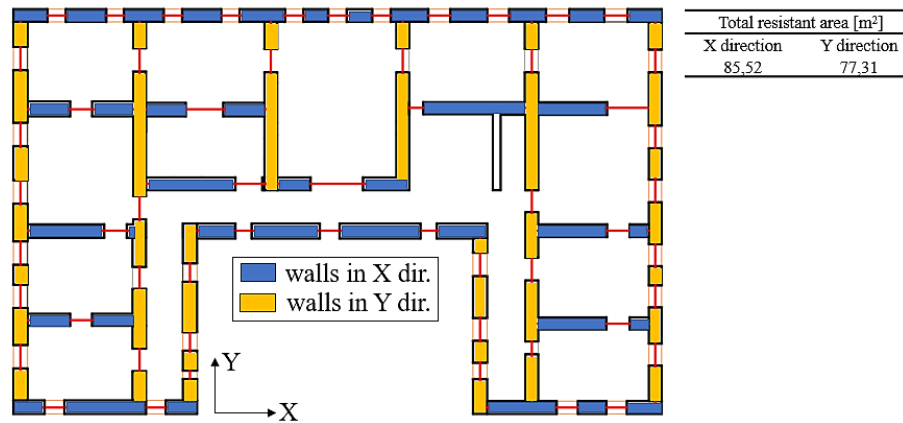


Figure 4.15: Effective walls resistant area.

as can be seen from the previous figure, the structure has a resistant area in X direction ( $A_X = 85.52 \text{ m}^2$ ) of 10% greater than in the orthogonal direction, Y ( $A_Y = 77.31 \text{ m}^2$ ).

Once the resistant areas were identified, it has been possible to estimate the stiffness degradation associated with the global behaviour of the case study building.

As is known, in a generic hysteretic cycle, consisting of an unloading and a reloading path, both force ( $F_i$ ) and displacement ( $d_i$ ) decrease during the sign reversal phase. In particular, the force decreases up to a certain predetermined load threshold (set at 70% of the force value at the maximum unloading peak) and the structural system presents a degraded stiffness compared to the elastic one in the initial phase ( $K_0$ ) [178].

The analysis of the stiffness degradation is an important step to take into consideration since it provides indications regarding the safety level (local or global) of the structural system and the corresponding energy dissipation.

In this perspective, the stiffness degradation was calculated using Equation 4.5 [211]:

$$K_i = \frac{|+F_{\max,i}| - |-F_{\max,i}|}{|+\Delta_{\max,i}| - |-\Delta_{\max,i}|} \quad (4.5)$$

where  $F_{\max,i}$  is the absolute value of the positive and negative peak lateral forces of the  $i$ -th cycle and  $\Delta_{\max,i}$  represents the corresponding absolute value of the positive and negative displacements associated with the  $i$ -th cycle.

To this purpose, Figure 4.16 has been presented the results in the two-analysis direction, X and Y, respectively.

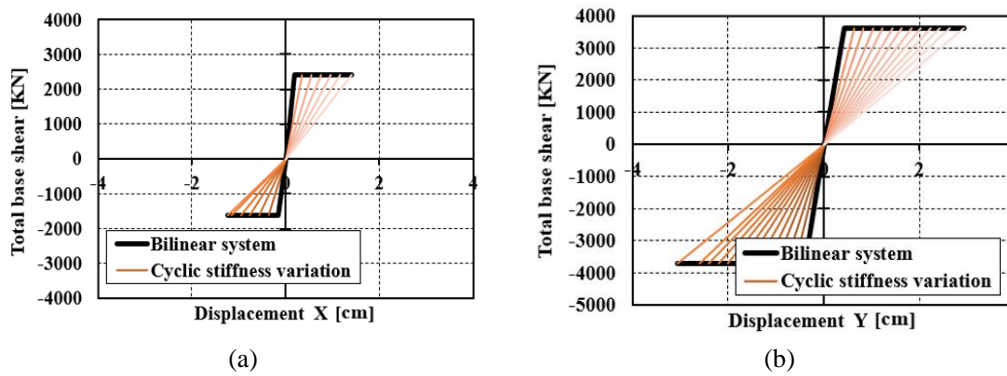


**Figure 4.16:** Cyclic stiffness degradation in, (a) X direction and (b) Y direction.

The results showed how the behaviour of the structure in the two analysis directions presents substantial differences. In particular, for negative displacements ( $\Delta^-$ ) by comparing the maximum shear thresholds, it can be seen that in X direction, the resistance was 44% lower (1609.94 kN) than the corresponding value in Y direction (3270.52 kN). Similarly, for positive displacements ( $\Delta^+$ ), the maximum shear threshold plotted in X direction ( $F_X=2410.2$  kN) was 32% lower than that corresponding to the orthogonal direction ( $F_Y=3597.02$  kN). Consequently, comparing the displacements, it was noted that on average, in X direction, the displacements associated with the entire hysteretic cycle ( $\Delta^X_{mean}=1.31$  cm) were 56% lower than the corresponding mean displacements in Y direction ( $\Delta^Y_{mean}=3.00$  cm).

Besides, the stiffness degradation curve was plotted in Figure 4.17.

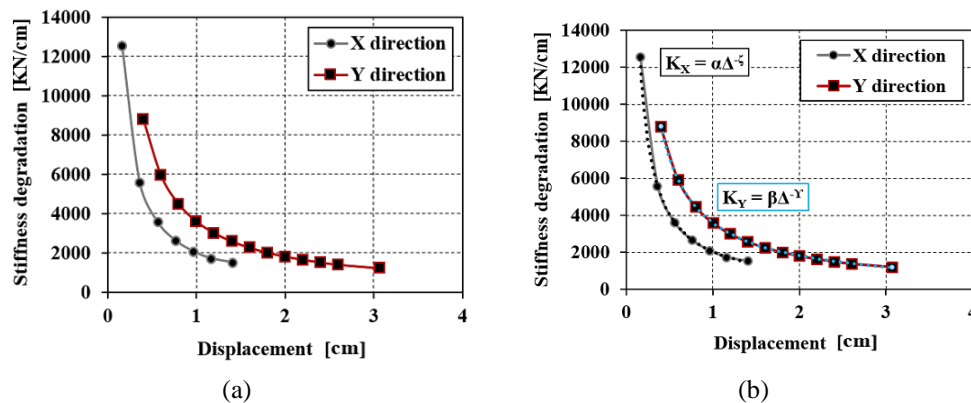


**Figure 4.17:** Stiffness degradation curves in X and Y directions (a) and descriptive power function of the stiffness degradation (b).

The curves presented in Figure 4.17 (a) provide important indications regarding the expected stiffness degradation during the seismic scenario

analysed. In particular, by comparing the two analysis directions it was possible to assert that the secant stiffness ( $K^X_0=12559 \text{ KNcm}^{-1}$ ) in X direction was 70% greater than that in Y direction ( $K^Y_0= 8794 \text{ KNcm}^{-1}$ ). Moreover, comparing the ultimate displacements in X and Y directions, it was possible to note how  $d_{uX}$ , was 56% lower than the ultimate displacement that was reached in Y direction.

Also, to analyse the stiffness variation associated with the whole hysteretic cycle, in Figure 4.17 (b) it has been possible to define two mathematical power functions that best approximate the degradation curve. As can be seen, it is a non-linear increasing monotone function with  $x=\Delta>0$  and exponents  $\zeta$  and  $\Upsilon<0$ . This function tends to approximate the abscissa axis more closely when the exponent is less than zero and allows the investigation of the degradation of the stiffness as a function of the displacements,  $\Delta$  reached each  $i$ -th hysteretic cycle.

The mathematical formulations are reported in Equations 4.6 and 4.7.

$$K_X = \alpha \cdot \Delta^{-\zeta} \tag{4.6}$$

$$K_Y = \beta \cdot \Delta^{-\Upsilon} \tag{4.7}$$

where the coefficients,  $\alpha$  and  $\beta$  have been estimated equal to 3592 and 2040 considering X and Y directions, respectively. Furthermore, the exponents  $\zeta$  and  $\Upsilon$  have been equal to 0.979 and 0.986, respectively.

Finally, in Figure 4.18, the estimated degradation percentage associated with each cycle of expected losses in terms of stiffness has been presented.

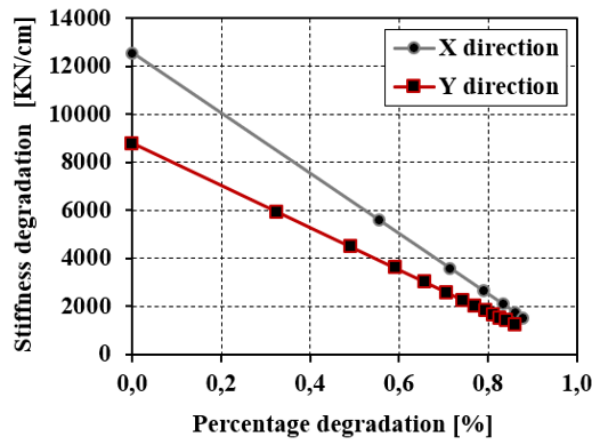


Figure 4.18: Stiffness percentage degradations.

From the results achieved, it has been noted that the stiffness degradation in both directions, X and Y, presented a linear regression, respectively.

There was a direct proportionality between the loss of stiffness and the percentage of degradation associated with each hysteretic cycle. In fact, regarding the X direction, considering an initial stiffness,  $K^X_0=12559.9 \text{ KNcm}^{-1}$ , a maximum degradation of 87% ( $K^X_u=1523.1 \text{ KNcm}^{-1}$ ) was obtained for the ultimate displacement ( $d_u$ ) equal to 1.40 cm. Similarly, in Y direction it was noted how considering an initial secant stiffness of  $K^Y_0= 8794.02 \text{ KNcm}^{-1}$ , has been obtained a maximum stiffness degrade,  $K^Y_u$ , equal to  $1220 \text{ KNcm}^{-1}$  (approximately 86% of  $K^Y_0$ )

Therefore, as far as analysed it has been possible to assert as follows:

- i. in terms of stiffness degradation, it has been shown how in X direction the initial secant stiffness,  $K_0$ , is greater than 70% concerning the secant stiffness offered in the perpendicular direction, Y;
- ii. by comparing the displacements, it was noted that in X direction, the displacements associated with the entire hysteretic cycle ( $\Delta^X_{\text{mean}}= 1.31 \text{ cm}$ ) were 56% lower than the corresponding mean displacements in Y direction ( $\Delta^Y_{\text{mean}}= 3.00 \text{ cm}$ ), confirming what has been reported in paragraph § 4.2.3.1 according to which, the torsional effects reduced the expected displacements ductility;
- iii. by considering the percentage degradation associated with each hysteresis cycle, it was observed that the maximum expected stiffness reduction was 86.5% for both analysis directions, X and Y, respectively;

#### 4.2.3.3 Evaluation of the behaviour factor, $q$ , in case of a near-field earthquake

The capacity of a structural system towards the seismic action in the non-linear field allows verifying the generic building using a linear analysis with a design value of seismic forces lower than those corresponding to a linear elastic response. This is expressed through the use of a reduced response spectrum, compared to the elastic one, through the behaviour factor,  $q$  [212-214].

The behaviour factor, as known, represents the parameter that allows, in a simplified way, to investigate the deformation capacity of a structural system in the inelastic range through energy dissipation. In this circumstance, the energy dissipation occurs through the redistribution of plasticity beyond the first damage of one or more structural elements.

The q-factor is defined as the ratio between the force to which the structure would be subjected if the structural response were completely elastic ( $F_{el,max}$ ) and the corresponding yield strength of the ideal elastic-plastic system ( $F_y$ ). This method is denominated forces approach as suggested in [215].

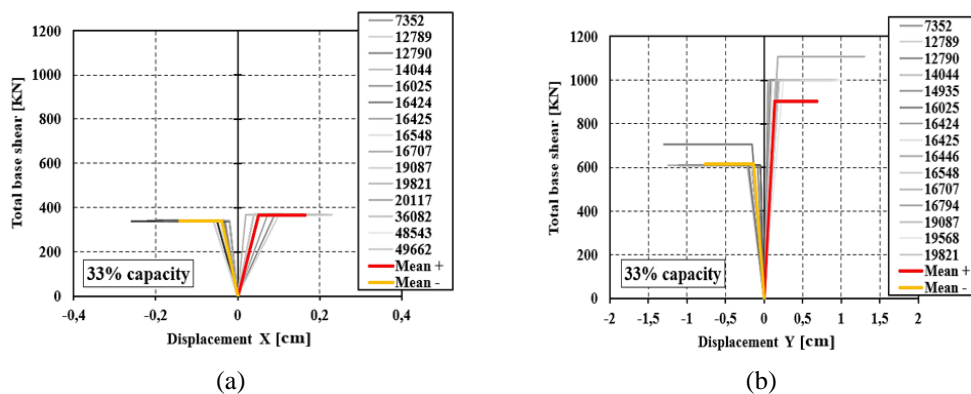
However, as proposed by [212], the q-factor can also be evaluated through an energetic approach (equivalence of the areas between the elastic system and the elastic-plastic one) which depends exclusively on the ductility of the structural system,  $\mu_s$ , without necessary to depend on the elastic response spectrum and the soil type. The mathematical formulation is reported in Equation 4.8.

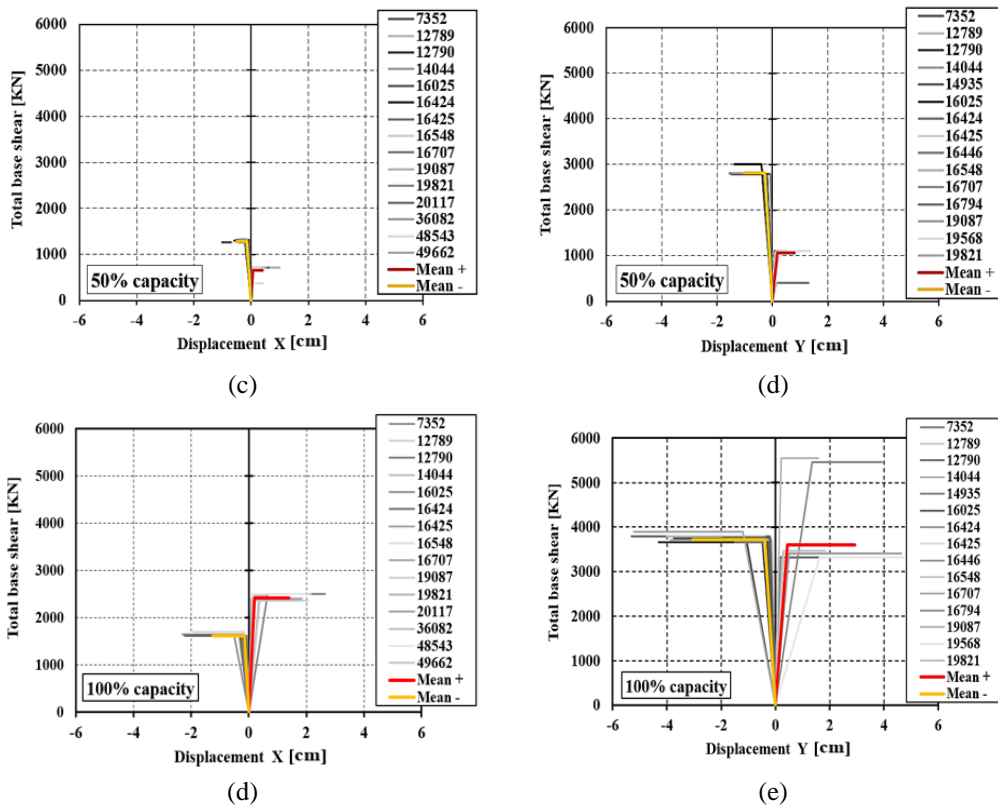
$$q = \sqrt{(2 \cdot \mu_s - 1)} \quad (4.8)$$

Based on these considerations, the evaluation of the q-factor was analysed in terms of both, energetic and forces approach by considering the influence of the ground motion vertical component, (H+V).

In particular, three distinct cases were analysed, by considering (i) maximum vertical decompression peak, estimated at 2 sec, which corresponds to 33% of the energy dissipation; (ii) maximum compression due to vertical seismic motion, estimated at 3 sec, which corresponds to 50% of the structural capacity; (iii) the entire time-history,  $t=6$  sec, i.e. 100% of the hysteretic dissipation. This choice was supported by investigating the influence of the ground motion vertical component on the expected behaviour factor, q.

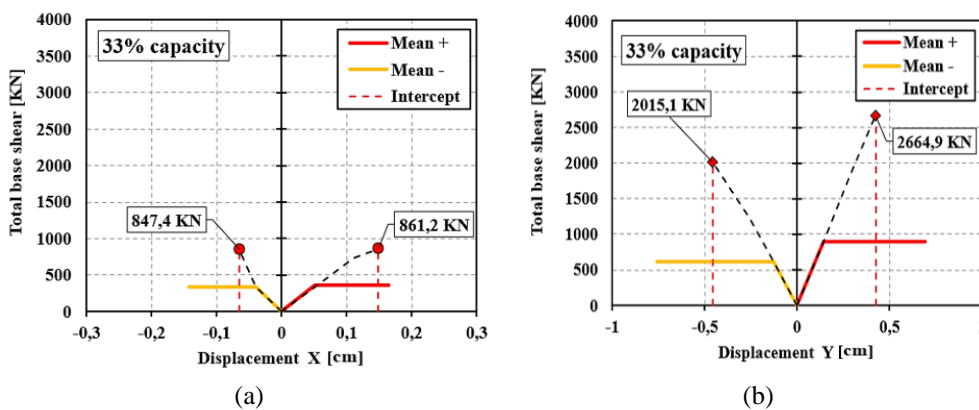
First of all, retracing the steps that led to defining the capacity curves for the case study structural system (see paragraph §4.2.3.1), Figure 4.19 shows the bilinear system associated with the energy dissipation variation at 67%, 50%, and 100% of the structural capacity.





**Figure 4.19:** Estimation of the mean capacity curves at 67%, 50%, and 100% of the structural capacity.

Subsequently, according to the equivalence of the criteria of the area [215] between both, elastic and elastoplastic systems, it has been possible to determine the maximum elastic force ( $F_{el, \max}$ ) for each condition previously analysed (Figure 4.20).





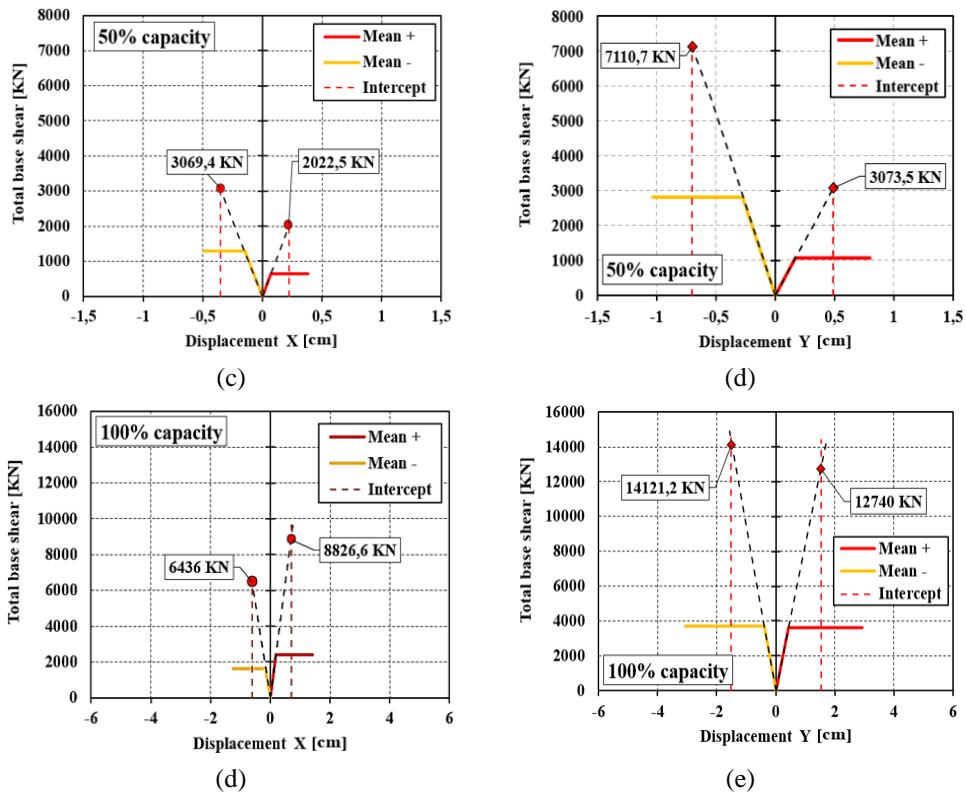


**Figure 4.20:** Equivalence of the areas for the case study structural system at 67%, 50%, and 100% of the capacity.

As can be seen, in Y direction, the structure, presenting a symmetrical behaviour, reaches a greater capacity than in the X-direction. The archived data are presented in Table 20:

**Table 20:** Yield and maximum forces associated with the capacity variations.

Capacity [%]	Time [sec]	$F_y$ [KN]				$F_{el, max}$ [KN]			
		X <sup>+</sup>	X <sup>-</sup>	Y <sup>+</sup>	Y <sup>-</sup>	X <sup>+</sup>	X <sup>-</sup>	Y <sup>+</sup>	Y <sup>-</sup>
67	2.0	366	340	901	614	861	847	2665	2015
50	3.0	653	1291	1068	2808	2022	3069	3073	7111
Full	6.0	2410	1609	3597	3720	8827	6436	12740	14121

As can be seen, for the condition of energy equivalence of the areas, the elastic force is, on average, 30% greater than the corresponding forces of the elastoplastic system. Moreover, the displacement's comparison has been presented in Table 21, having indicated with  $d_{el, max}$  the displacement in which the energetic equivalence between the elastic and elastoplastic systems have been reached.

**Table 21:** Yield and maximum displacements associated with the capacity variations.

Capacity [%]	Time [sec]	$d_y$ [cm]				$d_{el, max}$ [cm]			
		X <sup>+</sup>	X <sup>-</sup>	Y <sup>+</sup>	Y <sup>-</sup>	X <sup>+</sup>	X <sup>-</sup>	Y <sup>+</sup>	Y <sup>-</sup>
67	2.0	0.055	0.04	0.14	0.12	0.14	0.06	0.42	0.46
50	3.0	0.070	0.15	0.17	0.30	0.48	0.70	0.49	0.69
Full	6.0	0.190	0.15	0.43	0.39	0.20	0.60	0.20	1.51

Furthermore, the energy dissipation has been estimated as the envelope of the single hysteretic cycles associated with the n-control nodes, MPs, assumed following § 4.2.2.2. Moreover, the dissipation has been evaluated according to Equation 4.9 [216]:

$$E_d = \frac{A_h}{2\pi \cdot F_m \cdot \Delta_m} = \frac{A_h}{4\pi \cdot A_{el}} \quad (4.9)$$

in which  $A_h$  is the hysteretic energy loss per cycle and  $A_{el}$  represents the elastic strain energy associated with the equivalent linear elastic system. The results have been summarized in Table 22.

**Table 22:** Hysteretic energy dissipation at 67%, 50%, and 100% of the structural capacities.

Capacity [%]	Time [sec]	Energy dissipation [kNcm]	
		X	Y
67	2.0	142.85	244.88
50	3.0	829.51	1765.18
Full	6.0	1659.01	3530.37

From the gotten results it is worth noting how the structure in Y direction dissipates more energy than in the orthogonal direction X since, in the latter, the torsional phenomena reduce the capacity of the structure. However, it is worth noting how the energy contribution of the seismic vertical component only at  $t=2.0$  sec in X and Y directions is very low since the structure being in elastic conditions dissipating a small amount of energy.

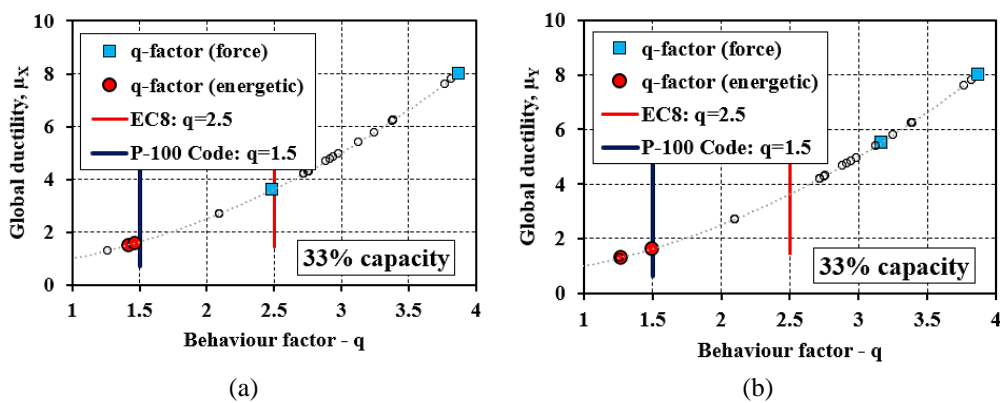
Consequently, the q-factor has been estimated with both approaches, forces, and energy, according to what has been reported in [38] and in Equation 4.8. The summary of the results is shown in Table 23 according to the cases analysed:

**Table 23:** Estimation of the behaviour factors  $q$ .

$q$ -factor (forces approach)	Cap. variation [%]			$q$ -factor (energetic approach)	Cap. variation [%]		
	67	50	Full		67	50	Full
$q_{x+}$	2.48	3.10	3.66	$q_{x+}$	1.41	1.39	1.46
$q_{x-}$	2.62	2.38	3.86	$q_{x-}$	1.46	1.41	1.53
$q_{y+}$	3.17	2.88	3.54	$q_{y+}$	1.26	1.18	1.65
$q_{y-}$	3.48	2.53	3.80	$q_{y-}$	1.50	1.53	1.67
Minimum X	2.48	2.38	3.66	Minimum X	1.41	1.39	1.46
Minimum Y	3.17	2.53	3.54	Minimum Y	1.26	1.18	1.65

From the gotten results, it has been noted that in terms of force approach, the results achieved for a capacity reduction of 67% ( $q=2.48$ ) and 50% ( $q=2.53$ ), have been very similar to the prescription of EC8 [38], which suggested  $q=2.5$  as the upper limit of the behaviour factor for URM buildings [23]. However, by adopting the energetic approach in terms of displacement, the minimum behaviour factor evaluated in the case of VGM only was equal to 1.26 in Y direction. On the contrary, for a capacity dissipation equal to 50%, the  $q$ -factor is equal to 1.18, resulting in compliance with the provisions prescribed by the Romanian Design Code P-100 [39] which establishes for URM buildings  $q=1.5$ . Furthermore, it is worth noting how the behaviour factor evaluated in the case of a complete-time history cycle ( $t=6.0$  sec) in Y direction provides values slightly higher than the assumed threshold of 1.50 since the structure dissipates much more seismic energy.

For an exhaustive overview, Figure 4.21 graphically shown the summary of the results just motivated in which the variation of the expected ductility is related to the behaviour factor, for all the capacity thresholds, at 33%, 50%, and 100%.



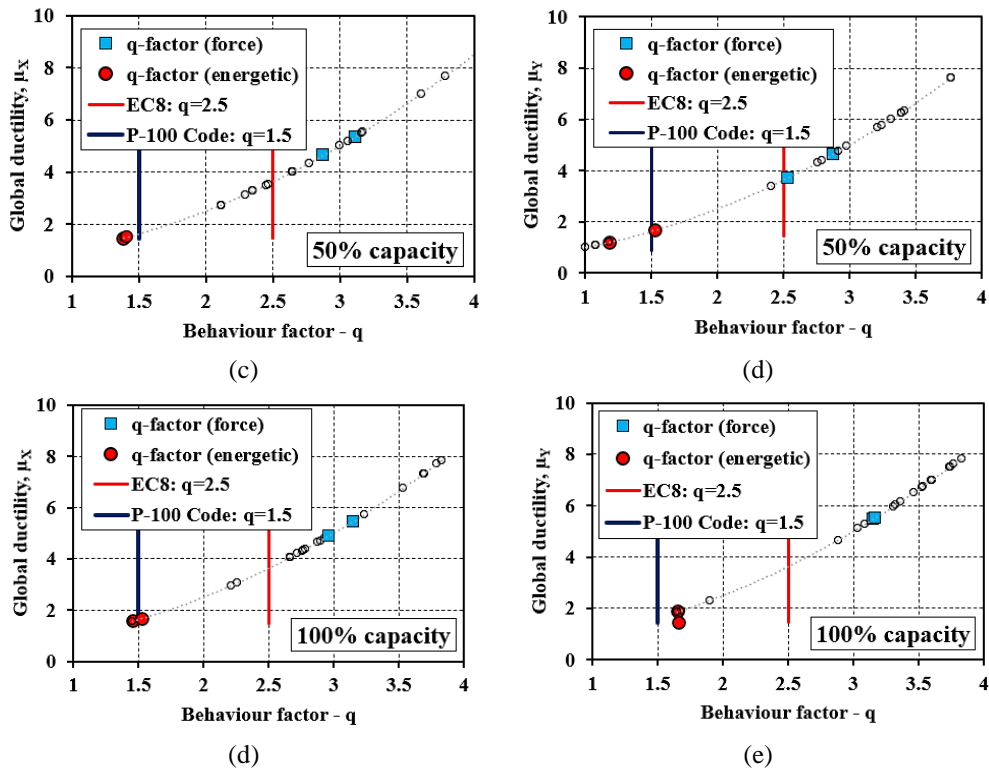


**Figure 4.21:** Ductility-q factor law for different capacity variations (a-b) 67%, (b-c) 50% and (d-e) 100%.

In conclusion, the acquired results show interesting insights that can be summarized as follows:

- i. three different boundary conditions have been assumed considering the variation of the seismic capacity concerning the case study structure at 67%, 50%, and 100% of energy dissipation;
- ii. as reported in Table 22, the energy dissipation evaluated at  $t = 2.0$  sec (maximum vertical acceleration peak) was approximately 6 times lower than that dissipated at 3 seconds and 11 times lower considering the entire-time history in X direction. Moreover, in Y direction, the energy dissipated at  $t = 2.0$  sec was 7 times lower than the corresponding dissipated energy at 3 seconds and 14 times lower than that dissipated for the entire-time history;
- iii. by comparing the values of the behaviour factor,  $q$ , obtained using the force approach for energy dissipation of 67% ( $q = 2.48$ ) and 50% ( $q = 2.53$ ), was very close to the prescription of EC8 [38];

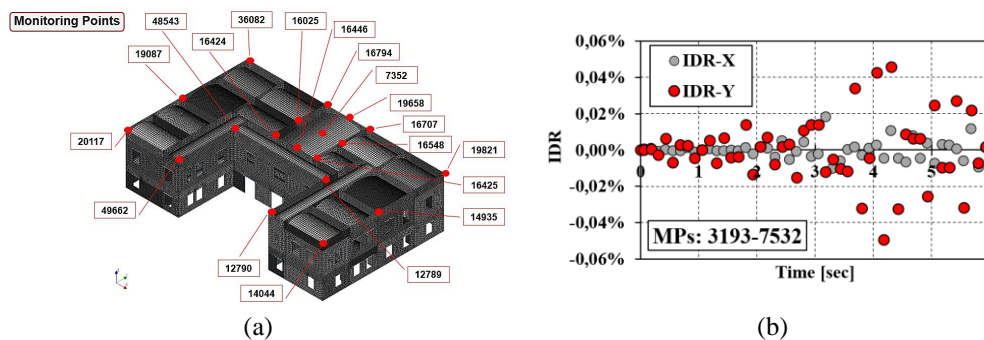
- iv. by considering the energetic approach, the estimated behaviour factor,  $q$ , was contained in the range [1.18-1.46] resulting in complies with the limit of 1.50 imposed by the Romanian Design Code P-100 [39];

#### 4.2.3.4 Inter-story drift ratio (IDR) in case of near-field ground motion

In this section, the inter-story drift ratio (IDR) demands of the case study building have been analysed considering the influence of near-field ground motion which has impulsive characteristic effects.

It is worth distinguishing two important concepts relating to the evaluation of drift. In particular, it is possible to particularize: (i) story drift (commonly called inter-story drift ratio), understood as the ratio between the relative displacement between two successive floors and the corresponding floor height ( $\Delta_i/H$ ). It represents the "residual displacement" generated by the seismic action between two MPs placed on the same alignment; (ii) story displacement, meaning the absolute displacement of a control node located on a generic floor concerning the base of the structure ( $\Delta/H_i$ ), [15], [192].

In this context, the variation of the IDR for each time-step was evaluated considering all the previously selected MPs (see paragraph § 4.2.2.2) to characterize the impulsive effect of the seismic action on the response of the structure. Specifically, all the IDRs associated with the n-MPs were evaluated to identify which "alignment" provides the most unfavourable condition. The results have been presented in Figure 4.22.



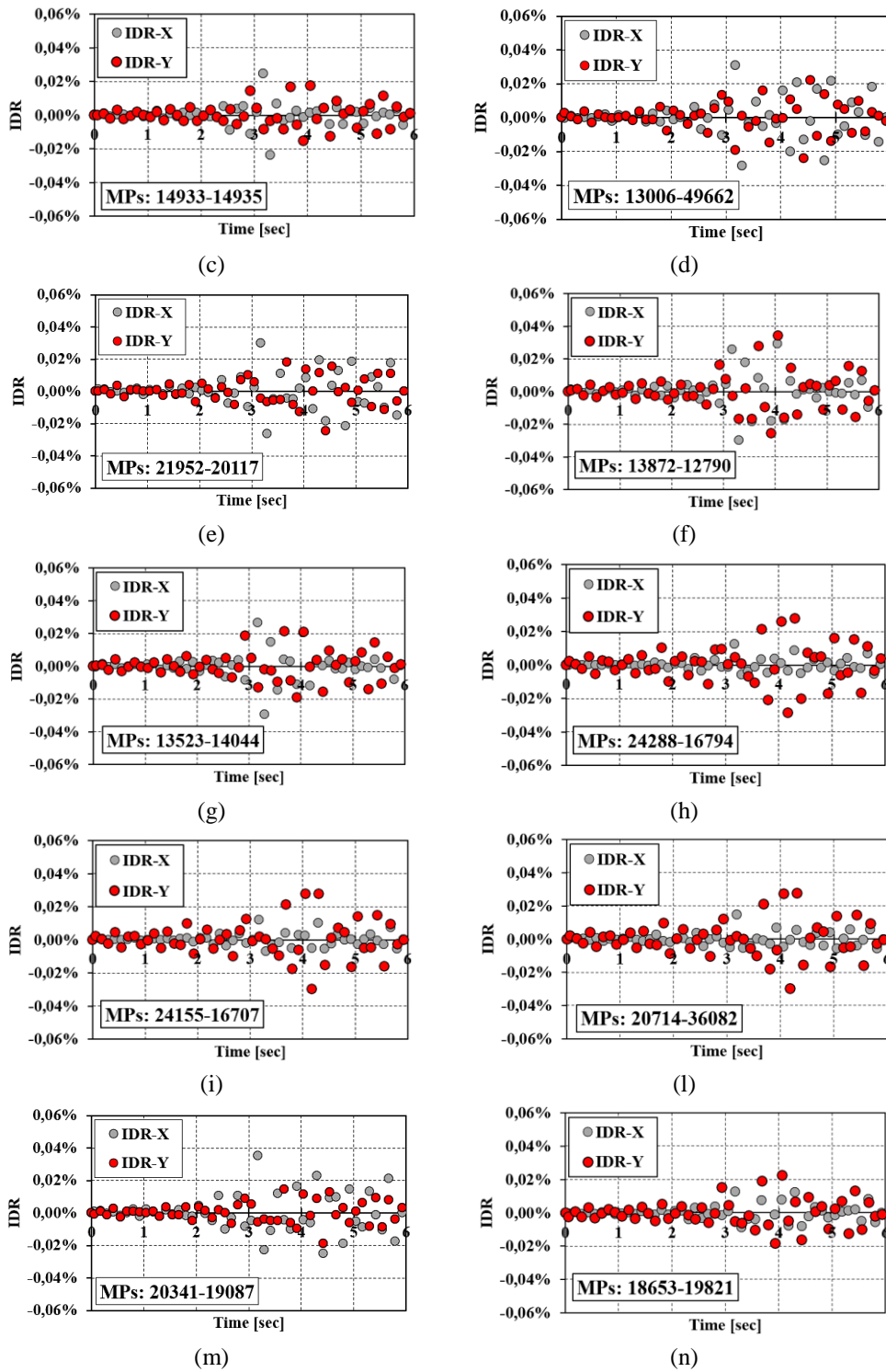
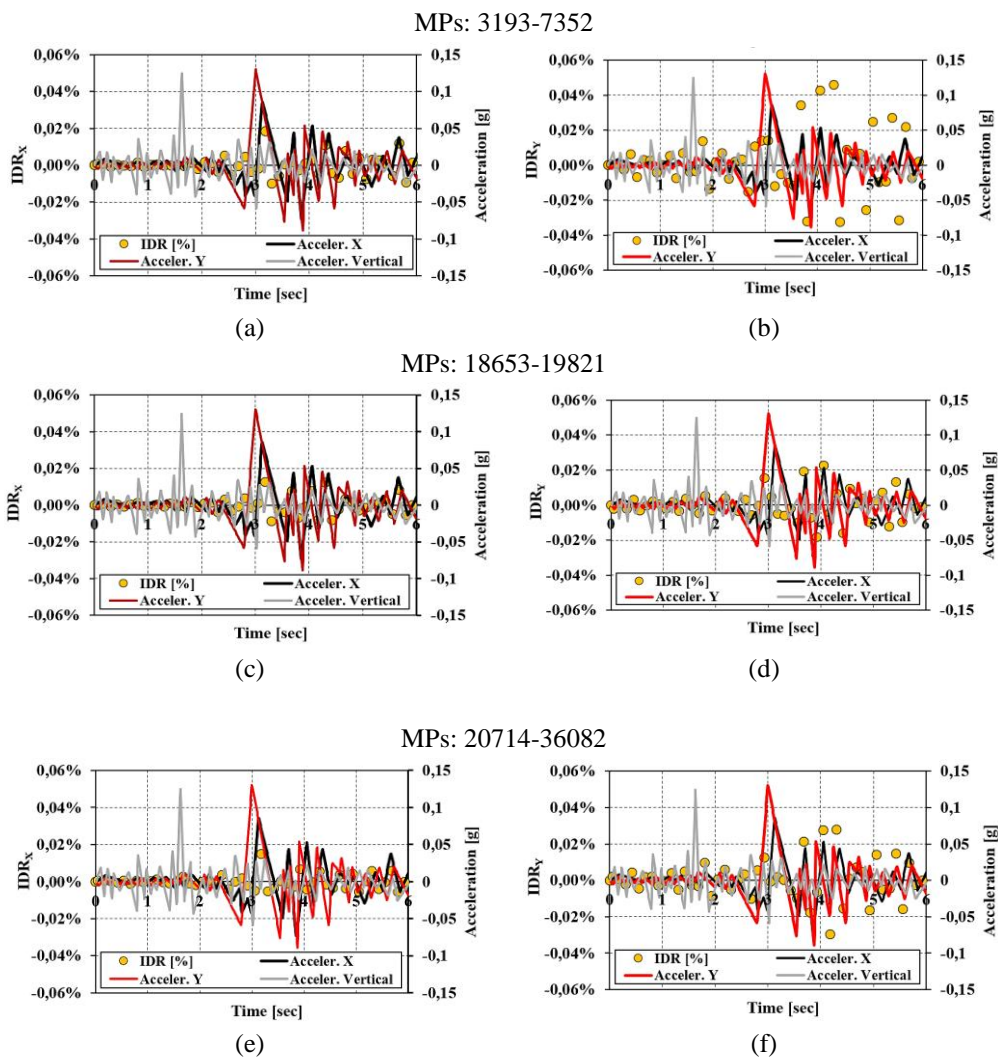


Figure 4.22: IDR variations associated with the MPs for each time step.



As can be seen from the previously Figure 4.22, the mean variation of the IDR was contained in the IDR range  $\pm 0.05\%$  for the MPs located in the central position, instead the IDR variations for the MPs located in the external corner position were of  $\pm 0.03\%$ , finally, for the MPs, placed in the centre of the façade in Y direction, the variation of the IDR was of  $\pm 0.025\%$ . Also, for a more comprehensive understanding concerning the influence of the impulsive seismic action on IDR variation, Figure 4.23 has been shown the congruence accelerations-displacements considering both MPs located in the central (see Figure 4.22 (b)) and in the corner positions (Figure 4.22 (n)).



**Figure 4.23:** Acceleration-IDR variations for different MPs.

From the results, it was possible to highlight how the IDR variation was congruent with the accelerations of the analysed seismic event.

It was noted that the IDR in the three cases analysed in Figure 4.23, presents a greater contribution in Y direction in which the structure exhibits symmetrical behaviour. As can be seen, in the first two seconds of the time history the ground motion vertical component affects the variation of the IDR in Y direction, consecutively, the increase of IDR for  $t > 3$  sec was essentially due to the cyclical degradation of the stiffness (see paragraph § 4.2.3.2). due to the simultaneous and cumulative effect of the three seismic components.

Vice versa in X direction, in the first two seconds of the time history, the IDR was not affected by the effect of the vertical component and tends to slightly increase at  $t > 3.0$  sec, when there was the concomitance of horizontal and vertical seismic actions.

Furthermore, considering the damage thresholds deduced from FEMA-365 [74], as proposed in [192], it was noted that the variation of the IDR did not generate any substantial damage or incipient collapse (partial or total) as reported in Table 24:

**Table 24:** IDR-damage correlation according to FEMA-356 [74].

Typological class	Damage state D2 (slight)	Damage state D3 (moderate)	Damage state D4 (severe)	Damage state D5 (collapse)
URM	IDR < 0.1%	0.1% < IDR < 0.3%	0.3% < IDR < 0.6%	0.6% < IDR

The correlation proposed in Table 24 has shown how the structure, globally, was in the elastic range since the IDRs evaluated were very low compared to the limits proposed by FEMA-356 [74].

The drift analysis could depend on three main factors:

- i. *type of seismic event*: in this hypothesis, the energy released by the seismic phenomenon must be correlated to the displacement capacity of the structure which, globally, generates relative displacements that can be correlated to a certain damage threshold. Impulsive seismic phenomena characterize their seismic energy input in a reduced number of cyclic acceleration peaks which did not allow to fully description the variation of the IDR and consequently the damage;
- ii. *type of building*: buildings characterized by deformable floors cannot be analysed through a global analysis but local analysis. This motivation is supported by the fact that for buildings with deformable floors, it was impossible to identify several MPs which were to be able to estimate the residual displacement between two consecutive floors;

- iii. *type of analysis*: influences the estimation of IDRs. If a non-linear static analysis is used, the displacements would increase monotonically with the force applied. However, this type of analysis would provide very conservative results in terms of IDRs values compared to a non-linear dynamic analysis that responds to the structure based on real seismic events.

Summarizing what has been introduced and analysed, salient points can be highlighted:

- i. the IDR evaluated in the first two seconds of the time domain was not affected by the vertical seismic component, at the same time, at  $t > 2$  sec, the IDR progressively increases given the ground motion horizontal components;
- ii. the mean IDR variation evaluated in the time domain has shown how the MPs placed on the vault (see Figure 4.22 (b)) have provided a range of values of  $\pm 0.05\%$  resulting more susceptible to displacement caused by the impulsive vertical seismic phenomenon;
- iii. by comparing the average IDR of the MPs placed in the corner positions of the case study building, they have provided a variation of  $\pm 0.03\%$ , resulting to be approximately 20% greater than the corresponding IDR evaluated for the those placed in the centre of the façade oriented in Y directions which corresponds an  $IDR = \pm 0.025\%$ ;
- iv. by comparing the congruence between response spectral accelerations and IDR it was noted that the drift calculated in Y direction was more susceptible to the influence of the vertical component since the structure, have presented a symmetrical configuration. Moreover, it was noted that at  $t > 3.0$  sec, the IDRs were increased since the simultaneous action of the horizontal and vertical components of ground motions were reached and, consequently, the stiffness in Y direction degrades more than that in orthogonal direction;

## 4.2.3.5 Evaluation of global seismic safety index

Very often, the quantification of the seismic effects is quantified in terms of direct and indirect damage (or losses). Direct damages are those caused directly to the building itself, while indirect damages refer to the amount of damage suffered by the exposed elements contained within the building such as objects, activities, and, in serious cases, human lives.

In this view, it is appropriate to identify a seismic safety condition to safeguard the building and therefore the lives of people. To this purpose, it is possible to define the global seismic safety index,  $\alpha_{PGA}$ , intended as the ratio between the collapse acceleration and the corresponding acceleration demand, as appropriately shown in Equation 4.10:

$$\alpha_{PGA} = \frac{PGA_C}{PGA_D} \geq 1 \quad (4.9)$$

According to [217] the collapse acceleration ( $PGA_C$ ), can be intended as the ratio between the collapse pseudo-acceleration,  $Sa_C$ , and the coefficients,  $\alpha_i$ , which are correlated to the dynamic behaviour of the structure, as mathematically shown in Equation 4.10:

$$PGA_C = \frac{Sa_C}{\alpha_{PM} \cdot \alpha_{AD} \cdot \alpha_{DT} \cdot \left(\frac{1}{q}\right)} \quad (4.10)$$

in which  $\alpha_{PM}$ , is the modal participation coefficient, equal to 0.80 for multi-story masonry buildings and 1.00 for single-story masonry buildings;  $\alpha_{AD}$  is the spectral amplification coefficient, equal to 3.0 about the design spectrum of the Banat Seismic Region for crustal earthquake and  $PGA=0.2$  g (see paragraph § 3.5.2),  $\alpha_{DT}$  is the coefficient that takes into account the dissipative phenomena, equal to 0.80 if the infills are not considered and 1.00 if the contribution of the infill panels is significant compared to that of the resistant system and finally,  $q$ , is the q-factor, equal to 2.5 for masonry buildings and 2.00-3.00 for reinforced concrete buildings.

Consequently, the collapse pseudo-acceleration,  $Sa_C$ , can be defined as the ratio between the total shear force (in all analysis directions, X and Y, respectively) and the corresponding stabilizing action induced by vertical loads,  $W_i$ , as reported in Equation 4.11:

$$Sa_C = \frac{V_i|_{x,y}}{W_i} \cdot g \quad [m \cdot s^{-2}] \quad (4.11)$$

As far as  $PGA_D$ , it is estimated as the product between the spectral amplification factor,  $\beta_0$ , depending on the design spectrum (assumed equal to 3 for the design spectrum of Banat Seismic Region) and the anchoring PGA (0.2g for the Banat Seismic Region) [39] as reported in Equation 4.12:

$$PGA_D = \beta_0 \cdot a_g \quad (4.12)$$

Based on the foregoing, Table 25 presents the summary of the results:

**Table 25:** Characterization of the seismic safety factor,  $\alpha_i$ , in the two analysis directions, X and Y, respectively.

$V_x$ [KN]	$V_y$ [KN]	$W_i$ [KN]	$Sa_x$ [g]	$Sa_y$ [g]
1284140	1284312	2132267	0.6	0.6
$PGA_{C, X}$ [g]	$PGA_{C, Y}$ [g]	$PGA_D$ [g]	$\alpha_x$ [-]	$\alpha_y$ [-]
0.47	0.47	0.6	0.78	0.78

having assumed,  $\alpha_{PM}$  equal to 0.8,  $\alpha_{AD}=3$ ,  $\alpha_{DT}=0.8$ , and  $q=1.5$  as suggested by the Romanian Design Code [39].

From the gotten results has been observed how, globally, the building is not able of offering an adequate resistance towards the simulated seismic event. It is noted that both indices  $\alpha_i$  are equal to 0.78, which means that the building capacities are 78% in X and Y directions, respectively. It is worth noting that the seismic verification was conducted in terms of PGA, therefore, the results showed a safety degree equal to -22% concerning the minimum threshold (set at 1), taking into account a high accelerations range which compromised the susceptibility of the structure.

Instead, considering the seismic verification, in terms of demand on capacity ratio, D/C, this was attested at a value equal to 1.27 (+27% over the maximum safety threshold).

Although, it is important to perform local analyses to catch the problem of its intrinsic vulnerability.

### 4.3 Local analysis

As stated in the previous chapter, it is clear that the behaviour of historic masonry buildings essentially depends on the type of floors present. Based on the degree of connection between horizontal and vertical elements, it is possible to understand the global behaviour of the entire building. In some hypotheses, it is easy to understand how, masonry buildings are equipped with rigid floors, which guarantee the box behaviour, the walls are stressed uniformly since the rigid floor allows a redistribution of the seismic action equally. In the specific case analysed, the case study building belongs to the first-class buildings, for which there are vaulted floors, therefore characterized by important flexural deformability. In this circumstance, the walls are an essential component of the building since they represent the seismic-resistant parts and the distribution of the seismic actions takes place through a direct proportionality between the cause (dynamic seismic effect) and the effect (lateral resistance). The lack of floor constraints makes the walls not connected to the floors and the global analysis procedure can be considered complex and sometimes inappropriate [171].

For this reason, it seems evident that the complications deriving from the spatiality of the structural system are multiple and strictly correlated to the degree of uncertainty induced by local factors (degree of constraint between orthogonal walls, degree of constraint offered by horizontal to vertical structures, presence of local motions, etc ...). As is known, the floor must constitute the mutual horizontal link for the different walls it connects, performing the dual function (i) to avoid out-of-plane mechanisms; (ii) redistribute the seismic action.

Therefore, concerning the first aspect is essential as the risk of overturning is the major cause of vulnerability of the masonry building, the second one, however, although important, does not represent a critical issue for the building.

In case it is not possible to identify a rigid diaphragm, it is worth resorting to local analysis, according to which the walls are analysed separately. To this purpose, it seems appropriate to "decouple" the building into a system of single masonry walls, bypassing the cumbersome three-dimensional model. In some cases, the walls are characterized by kinematic independence according to which, based on their stiffness, they are able of absorbing the dynamic action induced by the earthquake [171]. Based on these considerations, in the following paragraphs, the behaviour of the individual walls in the two analyses has been discussed to identify the type of prevailing mechanisms induced by the seismic action and establish an indispensable failure hierarchy by adopting the strength domains to capture the real seismic behaviour of the structural elements.

### 4.3.1 Identification of the structural typology of the wall systems

First of all, the walls can be distinguished in (i) bracing walls (or shear walls) that represent the structural elements that equilibrate the seismic forces in the longitudinal direction (parallel to the seismic action); (ii) connecting walls, identify the wall elements arranged orthogonally to the direction of the seismic action. In a local analysis type, for what has been described in the previous paragraph, the walls can be decoupled from the entire building when the conditions of the third class of buildings, cannot be valid. In this circumstance, the walls can be classified as follows [171]:

- i. *First-class walls*: the spandrel beams have no flexural and extensional stiffness, the node panels do not exist and the walls are made up of a system of kinematically decoupled isostatic cantilevers. The failure crisis for these elements occurs due to bending (slender panel), while for the squat panels, the crisis is due to shear mechanisms;
- ii. *Second class walls*: the spandrel beams have no flexural stiffness, the possible presence of a concentrated element resistant to traction (parallel to the wall) guarantees a minimum extensional resistance. However, the wall panels can be schematized as isostatic cantilevers and the mechanisms occur mainly due to flexural bending. Nodal panels do not exist;
- iii. *Third class walls*: the spandrel beams have their stiffness (flexural and shear) given by the presence of rigid floors. The masonry walls have the height of the floor and are contained between two consecutive spandrel beams. There is the presence of node panels in the structural scheme. In this circumstance, the crisis of the masonry panels can be either by both, shear or bending.

However, it is worth pointing out that in the case of the second type of walls, two different types of structural behaviour can be distinguished, in particular: (i) in-plane-behaviour (generally identified as II mode mechanisms), the steel tie-rod is positioned parallel to the longitudinal extension of the wall, consequently, it does not invalidate the analysis of the single wall; (ii) out-of-plane behaviour (identified as I mode mechanisms), the presence of steel tie-rod must be considered in the case of out-of-plane collapse mechanisms of the walls arranged orthogonally to the direction of the steel tie-rod. In this case, it provides a constraint for the kinematics that could be activated.



From this, it can be deduced that the in-plane behaviour of both, first and second-class type is similar but varies in the case of out-of-plane behaviour.

In the specific case of the analysed historical building, in a safe condition point of view, in the reality, the presence of the steel tie-rods is effective since they avoid the overturning mechanism of the walls. However, from what can be deduced from the analyses performed, the steel tie-rods seem superfluous because the out-of-plane kinematics does not occur.

For this reason, the walls have been typologically characterized as first-class walls.

By extending these concepts to the case study building, in Figure 4.24 the analysed wall systems, in the two analysis directions, have been identified.

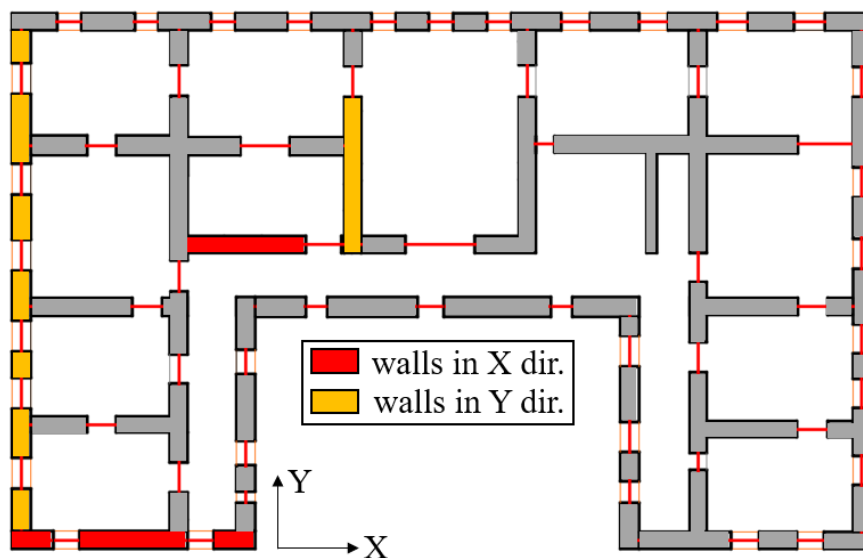


**Figure 4.24:** Identified wall systems for local analysis in X and Y directions, respectively.

In particular, as can be seen from Figure 4.24, only the two alignments of the perimeter walls have been considered since (i) the structure has a structural symmetry in Y direction; (ii) the perimeter wall systems are those most affected by the seismic action. Besides, two internal walls were considered as affected by the load of the masonry vaults, for which greater damage could be expected.

### 4.3.2 In-plane mechanisms

#### 4.3.2.1 Gravitational check conditions

The gravitational verification represents the "basic" condition of the analysis of vertical structures. In particular, the vertical load condition is intended as the most common load combination consisting of gravitational loads only.

Each masonry wall panel, intended as continuous from the ground floor to the top, behaves as an isostatic cantilever subject to gravitational loads, consisting of the weight of the masonry and the load of the vaulted floors. Furthermore, it is worth underlining that any tapering of the masonry at the various levels, generally asymmetrical in the perimeter walls, strongly affects the performing verification since the generated eccentricity represents an increase in terms of stress due to the vertical loads. For this reason, the perimeter wall panels are more vulnerable. Therefore, the general principle was to guarantee safety both in terms of equilibrium of the isostatic cantilevers conceived as rigid block and resistance of the sections.

In this circumstance, the verifications have been carried out considering the demand/axial capacity ratio,  $\psi_N$ , to assess the axial rate of the masonry cantilevers in purely static conditions. Thus, in Equation 4.13 it has been defined the axial resistance,  $N_{Rd}$ , for a generic masonry walls system:

$$N_{Rd} = \sigma_K \cdot B \cdot s \quad (4.13)$$

where the parameter  $B$  identified the width of the wall,  $s$  identifies the thickness of the wall and, finally,  $\sigma_K$  which represents the axial characteristic resistance of masonry, as defined in Equation 4.14:

$$\sigma_K = 0.85 \cdot f_d \quad (4.14)$$

in which, in a simplified way, a rectangular-shaped compression stress diagram was taken with a maximum value equal to 85% of the compressive strength of the masonry ( $f_d$ ).

Figure 4.25 has shown the identifiers, ID, of the masonry walls in the two analysis directions, X and Y, respectively.

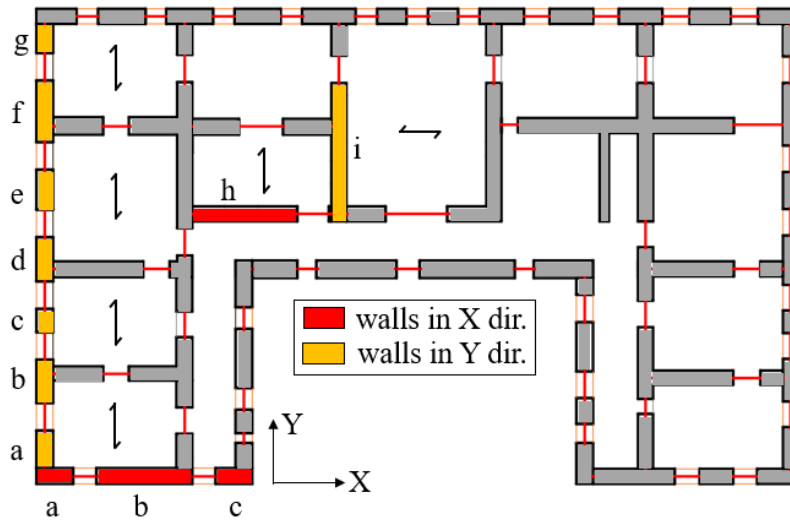


**Figure 4.25:** Identifiers, ID, of masonry walls considered in the two analysis directions, X and Y, respectively.

Following these conditions, Table 26 shows the geometric characteristics of the wall panels in X direction, taking into account that the masonry panels analysed have been identified as slender since the ratio between height, H, and width, B, were greater than 1.5 according to [38], [40].

**Table 26:** Characteristics of the analysed wall panels in the X-direction.

Panel	Direction	H [cm]	B [cm]	s [cm]	A [cm <sup>2</sup> ]	H/B [-]	$f_d$ [KNcm <sup>-2</sup> ]	$N_{Rd}$ [KN]	$\psi_N$ [%]
a			196		17640	>1.5		26510	94.0
b	X	899	479	90	43110	>1.5	0.177	64786	74.0
c			176		15840	>1.5		23804	82.0

The summary of the results has been presented in Figure 4.26 in which has been considered the demand/axial capacity ratio as reported in Equation 4.15:

$$\Psi_N = \frac{N_{Sd}(t)}{N_{Rd}(t)} \quad (4.15)$$

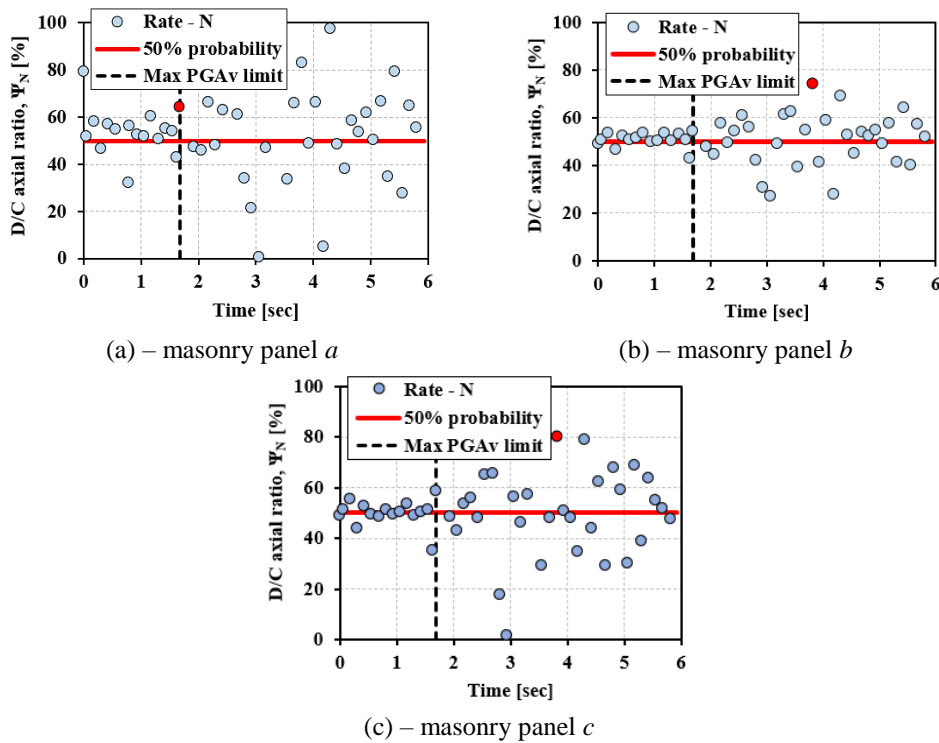


**Figure 4.26:** D/C axial ratio associated with the masonry panels analysed in X-direction.

First of all, the static verification was carried out considering the variation of the axial stress regime in the time domain,  $N(t)$ . This axial variation represents the contribution of the axial force under gravitational load conditions (demand) compared with the capacity, previously defined according to Equation 4.13.

Furthermore, three thresholds have been identified corresponding to (i) the limit of 50% probability of exceeding the capacity value; (ii) the limit concerning the vertical seismic action, fixed at 1.68 seconds; (iii) maximum limit reached by the D/C ratio. As it was possible to notice from the acquired results, the stress rate in terms of the axial regime was very low. The minimum axial stress threshold reached for wall panel *c* was equal to 82%. This circumstance was conditioned by the fact that this wall panel has a lower resistant area than the other two panels analysed, *a* and *b*, respectively.

However, globally, it has been possible to assert that the vertical action due to gravitational loads does not induce any deficiency since the capacity of the wall panels is undoubtedly greater than the respective demand.

Therefore, in conclusion, it was possible to note how in terms of axial load the wall panels were used only for 94%, 74%, and 82% of their capacity ( $N_{Rd}$ ), respectively.

Similarly, this procedure was adopted in Y direction, therefore, the geometric characteristics have been summarized in Table 27:

**Table 27:** Characteristics of the analysed wall panels in Y direction.

Panel	Direction	H [cm]	B [cm]	s [cm]	A [cm <sup>2</sup> ]	H/B [-]	$f_d$ [KNcm <sup>-2</sup> ]	N <sub>Rd</sub> [KN]	$\Psi_N$ [%]
a	Y	899	278	90	25020	>1.5	0.177	37600	56.0
b			222		19980	>1.5		30026	76.0
c			137		12330	>1.5		18529	61.0
d			227		20430	>1.5		30703	77.0
e			218		19620	>1.5		29485	69.0
f			324		29160	>1.5		43822	59.0
g			217		19530	>1.5		29350	64.0

Subsequently, in Figure 4.27, the results concerning the wall panels identified as *a*, *c*, *f*, have been suitable analysed.

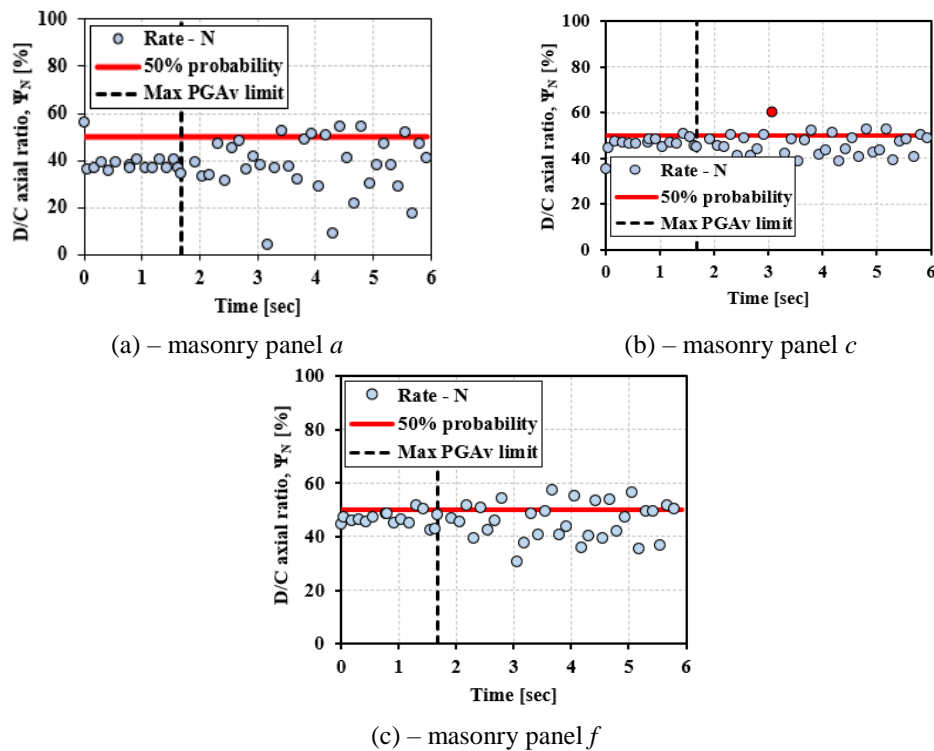


**Figure 4.27:** D/C axial ratio associated with the masonry panels analysed in Y direction.

In these examined cases, it was possible to notice how the wall panels have a very high structural capacity compared to the effective demand. Consequently, it was worth highlighting how the wall section has been used only for 56%, 61%, and 59% of the full capacity, resulting in abundantly verified.

Globally, this result was desirable since the gravitational load was lower than the corresponding capacity of the walls ( $N_{Rd}$ ), so, no bending crises were found.

A similar procedure was adopted for the internal wall panels  $i$  and  $h$ , respectively. In this sense, the geometric and stressing characteristics are shown in Table 28:

**Table 28:** Characteristics of the analysed internal wall panels in X and Y directions.

Panel	Direction	H [cm]	B [cm]	s [cm]	A [cm <sup>2</sup> ]	H/B [-]	$f_d$ [KNcm <sup>-2</sup> ]	$N_{Rd}$ [KN]	$\psi_N$ [%]
h	X	899	537	90	48330	>1.5	0.177	72632	73.0
i	Y	899	705		63450	>1.5		95354	50.0

Thus, the archived results for the panels analysed were reported in Figure 4.28.

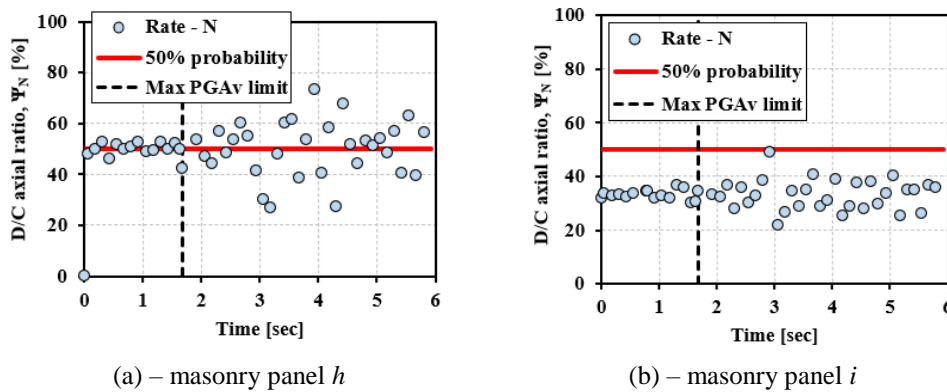


**Figure 4.28:** D/C axial ratio associated with the masonry panels analysed in, (a) X and (b) Y direction.

From the results presented, it was possible to note for the panels analysed a load increase, in the two directions X and Y, of 8% and 55% respectively. This increase was mainly due to the load transferred by the masonry vaults.

In particular, it was observed that in X direction, the wall section presented a D/C axial ratio equal to 73% while in Y direction was equal to 50%, demonstrating how the capacity of the wall panels was greater than the corresponding demand. Based on the results analysed, it was possible to note that in static conditions, the verification was satisfied for all the wall panels distributed in the two main directions, X and Y, respectively.

As noted, the induced compression stress has been strongly influenced by the resistant area of the panels. Consequently, there was an indirect proportionality such that wall panels with a smaller resistant area absorbed part of the load

compression stress, independently of the associated normal stress. So, it was possible to establish that:

- i. in X direction, panel *a* was identified as the most stressed since 94% of the maximum axial capacity was reached;
- ii. in Y direction, the panel *c* was the most stressed, which corresponds to 64% of the maximum axial stress capacity;
- iii. as regards the internal wall panels, the panel *h* had a maximum D/C equal to 70% which correspond to a  $N_{Rd}=72632$  KN. This value was 28% higher than what was obtained for panel *i*, in direction Y. The main reason was that in terms of resistant area, panel *h* had a smaller area than the masonry panel in the other direction (panel *i*). Furthermore, from a geometric point of view, the vaults afferent to the two panels analysed have a different length, therefore the load of the vault is proportionally redistributed on the resistant areas of the panels.

#### 4.3.2.2 Seismic check conditions in case of VGM

In the case of a seismic condition, the walls are generally affected by both gravitational loads and the effect of the earthquake. In this circumstance, to emphasize the importance of considering the ground motion vertical component, the scenario (H+V) was considered as a reference model, according to which, as mentioned in the previous chapters, the combined effect of the vertical and horizontal seismic actions was considered.

As previously analysed in paragraph § 4.3.1, the building is characterized by local behaviour, according to which the masonry walls were considered independent from a kinematic point of view. In the specific case, the seismic analysis has been conditioned by the behaviour of the walls towards the main failure mechanisms, such as shear and bending moment. In these conditions, the seismic capacity of the masonry walls was analysed in the time domain, to estimate the propensity to damage due to the effect of the seismic actions.

As is known, the basic hypothesis was to characterize the masonry by high compressive strength, considering the tensile strength to be zero. Masonry panels, subject to compressive and shear stresses, can collapse due to various boundary conditions.

In particular, the following failures could occur: (i) cracks induced by tensile stresses at the base of the panel due to excessive compression (rocking); (ii) horizontal and/or vertical sliding cracks of the mortar joints (sliding shear), or



due to a biaxial state due to of both tension and compression that produces localized diagonal cracks in the panels (diagonal shear) as reported in paragraph § 3.7.3.6 (see Figure 3.41).

#### 4.3.2.2.1 Axial force regime

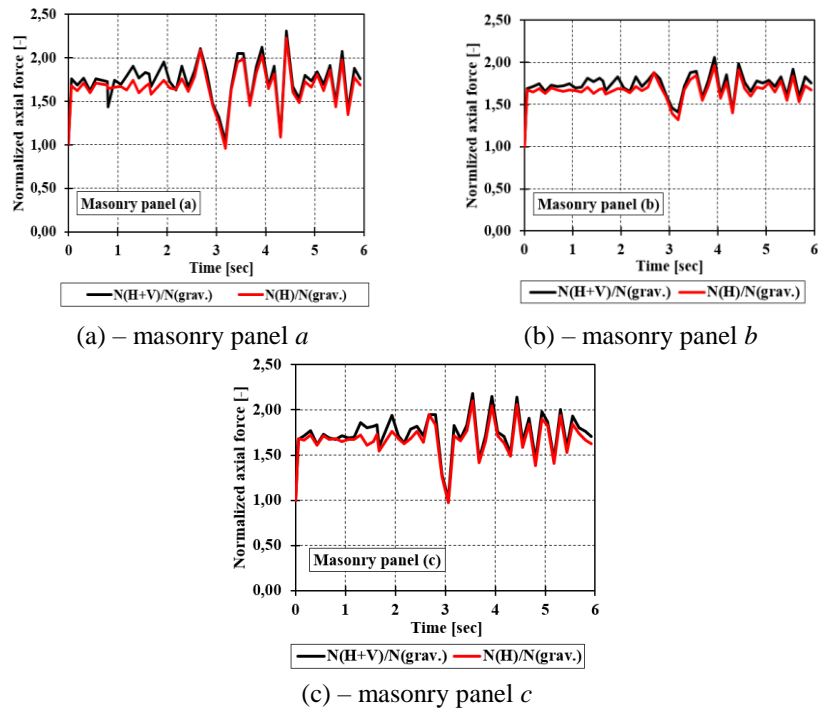
First of all, one of the key factors of the engineering demand parameters (EDPs) is the variation of the axial force in the case of the ground motion vertical component. As reported, the seismic vertical component could generate a variation in terms of normal stress. In particular, when the axial stress regime, induced by vertical loads, is modest and/or limitedly reduced, the vertical component of the ground motion could determine axial decompression phenomena. In fact, in this circumstance, the variation of the axial action changes the sign direction and the masonry panel undergoes tension.

Should such circumstances occur, they could also have repercussions in terms of shear verifications.

As shown in [32], the variation in normal stress is influenced by the type of fault mechanisms and by the site-to source distance ( $R_{JB}$ ). From these studies, it emerged that for distances very close to the seismogenic source (<5 km) the variation of the axial forces exceeded the maximum capacity of the masonry walls (>>100%). These variations have been evaluated concerning vibratory earthquakes, such as Kobe [18], which occurred in 1995 with a moment magnitude,  $M_w=6.9$  and  $R_{JB}=0.9$  km, L'Aquila (2016,  $M_w=6.8$ ) [30] and Gazli (1976,  $M_w=6.8$ ) [32], simulating approximately 35 synthetic records.

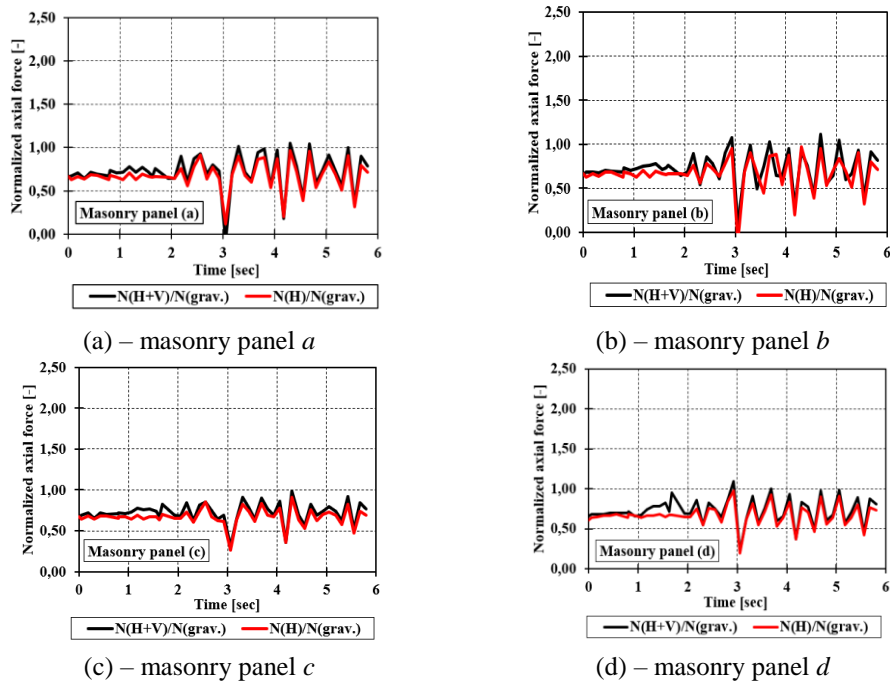
In this framework of activity, two scenarios such as, (H) and (H+V) were analysed in the two main directions X and Y, respectively, to circumscribe the effective seismic response of the masonry piers when they were subjected to vertical seismic action. It is important to point out that the comparison between the two scenarios considered emphasizes the seismic response of the masonry walls in case of an impulsive seismic phenomenon.

So, based on these observations, Figure 4.16 has been presented the results obtained considering the masonry wall panels in X-direction. For each of them, the comparison in terms of axial force-time history, normalized concerning the axial load due to gravitational loads,  $N_{grav.}$ , has been simulated for the scenario (H) and (H+V), respectively.



**Figure 4.29:** Normalized axial force in case of impulsive earthquake for the masonry walls in X directions.

Similarly, this verification was also carried out for the panels oriented in Y direction, as shown in Figure 4.30.



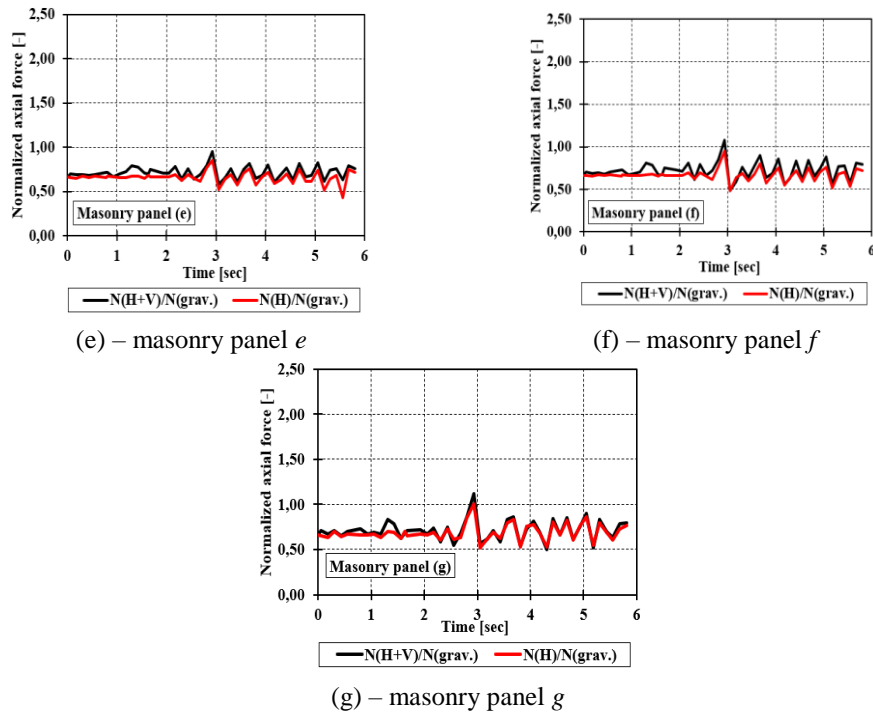


**Figure 4.30:** Normalized axial forces for the masonry panels in Y direction.

The seismic response of the analysed walls was heterogeneous by comparing the two analysis directions.

First, as reported in Figure 4.29 in the first two seconds of the time domain, it was observed that in X direction, the axial force generated by ground motion vertical component, (H+V), globally, was approximately +10% greater than the corresponding scenario (H) in which the vertical component has been neglected. Subsequently, at  $t > 2$  sec, the examined scenarios were comparable. Moreover, the orientation of the masonry vaults increases the axial capacity of the panels in X direction without reaching the compressive strength of the panel.

On the contrary, in Y direction (see Figure 4.30), the wall panels are slightly affected by the ground movement vertical component with an average increase of 33% respect the scenario (H). Furthermore, at  $t = 3.18$  sec, the normalized axial ratio was maximum for panels *a* and *b*,  $N_{(H+V)}/N_{grav.} \approx -0.12$  given the concomitance of the horizontal and vertical compressive seismic actions. However, considering the panel *g* (see Figure 4.30 (g)) at  $t = 3.18$  sec the ratio  $N_{(H+V)}/N_{grav.}$  was equal to 1.10 which is a decrease of 10% of the axial load due to the effect of the decompressive vertical seismic action.

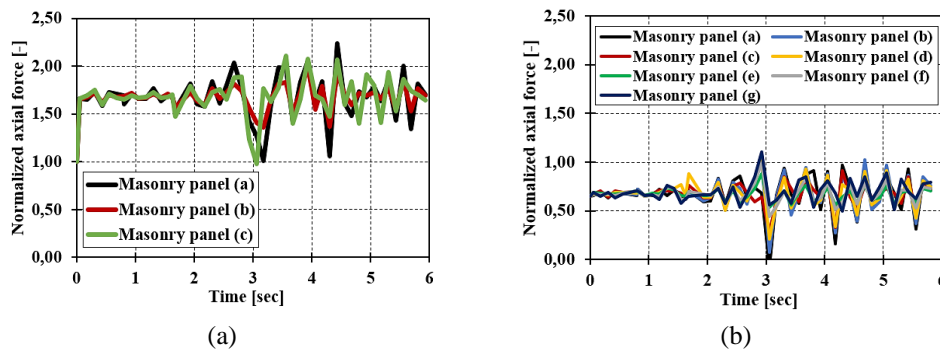


**Figure 4.31:** Normalized axial ratio for the masonry panels in (a) X direction and (b) in Y direction.

In Figure 4.31 it was summarized what has been previously explained, noting how the walls in both analysis directions were sensitive toward VGM. Thus, based on this consideration a preliminary consideration has been proposed as shown below:

- i. the results have shown that in X direction, the compression range varies between the minimum of 1 ( $N_{(H+V)}/N_{grav.}=1$ ) and 2.5 ( $N_{(H+V)}/N_{grav.}=2.5$ ) given the influence of gravitational load, while in Y direction, this range was very small, roughly 50%;
- ii. it has been noted that in the first two seconds of the time domain, the wall panels oriented in X direction are more influenced by the seismic vertical component which caused a variation of the axial stress regime without compromising the resistance of the panels. Moreover, at  $t > 2$  sec, the scenario (H) and (H+V) were not dissimilar;
- iii. in Y direction, in the first seconds of the time domain, the VGM has affected the masonry panels with an axial stress variation of 33% compared to case (H). Furthermore, at  $t=3.18$  sec, the concomitance of both, vertical and horizontal seismic actions, have provided an axial force decrease of 10% given the effect of the decompressive action of the VGM.

Furthermore, for the panels analysed, the variation of the axial force regime could also influence the shear behaviour in the two main directions.

In these circumstances, the panels located in X direction could be subject to a reduced shear behaviour for  $t=3.18$  sec due to the occurrence of both, horizontal and vertical seismic actions. In fact, at this time step, the ratio  $N_{(H+V)}/N_{grav.}=1$ , e.g. the minimum compressive stress,  $\sigma_0$ , was reached.

In Y direction, the wall panels oriented near the Sout façade could be affected by a deficient behaviour towards the shear failure since they had a reduced axial compressive capacity.

However, the shear verification has been carried out considering only the worst scenario (H+V) in which the ground motion vertical component has been taken into account.

#### 4.3.2.2.2 Diagonal shear failure - Turnsek and Cacovic criteria

As suggested by [38], [40], in the case of seismic analysis the condition that determines the occurrence of a specific damage state has been established by the activation of the mechanism that induces the minimum shear stress, as reported in Equation 4.16.

$$V_i = \min [V_i^{ss}; V_i^{ds}; V_i^r] \quad (4.16)$$

having indicated with  $V_i^{ss}$ ,  $V_i^{ds}$ , and  $V_i^r$ , the shear mechanisms induced by sliding shear, diagonal shear, and rocking, respectively.

It is worth noting the difficulty of estimating the sliding shear since the parameter  $f_b$  (normalized compressive strength of the block) has been difficult to determine and was not reported in the standard codes. To this purpose only diagonal and rocking shear capacities have been analysed.

Thus, based on these observations, the seismic checks were conducted in the two main directions, X and Y for the wall panels analysed previously.

In particular, referring to the walls in X direction, it was possible to carry out the shear verification for diagonal cracking as foreseen by [189] according to the formulation reported in Equation 4.17:

$$V_{Rd} = l \cdot t \cdot \frac{f_{tb}}{b} \cdot \sqrt{1 + \frac{\sigma_0}{f_{tb}}} \quad (4.17)$$

where  $l$  and  $t$  were the pier length and thickness, respectively;  $\sigma_0 = N/(l \cdot t)$  was the normal stress;  $f_{tb}$  was the masonry tensile strength for diagonal cracking and  $b$  is a corrective factor that depends on the stress distribution on the wall panels and its slenderness ( $1 < b = h/l \leq 1.5$ ). Furthermore, it is worth highlighting how by adopting the criterion proposed by [189], shear failure occurs due to the overcoming of the material's tensile strength, albeit small.

In this case, the maximum horizontal force that the panel can bear was equal to the value of  $V_i$  (shear force), for which the typical diagonal cracks occur which affect both, the masonry elements and the mortar in the centre of the panel, where the tangential tension was maximum and the tensile stresses no longer tolerated by the material cause a diagonal crack that extends progressively from the centre along the entire surface of the panel.

In detail, considering and a masonry panel stressed in its plane by shear ( $V$ ) and axial force that produced bending moment ( $N$ ), the centre of the panel will be subjected to the combined effects of normal and tangential tension:

$$\sigma_0 = \frac{N}{(l \cdot t)} \quad (4.18)$$

$$\tau_{\max} = p \cdot \tau_0 = p \cdot \frac{V}{(l \cdot t)} \quad (4.19)$$

The distribution of the shear stresses is parabolic, the maximum value  $\tau_{\max}$  has been reached in the middle of the section. The coefficient  $p$  takes into account the distribution of the tangential stresses along the cross-section of the panel, which varies as a function of both, geometric and stress state characteristics, respectively. In particular, assuming  $p=1.5$  it was possible to use a tangential plane stress state instead of a non-linear stress state (parabolic) as shown in Figure 4.32.

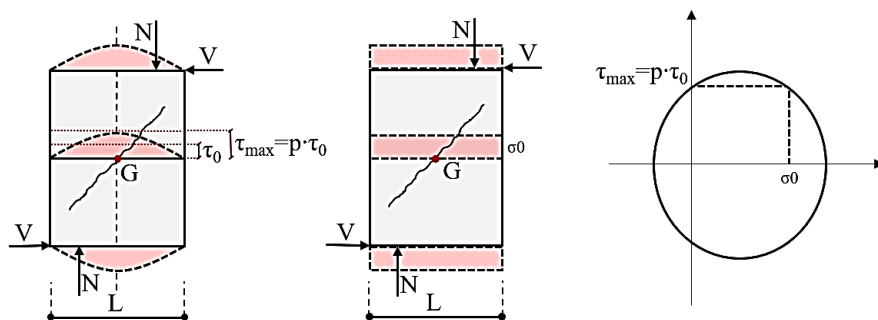


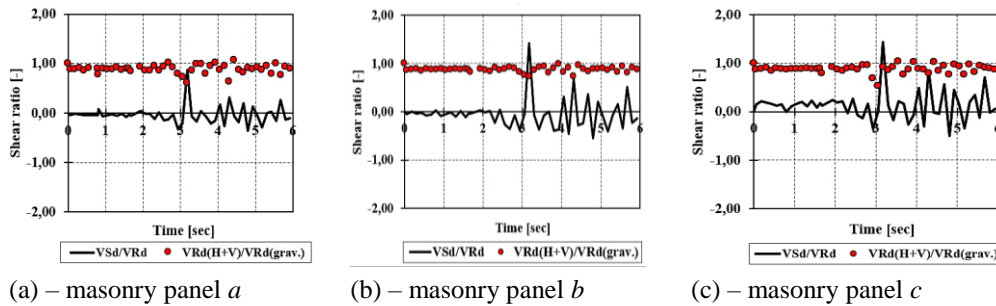
**Figure 4.32:** Stress distribution in the masonry wall panel, and stress state in the geometric centre of gravity, G, of the wall.

The failure mechanism of the panel occurs when, keeping the normal stress constant ( $N$ ), increasing the shear ( $V$ ), the principal tensile stress has reached the cracking value,  $f_{td}$ .

It is worth underlining how the method proposed by [189] is mainly based on the theory of the Mohr circle according to which both conditions of equilibrium and congruence were not respected [189].

Setting  $N=0$ , the corresponding shear value was  $V \neq 0$  thus assigning a residual bearing capacity of the panel [171].

To this purpose, Figure 4.33 have been reported the time history of the shear demand and shear capacity considering for each time step, the variation of axial force,  $N(t)$ , since the variation of axial regime induced by the VGM component tends to modify the shear behaviour of the masonry panels [32], [108].



(a) – masonry panel *a*                      (b) – masonry panel *b*                      (c) – masonry panel *c*  
**Figure 4.33:** Time histories of normalized shear capacity and shear demand/capacity ratios for the masonry walls analysed in X-direction.

More specifically, the red points denoted the shear time histories capacity at each time step evaluated according to Equation 4.16,  $V_{Rd}(t)$ , normalized concerning the corresponding shear strength induced by axial force due to the gravity condition,  $V_{Rd}(grav.)$ . Moreover, the black lines identified the time histories of the shear demand/capacity ratio,  $V_{Sd}(t)/V_{Rd}(t)$ .

As can be seen, the wall panel *a*, at  $t= 3.18$  sec (concomitance of the horizontal and vertical actions) was in a condition of limit equilibrium between demand and capacity,  $V_{Sd}(t)/V_{Rd}(t) \approx 1$ , while for the panels *b* and *c*, it has been noted as at  $t= 3.18$  sec, the seismic demand significantly exceeds the corresponding capacity, resulting, therefore,  $V_{Sd}(t)/V_{Rd}(t) > 1$  due to the variation of axial force.

In these circumstances, it was possible to analyse the shear stress rate of the panels previously considered to understand the effective capacity of the panels themselves against vertical seismic action. The shear stress rate has been assessed using the demand on capacity ratio, according to Equation 4.20:

$$\Psi_V = \frac{V_{Sd}(t)}{V_{Rd}(t)} \tag{4.20}$$





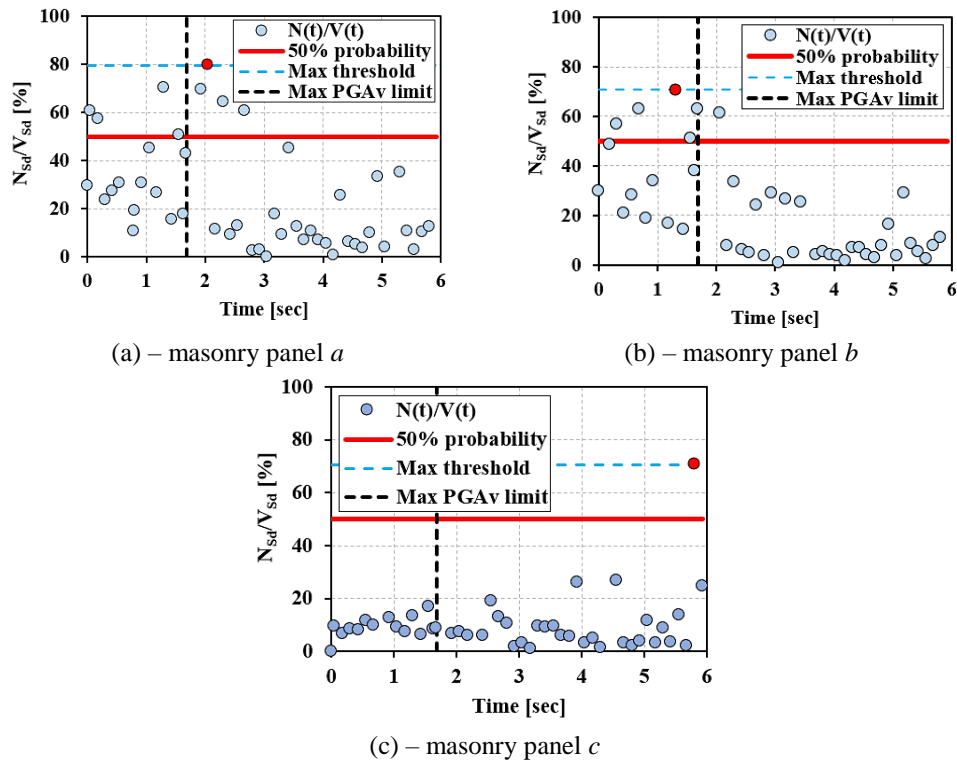


**Figure 4.35:**  $N(t)/V(t)$  ratio for the panels analysed in X-direction.

The results showed that the effect of the shear component is small compared to the corresponding axial action,  $N(t)$ . It can be noted that for panel *a*, the axial action was about 80% of the respective shear stress  $V(t)$  (see Figure 4.35 (a)), similarly, for both panels *b* and *c*, a maximum of 70% has been reached in both cases (see Figures 4.35 (b) and (c)). It is worth noting that in the first two seconds of the time history, in which only the ground motion vertical component was acting, the  $N(t)/V(t)$  ratios were high for wall panels *a* and *b* while for the panel *c* was close to 20%. Moreover, for panel *c*, the  $N(t)/V(t)$  ratios were reduced since it has a smaller resistant area than the other panels, therefore the shear forces, even if less than the corresponding axial actions, has greater incidence studies [32], [108].

Similarly, in Y direction, the seismic verification performed offers opposite results to what have been discussed in the orthogonal direction.

The main reason is that in Y direction, the structure presented symmetrical behaviour, therefore, the distribution of the seismic action was distributed according to the lateral stiffness of the individual panels, consequently in the same direction, there were a greater number of wall panels, this involves a redistribution of the seismic action proportionally to the number of panels.

Furthermore, as highlighted in the previous paragraphs, in X direction, the structure has presented a structural asymmetry and the torsional phenomena reduced the seismic capacity.

The results have been summarized in Figure 4.36 according to the wall panels *a*, *c* and *f*.

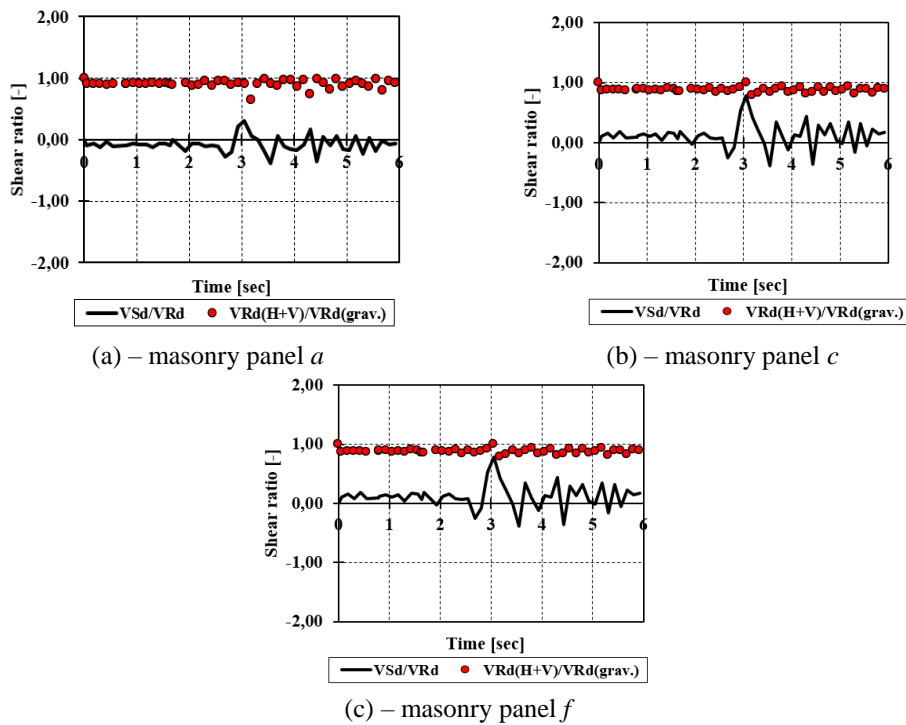


**Figure 4.36:** Time histories of normalized shear capacity and shear demand/capacity ratios for the masonry walls analysed in Y direction.

As can be seen from the results, at  $t=3.18$  sec, the verification is abundantly satisfied for both panels *a* (see Figure 4.36 (a)), while for panels *c* and *f*, a limit equilibrium condition are determined according to which the seismic demand has equalled the structural capacity (see Figures 4.36 (b) and (c)). About panel *f*, this condition has been considered verified since being near the corner of the building, it was affected by the torsional effects induced by the concomitance of the horizontal and vertical seismic actions.

Similarly, as previously defined by Equation 4.20, the shear rate for the panels considered was evaluated and reported in Figure 4.37.

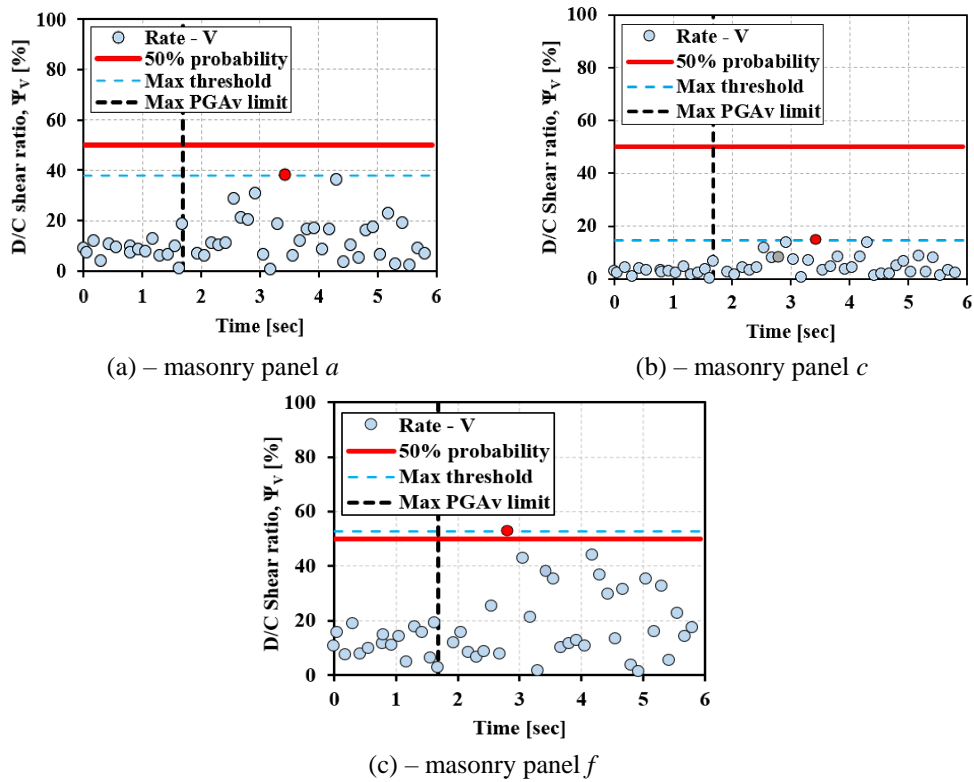


**Figure 4.37:** Shear stress rates for the analysed masonry panels in Y direction.

First of all, it was noted that in the first seconds of the time history, the vertical seismic action at  $t = 1.68$  sec, tends to increase the shear force in the direction examined. Secondly, there was heterogeneity in terms of stress rate for the panels analysed. In particular, for the masonry panels *a* and *f*, (see Figures 4.37 (a) and (c)) being in a more external position, the maximum shear rate reached was 38.07% and 52.75%, respectively, since both, stresses and displacements, increased with the distance from the centre of the alignment of the panels. As a result, the external panels were much more stressed than those placed in an intermediate position.

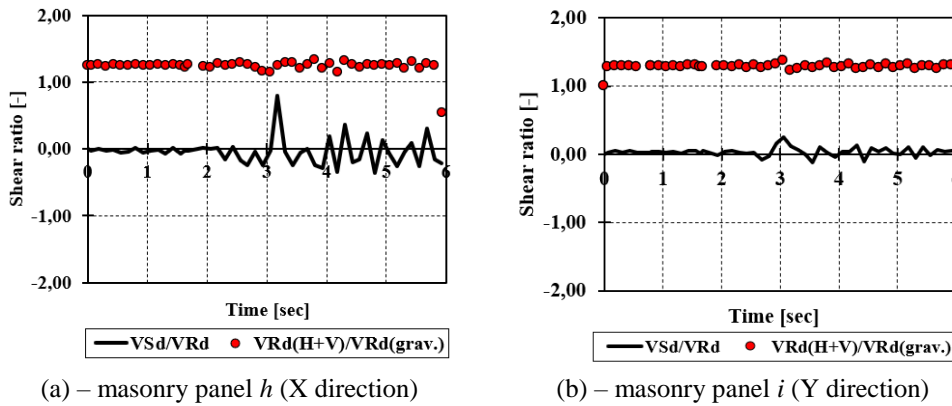
As far as panel *c*, as reported in Figure 4.37 (b), the maximum stress rate was 14.63% reached at  $t = 3.43$  sec since it was located in the centre of the alignment of the wall panels.

Consequently, to take into account the influence of the vertical component of the earthquake, on the panels analysed, the  $N(t)/V(t)$  ratio has been considered as previously described for the panels in the orthogonal direction. Figure 4.38 have been shown the archived results.



time step the axial and shear forces were comparable ( $N=80.31$  KN and  $V=53.74$  KN) providing an  $N(t)/V(t)$  ratio equal to 55.13%.

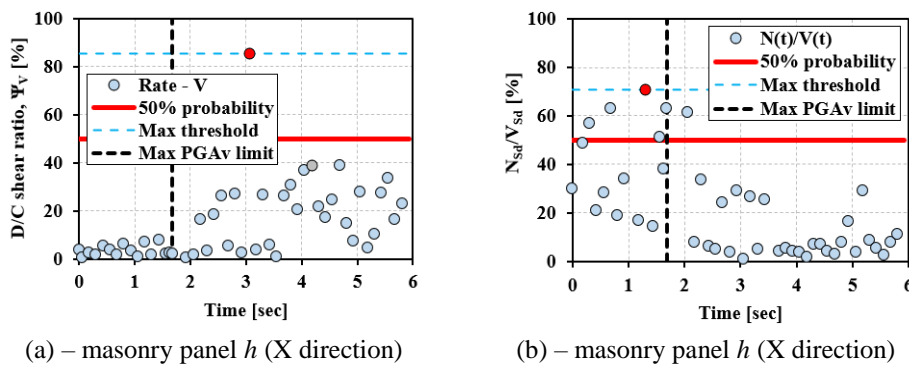
Similarly, the behaviour of the wall panels  $h$  and  $i$ , have been respectively analysed in the case of seismic conditions in terms of normalized shear ratio, as reported in Figure 4.39.

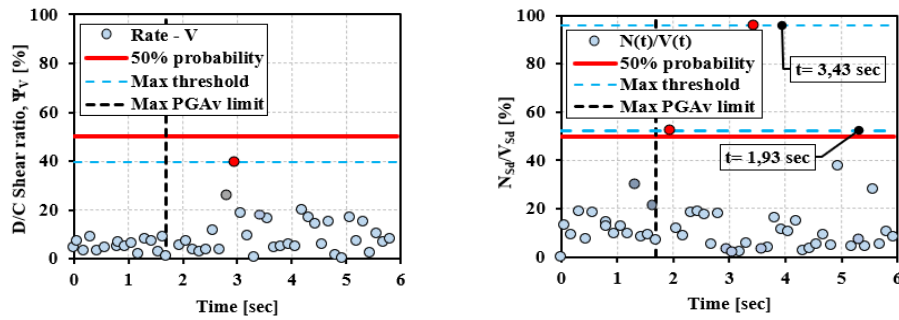


**Figure 4.39:** Normalized shear ratio for the masonry panels  $h$  and  $i$ , in X and Y directions, respectively.

As the results summarized in the previous figure show, for both wall panels, the verification is satisfied. As reported in Figure 4.39 (a), it was possible to notice how the panel  $h$ , at time  $t=3.18$  sec, had a maximum peak equal to 0.79, this means that the seismic (demand was equal to 29% of the capacity offered by the bearing capacity of the wall). In Y direction, however, the wall panel  $i$  has been extensively verified (see Figure 4.39 (b)).

Consequently, as far as both, shear rate and  $N(t)/V(t)$  ratio, the results have been summarized in Figure 4.40.





(c) – masonry panel *i* (Y direction)

(d) – masonry panel *i* (Y direction)

**Figure 4.40:** D/C shear ratio and  $N(t)/V(t)$  ratio for the panels *h* and *i*, respectively.

From the results shown in the previous figure, it was possible to notice how in X direction, the panel *h* had a maximum peak of  $\psi_V$  of 85.45% of its capacity at  $t=3.055$  sec (see Figure 4.40 (a)). Similarly, in Y direction, the panel *i* have presented a maximum peak of 40% at  $t=3.00$  sec, with a decrease D/C shear ratio of 53% compared to the orthogonal direction as depicted in Figure 4.40 (c).

Considering the  $N(t)/V(t)$  ratio, as reported in Figure 4.40 (b), in X direction, it has been noted that at  $t=1.30$  sec the maximum peak was equal to 71% while for  $t=1.68$  sec (maximum peak of vertical acceleration) the ratio  $N(t)/V(t)=63.23\%$ , roughly about 12% lower.

In Y direction, at  $t=1.93$  sec the maximum ratio  $N(t)/V(t)$  was equal to 52.26% (while at  $t=1.68$  sec  $N(t)/V(t)=7\%$ ) and at  $t=3.43$  sec a peak of 96% was reached, denoting a marked preponderance of the axial force regime over the horizontal one (see Figure 4.40 (d)).

So as results of what has been analysed, it appears to be essential to point out as properly investigated:

- i. the Turnsek and Cacovic criteria [189] were used to evaluate the propensity for the occurrence of the shear failure mechanism for the panels examined in the two analysis directions X and Y, respectively. To this purpose, the evaluation of the shear capacity was evaluated using the D/C ratio. In this circumstance, the shear capacity has been normalized concerning the corresponding resistance induced by axial loads in case of gravitational condition;
- ii. in X direction, three masonry panels have been analysed which were located in a corner position (panels *a* and *c*) and intermediate (panel *b*). At  $t=3.18$  sec (time step in which there was the simultaneous action of the horizontal and vertical components), the wall panel *a*, have shown a limit equilibrium condition, which has been characterized by



- $V_{sd}(t)/V_{rd}(t) \approx 1$ , while for the others two panels, *b*, and *c*, this ratio was greater than 1 caused by the variation of the axial stress regime;
- iii. in Y direction, three wall sections were analysed such as panels *a*, *c*, and *f*, respectively. It has been noted that the  $V_{sd}(t)/V_{rd}(t)$  ratios were satisfied for all the panels considered. However, the panels *c* and *f* presented a limit equilibrium condition at  $t=3.18$  sec since the masonry panel *c* had a smaller resistance area and the panel *f* was affected by the torsional phenomena that occurred in the orthogonal direction;
  - iv. similarly, two internal panels have been analysed, *h* and *i*, respectively. For such panels, it was demonstrated that the shear check was satisfied. In particular, the panel *h*, located in X direction, had a maximum shear peak of 0.79, which meant that the panel retained a residual bearing capacity of 29%. In Y direction, panel *i* was largely verified;

The D/C shear stress rate and vertical to horizontal ratio,  $N_i(t)/V_i(t)$  have been analysed in the two analysis directions to take into consideration the influence of VGM and quantitatively estimate the effective capacity of the investigated wall panels. In this circumstance it was possible to deduce:

- i. as reported in Figure 4.34, in X direction, the masonry panel *a* reached a D/C stress rate equal to 80% at  $t=3.18$  sec. This means that the seismic demand reaches 80% of the structural capacity. Similarly, as can be observed, panels *b* and *c* showed a peak of 142% and 143% at  $t=3.18$  sec, denoting an exceeding of seismic demand compared to the structural capacity;
- ii. in Y direction, it was noted that in the first seconds of the time history, the vertical seismic action at  $t=1.68$  sec, the masonry panels *a* and *f*, the maximum D/C shear rate reached was equal to 20%. Moreover, panel *c*, have presented a maximum stress rate equal to 15%. Moreover at  $t > 2$  sec, with the arrival of the ground motion horizontal components, the D/C ratio globally increases from a minimum of 16% to a maximum of 52% (see Figure 4.37);
- iii. considering the internal masonry panels, it has been noted that in X direction, the panel *h* has presented a maximum peak of  $\psi_v$  equal to 85.45% of its capacity. Similarly, in Y direction, panel *i* has presented a maximum peak of 40% at  $t=3.00$  sec, with a decrease D/C shear ratio of 53% compared to the orthogonal direction;

- iv. concerning the  $N(t)/V(t)$  ratio evaluated in X direction (see Figure 4.35), it was noted that for panel *a*, the axial force was equal to 75% at  $t=1.68$  sec, while at  $t>2$  sec, the maximum ratio reached was equal to 80%. Similarly, for the panel *b* when the maximum vertical acceleration was reached, the  $N(t)/V(t)=70\%$ , consequently, when the VGM attenuates the impulsive effect during the time domain, the  $N(t)/V(t)$  was equal to 30%. Panel *c* has provided an  $N(t)/V(t)$  ratio close to 20% at  $t=1.68$  sec.
- v. for the internal masonry panels (panel *h*), it has been observed that in X direction at  $t=1.30$  sec the maximum peak was equal to 71% while at  $t=1.68$  sec (maximum vertical acceleration peak) the ratio  $N(t)/V(t)=63.23\%$ , roughly about 12% lower as reported in Figure 4.40 (b). In Y direction (panel *i*), at  $t=1.68$  sec, the maximum ratio  $N(t)/V(t)$  was equal to 30%. Moreover, at  $t=1.93$  sec the maximum ratio  $N(t)/V(t)$  was equal to 52.26% and at  $t=3.43$  sec a peak of 96% was reached, denoting a marked preponderance of the axial force regime over the horizontal one.

4.3.2.2.3 Rocking shear failure

The resistant mechanism can be described considering the generic masonry panel, subject to a relative translation between the bases due to the seismic shear action ( $V$ ) as reported in Figure 4.41:

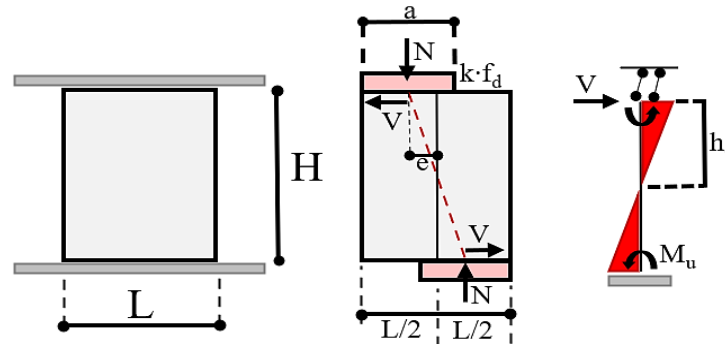


Figure 4.41: Identification of rocking failure induced by shear force,  $V$ .

The rotations at the top and bottom parts of the panel are prevented by the presence of rigid nodes. The panel is characterized by both stresses due to bending moment and shear ( $M$ ;  $V$ ); when the shear ( $V$ ) increases, with the same axial force ( $N$ ), the moment,  $M$ , and, therefore the eccentricity, proportionally increase. This condition involves the partialization of the section, given the non-tensile strength of the masonry. To equilibrate the internal forces, an ideal strut must be formed inside the panel (which identifies only the reacting part of the material) having as end sections those of length  $a$ , coinciding with the portions compressed part.

Therefore, due to the effect of the shear force,  $V$ , a part of the panel will be compressed (having length “ $a$ ”), while the remaining part will be in tension. The resistance of the masonry pier is entrusted only to the compressed part. The compression stresses at the base are schematized through a defined rectangular stress-block behaviour, assuming  $0.85f_d$  as a maximum value ( $f_d$  is the design compressive strength of the masonry) [171].

In such hypotheses, the ultimate moment, and therefore the flexural strength of the panel, can be determined by multiplying the axial force,  $N$ , by the eccentricity at the base of the panel “ $e$ ”, indicating with  $\sigma_0$  the average value of the normal stress, referred to the total area of the section ( $\sigma_0=N/t$ ), as reported in the Equation 4.21.

$$M_{Rd} = \frac{l^2 \cdot t \cdot \sigma_0}{2} \cdot \left( 1 - \frac{\sigma_0}{0.85 \cdot f_d} \right) \quad (4.20)$$

However, the equation just exposed, can be particularized by expressing the moment as a function of the shear force,  $V$ , as reported in Equation 4.21:

$$V_{Rd}^M = \frac{2 \cdot M_{Rd}}{H} = \frac{l^2 \cdot t \cdot \sigma_0}{H} \cdot \left( 1 - \frac{\sigma_0}{0.85 \cdot f_d} \right) \quad (4.21)$$

where  $V_{Rd}^M$  is the shear resistance induced by bending moment,  $M$  and  $H$  is the panel height.

Thus, considering the wall panels oriented in X and Y directions, the seismic verification has been estimated. In particular, the shear stresses induced by the diagonal cracking failure were compared with those of the rocking mechanism to have an overview of which mechanism is triggered first. The results have been showing in Figure 4.42:

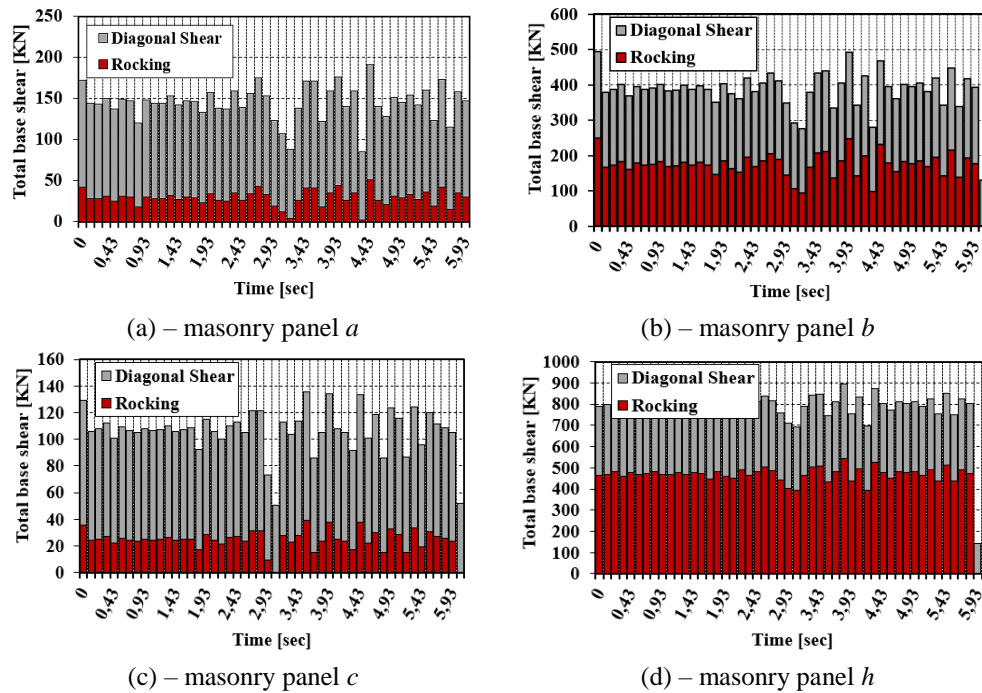


**Figure 4.42:** Diagonal Vs Rocking shear failure mechanisms reached in X-direction.

Similarly, in Y direction only panels *a*, *c*, *f* and *i* have been evaluated, since if in X direction the rocking mechanism was activated earlier, also in Y direction it occurs first concerning the diagonal failure. The results have been plotted in Figure 4.43:

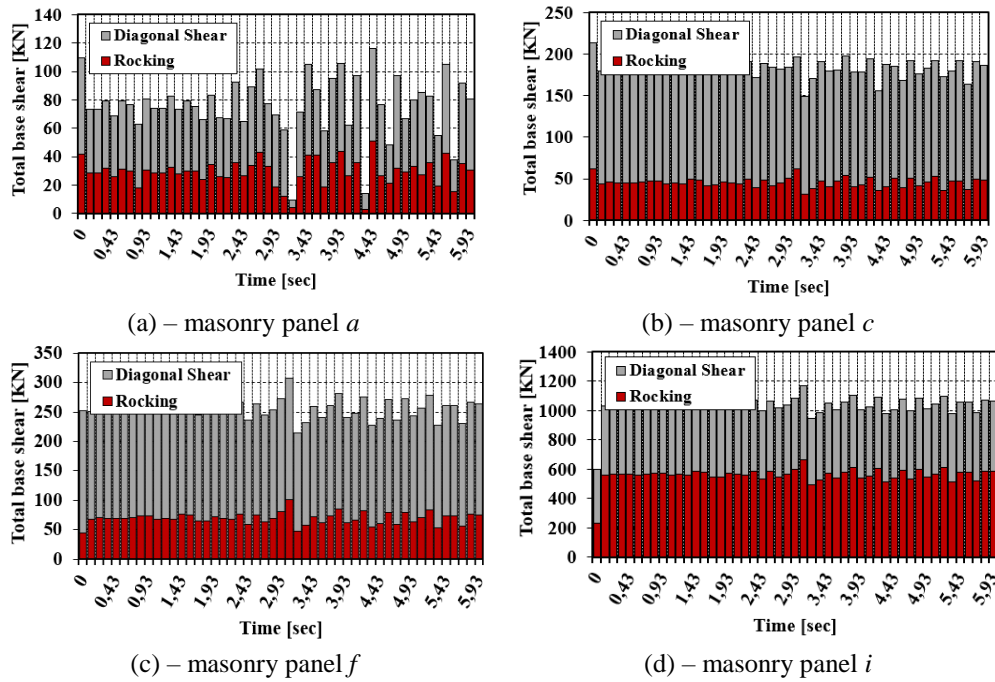


**Figure 4.43:** Diagonal Vs Rocking shear failure mechanisms reached in Y direction.

As can be seen from the results obtained, the mechanism induced by rocking was activated first in both analysis directions, X and Y, respectively. Therefore, this condition satisfies the basic hypotheses set out in paragraph § 4.3.1 and has been reported in Equation 4.16, according to the type of failure mechanism reached by the masonry walls.

As it was possible to notice, the variation of the resistant shear force in the time domain favoured the triggering of the rocking mechanism concerning the corresponding diagonal mechanism. The results have shown that for all the masonry panels, located in the two analysis directions, the precursor mechanism was induced by rocking. From this condition, it seems evident that to achieve a shear failure due to diagonal cracking, very high shear thresholds should occur, on average, equal to two times greater than what has been occurred for rocking failure.

### 4.3.3 Numerical damage identification

Historic masonry structures are built with materials that show significant variations in mechanical properties, very often characterized by a complex geometry. Therefore, the selection of appropriate numerical models for structural analysis is a very delicate phase [176] to obtain refined results both in terms of structural response and expected damage.

The quantification of the deformation capacity of masonry structures requires more attention due to the need for displacement-based concepts for seismic assessment and design purposes. As is well known, during a seismic event, parameters such as ductility and deformability of a structure are essential to describe the inelastic performance of a structural system in the time domain. In particular, ductility is fundamental for the analysis of the structural response since it represents the capability of the structure to suffer plastic deformations with minimal degradation, or without significant loss of strength which could compromise its integrity. In general, masonry is a material that exhibits a fragile behaviour towards tension, which certainly cannot be considered one of the main characteristics of resistance unlike compression, which is very high.

In this context, an approach is presented for the identification of damage deriving from numerical analysis using the *Total Strain Crack Model* (TSCM) according to which it has been possible to identify structural damage through the capacity of the structure to undergo inelastic deformations during the time history cycle. In this perspective, the non-linearities of the material, described in paragraph § 3.7.3.3, have been considered [218]. The constitutive model based on total strain [194] is developed according to Modified Compression Field Theory, originally proposed by [199]. This approach considers the dissipation of the fracture energy in cyclic conditions, according to Equation 4.22:

$${}^{t+\Delta t}_{i+1}\boldsymbol{\varepsilon}_{xyz} = {}^t\boldsymbol{\varepsilon}_{xyz} + {}^{t+\Delta t}_{i+1}\Delta\boldsymbol{\varepsilon}_{xyz} \quad (4.22)$$

where,  $\boldsymbol{\varepsilon}_{xy}$  is the deformation vector at the time  $t$  evaluated in the direction of the crack propagation,  $x$ ,  $y$ ,  $x$  and  $\Delta\boldsymbol{\varepsilon}_{xy}$  represents the deformation increments at each time step [194]. Moreover, the vector  $\boldsymbol{\varepsilon}_{xy}$  is transformed into the strain vector in the crack directions with the strain transformation matrix,  $T$ , as reported in Equation 4.23:

$${}^{t+\Delta t}_{i+1}\boldsymbol{\varepsilon}_{nst} = T + {}^{t+\Delta t}_{i+1}\boldsymbol{\varepsilon}_{xyz} \quad (4.23)$$

Based on these preliminary considerations, the damage of the case study structure is presented. In particular, regarding Figure 4.44, the global damage in the time domain has been reported to identify the most vulnerable structural parts.

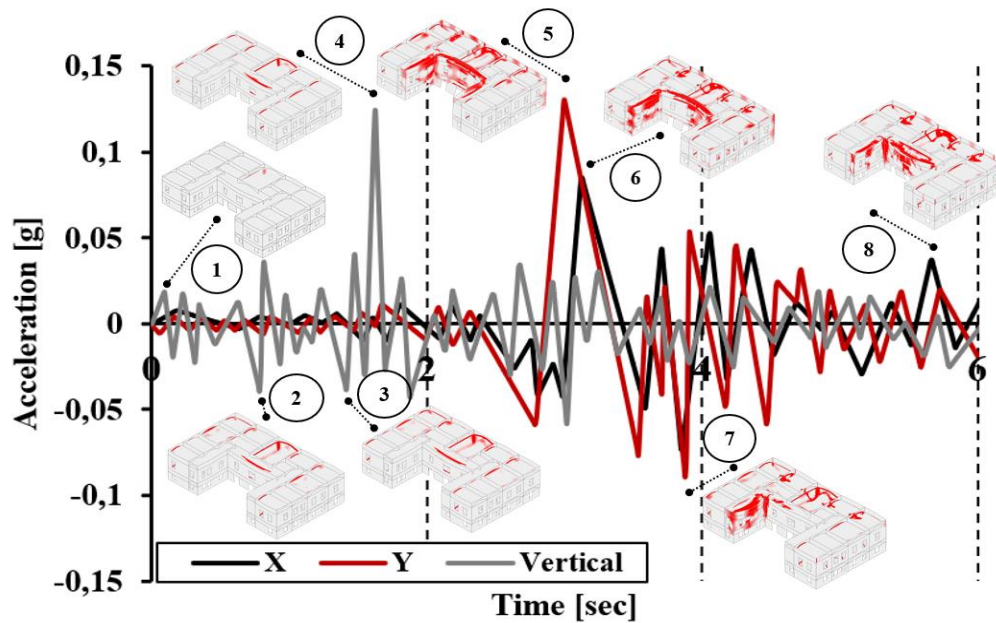


Figure 4.44: Identified structural damage in the time domain.

From the analysis of the previous Figure, it was possible to observe how the damage increases progressively as the time-step increases. Referring to two consecutive time steps, the cracks open and close and reopen so they vary according to the time interval considered, however only the main acceleration peaks of the time domain have been considered.

The results, relating to the time steps considered, were archived in Table 29 concerning the number of open, closed, and active cracks.

Table 29: Number of propagating cracks during the time history.

Step	Time [sec]	PGA [g]	Crack	Open	Closed	Active	Inactive	Arises	Re open	
1	0.10	0.014	V	923	923	0	923	0	313	0
2	0.80	0.040	V	4101	4104	0	302	3802	4	0
3	1.42	0.038	V	4527	4527	0	12	4515	0	0
4	1.68	0.130	V	4927	4927	0	6	4921	0	0
5	3.00	0.120	H+V	20458	20354	104	9520	10938	656	3
6	3.18	0.090	H+V	29000	28897	103	8350	20650	331	0
7	3.88	0.080	H+V	40853	40334	519	2863	37990	17	43
8	5.68	0.034	H+V	57530	57012	518	3135	54935	1	9

From the results acquired, it can be seen how the cracks progressively increase during the time history. In detail, as it was possible to notice, in purely static conditions (t=0.10 sec) the structure shows damage concentrated in the vault located in a central position.



The number of open cracks was estimated equal to 923 for a  $PGA_V$  equal to 0.018g. Due to the vertical earthquake, the maximum failure condition is reached at  $t=1.68$  sec, which corresponds to a  $PGA_V=0.13g$ .

The vertical earthquake caused a damage increase in the vaults which, being structures with high flexural deformability, were the first to suffer damage.

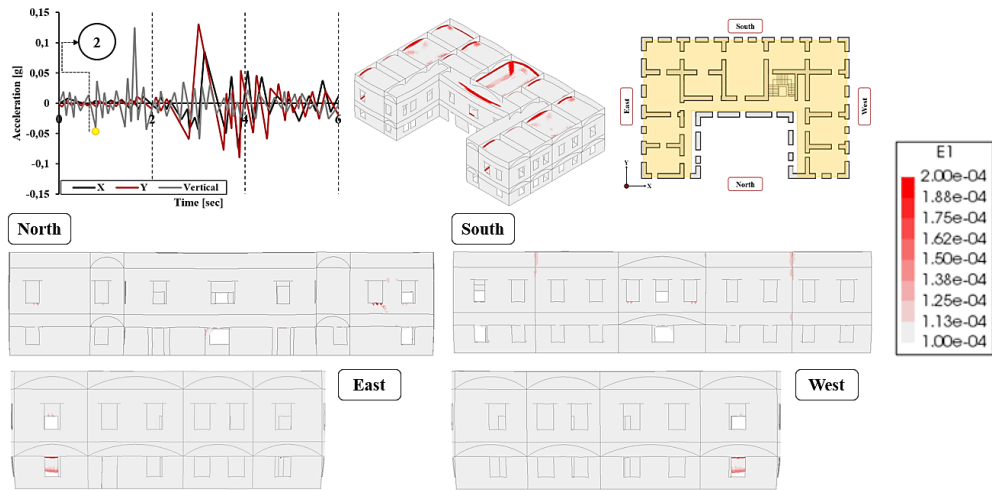
In this circumstance, the cracks have been developed by exceeding the material tensile strength (tensile fracture energy).

Subsequently, with the simultaneous action of the horizontal and vertical components of the ground motion, it was noted how the damage significantly increases. In particular, at  $t=3.00$  sec (maximum peak of horizontal acceleration in Y direction), the damage was extended to the vertical structures. The concomitance of the vertical and horizontal seismic actions caused a double effect in the structure in terms of expected damage. In particular, the horizontal components were responsible for induced shear failures mainly concentrated in the masonry walls, which, as analysed in the previous paragraph, activates the rocking mechanism, while the vertical seismic action, due to the high-frequency content, induced vertical cracks. This asynchrony of the ground motion vertical component produces damage to the structure that has followed the sinusoidal displacement profile of the ground. In this circumstance, it was evident that the vertical cracks that could occur were more concentrated especially in the spandrel beams which were part of the structural systems characterized by poor load transfer capacity.

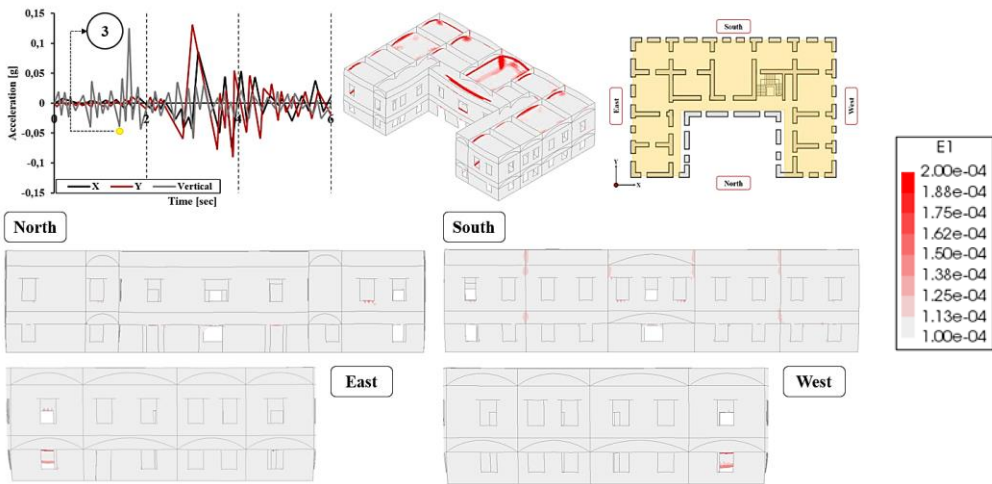
To this purpose, it was easy to prove how the number of open cracks was 20458 in which 9520 were actively considering a maximum  $PGA^Y_H=0.13g$  in Y direction (with both, horizontal ( $PGA^X_H$ ) and vertical ( $PGA_V$ ), PGAs equal to 0.06g, respectively).

Finally, during the time history, the structure, degrading its stiffness, was more vulnerable and at  $t=5.68$  sec in which the number of open cracks was 57530, ie +64% compared to those obtained at 3 seconds.

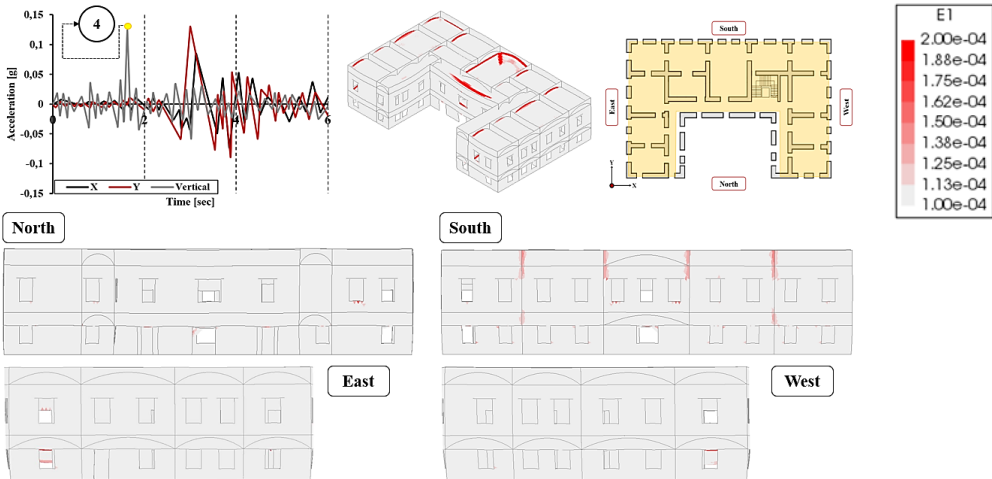
To give indications about the extent of the damage that occurred in each façade of the building and for each time step considered (except for purely static position 1), the damage analysis has been reported in Figure 4.45.



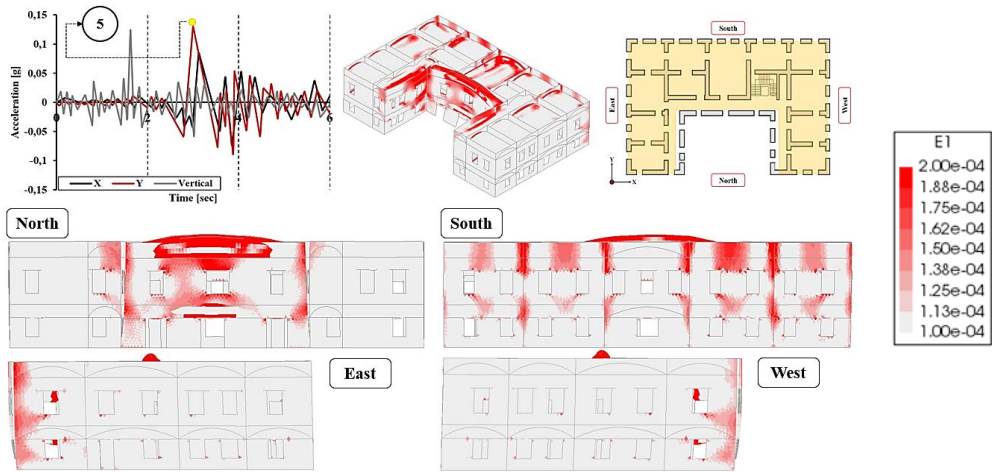
(a) – time step  $t=0.80$  sec,  $PGA_V=0.040g$ ,  $PGA_H=0$



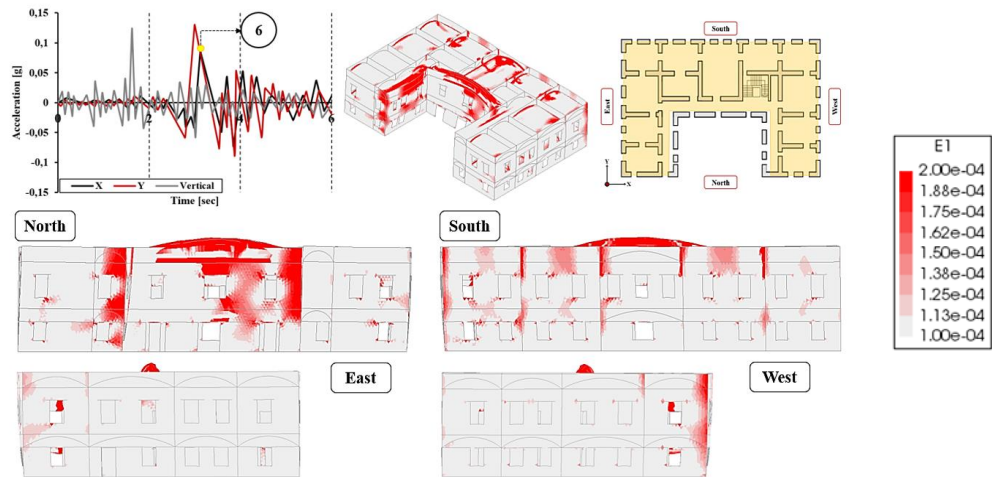
(b) – time step  $t=1.42$  sec,  $PGA_V=0.038g$ ,  $PGA_H=0$



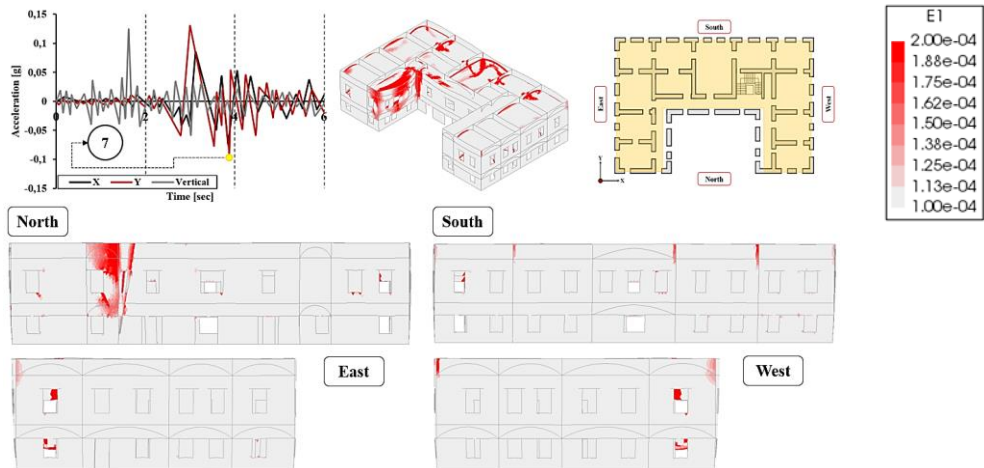
(c) – time step  $t=1.68$  sec,  $PGA_V=0.13g$ ,  $PGA_H=0$



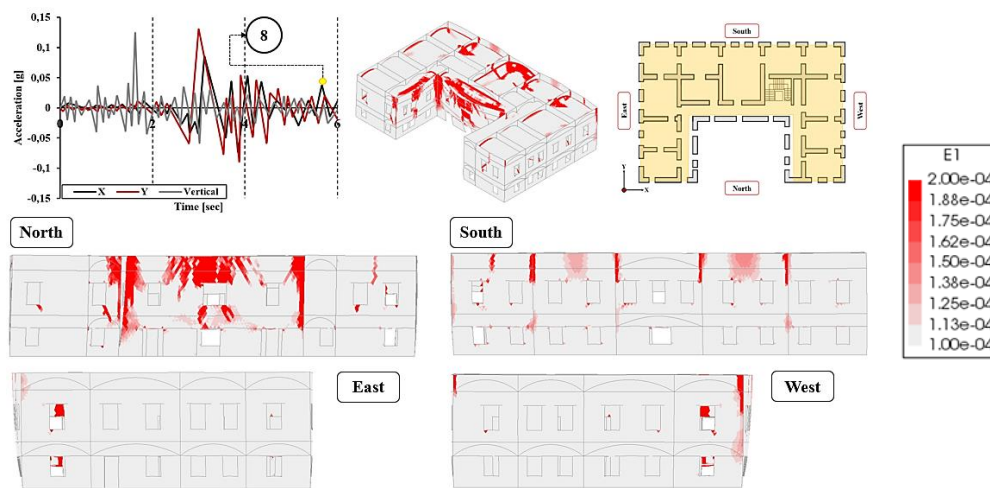
(d) – time step  $t=3.00$  sec,  $PGA^X_H=0.03g$ ,  $PGA^Y_H=0.13g$ ,  $PGA^V=0.06g$



(e) – time step  $t=3.18$  sec,  $PGA^X_H=0.09g$ ,  $PGA^Y_H=0.093g$ ,  $PGA^V=0.009g$



(f) – time step  $t=3.88$  sec,  $PGA^X_H=0.04g$ ,  $PGA^Y_H=0.09g$ ,  $PGA^V=0.011g$



(g) – time step  $t=5.68$  sec,  $PGA^X_H=0.034g$ ,  $PGA^Y_H=0.02g$ ,  $PGA_V=0$

**Figure 4.45:** Numerical damage assessment at each time steps considered.

The numerical damage obtained has been conformed to what was predicted regarding the global and local behaviour of the case study building. In particular, it was possible to note that two main conditions exist: (i) in the first step of the time history only the vertical seismic action has been activated; (ii) in the second step, the concomitance of vertical and horizontal seismic actions have occurred. This circumstance has shown that in the case of vertical seismic action only (in the first two seconds of the time domain), the structure has vertical shear cracks which were distributed at the contact surfaces between the wall panels and spandrel beams in the South façade.

This vertical shear mechanism was caused by a relative sliding shear due to the asynchronous vertical displacement generated by the ground motion vertical component in case of impulsive near-field phenomenon. This damage condition tends to increase up to  $t=1.68$  sec, according to which the  $PGA_V$  was maximized and equal to  $0.13g$ . Furthermore, the damage was concentrated in the masonry vaults especially in the centre of the horizontal element (surface area of maximum deformation) and close to the vault supports between the masonry vault and wall panels (see Figure 4.45(a) and (b)).

Consequently, with the arrival of the horizontal components, the damage was increased. As can be seen from Figures 4.45(e)-(g), a condition of widespread damage has occurred in all the structural elements. In particular, it was noted that the North façade (left side view) was more influenced by both, rocking and out-of-plane mechanisms, thus determining a significant damage condition.

More precisely, the mechanism that existed in the North façade was developed by the rocking mechanism which triggers, in correspondence with the façades, the internal courtyard of the building, out-of-plane mechanisms.

In some circumstances, the damage occurred since the cohesive internal force between mortar and brick was exceeded, and consequently, horizontal and vertical sliding surface fractures were created which facilitated the mechanism itself. In certain conditions, the vertical component of ground motion, concomitant with the horizontal actions, favoured the relative vertical displacement between the orthogonal portions of the wall, facilitating the mechanism formed.

Many damages highlighted in the past earthquakes (for example L'Aquila earthquake) have shown vertical cracks developed near the connections between orthogonal walls, as reported in Figure 4.46 [31], [219].

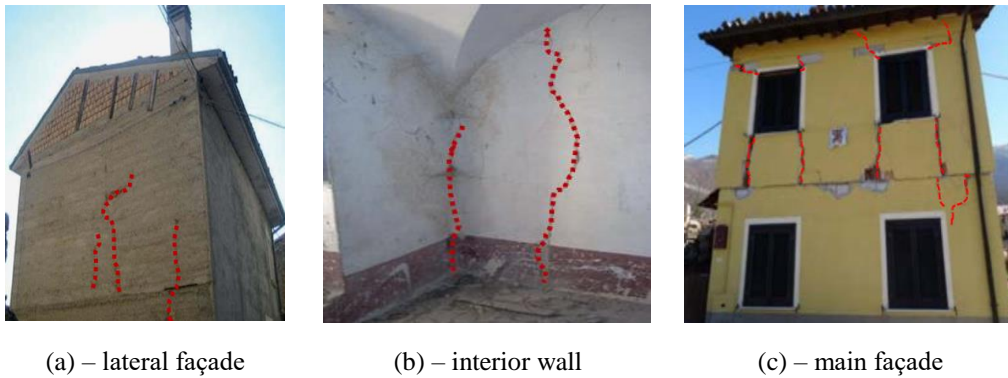


**Figure 4.46:** Vertical shear cracks generated by ground motion vertical component detected after the L'Aquila earthquake [31].

The resultant of the attractive forces that could develop along the height between orthogonal walls (vertical or pseudo vertical cracks, assuming almost uniform constraint characteristics) can be approximated following Equation 4.24 as proposed by [40]:

$$F = 0.4 \cdot n \cdot (n+1) \cdot \phi \cdot \mu \cdot l^2 \cdot t_s \cdot w \quad (4.24)$$

having assumed,  $n$  is the number of masonry rows affected by the vertical cracks ( $n=(h/h_b)$  where  $h_b$  is the average height of the masonry elements);  $l$  is the length of the single mortar frictional joint;  $\phi$  is the masonry mesh coefficient depending on the height,  $a$ , and length,  $b$ , of the bricks involved ( $\phi =a/b$ );  $\mu$  is the friction coefficient which, in the absence of experimental tests, can be



assumed to be 0.4;  $t_s$  is the thickness of the transverse wall and  $w$  is the weight of the masonry. When the force  $F$  exceeds the tensile strength of the material, the damage, characterized by the presence of vertical shear cracks, was propagated.

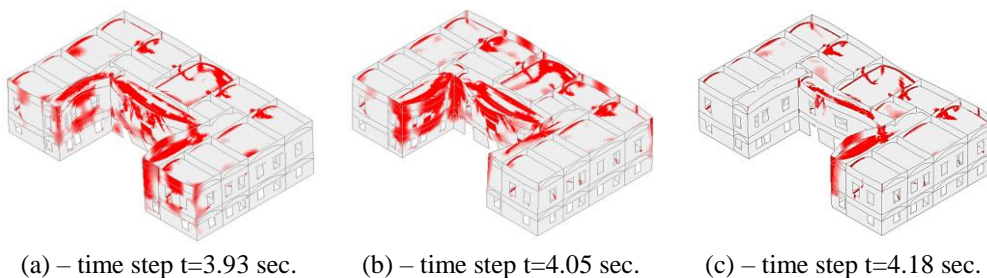
Consequently, the damage that was obtained in correspondence to the wall panel located in the corner of the building (North façade), was attributed to the overcoming of the attractive force that could develop along with the height,  $H$ , between the panel considered and the orthogonal ones, developing a vertical crack (or pseudo vertical fracture). Furthermore, it is worth underlining how the structure in X direction presented a non-symmetrical behaviour, presenting torsional deformability, therefore the damage was markedly evident.

The South façade, on the other hand, presented the evident effects of the concomitance of the seismic actions, horizontal and vertical, respectively. It was possible to observe how the vertical component of the seismic action produced vertical cracks at the wall-spandrel interface, while the diagonal shear failure (identified the spandrel beams) was attributed to the horizontal seismic action. Even in these circumstances, it is worth highlighting how the basic hypothesis assumed for the model adopted in the case of local analysis, fully reflects the damage that occurred through numerical simulation since the spandrel beams were unable to transfer the loads to the wall panels, getting damaged.

As for the East and West façades, respectively, oriented in Y direction (geometric symmetry) they were affected by the rocking mechanism without showing any significant damage. Moreover, the damage that occurred in the external masonry walls was attributed to the possible out-of-plane mechanism developed in the orthogonal walls.

From the foregoing, it can be understood how the damage to the structure, seen in its global point of view, is given by the concomitance of vertical and horizontal seismic actions, and, on the other hand, by the combination of both effects which are in-plane and out-of-plane mechanisms, respectively.

Finally, in Figure 4.46, other damage simulations for time steps greater than  $t=3.18$  sec are shown, to provide a complete overview of what has been achieved monitoring the North façade, more damaged.



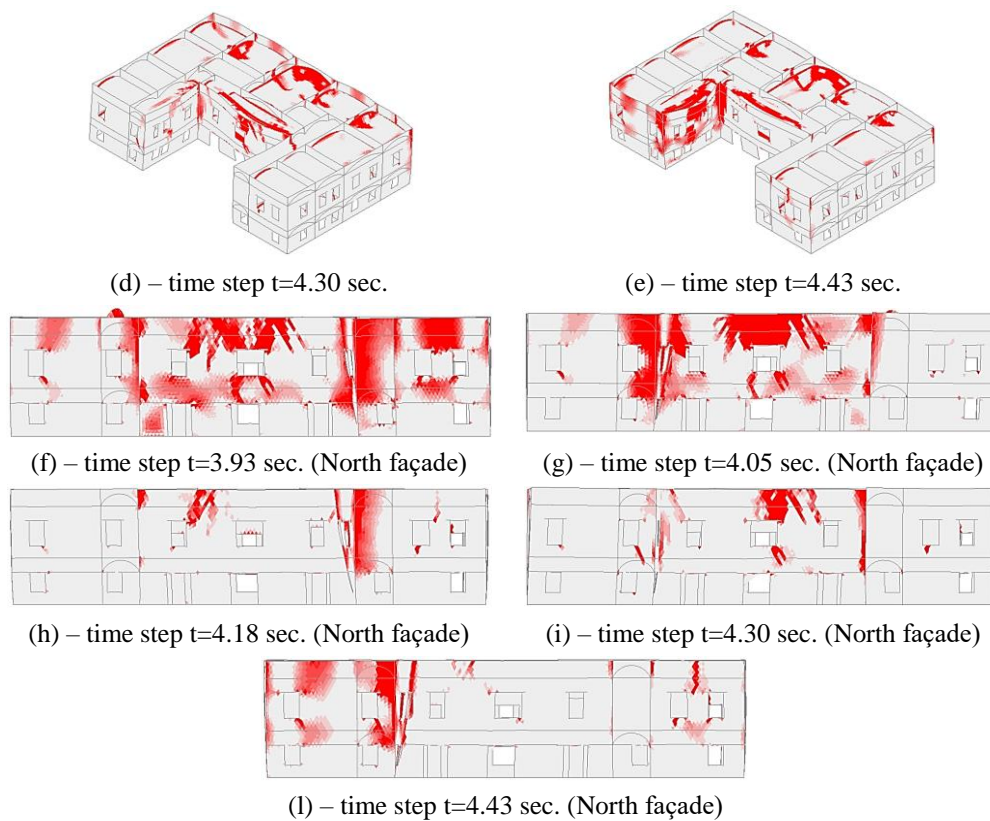


**Figure 4.47:** Damage identification for  $t > 3.18$  sec, (a)-(e) global overview, (f)-(l) North façade.

#### 4.3.4 Strength domain and failure hierarchy

The strength domains are a useful tool to validate the possible failure mechanisms that could occur in a wall system when subjected to seismic action.

As a result of these seismic actions, it is possible to use the flexural and shear resistance domains to define the strength capacity of each masonry wall. As seen in the previous paragraphs §4.3.1, the walls have been typologically classified as first-class according to which there is no kinematic congruence between the masonry walls, therefore each wall panel has been subject to specific deformation components due to the associated displacements. The main aspect is that in the case of the first-class wall there is no kinematic compatibility between the masonry walls and the resistance to horizontal and vertical seismic actions depends only on the domains. The latter is sufficient to define the strength of the wall systems.

In particular, the strength domains are characterized by specific rupture boundaries that identify the main failure mechanisms.



Moreover, there are different failure thresholds to consider: (i) non-cracked elastic condition; (ii) cracked elastic condition; (iii) plastic condition due to bending and the interaction with the failure mechanisms induced by shear. The damage condition occurs when the generic point crosses the boundary condition. Operationally, for a given wall panel, once a normal stress level in seismic condition (H+V) has been fixed,  $N_{i(H+V)}$ , it is possible to define the maximum shear threshold, that the panel can tolerate, employing the domain boundaries.

So, as analysed in paragraph § 4.3.2.2, the verification formulas adopted are functions of the compression stress,  $\sigma_0$ , and therefore intrinsically depends on the axial force,  $N_i$ . For this purpose, their representation of the strength domain is in the dimensionless plane  $\bar{V} - \bar{N}$  as suggested in [176]. From these considerations, the resistance domains associated with each failure mechanism will be dimensionless, according to [220], as a function of the ultimate axial force ( $N_u$ ) as indicated in the following Equations.

$$\bar{N} = \frac{N}{N_u} \quad (4.25)$$

$$\bar{V} = \frac{V}{N_u} \quad (4.26)$$

According to [171], different stress state thresholds are identified:

- i. *linear elastic state with fully reacting section*: the normal stresses affect the entire section and have a linear distribution, with maximum ordinate lower (or equal) than (to) the material compressive stress ( $\sigma_k < \sigma_{\max}$  or  $\sigma_k = \sigma_{\max}$ ). The material remains in the linear elastic range and the cracking phase, associated with the panel, is reversible (Figure 4.48(a)-(b));
- ii. *elastic limit state with partially reacting section*: the normal stresses affect only a part of the section but have a linear distribution, with maximum ordinate equal to the maximum compressive stress  $\sigma_k = \sigma_{\max}$  and minimum ordinate zero; in this case, cracking occurs in correspondence to the tensile fibres of the section. The reacting part of the material is still in the linear elastic range, so, the panel can suffer new stresses, of the same or opposite sign, but the stress-strain behaviour of the entire section is not proportional (Figure 4.48(c));
- iii. *elasto-plastic state with partially reacting section*: one part of the section is completely plasticized, with a constant maximum stress value equal to

$\sigma_k = \sigma_{max}$  while the other reacting part remains in a linear elastic range, with an even maximum ordinate  $\sigma_k$ ; In the area where tensile stresses are reached, the section is cracked and the deformations are irreversible (Figure 4.48(d));

- iv. *plastic limit state with partially reactive section*: the normal stresses affect only a part of the section and all of them are constant values and equal to  $\sigma_k = \sigma_{max}$ . In this case, a part of the section is completely plasticized, while the remaining part is only cracked, the maximum normal stress tolerated is  $N_u = \sigma_k \cdot b \cdot s$  and the panels are unable to suffer new stress states, whether of the same or opposite sign (Figure 4.48(e));
- v. *plastic limit state with fully reacting section*: normal stresses affect the entire section with a constant value equal to the ultimate compression stress  $\sigma_k = \sigma_{max}$ . In this case, the normal stress assumes the maximum value that can be tolerated by the section,  $N_u = \sigma_k \cdot b \cdot s$  (having plasticized all the fibers) and the panel is close to the collapse, no longer retaining its bearing capacity (Figure 4.48(f)).

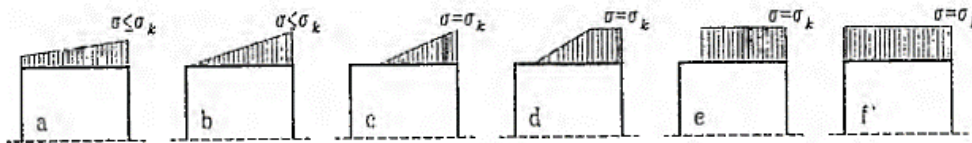


Figure 4.48: Evolution of the compressive stress state thresholds [171].

Therefore, to evaluate the maximum shear force that the panel can support in the case of flexural bending moment, it is necessary to define the range in which the non-dimensional axial force can vary. In particular, referring to the theory proposed by [171], [220], it was possible to define the equations that describe the boundaries of the iteration domains ( $\bar{V} - \bar{N}$ ) in the elastic and plastic limit states, as reported in the following Equations:

$$\bar{V}_{el} = \frac{1}{3} \cdot \frac{B}{H} \cdot \bar{N} \quad \begin{array}{l} \text{Linear elastic state, fully reagent section} \\ \text{(cracking condition)} \end{array} \quad (4.27)$$

$$\bar{V}_l = \frac{1}{3} \cdot \frac{B}{H} \cdot [1 - \bar{N}] \quad \begin{array}{l} \text{Linear elastic state, partialized section} \\ \text{(non-proportional condition)} \end{array} \quad (4.28)$$

$$\bar{V}_p = \frac{B}{H} \cdot [\bar{N} - \bar{N}^2] \quad \text{Plastic state (ultimate condition)} \quad (4.29)$$

Similarly, considering the shear mechanisms (diagonal and sliding shear) it is possible to define in the  $(\bar{V} - \bar{N})$  plane the frontier of a semi-defined domain [171], [220], according to the Equation presented:

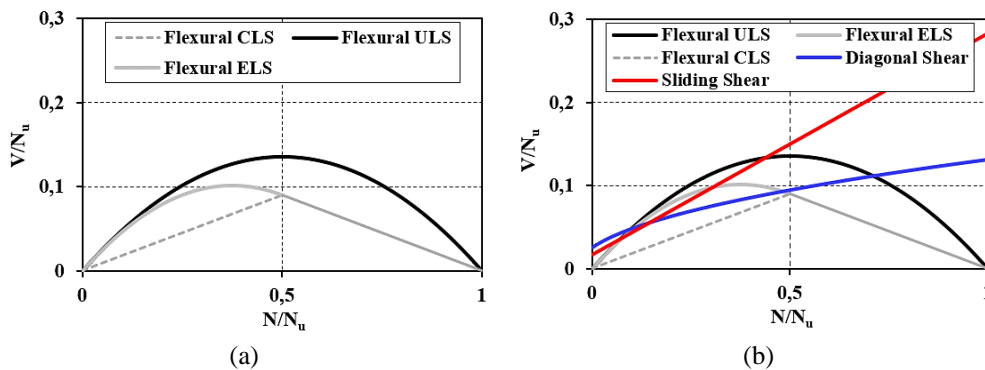
$$\bar{V}_t = \beta \cdot \sqrt{1 + \frac{\bar{N}}{p \cdot \beta}} \quad \text{Diagonal shear} \quad (4.30)$$

$$\bar{V}_s = \frac{1}{p} \cdot [\gamma + \mu_a \cdot \bar{N}] \quad \text{Sliding shear} \quad (4.31)$$

where  $\beta$  represents the ratio between the average shear stress,  $\tau_k$  and the corresponding average normal compressive stress,  $\sigma_k$ ;  $p$  is the shape coefficient relating to the distribution of tangential stresses in the masonry section, assumed to be 1.5 (see paragraph § 4.3.2.2.2) and  $\mu_a$  is a friction coefficient assumed equal to 0.4 according to [171], [189].

Consequently, the points of coordinates  $(N, V)$  belonging to the boundaries of the domain, are the points for which the panel is verified, vice versa, the points that are outside the domain are those for which the crisis is maintained. The points belonging to the border of the domain are those for which the integrity of the masonry is not necessarily equilibrated.

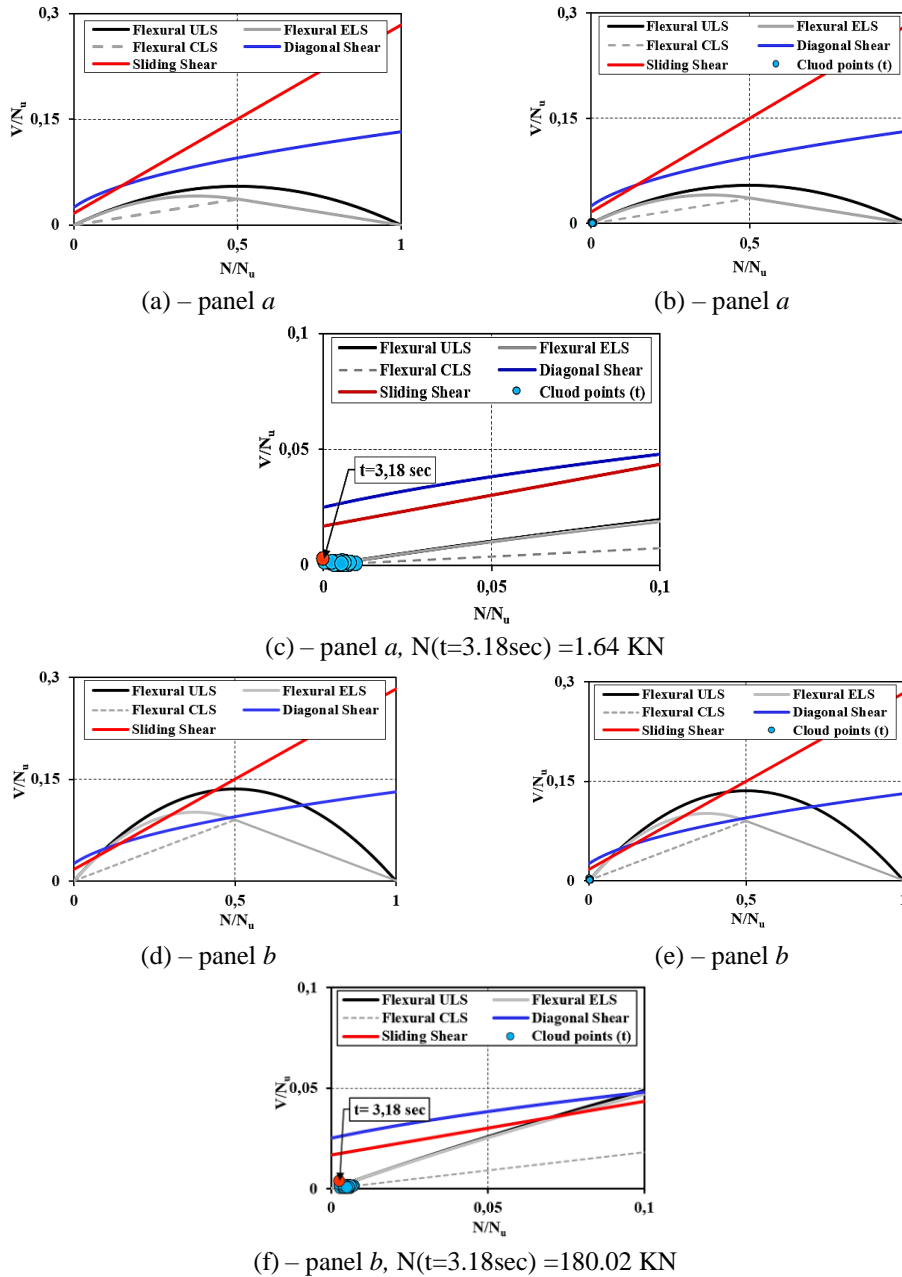
An example of a strength domain has been shown in Figure 4.49 considering both, flexural and shear limit conditions:



**Figure 4.49:** Strength domain in case of (a) flexural conditions and (b) flexural and shear conditions.

where flexural CLS, ELS, and ULS represent *cracking limit state* (linear elastic state), *elastic limit state* (post-elastic condition, partialized section), *ultimate limit state* (plastic condition), respectively.

Therefore, extending what has just been explained to the analysed case study building, the resistance domains for the wall panels in X and Y direction are presented. In particular, the strength domains for panels *a*, *b*, *c*, and *h*, in X direction, were analysed, as shown in Figure 4.50.



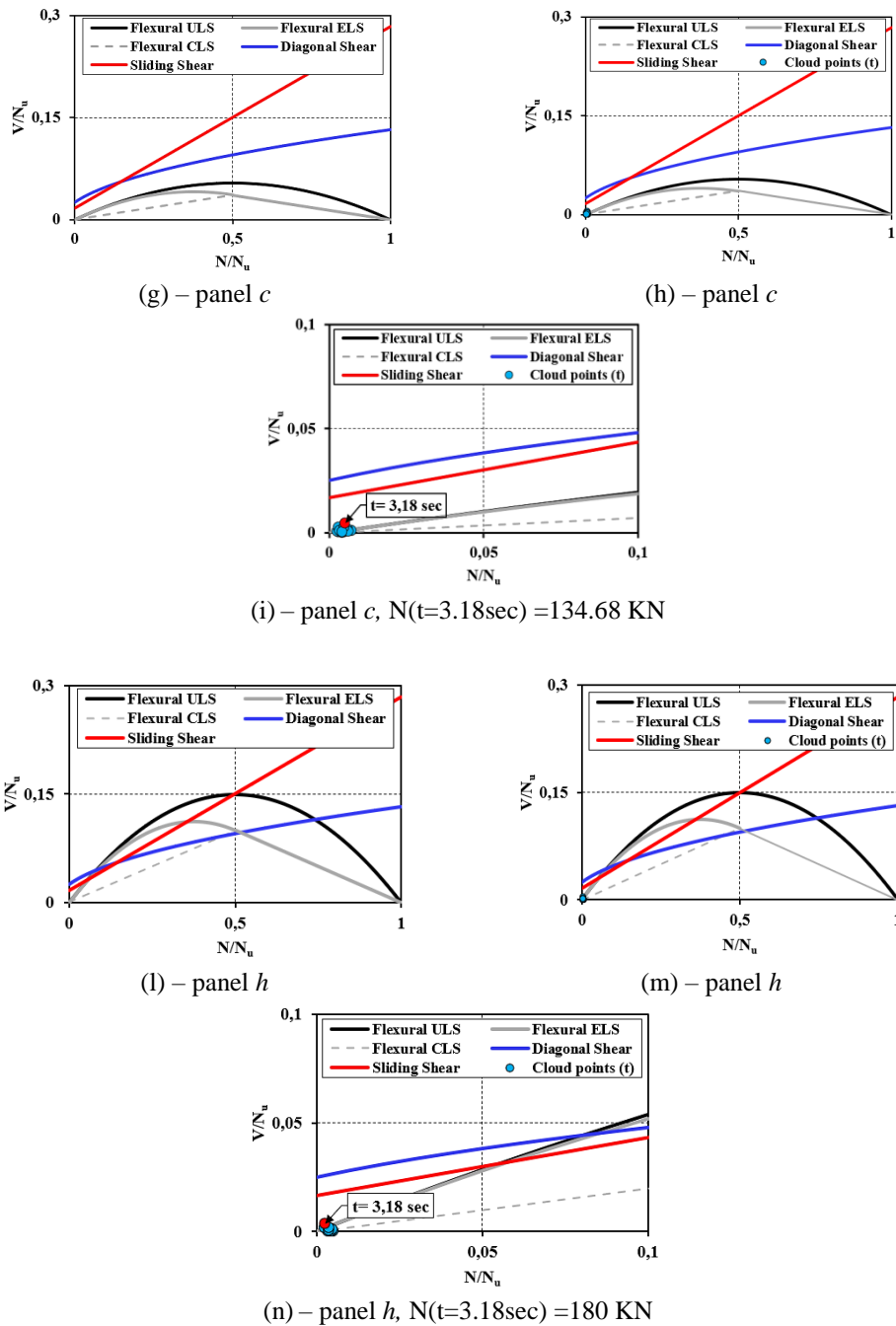


**Figure 4.50:** Resistance domains for the selected masonry panels oriented in X-direction.

From the results acquired, it was noted how the amplitude of the domain changes as a function of the geometry of the panel, in fact, panels with a greater resistant area, presented a more elongated domain (panels *b* and *h*) than the other panels *a* and *c*, respectively, for which the strength domain was more flattened.

Moreover, the previous Figures showed the analytical construction of the resistance domains (Figures 4.50 (a), (d), (g), (l)), the corresponding variation of the axial force for each time step (Figures 4.50 (b), (e), (h), (m)) and finally an enlargement of the maximum axial stress threshold for a specific time step (Figures 4.50 (c), (f), (i), (n)).

Focusing on this last aspect, it was noted that for all the selected panels, at the time step  $t=3.18$  sec, the ELS condition has been exceeded (reversible elastic conditions, post-cracking phase). At this time step, the wall sections were in a condition of linear distribution of the compressive stresses that reached the maximum compressive strength ( $\sigma_k=\sigma_{max}$ ). In this circumstance, the sections were cracked in correspondence to the tensile areas and, although retaining the load-bearing capacity, the panels exhibited a non-proportional stress-strain behaviour. Furthermore, the axial and shear forces thresholds that were reached at  $t=3.18$  sec, have been shown in Figure 4.51

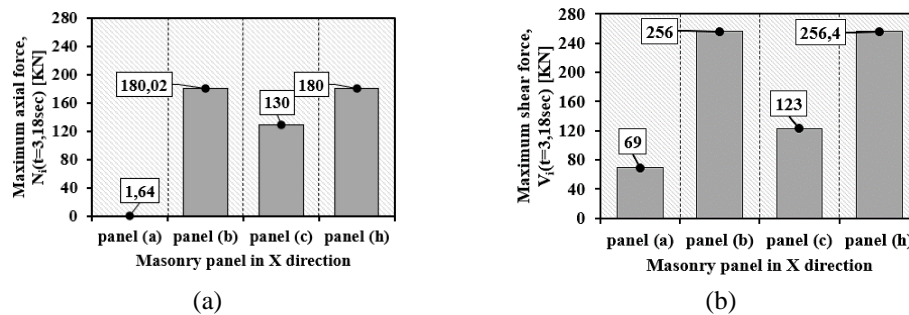
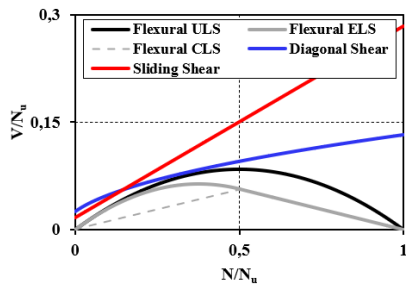


**Figure 4.51:** Maximum axial (a) and shear force (b) levels reached  $t=3.18$  sec associated with the rocking failure mechanisms.

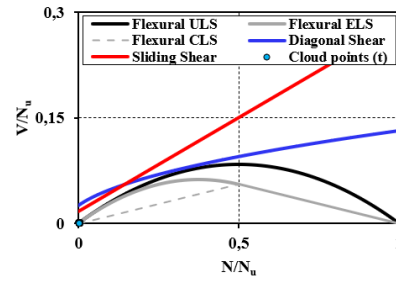
As shown in paragraph § 4.3.3, the damage that occurred for the panels analysed corresponds perfectly to what has been proposed. Panel *a*, although characterized by a rocking mechanism, did not reach a significant level of damage, unlike panel *c* which was influenced by the out-of-plane mechanism of the wall orthogonal to it. Finally, panel *b*, located in a central position, had induced cracks intermediate to the other external panels as it had a greater resistant area.

However, it should be noted that to reach a shear crisis (sliding or diagonal), once an axial force value has been set, the shear force should increase until it reaches a value of  $V/N_u$  equal to 0.016 (sliding) and 0.028 (diagonal), respectively.

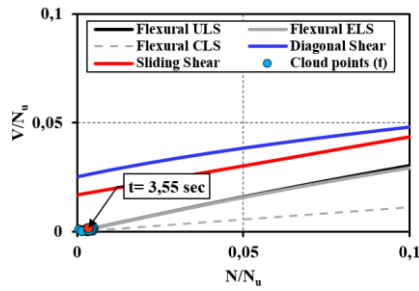
Similarly, in Y direction, the interaction domains for the panels, *a*, *f*, and *i*, were analysed and proposed in Figure 4.52.



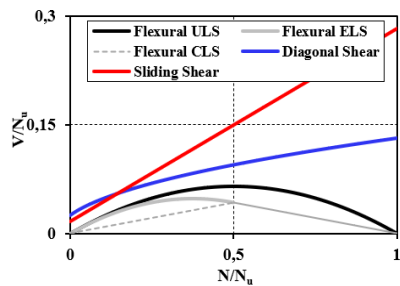
(a) – panel *a*



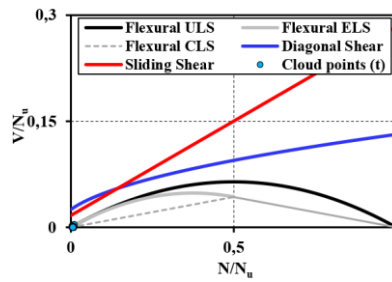
(b) – panel *a*



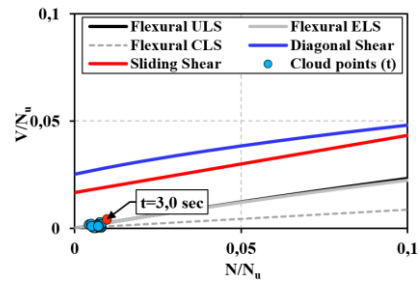
(c) – panel *a*,  $N(t=3.55 \text{ sec}) = 139.54 \text{ KN}$



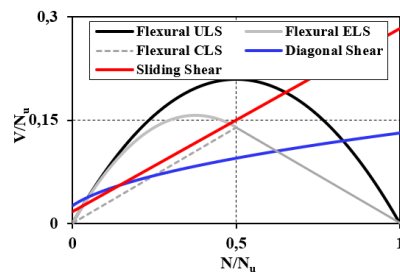
(d) – panel *f*



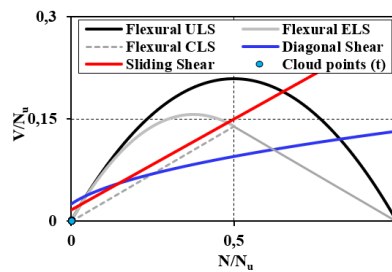
(e) – panel *f*



(f) – panel *f*,  $N(t=3.00 \text{ sec}) = 301 \text{ KN}$

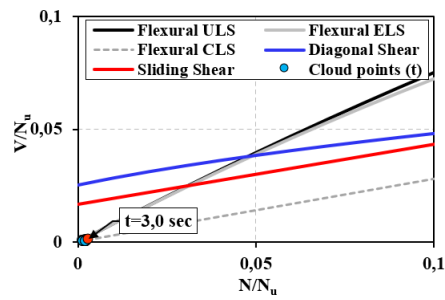


(g) – panel *i*



(h) – panel *i*



(i) – panel  $i$ ,  $N(t=3.00\text{sec}) = 300 \text{ KN}$ **Figure 4.52:** Resistance domains for the selected masonry panels oriented in Y direction.

The panels oriented in Y direction have presented an axial force threshold greater than those oriented in the orthogonal direction due to the structural asymmetry. Consequently, it was noted that the prevalent failure mechanism was rocking ELS for all the panels analysed. As a result, although widely demonstrated for masonry piers in X direction, shear failure (sliding or diagonal) could occur only for high shear values.

By adopting the resistance domains, it was possible to demonstrate how there is any inconsistency between the method proposed by [189] and what has been obtained by using the interaction domains. As anticipated in paragraph § 4.3.2.2.2, the method proposed by [189] tends to overestimate the effective deformation capacity of the masonry panel since for values of axial force equal to zero, the corresponding shear force,  $V$ , was different from zero, giving the panel a residual deformation.

From this consideration, it follows that the criterion proposed in paragraph § 4.3.2.2.2, was a resistance criterion but not a verification criterion, guaranteeing the integrity of the panel but not its equilibrium.

Besides, as analysed, it was noted that the rocking mechanism was activated for  $t > 2.0 \text{ sec}$ , i.e. when the concomitance of the vertical and horizontal seismic actions occurred. This aspect is very significant since, being an impulsive seismic phenomenon, the vertical seismic action, in the first two seconds of the time history, did not affect the tensile strength of the wall panels, so the panel was never decompressed. However, at  $t > 2.00 \text{ sec}$ , the high-frequency content of the vertical seismic action, affected the activation of the mechanism as it locally reduced the compression stress favouring the formation and development of cracks.

Therefore, summarizing what has been analysed previously, it was possible to deduce the following points:

- i. the strength domains have allowed investigating the behaviour of the masonry wall panels taking into account the different expected performance levels such as flexural (CLS, ELS, ULS), shear (sliding or diagonal) associated with the main failure mechanisms;
- ii. the panels analysed showed different behaviour in the two main directions. In X-direction, the axial stress thresholds activated have been lower than those obtained in the orthogonal direction, Y, given the condition of geometric symmetry;
- iii. the panels oriented in X direction showed an axial action peak for  $t > 2.0$  sec, highlighting a condition of rupture induced by rocking, mainly at the elastic limit state according to which, the compressive stress of the material was equal to the maximum expected one. The mechanism has shown reversibility of the cracking that occurred. However, the stress-strain law was non-proportional;
- iv. in X direction the sliding and diagonal shear mechanisms were activated for values of the dimensionless cutting thresholds ( $V/N_u$ ) greater than what has been achieved with values equal to 0.016 and 0.028 respectively;
- v. the panels oriented in Y direction showed a behaviour similar to those in X direction, first activating the ELS rocking mechanism at  $t > 2.0$  sec;
- vi. the method proposed by [189] tends to overestimate the effective deformation capacity of the masonry panel since for values of axial force equal to zero, guaranteed a residual bearing-capacity to the masonry panel;
- vii. in general, it was noted that the rocking mechanism was activated at  $t > 2.0$  sec, precisely at  $3.18 \text{ sec} < t < 3.55 \text{ sec}$ , that was when the concomitance of vertical and horizontal seismic actions occurred. This relevant aspect allowed us to understand how the vertical seismic action, in the first 2 seconds of the time history, did not generate any decompression in the wall panels instead at  $t > 2.0$  sec, the high-frequency content of the vertical seismic action influenced the activation of the mechanism since it locally reduced the compression strength favouring the formation of cracks.

## 4.3.4.1.1 Failure hierarchies

The proposed methodology aims to define a failure hierarchy for a generic wall panel. Therefore, for a given value of axial force,  $N_i$ , the corresponding expected shear thresholds are determined to identify the possible in-plane mechanisms that could be activated. This procedure allows estimating the maximum shear force tolerable by each masonry panel in seismic conditions (H+V) through the characteristic curves of the single walls. These characteristic curves allow us to characterize the relationship that exists between the shear action,  $V_i$ , and the displacement component, ( $\delta$ ) that generates the mechanism ensuring kinematic congruence.

According to [171] the displacement,  $\delta$ , of a generic wall panel is a function of the shear ( $\delta_V$ ) and flexural ( $\delta_M$ ) contribution as defined in Equation 4.32:

$$\delta = \delta_V + \delta_M = \chi \cdot \frac{V \cdot H}{G \cdot A} + \frac{V \cdot H^3}{12 \cdot E \cdot I} \quad \text{elastic displacement (CLS)} \quad (4.32)$$

where shear coefficient,  $\chi$ , is equal to 1.2,  $V$  is the shear threshold reached specific limit state, according to the strength domain,  $H$  is the panel height,  $G=0.4 \cdot E$  is the shear modulus,  $E$  elastic modulus of the masonry and  $I$  is the inertia of the section.

Furthermore, to have a clear and effective representation of the characteristic curves, according to [171], it is possible to define the displacement thresholds at the cracking limit state (post-elastic phase) and the ultimate limit state as reported in the following Equations 4.33 and 4.34:

$$\delta_f = 1.2 \cdot \delta \quad \text{post-elastic displacement (ELS)} \quad (4.33)$$

$$\delta_u = 1.5 \cdot \delta \quad \text{ultimate displacement (ULS)} \quad (4.34)$$

Operationally, the procedure that leads to the definition of the characteristic curves and therefore to the failure hierarchy is as follows: (i) having defined the strength domain for a generic panel, the average axial force deriving from the cloud points  $N_i(t)$  is considered; (ii) for this axial force average value, all the frontiers of the resistance domain are intercepted; (iii) at each intersection with the strength domain correspond values of the shear thresholds identifying the maximum shear capacity of the panel. It is important to underline how the V-N relations define the boundaries of the domain for which it is possible to obtain

the shear level,  $V$ , for an assigned  $N$ , guaranteeing an equilibrium limit state condition.

Therefore, based on these considerations, the characteristic curves (or capacity curves) for the masonry panels in  $X$  and  $Y$  direction have been determined. Thus, Figure 4.53 have been presented the characteristic curves concerning panels  $a$ ,  $b$ ,  $c$  in direction  $X$ .

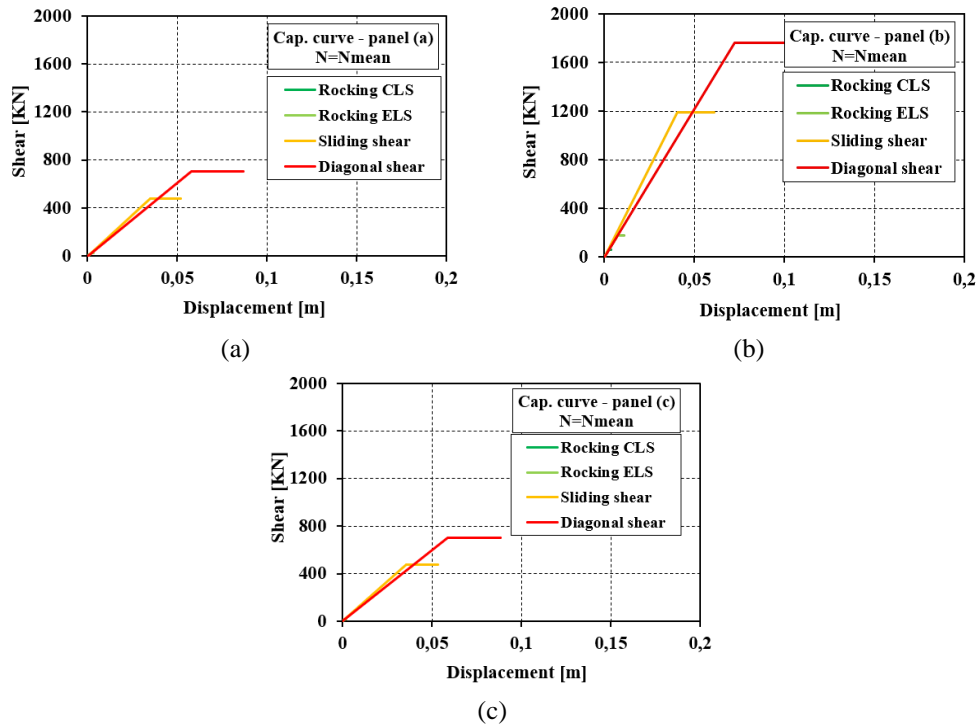


**Figure 4.53:** Characteristic curves for panels  $a$ ,  $b$ ,  $c$  in  $X$ -direction.

It should be pointed out that in the previous figure, for the three panels, the characteristic curves corresponding to the limit states CLS and ELS have been graphed even though they have an order of magnitude lower than the other curves. Subsequently, it was possible to compare the capacity, deduced from the characteristic curves, with the seismic demand evaluated for each wall panel considering the scenario event (H+V), as shown in Figure 4.54:

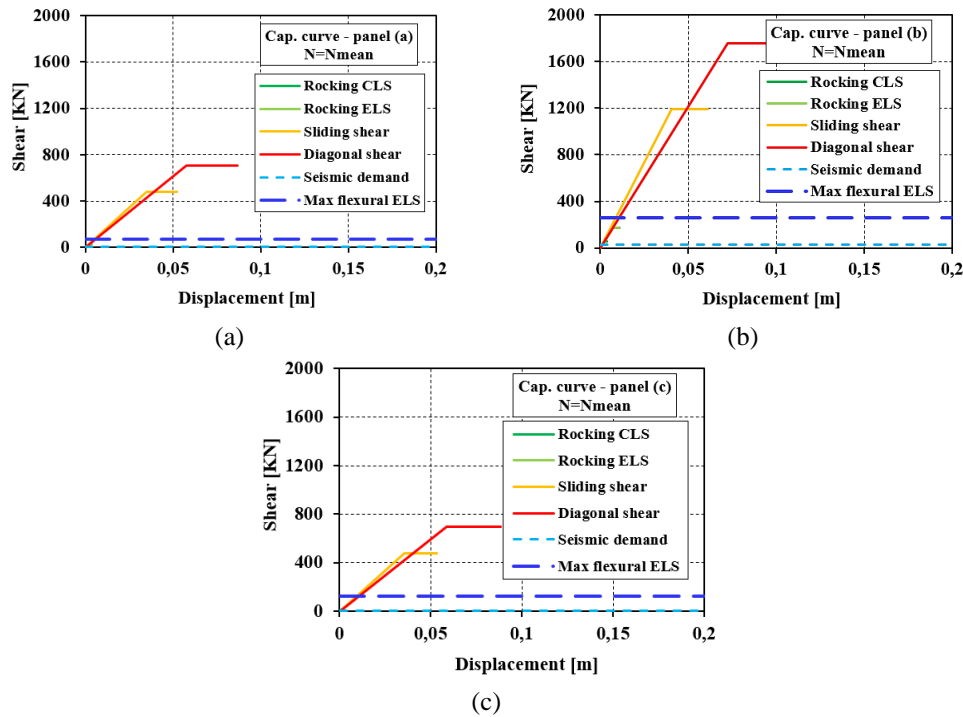


**Figure 4.54:** Comparison between capacity and the corresponding seismic demand for the analyzed wall panels in X-direction.

Thus, from the previous figure, it was possible to define a failure hierarchy. In particular, the following conditions have been deduced:

Panel *a* -  $\bar{N}_{mean} = 0.0052 \rightarrow N_{mean} = 137.74 \text{ kN}$

- i. the mechanism activated was rocking CLS according to which  $N=0.04\%N_u$  ( $N_u=26509 \text{ kN}$ ), the mechanism was ductile and reversible, the section was fully reagent with a maximum shear value,  $V$ , equal to  $9.63 \text{ kN}$ . The displacements associated for each limit state, defined according to the Equations 4.32-4.34 have been equal to  $\delta=0.79 \text{ mm}$ ,  $\delta_f=0.94 \text{ mm}$ ,  $\delta_u=1.8 \text{ mm}$ , respectively;
- ii. the ELS rocking mechanism was activated for maximum shear values  $V=28.51 \text{ kN}$  which corresponded to  $N=0.1\%N_u$  the section was partialized. The displacements associated have been equal to  $\delta=2.3 \text{ mm}$ ,  $\delta_f=2.8 \text{ mm}$ ,  $\delta_u=3.5 \text{ mm}$ , respectively;
- iii. the shear mechanism, sliding shear (SS) was activated for maximum shear values  $V=479.12 \text{ kN}$  which corresponded to  $N=2\%N_u$  the section was partialized and the mechanism has identified as fragile. The displacements associated have been equal to  $\delta=34 \text{ mm}$ ,  $\delta_f=41 \text{ mm}$ ,  $\delta_u=52 \text{ mm}$ , respectively;

- iv. the shear mechanism, diagonal shear (DS) was activated for maximum shear values  $V=707.24$  KN which corresponded to  $N=3\%N_u$  the section was partialized and the mechanism has identified as fragile. The displacements associated have been equal to  $\delta=57$  mm,  $\delta_f=69$  mm,  $\delta_u=90$  mm, respectively;
- v. the seismic demand generated by the seismic event considered has provided a horizontal force equal to 6.7 KN (cyan dashed line), resulting in less than the minimum capacity shown for the rocking CLS mechanism;
- vi. for  $t=3.18$  sec, the maximum rocking threshold has produced a shear  $V=68$  KN (blue dashed line) resulting in greater than the CLS condition which was not verified.

Panel *b* -  $\bar{N}_{mean} = 0.0051 \rightarrow N_{mean} = 336KN$

- i. the mechanism activated was rocking CLS according to which  $N=0.09\%N_u$  ( $N_u=64786$  KN), the mechanism was ductile and reversible, the section was fully reagent with a maximum shear value,  $V$ , equal to 57.53 KN. The displacements associated with each limit state, have been equal to  $\delta=0.51$  mm,  $\delta_f=0.62$  mm,  $\delta_u=0.77$  mm, respectively;
- ii. the ELS rocking mechanism was activated for maximum shear values  $V=170.29$  KN which corresponded to  $N=0.3\%N_u$  the section was partialized. The displacements associated have been equal to  $\delta=1.54$  mm,  $\delta_f=1.85$  mm,  $\delta_u=2.31$  mm, respectively;
- iii. the shear mechanism, sliding shear (SS) was activated for maximum shear values  $V=1170$  KN which corresponded to  $N=1.8\%N_u$  the section was partialized and the mechanism has identified as fragile. The displacements associated have been equal to  $\delta=6.21$  mm,  $\delta_f=7.46$  mm,  $\delta_u=9.32$  mm, respectively;
- iv. the shear mechanism, diagonal shear (DS) was activated for maximum shear values  $V=1728$  KN which corresponded to  $N=2.7\%N_u$  the section was partialized and the mechanism has identified as fragile. The displacements associated have been equal to  $\delta=15$  mm,  $\delta_f=19$  mm,  $\delta_u=24$  mm, respectively;
- v. the seismic demand generated by the seismic event considered has provided a horizontal force equal to 50 KN (cyan dashed line), resulting in less than the minimum capacity shown for the rocking CLS mechanism;

- vi. for  $t=3.18$  sec, the maximum rocking threshold has produced a shear  $V=256$  KN (blue dashed line) resulting in greater than the CLS and ELS condition, respectively.

Panel *c* -  $\bar{N}_{mean} = 0.0045 \rightarrow N_{mean} = 118KN$

- i. the mechanism activated was rocking CLS according to which  $N=0.04\%N_u$  ( $N_u=23804$  KN), the mechanism was ductile and reversible, the section was fully reagent with a maximum shear value,  $V$ , equal to  $7.76$  KN. The displacements associated with each limit state, have been equal to  $\delta=0.85$  mm,  $\delta_f=1.0$  mm,  $\delta_u=13$  mm, respectively;
- ii. the ELS rocking mechanism was activated for maximum shear values  $V=23$  KN which corresponded to  $N=0.1\%N_u$  the section was partialized. The displacements associated have been equal to  $\delta=2.5$  mm,  $\delta_f=3.0$  mm,  $\delta_u=3.7$  mm, respectively;
- iii. the shear mechanism, sliding shear (SS) was activated for maximum shear values  $V=430$  KN which corresponded to  $N=1.8\%N_u$  the section was partialized and the mechanism has identified as fragile. The displacements associated have been equal to  $\delta=40$  mm,  $\delta_f=51$  mm,  $\delta_u=64$  mm, respectively;
- iv. the shear mechanism, diagonal shear (DS) was activated for maximum shear values  $V=653$  KN which corresponded to  $N=2.7\%N_u$  the section was partialized and the mechanism has identified as fragile. The displacements associated have been equal to  $\delta=71$  mm,  $\delta_f=86$  mm,  $\delta_u=107.8$  mm, respectively;
- v. the seismic demand generated by the seismic event considered has provided a horizontal force equal to  $6$  KN (cyan dashed line), resulting in less than the minimum capacity shown for the rocking CLS mechanism;
- vi. for  $t=3.18$  sec, the maximum rocking threshold has produced a shear  $V=62.7$  KN (blue dashed line) resulting in greater than the CLS and ELS condition, respectively.

Similarly, the study was extended to the wall panels *a*, *f* oriented in Y direction, as shown in Figure 4.55.



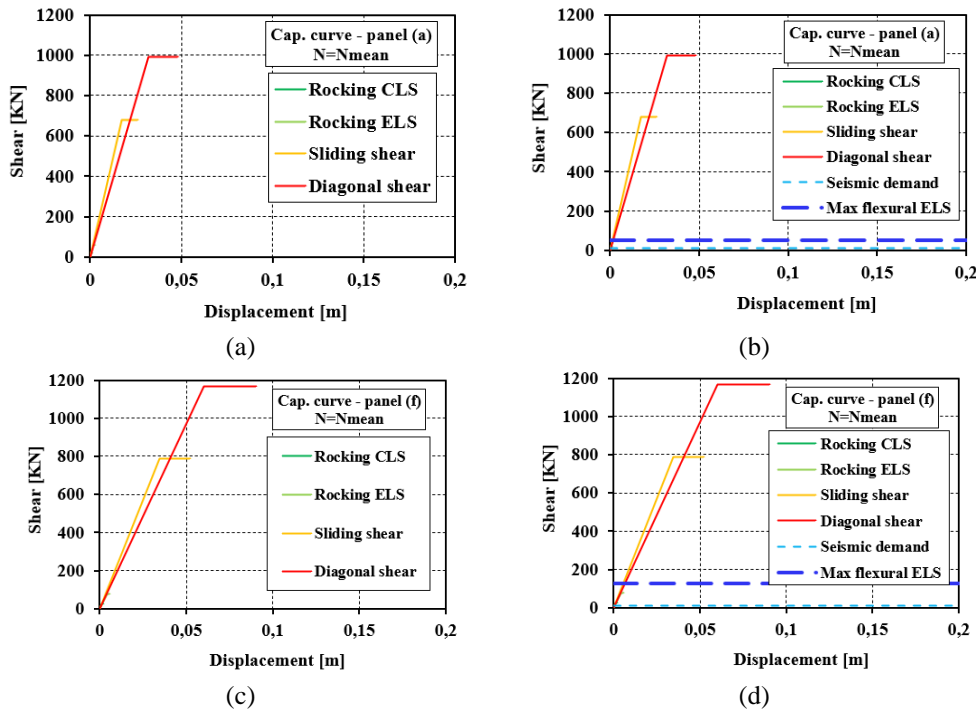


**Figure 4.55:** Comparison between capacity and the corresponding seismic demand for the analysed wall panels in Y direction.

From the acquired results, in the first instance, it was possible to notice how panels oriented in Y direction have a higher maximum shear threshold than those oriented in the orthogonal direction (except for panel *b* in X direction which had a higher resistance area). This aspect confirms what has been explained in the previous paragraphs according to which in Y direction, the load rate absorbed by the panels was substantially greater than the panels in X-direction. It can be seen that the wall panel *a* in Y direction has shown a maximum shear threshold, associated with the diagonal failure mechanism, equal to 990 kN which was +87% greater than the maximum shear level reached by the analogous panel oriented in X-direction.

Secondly, a failure hierarchy has been established, as follows:

Panel *a* -  $\bar{N}_{mean} = 0.0034 \rightarrow N_{mean} = 139.45 \text{ kN}$

- i. the mechanism activated was rocking CLS according to which  $N=0.1\%N_u$  ( $N_u=37600 \text{ kN}$ ), the mechanism was ductile and reversible, the section was fully reagent with a maximum shear value,  $V$ , equal to 19.37 kN. The displacements associated for each limit state, defined according to the Equations 4.32-4.34 have been equal to  $\delta=0.64 \text{ mm}$ ,  $\delta_f=0.74 \text{ mm}$ ,  $\delta_u=0.93 \text{ mm}$ , respectively;

- ii. the ELS rocking mechanism was activated for maximum shear values  $V=57.36$  KN which corresponded to  $N=0.2\%N_u$  the section was partialized. The displacements associated have been equal to  $\delta=1.8$  mm,  $\delta_f=2.2$  mm,  $\delta_u=2.7$  mm, respectively;
- iii. the shear mechanism, sliding shear (SS) was activated for maximum shear values  $V=679$  KN which corresponded to  $N=1.8\%N_u$  the section was partialized and the mechanism has identified as fragile. The displacements associated have been equal to  $\delta=18$  mm,  $\delta_f=21$  mm,  $\delta_u=26$  mm, respectively;
- iv. the shear mechanism, diagonal shear (DS) was activated for maximum shear values  $V=990$  KN which corresponded to  $N=2.7\%N_u$  the section was partialized and the mechanism has identified as fragile. The displacements associated have been equal to  $\delta=31$  mm,  $\delta_f=38$  mm,  $\delta_u=48$  mm, respectively;
- v. the seismic demand generated by the seismic event considered has provided a horizontal force equal to  $9.5$  KN (cyan dashed line), resulting in less than the minimum capacity shown for the rocking CLS mechanism;
- vi. for  $t=3.55$  sec, the maximum rocking threshold, has produced a shear  $V=50$  KN (blue dashed line) resulting in greater than the CLS and ELS condition which were not satisfied.

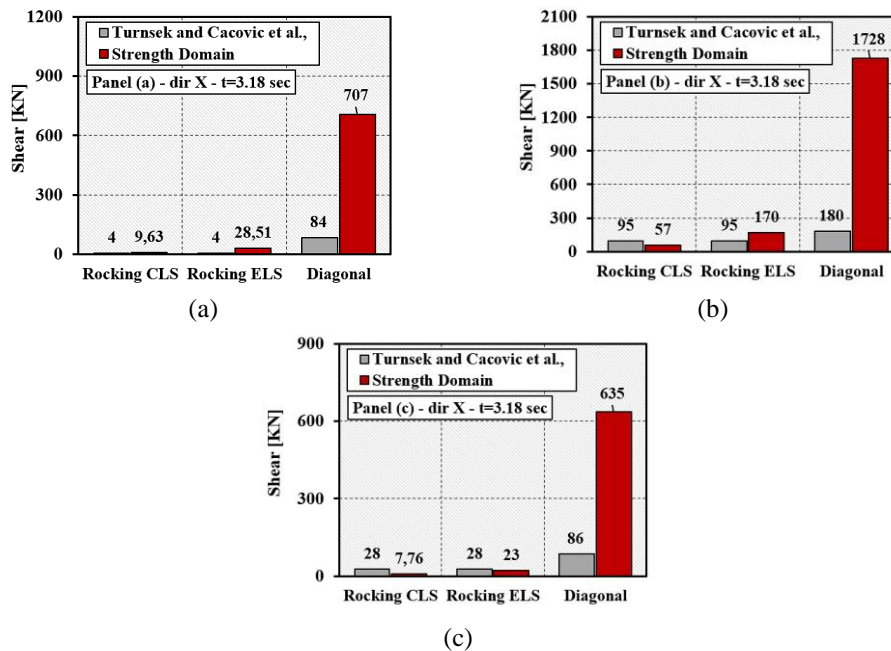
Panel *f* -  $\bar{N}_{mean} = 0.0064 \rightarrow N_{mean} = 203.60$  KN

- i. the mechanism activated was rocking CLS according to which  $N=0.04\%N_u$  ( $N_u=43822$  KN), the mechanism was ductile and reversible, the masonry section was fully reagent with a maximum shear value,  $V$ , equal to  $26$  KN. The displacements associated for each limit state, defined according to the Equations 4.32-4.34 have been equal to  $\delta=1.3$  mm,  $\delta_f=1.6$  mm,  $\delta_u=2.0$  mm, respectively;
- ii. the ELS rocking mechanism was activated for maximum shear values  $V=77$  KN which corresponded to  $N=0.2\%N_u$  the section was partialized. The displacements associated have been equal to  $\delta=4.0$  mm,  $\delta_f=4.8$  mm,  $\delta_u=6.0$  mm, respectively;
- iii. the shear mechanism, sliding shear (SS) was activated for maximum shear values  $V=792$  KN which corresponded to  $N=1.8\%N_u$  the section was partialized and the mechanism has identified as fragile. The displacements associated have been equal to  $\delta=34$  mm,  $\delta_f=41$  mm,  $\delta_u=52$  mm, respectively;

- iv. the shear mechanism, diagonal shear (DS) was activated for maximum shear values  $V=1169$  KN which corresponded to  $N=2.7\%N_u$  the section was partialized and the mechanism has identified as fragile. The displacements associated have been equal to  $\delta=60$  mm,  $\delta_f=72$  mm,  $\delta_u=90$  mm, respectively;
- v. the seismic demand generated by the seismic event considered has provided a horizontal force equal to 10.4 KN (cyan dashed line), resulting in less than the minimum capacity shown for the rocking CLS mechanism;
- vi. for  $t=3.00$  sec, the maximum rocking threshold has produced a shear  $V=128.546$  KN (blue dashed line) resulting in greater than the CLS and ELS conditions which were not verified.

Furthermore, it has been noted that the displacements of panel *f* are greater than panel *a*. This circumstance has been suitably explained in paragraph § 4.3.2.2.1, according to which the panels belonging to the North façade were more compressed than those close to the South façade. Consequently, by decreasing locally the axial compression, the displacement capacity was greater.

Finally, the maximum shear thresholds were compared between the criterion proposed by [189] and what has been obtained by applying the resistance domains for the set of wall panels analysed in both directions. The results are shown in Figure 4.56.



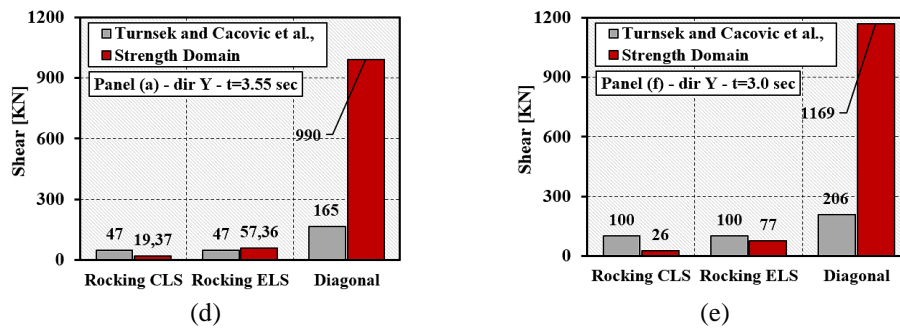


**Figure 4.56:** Comparison between the Cacovic criterion and strength domain in terms of maximum expected shear levels for the considered masonry walls in X and Y directions.

The gotten results have shown a heterogeneity of the shear levels obtained by comparing the two verification criteria. In general, it was noted that the Cacovic criterion, adopted for the evaluation of diagonal failure, provides very restrictive values concerning the real behaviour of the wall panels, which had a much higher bearing capacity. It is worth underlining, although asserted in the previous paragraphs, that the Cacovic criterion [189] was a resistance criterion for which it guarantees the integrity of the wall panel but not the equilibrium between the acting forces. Furthermore, Cacovic's formula [189] had a strong connection with the design strength of the masonry,  $f_{td}$ . It was observed that this dependence provides precautionary results since the quality of the masonry (identifiable with the  $f_{ib}$  parameter) showed, keeping the axial force constant, that the displacement capacity was limited since the quality of the masonry was not adequate.

As regards the rocking mechanism, the Cacovic criterion [189] presented the first limitation since it did not allow differentiation in terms of the limit state reached (CLS and ELS), providing a single shear force value. In this sense, by comparing mainly the ELS rocking condition, the values of the shear thresholds reached, using the two criteria, slightly differ. The difference lies in the fact that by using the resistance domain, the axial force was normalized concerning the maximum load-bearing capacity of the panel ( $N_u$ ) and, secondly, the wall section, to support an increasing shear force, the axial force needed to assume ever greater eccentricities, this meant a progressive increase in terms of the maximum compressive strength of the material from the elastic to the plastic range.

Finally, it was possible to assert that in the case of an impulsive earthquake characterized by high ground motion vertical accelerations, it is appropriate to use the strength domains concerning the verification criterion proposed by Cacovic [189] since, in these circumstances, the effective seismic response of the wall panels is taken into account when they are subjected to vertical seismic action.

4.3.4.1.2 Estimation of damage index,  $DI_\mu$ 

Several studies have focused on the definition of damage measures in seismic engineering, [220-223]. The correlation between potential damage measures, based on ground motion records, and those related to both, structural and non-structural components has not been adequately studied especially for masonry constructions, characterized by a non-linear dynamic behaviour.

In particular, as has been observed, some regions of Italy, have shown a particular seismogenic structure that has caused sequences of seismic events in short periods, and consequently, appropriate structural and safety assessments, for the estimation of retrofitting interventions, were not been considered. As observed in the various historical seismic sequences that occurred in Italy, for example, it is worth remembering the seismic sequence in Umbria and Marche in 1997 (it lasted about seven months), which generated events with magnitudes between 5 and 6 that have affected these two Apennine regions, causing serious damage and loss of human life, or the seismic sequence occurred in the province of L'Aquila (Central Italy).

Based on the aforementioned considerations, it is appropriate to define a synthetic parameter that takes into account the real level of damage that a generic masonry structure is subjected to. In this sense, [220], indicate the damage estimation that can be characterized by both, global and local analysis approaches. This procedure leads to the definition of the seismic damage index,  $DI_\mu$ , as expressly indicated in Equation 4.35:

$$DI_\mu = \frac{\mu_r - 1}{\mu_d - 1} \quad (4.35)$$

having indicated with  $\mu_r$  and  $\mu_d$  the request and demand displacement ductility's, respectively. So, the quantity in the numerator represents, in terms of displacement, how much the structural element is "far" from the elastic limit. If this limit is exceeded, the value is positive, vice versa negative. In this sense, exceeding the elasticity limit means that the structure exhibits a post-elastic behaviour.

The denominator represents the "distance" between the ultimate displacement and the elastic one and represents the "scale" of damage measurement. The more a condition exists whereby the ultimate displacement is "distant" from the elastic displacement, the more the damage is moderate. Furthermore, if the denominator is null, it means that the failure is fragile, that is, the element passes directly from a state of integrity to collapse; if the numerator is negative, it means that the

damage index is equal to zero since the elastic limit for which the element is not damaged has not been reached.

According to these considerations, the displacement ductility's have been defined as reported in the following Equations [171]:

$$\mu_d = \frac{\delta_u}{\delta_y} \quad (4.36)$$

$$\mu_r = \frac{\delta_{el}}{\delta_y} \quad (4.37)$$

where  $\delta_y$ ,  $\delta_{el}$  and  $\delta_u$  represent the yield, maximum and ultimate displacements, respectively. As regards the determination of the maximum required displacement ( $\delta_{el}$ ), it was calculated using the energetic principle based on the equivalence of the areas between the elastic and elastoplastic system by adopting the bilinear curves deriving from the failure hierarchy models.

Thus, in Tables 30 and 31 all the characteristics calculated according to the previously analysed panels have been reported:

**Table 30:** Input parameters used to estimate the  $DI_\mu$  for wall panels in the X-direction.

WP	$F_y$ [KN]				$F_{el}$ [KN]				$F_u$ [KN]			
	CLS	ELS	SS	DS	CLS	ELS	SS	DS	CLS	ELS	SS	DS
<i>a</i>	9.63	28.5	479	707	13.6	40.3	677	1000	9.63	28	479	707
<i>b</i>	57	170	1170	1728	80	24.0	1654	2443	57	170	1170	1728
<i>c</i>	7.76	23	430	923	10	32	608	923	7.76	23	430	923

WP	$F_y$ [KN]				$F_{el}$ [KN]				$F_u$ [KN]			
	CLS	ELS	SS	DS	CLS	ELS	SS	DS	CLS	ELS	SS	DS
<i>a</i>	0.8	2.3	34.7	57.8	1.2	3.3	49.1	81.7	1.2	3.5	52.1	86.6
<i>b</i>	0.5	1.5	6.2	15.7	0.7	2.2	8.8	22.2	0.8	2.3	9.3	23.5
<i>c</i>	0.9	2.5	42.9	71.9	1.2	3.6	60.7	101.7	1.3	3.8	64	107.8

**Table 31:** Input parameters used to estimate the  $DI_\mu$  for wall panels in Y direction.

WP	$F_y$ [KN]				$F_{el}$ [KN]				$F_u$ [KN]			
	CLS	ELS	SS	DS	CLS	ELS	SS	DS	CLS	ELS	SS	DS
<i>a</i>	19.4	57.4	679	990	27.4	81.1	961	1400	19.4	57.4	680	990
<i>f</i>	26.3	77.9	792	1169	37.2	110	1120	1653	26.3	78	792	1169
WP	$\delta_y$ [mm]				$\delta_{el}$ [mm]				$\delta_u$ [mm]			
	CLS	ELS	SS	DS	CLS	ELS	SS	DS	CLS	ELS	SS	DS
<i>a</i>	0.6	1.8	17.5	31.9	0.9	2.6	24.8	45.1	0.9	2.8	26.3	47.9
<i>f</i>	1.4	4.0	34.8	60.5	1.9	5.7	49.2	85.5	2.0	6.0	52.2	90.7

Based on the archived results, it was possible to graph the damage index as a function of both, displacements (demand, capacity) and shear forces for the masonry panels in the two analysis directions, X and Y, respectively. Furthermore, the results have been summarized in Figure 4.57 for the wall panels in the X-direction.

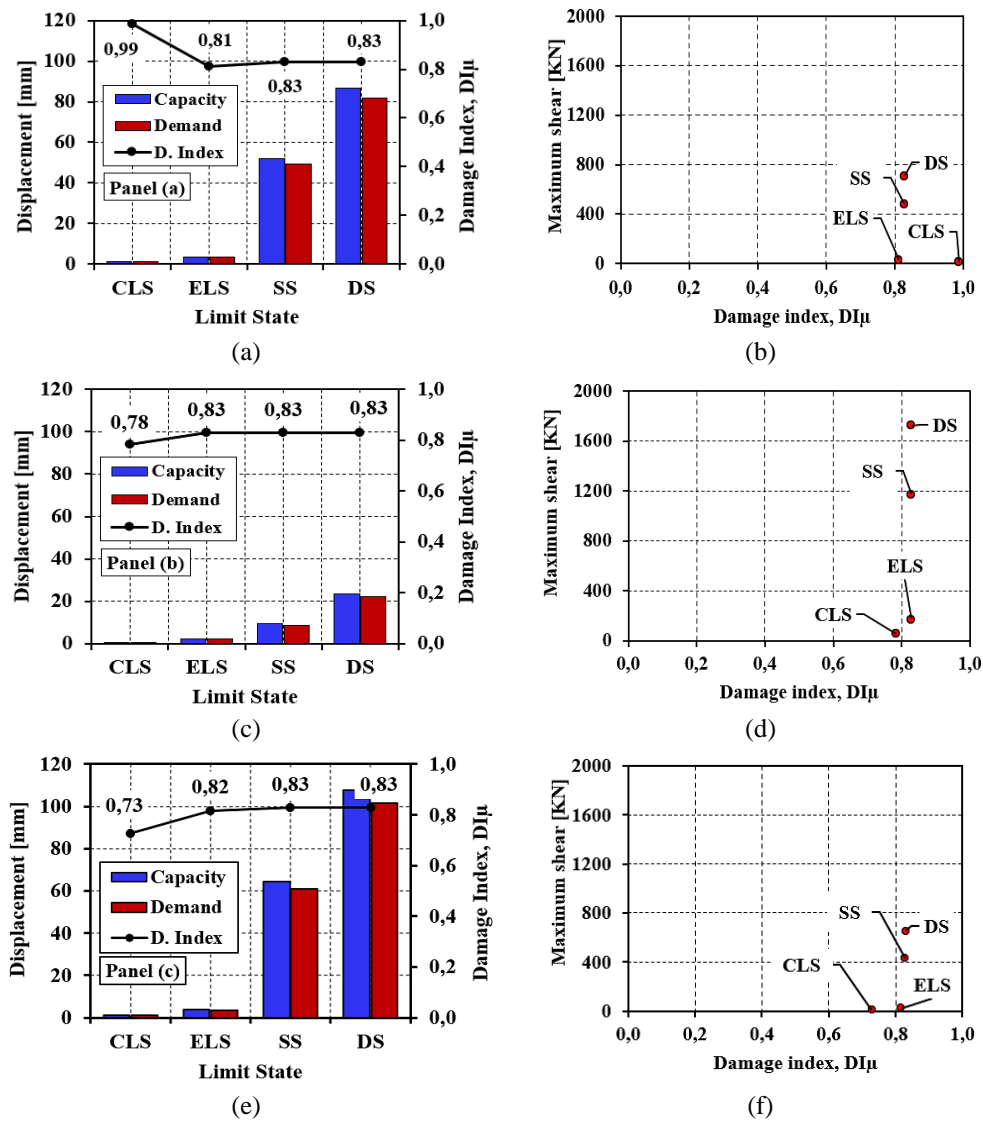


Figure 4.57: Correlation between displacements, maximum shear force, and damage index,  $DI_u$ , for panels in X-direction.

From the results obtained it was noted that for panel *a*, for CLS and ELS, demand and capacity were almost the same, while for SS and DS, the displacements were comparable and the capacity was 6% greater than the



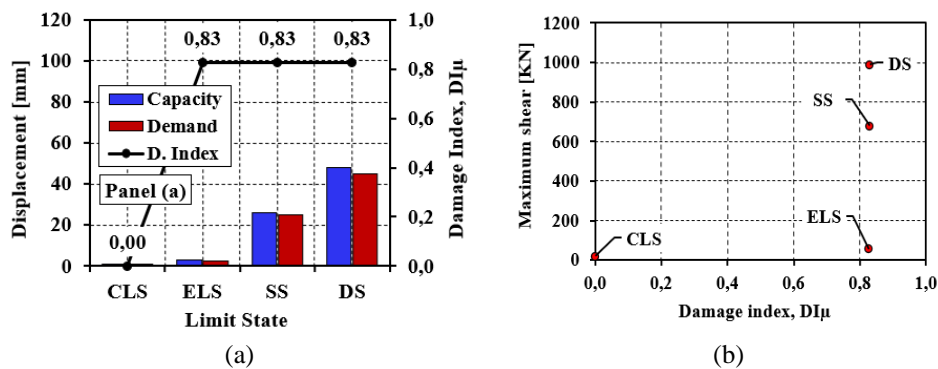
corresponding displacement demand (Figure 4.57 (a)). In terms of the expected shear force reached (Figure 4.57 (b)), a progressive increase of shear action was noted for the different failure mechanisms that have been presented. Regarding the damage index, it was possible to observe how in the case of CLS and ELS, the damage index was equal to 0.99 and 0.81, respectively. By mentioning the definition of the damage index given previously, it was possible to understand that in the case of CLS, the demand and capacity displacements were equal, consequently, the  $DI_{\mu}$  associated with this failure state was equal to 0.99, which means that there is a 99% probability that the mechanism occurs. Regarding the other damage thresholds, in terms of both, displacements and shear levels, the  $DI_{\mu}$  tends to be reduced, which means that the wall section tends to get damaged. In particular, 81% for ELS, 81% and 17% for SS and DS the damage state, respectively.

As far as panel *b* (Figure 4.57 (c)-(d)), it was noted that for CLS and shear value equal to 57 KN, the damage index,  $DI_{\mu}$  was equal to 78%.

For the other mechanisms, the maximum shear varying between 170 KN and 1728 KN, and the corresponding damage index assumed a constant value equal to 0.83, i.e. there was an 83% probability that the panel suffered such damage corresponding to the limit state considered. Similarly, for masonry wall panel *c* (Figure 4.57 (e)-(f))

As it was possible to notice, the damage to the cracking phase (CLS) was the one that occurs first for low shear values.

Consequently, following the same procedure previously proposed, Figure 4.58 has been presented the results obtained for the panels oriented in Y direction.



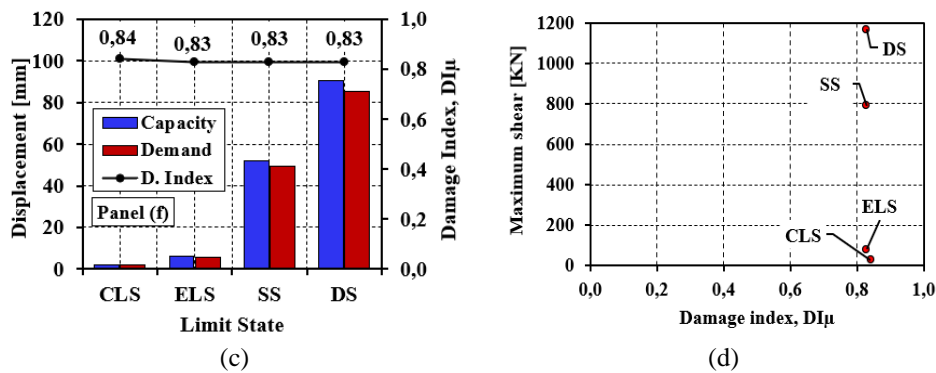


**Figure 4.58:** Correlation between displacements, maximum shear force, and damage index,  $DI_{\mu}$ , for panels in Y direction.

In general, it has been noted that the damage index was constant for both panels, for the CLS, ELS, SS, DS failure mechanisms, however, in Figure 4.58 (a), it was worth highlighting how for the CLS mechanism, it was observed a  $DI_{\mu}=0$ , this meant that the section was not damaged since the shear force reached CLS state was very low ( $F_y=19$  KN) and the associated displacement was equal to zero ( $\delta_y=0.6$  mm).

### 4.3.5 Out-of-plane mechanisms

#### 4.3.5.1 Linear kinematic analysis

Linear kinematic analysis is based on the modelling of the macro-element as a system of rigid blocks that highlights a rigid-labile behaviour. In general, the geometric articulation of a complex historical architectural-structural system does not guarantee, as seen in the previous paragraphs, the global behaviour of the structure. Consequently, the lack of both, rigid floors and effective connections between portions of walls, makes the structure particularly sensitive to seismic actions. For this reason, local analysis is carried out on portions of the structure identified with the name of macroelements, which represent the sectioning of structural parts that are analysed separately from the global context.

In non-seismic conditions, the macro-element is characterized by the presence of gravitational loads and, eventually, by horizontal actions induced by the wind and/or by the vaults. The safety factor concerning the overturning or kinematic sliding condition of one of the blocks (belonging to the same macro-element), due to the exceeding of the friction strength, expresses the evaluation of safety condition.

Vice versa, in seismic conditions, the macro-element is considered subjected to monotonously increasing the horizontal actions that lead to the failure of the wall panel by overturning, or by reciprocal sliding of one block concerning another [224]. The limit multiplier of the horizontal actions,  $\alpha_0$ , can be interpreted as the absolute acceleration to which the structural system is subjected ( $S \cdot ag$ ). However, it is worth highlighting that since the structural system consists of a rigid block, as the suggested following [225], the acceleration that leads to the formation of the kinematics is identical to all the blocks constituting a generic façade of the structural organism since the motion of the structural system coincides with the ground motion. Therefore, from what has been properly established, the kinematic analysis is applied to evaluate the seismic safety of the ultimate equilibrium limit state (ULS). In these circumstances, the gravitational actions are amplified by the partial safety coefficients,  $\gamma_G$ , and  $\psi_Q$ . Operationally, the principle of virtual works is adopted for the overturning and sliding mechanisms to determine the lowest collapse multiplier  $\alpha_0$ . From these considerations, the general formulation is made explicit regarding Equation 4.38 [40]:

$$\alpha_0 \cdot \left( \sum_{i=1}^n P_i \cdot \delta_{x,i} + \sum_{j=n+1}^{n+m} P_i \cdot \delta_{x,j} \right) - \sum_{i=1}^n P_i \cdot \delta_{y,i} - \sum_{i=1}^n F_h \cdot \delta_h = L_i \quad (4.38)$$

The term before equality represents the work of external forces,  $L_{est}$  and  $L_i$  indicate the work of internal attractive forces. So, about the Equation previously defined,  $P_i$  indicates the stabilizing weights of the blocks,  $\delta_{x,y,i}$ , are the virtual displacements,  $F_h$ , are the external horizontal forces (e.g. the action of the vaults, arcs, etc.) and  $\delta_h$  represents the pole of the external horizontal forces.

The mass to be adopted for the generic macro-element is understood as the participating mass of the kinematics considered, presented in Equation 4.39

$$M^* = \frac{\left( \sum_{i=1}^{n+m} P_i \cdot \delta_{x,i} \right)^2}{g \cdot \sum_{i=1}^{n+m} P_i \cdot \delta_{x,i}^2} \quad (4.39)$$

The spectral acceleration that activates the kinematics is defined according to Equation 4.40:

$$a_0^* = \frac{\alpha_0 \cdot \sum_{i=1}^{n+m} P_i}{M^* \cdot FC} \quad (4.40)$$

having indicated with FC the confidence factor, which is equal to 1.35 in the specific case.

Moreover, the verification of the mechanisms is performed considering that the acceleration that activates the mechanism ( $a_0^*$ , demand acceleration) is lower than the capable acceleration ( $a_{0,\min}$ ). Therefore, two conditions can occur in the case of SLV limit state:

- i. macro-element placed directly on the ground; Equation 4.41 is valid:

$$a_0^* \geq \frac{a_g(P_{VR}) \cdot S}{q} = a_{0,\min} \quad \text{Check 1} \quad (4.41)$$

having identified with  $a_g(P_{VR})$  the calculated acceleration for a given return period, S spectral amplification coefficient and q is the behaviour factor equal to 2 [40];

- ii. macro-element placed at a height, Z, concerning the total height, H, of the entire wall. In this condition, Equation 4.42 is valid:

$$a_0^* \geq \frac{S_e(T1)}{q} \cdot \psi(Z) \cdot \gamma = a_{0,\min} \quad \text{Check 2} \quad (4.42)$$

where  $\psi(Z)=z/H$  represents the relative displacement of the first normalized mode, defined as the ratio between the centre of gravity of the macroelement located at height z, and the height of the entire wall H, q is the behaviour factor equal to 2 and  $\gamma$  is the modal participation coefficient, which can be expressed in according to the number of floors, N, as reported in Equation 4.43:

$$\gamma = \frac{3N}{2N + 1} \quad (4.43)$$

It should be noted that generally, the location of the macro-element placed at a height Z higher than that of the ground, involves an increase in terms of acceleration demand.

## 4.3.5.2 Linear kinematic analysis in case near-field earthquake

In the case of near-field seismic phenomena (impulsive or vibratory), the kinematic analysis can be applied taking into account the influence of the vertical component of the ground motion on the seismic response of the macroelement.

The question to ask is, *how does the vertical seismic force need to be considered in the evaluation of the collapse mechanisms?* The study proposed by [41] has shown how the effect of the vertical seismic force creates a system of vertical inertial forces that contribute to the activation of the collapse mechanism. This vertical inertial action progressively tends to create a system of overpressures and decompressions that cyclically degrade the mechanical characteristics of the masonry material. In fact, as a result of this phenomenon, the earthquake that occurred in central Italy highlighted, especially poor quality masonry, the collapse due to disaggregation of the masonry. Physically, the vertical seismic forces, by cyclically changing the sign during the seismic event, generated an internal stress state incompatible with the active forces (acting loads) and consequently progressively losing the condition of mutual static interaction between mortar and stone.

Therefore, based on these considerations, the proposed procedure aims to analyse the possible out-of-plane mechanisms in the case of shallow earthquakes characterized by high horizontal actions and lower vertical acceleration. Thus, by articulating the formulations seen in the previous paragraph, it was possible to generalize the content in the case of the near-field seismic phenomenon, as reported below in Equation 4.44:

$$\alpha_0 \cdot \left[ \sum_{i=1}^n (P_i + E_v) \cdot \delta_{x,i} + \sum_{j=n+1}^{n+m} (P_i + E_v)_i \cdot \delta_{x,j} \right] - \sum_{i=1}^n (P_i + E_v) \cdot \delta_{y,i} - \sum_{i=1}^n F_h \cdot \delta_h = L_i \quad (4.44)$$

having indicated  $E_v$ , the vertical seismic force which increases (+) the mechanical characteristics of the masonry. Referring to the evaluation of the vertical seismic action,  $V$ , it is assumed as a basic hypothesis to estimate the compressive stress regime, generated by the vertical component, proportionally to the occurred compressive  $PGA_v$  at  $t=3.0$  sec.

In that case, Equation 4.44 can be appropriately modified as shown below in Equation 4.45:

$$\alpha_0 \cdot \left[ \sum_{i=1}^n (P_i + V_i) \cdot \delta_{x,i} + \sum_{j=n+1}^{n+m} (P_i + V_i)_i \cdot \delta_{x,j} \right] - \sum_{i=1}^n (P_i + V_i) \cdot \delta_{y,i} - \sum_{i=1}^n F_h \cdot \delta_h = L_i \quad (4.45)$$

Subsequently, considering the case study building, the North façade was analysed since it was characterized by out-of-plane mechanisms after the Banat-Voiteg earthquake. The damage condition analysed by numerical simulation in paragraph §4.3.3 has pointed out that the mechanisms observed in the aforementioned façades were given by the bending overturning [45]. Thus, the possible collapse mechanisms were suitably analysed using 3Muri software [226].

The software, starting from the definition of the basic geometry, automatically identifies the possible mechanisms that could be activated based on the mechanical characteristics of the masonry, constraint, and load conditions.

The results obtained were summarized in Table 32:

**Table 32:** Evaluation of compressive strength in case of VGM.

Time [sec]	PGA <sub>v</sub> [g]	W [KNm <sup>-3</sup> ]	W <sub>comp.</sub>
3.00	0.06	18.00	19.08

Consecutively, in terms of both, mean horizontal and vertical shear resistance,  $f_{vm}$ , calculated according to the Mohr-Coulomb criterion [31], has been detailed as reported in Equation 4.46:

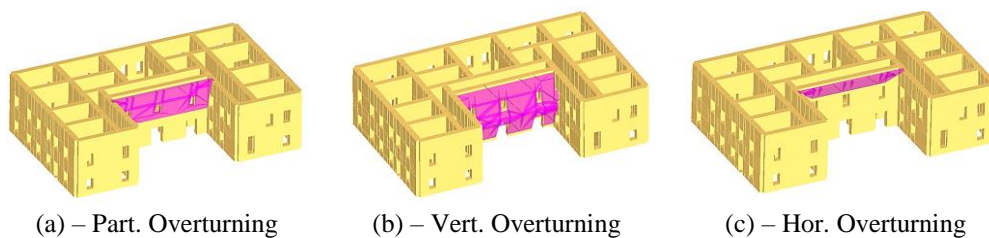
$$f_{vm} = f_{vm,0} + \sigma_n \cdot \tan g(\phi) \quad (4.46)$$

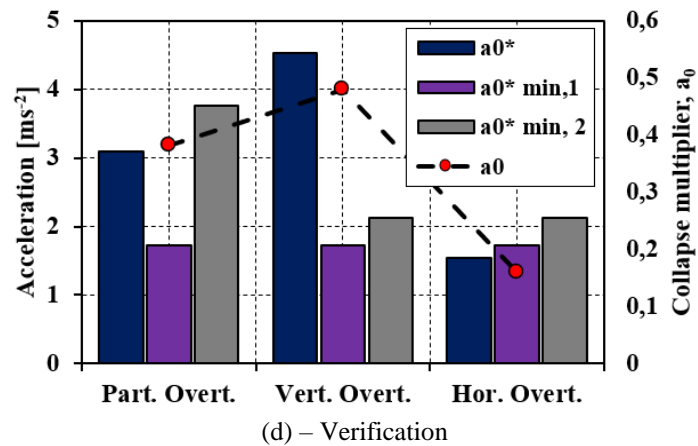
where  $\Phi$ , is the frictional resistance, assumed equal to 0.4 as reported in [176], and  $\sigma_n$  identified the normal stress calculated as reported in the Equation 4.47:

$$\sigma_n = \frac{(W_g + N_i) \pm V_i}{A_s} \quad (4.47)$$

where  $W_g$  identified the weight of the masonry,  $N_i$  was the axial force and  $A_s$ , represented the resistant area of the macroelement.

Based on these considerations, the results obtained have been plotted in the following Figure 4.59:





(d) – Verification  
**Figure 4.59:** Multiplier factor,  $a_0$ , Vs mechanisms considering the compressive effects of VGM for the North façade.

From the results acquired it was possible to note that the collapse mechanism activated was a partial mechanism that corresponds to a minimum multiplier,  $a_0$ , equal to 0.16. The achieved results were summarized in Table 33:

**Table 33:** Results deriving from the kinematic analysis for the North façade.

Mechanism	$a_0$ [-]	$a_0^*$ [ms <sup>-2</sup> ]	$a_{0,min}^*$ (Check 1) [ms <sup>-2</sup> ]	$a_{0,min}^*$ (Check 2) [ms <sup>-2</sup> ]	Verification	
					Check 1	Check 2
Part. Overt.	0.38	3.09	1.72	3.77	s.	n.s
Vert. Overt.	0.48	4.53	1.72	2.12	s.	s.
Hor. Overt.	0.16	1.54	1.72	2.12	n.s	n.s

Finally, based on what has been analysed, the following considerations are summarized:

- i. in the case of compressive  $PGA_V$  the mechanical properties of the basic material were proportionally increased to take into account the mutual cohesion between the brick and mortar;
- ii. the results have shown that the minimum collapse multiplier,  $a_0$ , has been attained for the horizontal overturning which corresponded to an acceleration  $a_0^*$  equal to  $1.54 \text{ ms}^{-2}$ . The safety check was not satisfied (n.s) and the safety index,  $S_I=D/C$  was equal to 1.11;
- iii. by comparing the real damage that occurred in the epicentral area with the simulated mechanism, a good correspondence was observed, indicating that the proposed methodology is reliable for predicting the collapse failures in the case of a shallow earthquake.



#### 4.3.6 Numerical Vs real damage correlation

In the case of near-field (or source) effects, the ground motion vertical acceleration is significantly higher than horizontal ones, consequently causing significant damage to structures. The main reasons are because, given the reduced site to source distance, the low frequencies generated by the vertical earthquake, negatively affect the global behaviour of the building.

Under such conditions, it was observed that the influence of the vertical component of the ground motion is significantly preponderant since it provided a high spectral ratio ( $V/H=2.2$  close to the seismogenic source). Therefore, it is clear that the damages that occurred, typical for buildings located in the epicentre area, are due to the concomitant effect of the horizontal and vertical seismic actions, respectively [122].

Physically, the mechanism that leads to the formation of the vertical cracks is symptomatic of a stress state purely induced by the sliding shear between two mutual portions of masonry. In particular, the near-field phenomenon can be understood as an asynchronous sinusoid of the ground movement which consequently causes the raising and descent of parts of the masonry. This vertical dislocation is the result of a cyclical condition which during the time history causes a local deterioration of the resistance characteristics and therefore, leads to the formation of cracks.

Therefore, as analysed in the previous paragraphs, the vertical earthquake induces a state of overpressure and decompression that cyclically affects the resistance of the material, which, exceeding the tensile strength, tends to damage.

The cracks activated, therefore, represents a condition of energy dissipation of the structure to the detriment of its static integrity. Once again, the ground motion vertical component locally modifies the mean shear stress (horizontal and vertical) since it intrinsically alters the compression stress regime according to Mohr's criterion [171].

In fact, during the time history cycle, the vertical component of the seismic action changes its sign, causing a continuous variation of the axial compression stress which also governs the shear resistance. Another important aspect is that the variation of the signal velocity of the vertical component affects the variation (compression and decompressions) of the compressive strength of the material there is a direct proportionality between these two factors which represent one of the major causes of extensive damage [120].

The most unfavourable condition concurs when decompression of the masonry is achieved, since the materials are susceptible to seismic actions which lead to lower local resistance, favouring the formation of cracks.

Based on these considerations, it was possible to compare the damages obtained by the mechanical stimulation to the real ones detected after the Banloc earthquake. More specifically, it was possible to focus on the fact that the damage that occurred is due to the coexistence of two very specific steps: (i) in the first two seconds of the time history, the maximum vertical peak acceleration produced extensive damage in the vaults, characterized by a brittle behaviour; (ii) consecutively, following the impulsive vertical action, the arrival of the horizontal components produced damage to the vertical structures, mainly in the spandrel beams due to the formation of rocking and shear failures.

So, as analysed in paragraph 4.3.3, in the first step of the analysis, the damages deriving from the numerical simulation were compared with the real ones [150], formalizing everything in the first two seconds of the time history (maximum  $PGA_V$ ). To this purpose, the South façade has been presented in Figure 4.60:



**Figure 4.60:** Damage correlation depicted in the South façade of the case study building.

As it has been possible to observe, the South façade of the considered building presents for  $t=1.68$  sec, typical vertical shear cracks induced by the vertical component of the seismic action. This condition was manifested exclusively in this façade since it was subject to a vertical displacement profile which was characterized by the relief of the affected part, while the North façade was compressed, as shown in Figure 4.61.

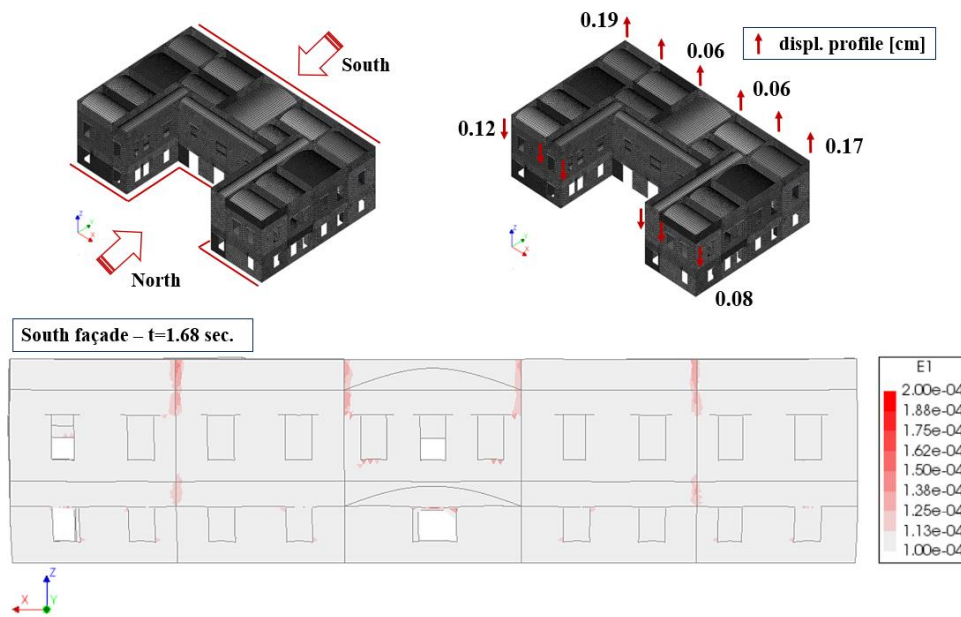


**Figure 4.61:** Vertical displacement profile achieved in the South façade.

From a physical point of view, vertical cracks were generated since the vertical displacement profile has shown a non-uniform distribution. Consequently, the masonry walls located at external parts of the façade, characterized by vertical displacements, have generated systems of a mutual shear vertical sliding plane with the intermediate adjacent walls. In this condition, the tensile strength of the masonry has been exceeded, respecting the kinematic congruence and equilibrium of the interacting masonry parts. Furthermore, as pointed out in paragraph § 4.3.3, the other façades of the building examined did not report any damage.

However, other structural elements that must be taken into consideration for the analysis of the damage that occurred, in the case of the seismic vertical component, are the horizontal structures. These structural elements present a functional model capable of "adapting" to the boundary conditions (loads, constraints), however presenting cracks.

The vaulted elements, therefore, if suitably modelled as shell element surface, present a plane state of tension along with one of the possible pressure surfaces, coinciding with the average surface line which, in the case of flexural stresses, cause the exceeding the tensile strength of the material. This aspect has been the subject of particular attention in the simulated damage model.

Figure 4.62 shows the damage evolution of the central masonry vault regarding the maximum vertical displacement peaks.

The choice to monitor this masonry vault was because it had a more dangerous geometric configuration since it covered a larger surface area than the other vaults present in the building. Furthermore, it had collapsed following the occurred Banat-Voiteg earthquake.

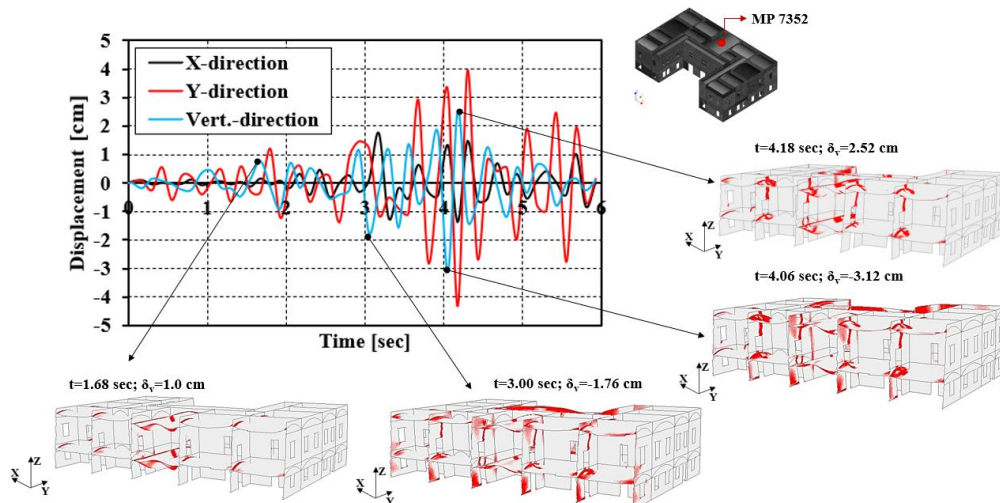


**Figure 4.62:** Damage evolution of the masonry vault due to ground motion vertical component of the simulated Banat-Voiteg earthquake.

From the displacements analysed in the previous Figure 4.62, it emerged that the vertical seismic action in the first two seconds of the time domain ( $t=1.68$  sec), has produced vertical displacements equal to 1.0 cm. It is worth noting how the seismic vertical component in that time step has generated a system of displacements such as to raise the vault analysed. As a consequence of this phenomenon, gravitational loads were opposed, which limited displacements impressed. Subsequently, at  $t>1.68$  sec, with the arrival of the horizontal components, the distribution of the damage was increased.

A progressive increase in terms of vertical displacements was noted. In particular, at  $t=3.00$  sec, the displacement of the monitoring point monitored was equal to -1.76 cm.

This consequence was reliable since at the time step was considered, the gravitational loads were the same as the direction of the seismic vertical component. Similarly, at  $t=4.06$  sec, the maximum vertical displacement,  $\delta_v$ , equal to -3.12 cm was obtained. At this time step, the most unfavourable condition occurred since the horizontal seismic action increased the vertical displacement of the point located in the centre of the examined vault by about 77%.

It has been noted, the increase of the damage coincided with the change of the concavity of the flexural deformation of the vault in which, exceeding the tensile strength of the masonry, was collapsed as shown in Figure 4.63.

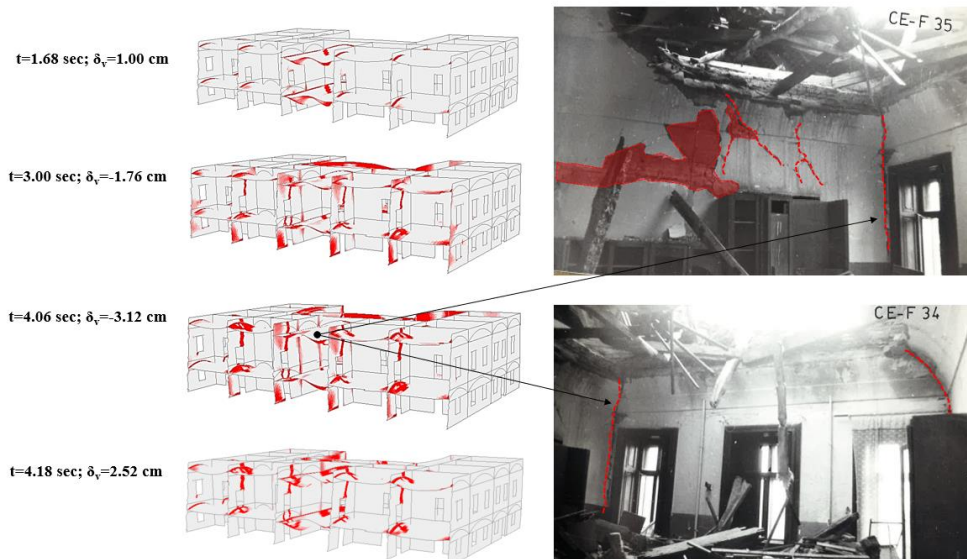
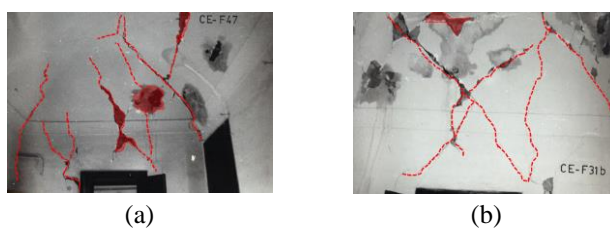


**Figure 4.63:** Damage influenced by the vertical seismic component for the monitored central vault.

Subsequently, for a concrete overview, the damages that occurred in the masonry vaults on the second floor for different time steps, were shown in Figure 4.64. As was desirable, the damage deriving from the numerical model for different time steps can be considered comparable with the damage obtained following the reference seismic event. It has been possible to observe that the vaults progressively tended to suffer a very accentuated level of damage when the effects induced by both, ground motion horizontal and vertical components occur.

This physical aspect can also be extended to the other masonry vaults present in the case study building since, as seen from the figures previously analysed in Chapter 3, the damage was localized in them since they were elements characterized by large spans and lower resistance than that of vertical structures.



(a)

(b)



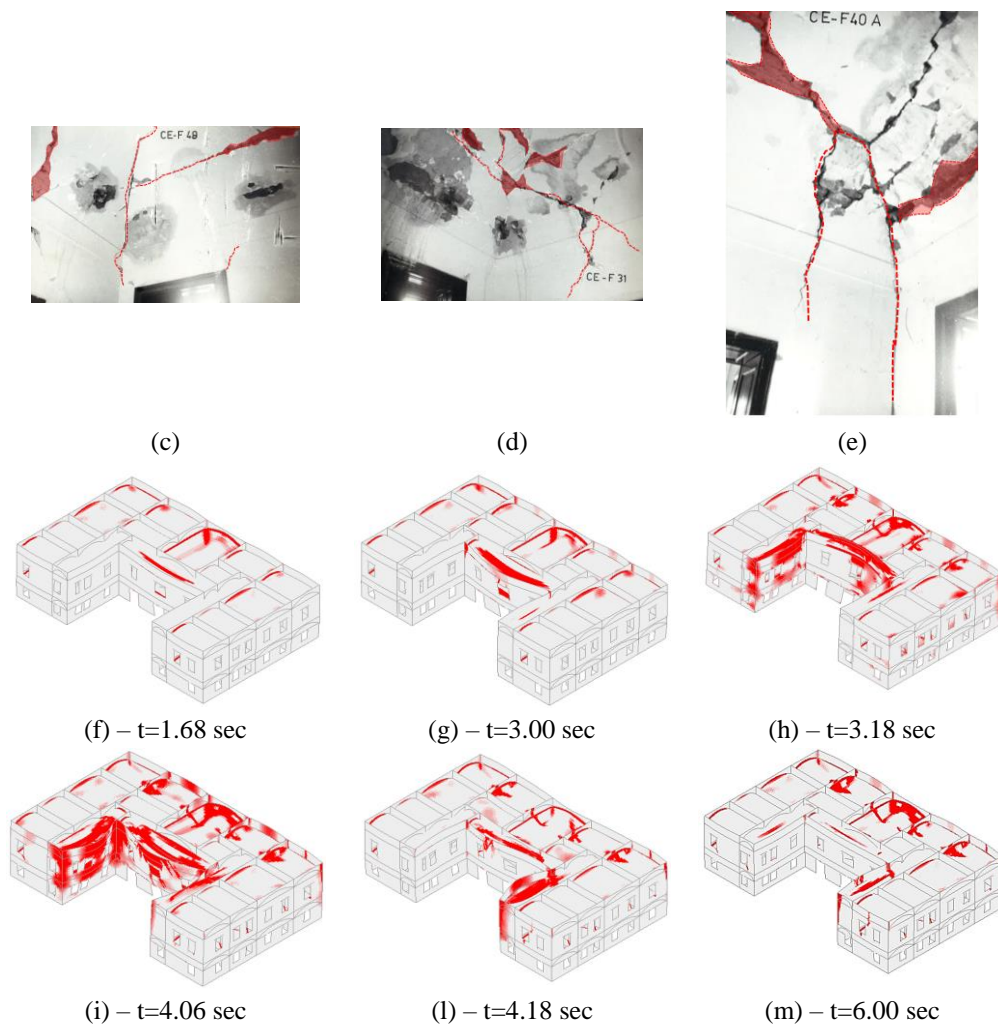


**Figure 4.64:** Damage comparison for masonry vaults at different time steps.

Regarding the vertical structures, the damages that occurred were examined for each main façade of the case study building, comparing them with the real ones deduced from on-site inspection activity after the Banloc earthquake.

The cracks that had occurred in the numerical model were analysed for different time steps to be able to exhaustively highlight the cumulative damage characterizing the examined structure.

First of all, the façades oriented in Y direction were analysed, since the condition of geometric symmetry existed.

Regarding Figure 4.65, for the analysis of the damage afferent to the East façade, two consecutive time steps have been considered, at 3.05 sec and 3.55 sec, respectively. This choice was adopted because it was considered the effects induced by the horizontal seismic component (Y direction) when the latter was concordant and discord with the global reference system.

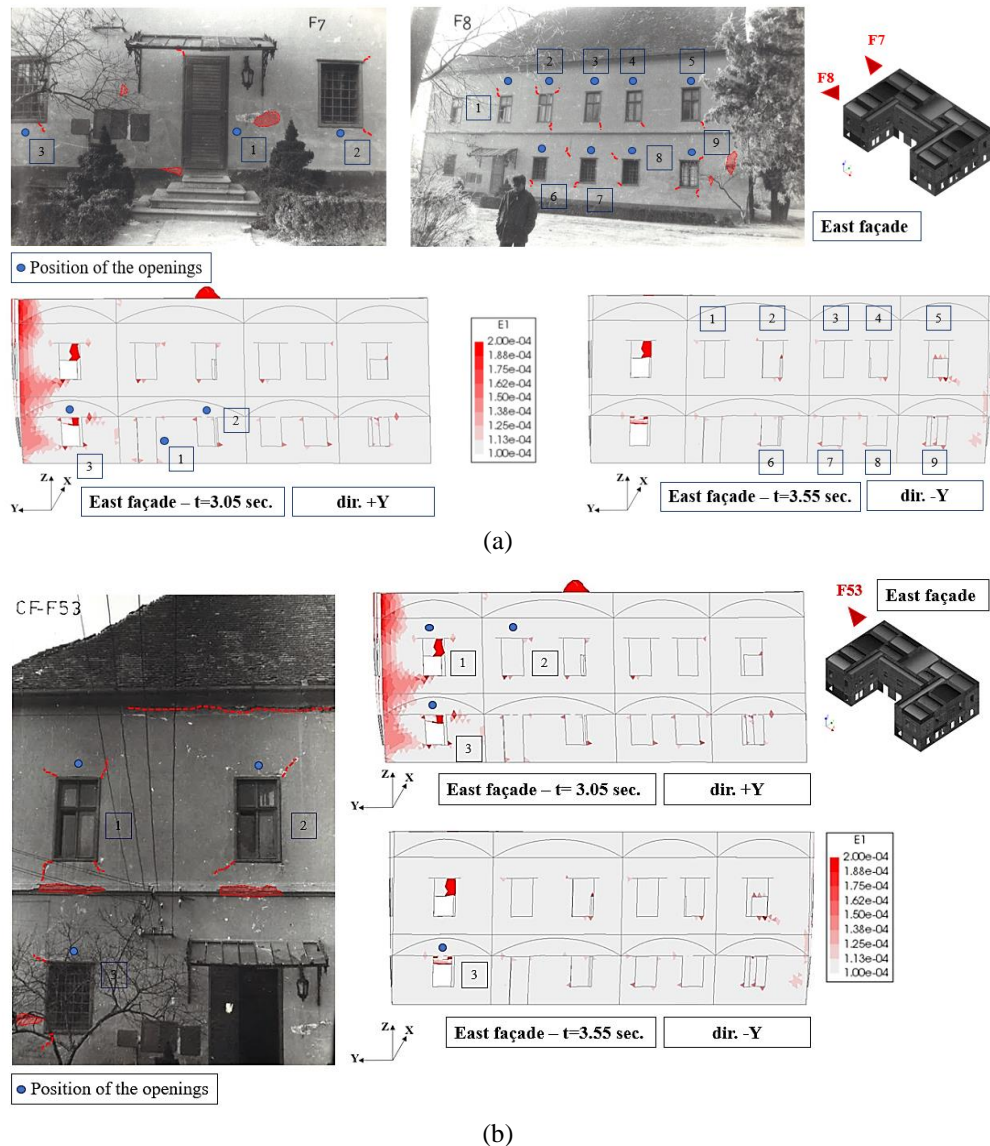


**Figure 4.65:** Damage detected in the East façade.

In particular, it was noted that when the seismic input was concordant with the direction Y of the global reference system ( $t=3.05$  sec), the cracks that have generated in correspondence of the openings made it possible to compare the real damage with the simulated one considering the damage positions 1-3. The cracks that occurred showed a fragile (pseudo vertical) shear mechanism. Consequently, when the seismic action was discordant with the Y direction of the global reference system ( $t= 3.55$  sec), the damage showed a variation of the stress tensor direction, identifying the cracks in positions 1-9.



Similarly, as shown in Figure 4.65 (b) two successive time steps were considered, analysing the cumulative damage effects since, in the numerical model the inversion of the seismic actions opens, closes, and reopens the cracks.

The formation of pseudo-vertical cracks is symptomatic of a state of biaxial stress induced by the concomitance of the horizontal and vertical seismic components. Physically, the vertical earthquake induced the formation of purely vertical sliding planes between mortar and bricks which, with the arrival of the horizontal seismic action, tended to open favouring the formation of cracks. In particular, during the seismic event, at every time step  $t > 2$  sec, the contributions of the shear deformations induced by vertical and horizontal seismic action were added, giving rise to a crack pattern obtained by superimposing effects.

Furthermore, it was possible to note how the masonry wall panels exhibited a typical rocking behaviour as reported in Figure 4.66, highlighting the conformity of the basic hypotheses, as suggested in § 4.3.2.

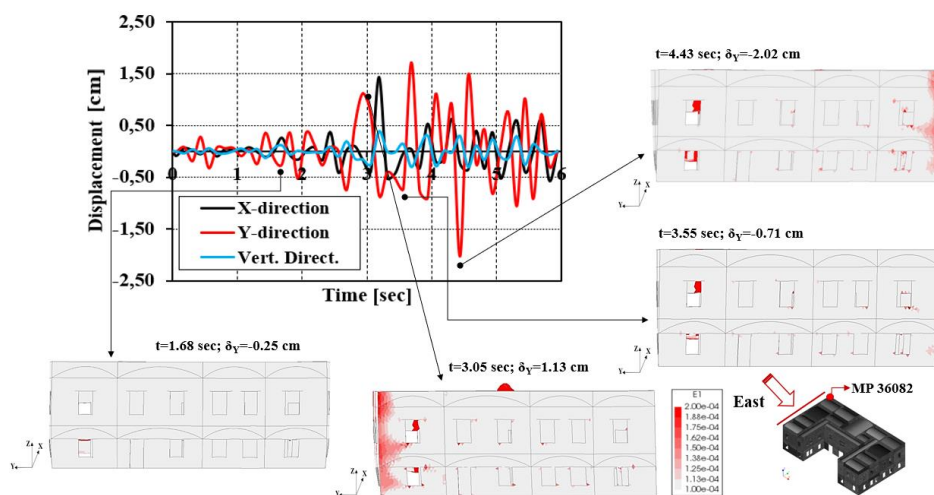


**Figure 4.66:** Rocking behaviour of the masonry wall panels constituting the East façade.

Subsequently, the West façade was analysed, again in Y direction. The results of the comparison between the numerical damage and the real ones have been summarized in Figure 4.67:

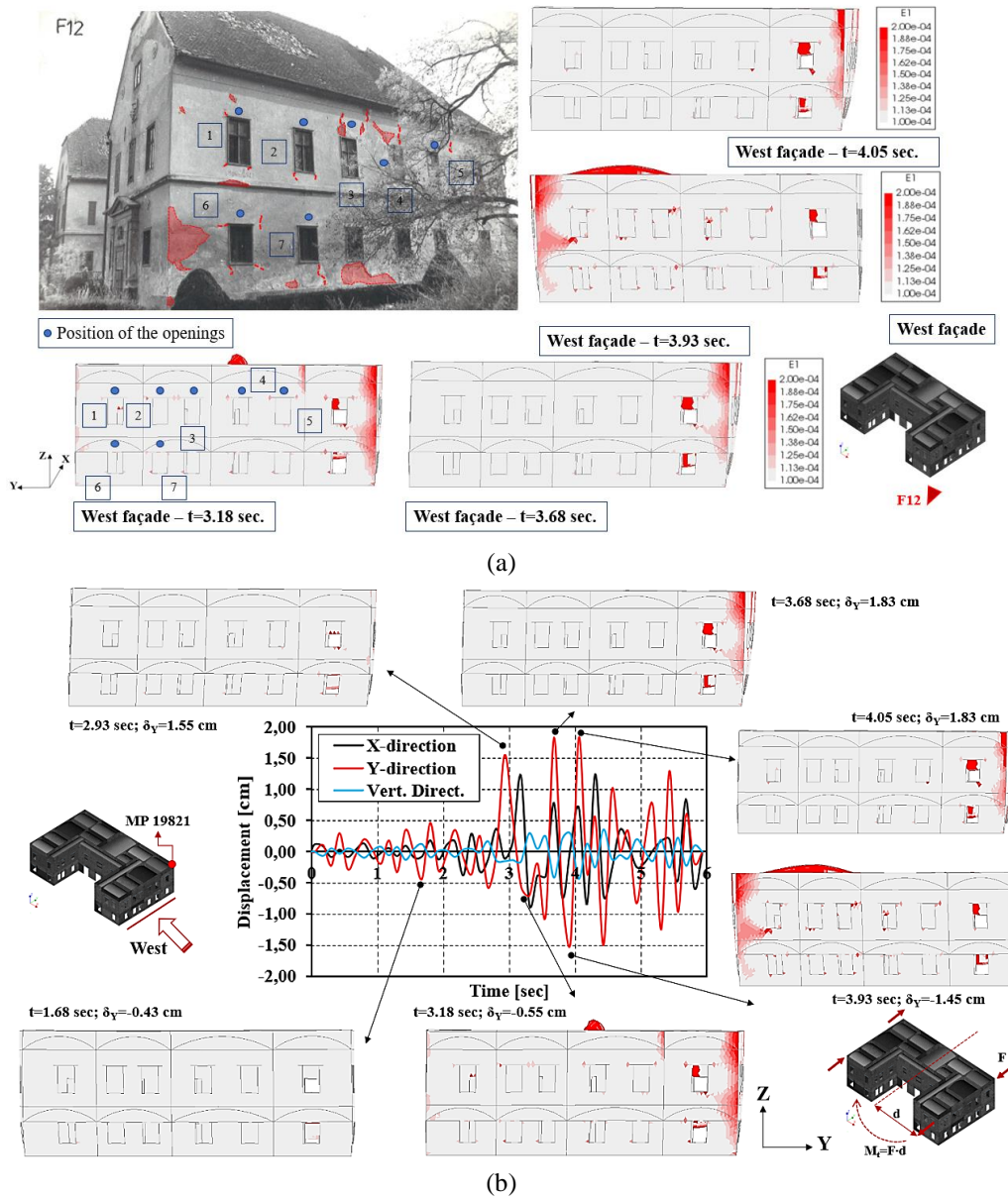


Figure 4.67: Damage correlation considering East façade.

First of all, the results are shown in Figure 4.67 (a) refer to the maximum horizontal displacement peaks. Consequently, as has been noted, there was a reliable correlation between the numerical damage and the real one. In particular, pseudo-vertical cracks were noted at the openings.

These cracks, as previously analysed for the East façade, occurred due to the simultaneous concomitance of horizontal and vertical seismic actions.

Besides, the areas highlighted in red showed a detachment of the plaster following the rocking mechanism triggered in the masonry wall panels.

Subsequently, in Figure 4.67 (b), the maximum displacement peaks have been reported, considering the MP 1982 placed in the corner position of the case study building. From what was analysed it emerged that at  $t < 2$  sec, the façade showed no damage, however for the same time step, the vertical component of the earthquake increased the displacements in the horizontal direction (Y direction), validating what has been reported in the paragraph § 4.2.2.2. Thus, at  $t > 2$  sec, the damage progressively increased since there was the simultaneous action of the horizontal and vertical components of the seismic action, respectively. It is worth noting how at  $t > 2$  sec the displacements that occurred for the analysed prospect were greater than those of the East façade. This circumstance highlighted a very important fact, the triggering of torsional phenomena,  $M_t$ , governed by the presence of the seismic action, causing left-handed floor rotations.

Furthermore, by providing an enlargement of the area adjacent to the right corner of the case study building (Figure 4.68), the damage was compared, provided, with good approximation, conforming results.



**Figure 4.68:** Damage deduced near the right corner of the West façade.

As can be seen from the previous results, following the impulsive action of the ground motion vertical component, the arrival of the horizontal components produced damage to the vertical structures, mainly in the spandrel beams due to the formation of shear failures. It is also worth underlining how the displacement field obtained from the numerical simulation was the result of a 6-second time

history analysis, consequently, by extending the analysis to the entire time history cycle, the displacements would be increased.

Accordingly, the North and South façades of the examined building were analysed and depicted in Figure 4.69.

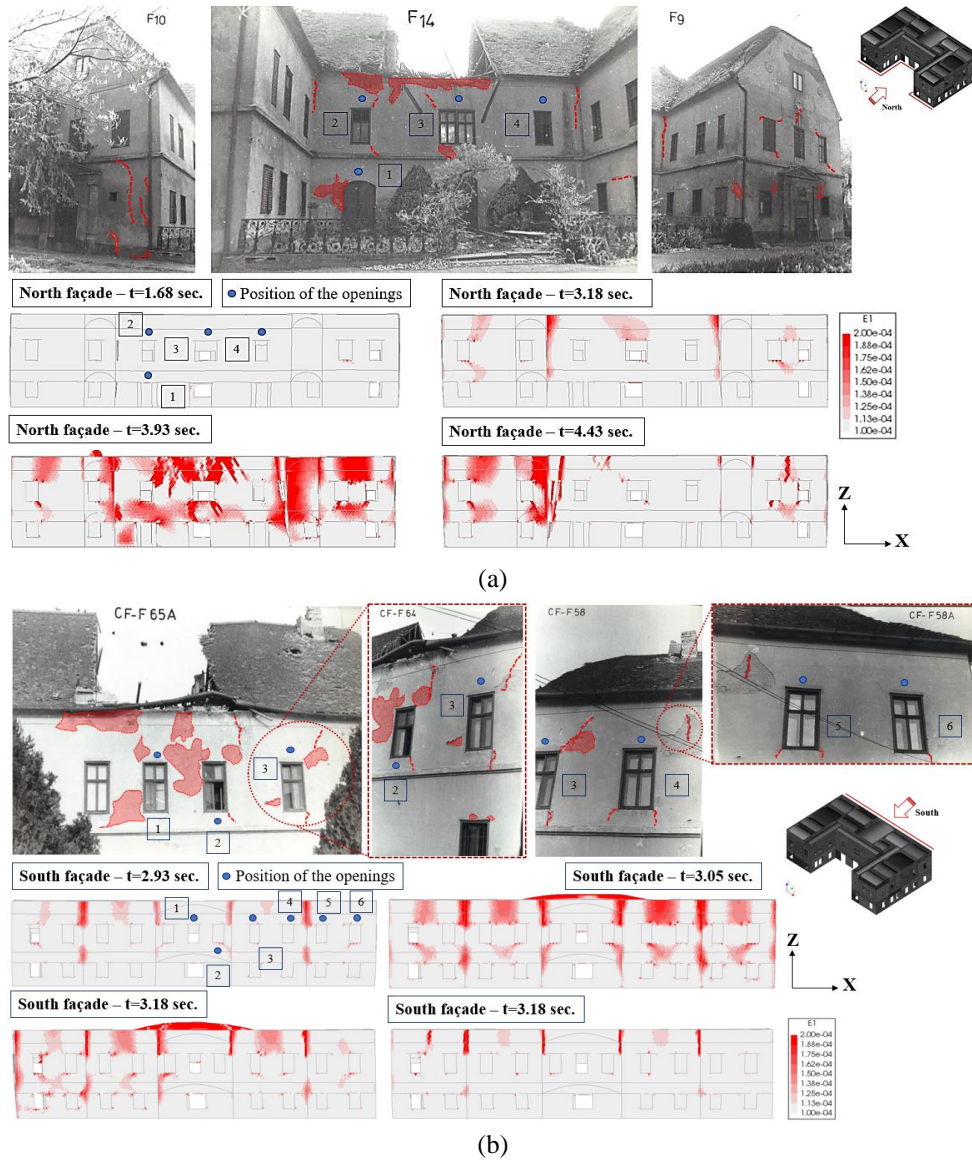


**Figure 4.69:** Damage comparison in the North and South façades, respectively.

By monitoring the control points, 19446 and 19658 regarding the North and South façades, respectively, it was possible to estimate the evolution of the damage by successive time steps, as expressly reported in Figure 4.70.



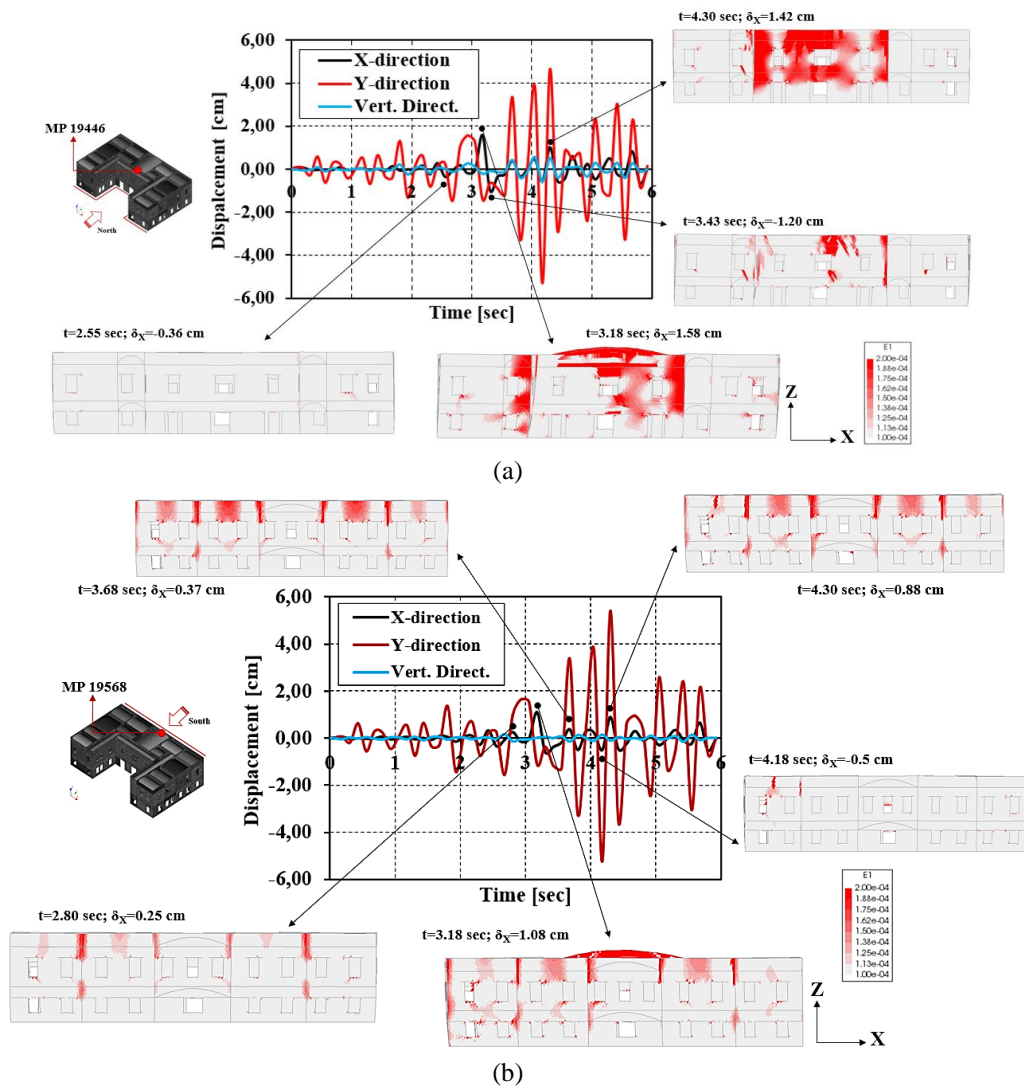


**Figure 4.70:** Evolution of the damage in (a) North façade and (b) South façade, respectively.

From the results shown in the previous figure, it was possible to observe how the displacements in X direction were limited compared to the orthogonal direction, however, the damage shown represented the cumulative effect of the seismic actions, horizontal and vertical, which simultaneously affect the study building. The combination of the seismic actions characterized the global damage, which manifested a uniform distribution of the cracks that corresponded, with good approximation, to what was found in the post-earthquake survey activity. Moreover, also in this case it was observed that in the first seconds of time history the effect of the vertical component of the seismic action tended to increase the displacements in Y direction in both monitored façades.

This aspect confirms what was reported in paragraph § 3.4.3, according to which the amplification action induced by the ground motion vertical component on the horizontal displacements were maximized in the direction of geometric symmetry of the structure. In conclusion, it is possible to summarize what has been examined as follows:

- i. the damage was assessed following the *Principal Total Strain Crack* model, according to which, once the tensile fracture energy ( $G_f$ ) was exceeded, the material cracked;
- ii. in the first two seconds of the time history the vertical cracks are attributable to a vertical shear sliding plane at the interface between adjacent walls (see Figure 4.61) generated by the maximum vertical decompression acceleration peak;
- iii. the effect of the impulsive ground vertical excitation has influenced the deformation of the monitored vault which reached a maximum vertical displacement of 1.00 cm. Subsequently, with the arrival of the horizontal seismic actions, the damage progressively increases extending to the vertical structures (see Figure 4.62).
- iv. it has been observed how the damage produced by the impulsive vertical acceleration caused the collapse of the monitored vault increases the flexural deformability of the masonry walls (see in Figures 4.63-4.64);
- v. in general from the results achieved by analysing Figures 4.66-4.70 it has been observed that in the first two seconds of the time domain no shear cracks have been propagated in the vertical structures. Consequently, with the arrival of the horizontal seismic action, at  $t=3.00$  sec, the shear cracking occurred since the decompressive vertical acceleration reduces the bearing capacity of the wall panels;
- vi. the activation of pseudo-vertical cracks was related to a biaxial stress regime induced by the concomitance effects of the horizontal and vertical seismic components. Physically, the vertical earthquake induced a decompression effect on the masonry elements favouring the detachment between the mortar and bricks, so, the internal cohesion was not guaranteed and the horizontal actions were responsible for the propagation of the cracks in the structural elements.

In general, what has been discussed represents a clear and exhaustive overview concerning a particular case of damage induced by a near-field earthquake on historic masonry buildings located in the Banat Seismic Region.

## 5 Derivation of analytical fragility and vulnerability functions in case of a near-field earthquake

### 5.1 Introduction

Concerning historical structural systems, there is a marked efficiency towards vertical actions but reduced capacity concerning the design seismic actions. In general, these buildings are susceptible to seismic forces since they have constructive deficiencies that intrinsically reduce the building's capacity.

This aspect is fundamental and strongly depends on the connection between the different wall systems that constitute the building. Once this performance limitation has been made known, these structures are therefore affected by a specific level of damage which essentially depends on the severity of a seismic event. In such circumstances, the propensity to damage a structural system can be described analytically through suitable non-linear functions commonly identified as fragility and vulnerability curves, respectively.

Therefore, the first, identify probabilistically, the overcoming of a certain level of damage due to a seismic event of given intensity measurement, IMs, while the second one, representing an empirical correlation between the synthetic damage parameter,  $\mu_D$ , and the variation of the macroseismic intensity.

The substantial difference between the two approaches derives from the different aims of the result. In the first case, using the fragility curves, the probability of exceeding a certain damage threshold is assessed by monitoring the EDPs parameter which can be understood both in terms of displacements or accelerations, respectively; in the second case, the propensity to damage is assessed due to the variation of the macroseismic intensity.

The proposed formulations for the evaluation of fragility and vulnerability curves have been extensively discussed in Chapter II.

However, the intent is to use these functions in the case of near-field seismic phenomena. In this circumstance, the objective is to compare the two simulations examined, such as (H) and (H+V) to evaluate the impact of the ground motion vertical component on the expected global damage for the case study building.



## 5.2 Definition of fragility curves

As mentioned, the fragility curves represent the probability of exceeding a certain damage threshold varying the intensity measurement, IMs. In the specific case, the fragility curves were derived considering the comparison between the two scenarios analysed, (H) and (H+V), respectively. In particular, it was possible to compare the effects induced by the ground motion vertical component on the global fragility assessment of the case study structure. It is also important to underline two fundamental aspects: (i) the simulated seismic phenomenon is impulsive and in the time domain the ground motion vertical component tends to maximize the effects at 1.68 sec; (ii) with the arrival of the horizontal components at  $t > 2$  sec, the vertical seismic input progressively attenuates.

However, according to the scientific literature research [105-107], a systematic procedure of derivation of analytical fragility curves that takes into account the influence of ground motion vertical component on masonry buildings has not been found. With this aim, it is interesting to understand how the simulated near-field phenomenon is related to the probability of exceeding a certain damage limit state. First of all, according to [105], the fragility curves were defined in terms of displacement,  $S_d$ . This choice is supported by the fact that, in the case of impulsive seismic phenomena, the seismic response of the structure was analysed in terms of displacements which provided a quick and clear identification of the influence of the vertical component of seismic action on the global behaviour of the considered study building.

Thus, based on this consideration, it has been appropriate to compare the capacity curves for the two scenarios analysed, that is, (H) and (H+V), respectively.

To fully understand the effects induced by the ground motion vertical, the capacity curves at 33%, 50%, and 100% of the capacity of the structure have been considered, as analysed in paragraph 4.2.3.3. The results were presented in Figure 5.1.

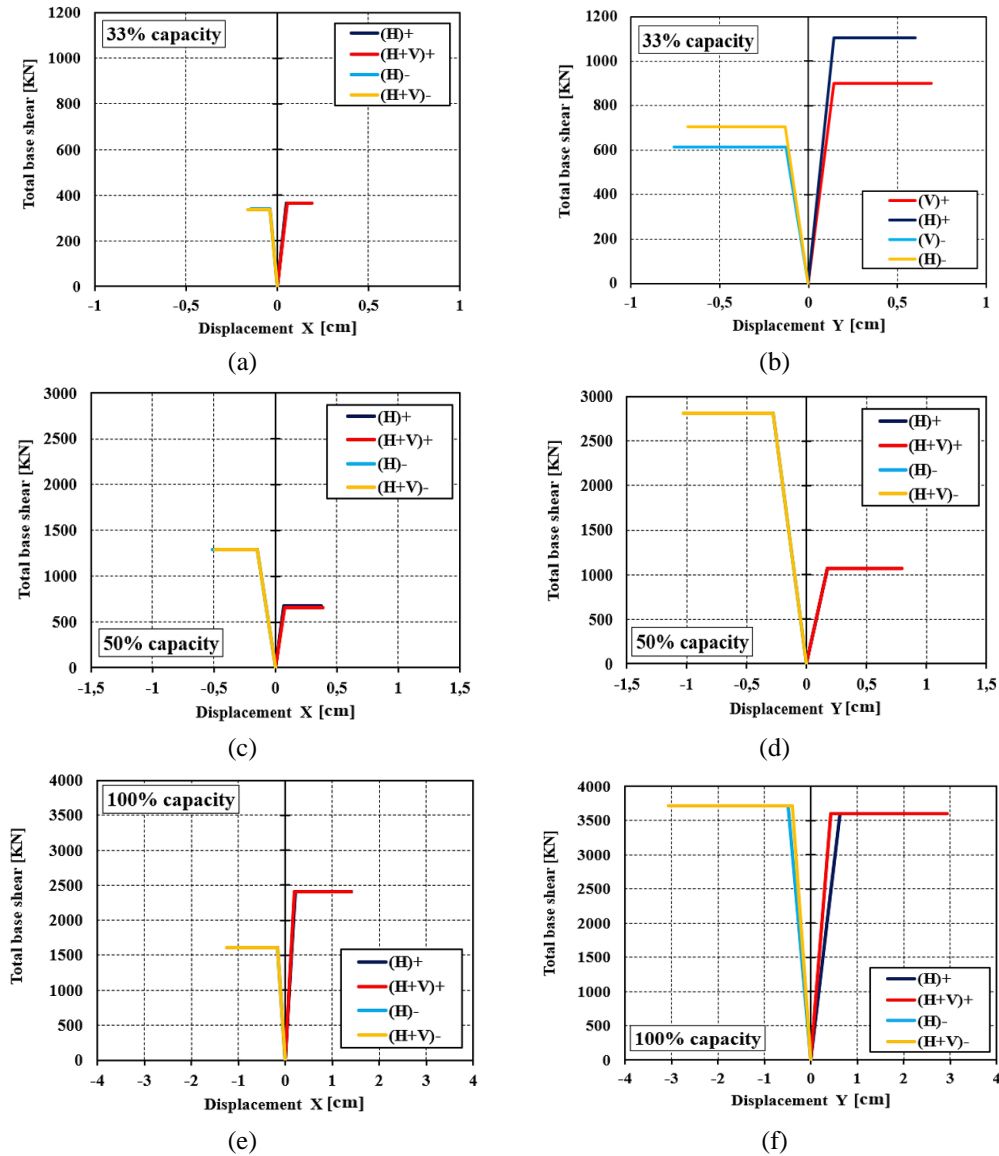


**Figure 5.1:** Capacity curves comparison between (H) and (H+V) scenario, considering (a-b) 33%, (c-d) 50% and (e-f) 100% of the structural capacities.

For completeness of the results obtained in Table 34 and Table 35, the monitored parameters have been summarized concerning the capacity curves presented:

**Table 34:** EDPs for the simulated scenario (H) and (H+V).

(H)

Cap. [%]	X <sup>+</sup> direction			X direction			Y <sup>+</sup> direction			Y <sup>-</sup> direction		
	d <sub>y</sub> [cm]	d <sub>u</sub> [cm]	F <sub>y</sub> [KN]	d <sub>y</sub> [cm]	d <sub>u</sub> [cm]	F <sub>y</sub> [KN]	d <sub>y</sub> [cm]	d <sub>u</sub> [cm]	F <sub>y</sub> [KN]	d <sub>y</sub> [cm]	d <sub>u</sub> [cm]	F <sub>y</sub> [KN]
33	0.05	0.18	366	-0.04	-0.17	340	0.14	0.79	1106	-0.12	-0.85	704
50	0.07	0.37	670	-0.14	-0.50	1294	0.17	0.76	1068	-0.27	-1.00	2808
100	0.19	1.40	2410	-0.15	-1.23	1609	0.62	2.84	3597	-0.49	-2.87	3720

**Table 35:** EDPs for the simulated scenario (H) and (H+V).

(H+V)												
Cap. [%]	X <sup>+</sup> direction			X direction			Y <sup>+</sup> direction			Y <sup>-</sup> direction		
	d <sub>y</sub> [cm]	d <sub>u</sub> [cm]	F <sub>y</sub> [KN]	d <sub>y</sub> [cm]	d <sub>u</sub> [cm]	F <sub>y</sub> [KN]	d <sub>y</sub> [cm]	d <sub>u</sub> [cm]	F <sub>y</sub> [KN]	d <sub>y</sub> [cm]	d <sub>u</sub> [cm]	F <sub>y</sub> [KN]
33	0.05	0.16	366	-0.04	-0.14	337	0.14	0.69	901	-0.12	-0.75	614
50	0.07	0.38	653	-0.14	-0.49	1291	0.17	0.80	1068	-0.27	-1.02	2808
100	0.20	1.40	2410	-0.16	-1.23	1614	0.43	2.92	3597	-0.39	-3.06	3720

As can be seen from the results presented, an increase in terms of both, shear forces and displacements, was observed due to the variation of the structural capacity. In particular, it was observed that in the first step of the analysis, in which only the vertical component of the seismic action was considered (t=1.68 sec), the structural response was suitable to the underlying assumptions (see paragraph 4.2.3.1). It was possible to notice how in X direction (direction of structural asymmetry characterized by torsional phenomena), the two compared scenarios, (H) and (H+V) have provided the same result in terms of shear and displacements, respectively.

Vice versa, in the direction Y, it has been shown, according to what has been stated in paragraphs 4.2.3.1 and 4.2.3.2, how the ground motion vertical component produces an increase in terms of both, base shear and displacements, respectively, if they were compared to the case in which the vertical component was neglected, (H). Subsequently, in the second step of the analysis corresponding at t=3.00 sec and t=6.00 sec, i.e. structural capacity at 50% and 100%, with the arrival of the horizontal components of the seismic action and the attenuation of the vertical component one, the scenarios (H) and (H+V) have provided the same results.

Subsequently, according to the study proposed in [105], the damage thresholds DS<sub>i</sub> (i=1, ..., 4) have been defined as a function of both, yield, d<sub>y</sub>, and ultimate, d<sub>u</sub>, displacements, respectively. In particular, referring to the definition provided in [105], the damage threshold can be defined as follow:

- (i) D1=no structural damage, the structural response is to be considered linear elastic;
- (ii) D2=moderate structural damage; the building is immediately usable after the earthquake, without the need for damage repair;
- (iii) D3=significant

structural damage; the structure is not immediately usable after the seismic event and the damage can be repaired; (iv) D4-D5=condition of incipient collapse; the structure cannot be repaired and must therefore be demolished after the seismic event. From an analytical point of view, the damage thresholds  $DS_i$  has been presented following the following Equations [105]:

$$D_1 = 0.7 \cdot d_y \quad (5.1)$$

$$D_2 = 1.5 \cdot d_y \quad (5.2)$$

$$D_3 = \frac{1}{2} \cdot (d_y + d_u) \quad (5.3)$$

$$D_4 - D_5 = d_u \quad (5.4)$$

Operationally, the fragility curves were derived using the lognormal distribution function, proposed in [106] as reported in Equation 5.5:

$$P[DS | S_d] = \Phi \cdot \left[ \frac{1}{\beta} \cdot \ln \left( \frac{S_d}{S_{ds}} \right) \right] \quad (5.5)$$

where  $P [DS|S_d]$  represents the probability of exceeding a considered limit state,  $\Phi$  is the standard normal cumulative distribution function,  $S_{ds}$  is the mean value of the displacement according to the previously defined limit states and  $\beta$  is the lognormal standard deviation. As proposed in [227], [228], [89], [107], an evaluation of the lognormal standard deviation for each set limit state was proposed, however, in the specific case, a single value of  $\beta$  parameter was assumed for the four limit states defined above. According to what was reported in [105], this choice lies in the fact that we tried to minimize the difference between the lognormal distribution and the cumulative binomial one.

In this circumstance, it was established that the probability limit of exceeding was equal to 50%. The standard deviation adopted has been presented in Equation 5.6 [105]:

$$\beta = 0.45 \cdot \ln(\mu) \quad (5.6)$$

having assumed  $\mu$  as the structural ductility.

So, based on these recommendations, first of all, the maximum capacity curves were selected referring to the global directions X and Y respectively, for

each verse direction (positive and negative) and each structural capacity variation.

This choice, therefore, led to a maximization of the expected effects by considering the most unfavourable condition. To this purpose, the results have been plotted in Figure 5.2 referring to the direct comparison of the scenario (H) and (H+V) respectively, having considered different capacity thresholds in the two analysis directions X and Y, respectively.

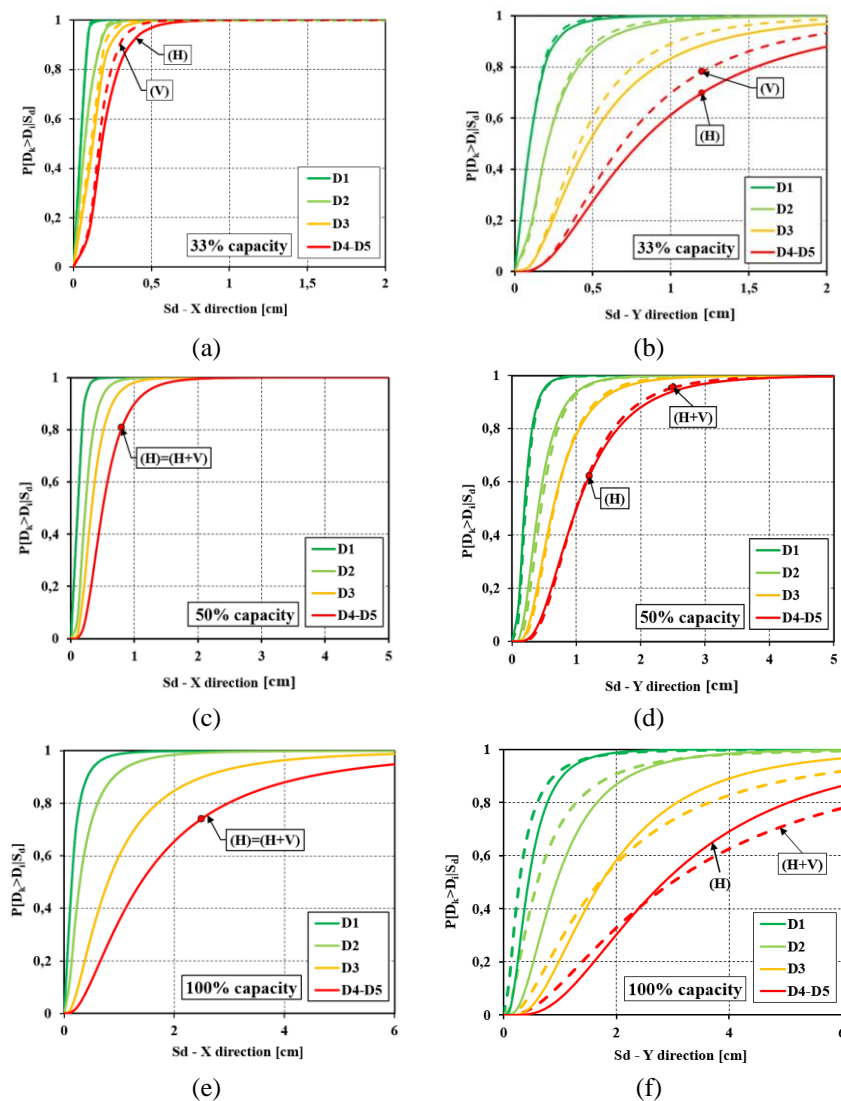


**Figure 5.2:** Fragility curves developed for (H) - (solid line) and (V) - (dashed line) scenario for a different level of structural capacity.

The results obtained reflect the behaviour of the structure considering the influence of the ground motion vertical component. First of all, the structural behaviour deriving from the simulated scenarios, (H) and (H+V), was suitably superimposed in the same graph and implicitly diversified by adopting two different line styles, that is, the continuous line for scenario (H) and dashed line for the scenario (H+V), respectively. This circumstance has allowed to directly compare the different expected damage conditions.

Subsequently, it is noted that by increasing the level of structural capacity, the displacements associated with both scenarios progressively increased. It is worth highlighting how the condition at 33% of structural capacity was purely induced by the ground motion vertical component, whose seismic input was concentrated in the first two seconds of the time history, provided reduced displacements since the structure was in a linear elastic range.

Therefore, referring to the condition of 33% of the structural capacity, it was noted that in both analysis directions, X and Y, the scenario (V) provides damage probabilities, associated with the damage thresholds D1 and D2, very close to the scenario (H). Furthermore, for a damage level D3 and D4-D5, it was noted that scenario (V) has provided a probability of occurrence of a specific damage threshold higher i.e. 13% than the scenario in which the vertical component of the seismic action was neglected, (H), resulting more vulnerable.

Furthermore, it was noted that in X direction the structure has shown reduced displacements, since, as described in paragraph § 4.2.2.2, the structure exhibited an asymmetrical behaviour and was affected by torsional phenomena.

Subsequently, considering the capacity at 50%, it was noted that both scenarios (H) and (H+V) in X direction, have provided the same probability of damage, resulting perfectly coincident. This condition was very significant since for this structural capacity threshold, the effect of the vertical component of the seismic action was dissipated and the horizontal components were maximized, therefore the two scenarios (H) and (H+V) were completely comparable. Moreover, in Y direction, it was noted that the scenario (H+V) has provided a slightly higher probability of damage than the corresponding scenario (H) for the damage thresholds D3 and D4-D5, respectively.

From a physical point of view, this phenomenon has allowed to further contextualize how in Y direction the displacement capacity was greater than in the orthogonal direction since the cumulative effects of the ground motion vertical component have produced a slight reduction in terms of global resistance for a time step of 3.00 sec.

Analysing the behaviour for a structural capacity equal to 100%, a significant increase of the spectral displacements has been noted compared to the cases examined previously. In this condition, the time history domain was completed and all the cumulative effects induced by vertical and horizontal seismic actions have been dissipated. It was noted as in X direction both scenarios analysed, (H) and (H+V), have provided the same probability in terms of damage thresholds D1-D5. Nevertheless, in Y direction, it was noted that for damage thresholds D1 and D2, the scenario (H+V) provided a slightly higher probability of damage than the corresponding (H) since in the elastic field, the vertical component influence the displacements of the scenario (H+V) in which reached the exceeding of the elastic damage states first. Moreover, for damage thresholds D3 and D4-D5, the vertical component produced an improvement in terms of mechanical characteristics since, as previously stated, the compressive vertical acceleration peak, despite their high-frequency content, has guaranteed an enhancement of the resistance while the decompressions peaks did not generate any type of localized structural deficit since they were properly balanced by gravitational loads.

So, the simulated shallow seismic phenomenon was an impulsive event since the ground motion vertical component released all the seismic energy input in the first seconds of the time history (when the structure was still in the elastic phase) providing a very small range of displacements. However, in a much broader overview, it may be considered appropriate to use the proposed treatment for the definition of fragility curves in case of a near-field phenomenon. In this circumstance, the parameters monitored were the displacements since they allowed to focus directly and comprehensively on the global behaviour of the structure. This condition can be considered advantageous in the case in which an adequate number of accelerometric recordings were not available to define the fragility functions in terms of acceleration and the control of the target displacements was easy even for professional purposes. Therefore, as a consequence of the acquired results, it was possible to derive the following considerations:

- i. the fragility curves were analytically processed for near-field earthquake emphasizing that were no other resources in the scientific literature;
- ii. in the case of VGM, the fragility curves in X direction presented the most unfavourable condition. It was observed that for a structural capacity of 33%, the two scenarios (V) and (H) have presented an exceeding probability of 80% and 60% respectively, for a damage threshold equal to D4-D5;



- iii. the displacements achieved in X direction for a structural capacity of 33% were reduced since the ground motion vertical component released all its energy input in the first seconds of the time domain. Moreover, in X direction, it has been noted that scenario (V) has provided little higher damage probability thresholds compared to scenario (H) since at  $t=1.68$  sec the structure was affected by the induced effects of the ground motion vertical component;
- iv. in X direction, for a structural capacity of 50%, the two scenarios (H) and (H+V) have provided the same results in terms of damage. In X-direction the structure was not affected by the VGM, therefore the curves were coincident. In Y direction, it was noted that the vertical component of the seismic actions tends to slightly reduce the capacity of the structure with a mean percentage reduction of 5% for the damage thresholds D3 and D4-D5.
- v. considering a structural capacity of 100%, in X direction the perfect coincidence of the fragility curves was observed, which provided the same probability of damage for both scenarios analysed, (H) and (H+V), respectively. In Y direction, it was noted that for damage thresholds D1 and D2, the vertical component increases the vulnerability for the scenario (H+V). However, for the damage thresholds D3 and D4-D5, the VGM has dissipated its energy input resulting lower than the corresponding horizontal accelerations.

### 5.3 Definition of vulnerability curves

The assessment of the propensity to damage a given structural system can be analysed in terms of macroseismic intensity by defining suitable vulnerability functions. In particular, the typological vulnerability curves represent to all effects a non-linear correlation between the degree of expected damage and the macroseismic intensity. These functions allow estimating, for each value of expected macroseismic intensity for a given site, the corresponding structural damage in terms of a synthetic parameter the mean damage grade,  $\mu_D$ .

This treatment, proposed by [75], is functional in the case in which there is no knowledge of the seismicity of the area in terms of PGA. As described in paragraph 2.2.1.2, Equation 2.8, shows the functional parameters of the formula that lead to defining the mean damage grade,  $\mu_D$ .

The main parameters are: (i) the normalized vulnerability index,  $V_I$ , which is indispensable for identifying the vulnerability of a given structural system, the damage level is identified from its value; (ii) the macroseismic intensity,  $I$ , ranging from V (minimum) to XII (maximum), intended as the hazard of a specific geographical area; (iii) the global ductility factor,  $Q$  which depends on the type of structure examined.

However, the original formulation proposed by [75], is not always applicable to every structural system, since it tends to underestimate the expected damage because it is calibrated on a set of buildings that are typologically and structurally different from what is generally found. The studies proposed by [87-89], [229], [230] have proposed some modifications to the formulation originally proposed by [75] for the evaluation of the mean damage grade. It was observed that the post-earthquake damage found in the scenario analyses obtained by using the mechanical approach was not correlated to the damage value achieved using the original formulation.

In this perspective, in this paragraph, the main objective is to propose a mathematical formulation that is easily usable and that takes into account the real damage caused by near-field events. In this perspective, the functional process that led to the definition of the macroseismic damage-intensity mathematical law was developed considering: (i) the evaluation of the seismic vulnerability index of the case study building using the ADRS spectrum [104] following the response spectrum for the Banat Region; (ii) the evaluation of the macroseismic intensity deriving from the hazard analysis of the Banat Seismic Region; (iii) the assessment of post-earthquake damage and damage found by mechanical analysis;

Thus, first of all, the ADRS spectrum relating to the Banat Seismic Region was defined, starting from the knowledge of the acceleration response spectrum ( $S_{ae}$ ) and displacement response spectrum ( $S_{de}$ ), respectively. Figure 5.3 has been presented both, response spectrums in terms of acceleration and displacement relative to the Banat Region.

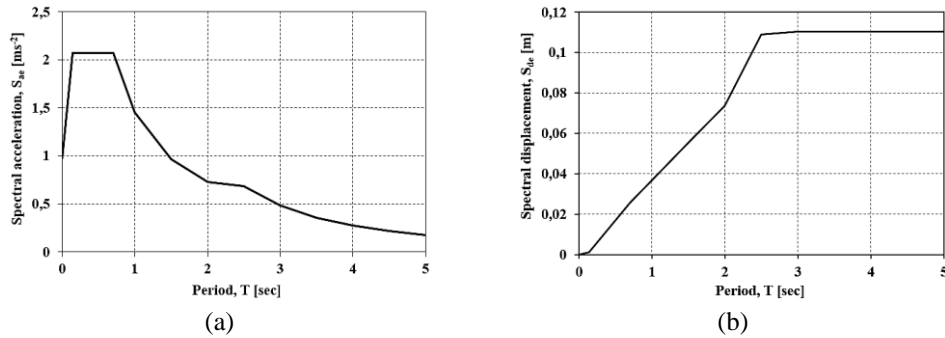


**Figure 5.3:** Banat design spectrum (a) acceleration response spectrum and (b) displacement response spectrum.

Subsequently, according to Equation 5.7, it was possible to define the ADRS spectrum (Acceleration Displacement Response Spectrum, [104]), as reported in Figure 5.4, to characterize the seismic vulnerability of the case study building.

$$S_{a,e} = \omega^2 \cdot S_{d,e} = \left( \frac{2 \cdot \pi}{T} \right)^2 \cdot S_{d,e} \quad (5.7)$$

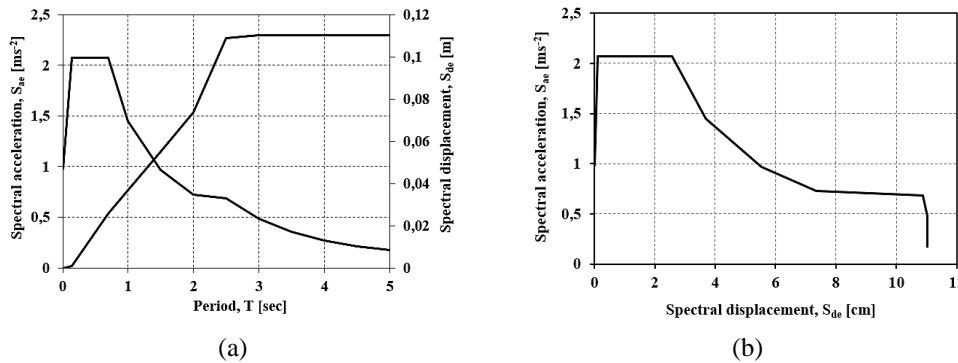


**Figure 5.4:** ADRS spectrum for the Banat Seismic Region.

Consecutively, it was possible to determine the mechanical vulnerability index associated with the MDoF system considering the global capacity of the structural system. To this purpose, in the two analysis directions, X and Y, have been evaluated the seismic safety index,  $V_I$ , through the ratio between the structural capacity,  $C$ , and the corresponding earthquake demand,  $D$ , as reported in Figure 5.5.

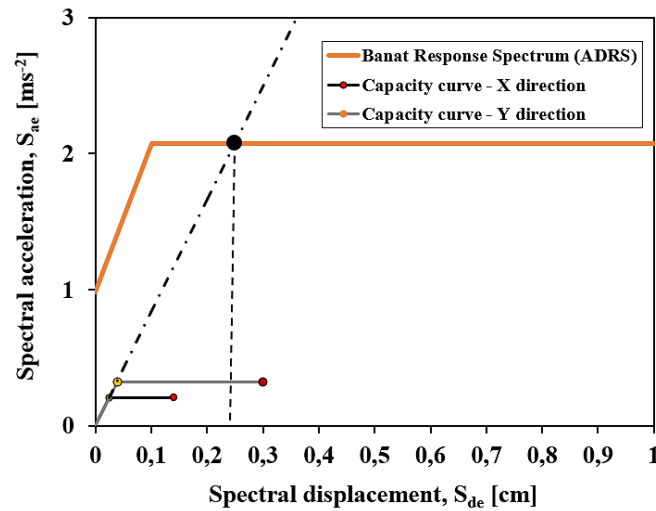


**Figure 5.5:** Evaluation of seismic vulnerability index of the MDoF system in the two-analysis direction, X and Y, respectively.

Thus, considering what has been shown in the previous figure, it was noted that the safety index in the two main analysis directions presented a variability of the results. It was noted that the most unfavourable condition has been reached in X-direction.

Specifically, in X direction, as described in § 4.2.2.2, the reduced capacity of the structural system was essentially attributed to a non-symmetrical behaviour that was further aggravated by torsional phenomena. In such circumstances, the aforesaid direction was not very influenced by the vertical seismic action, consequently, the reduced energy dissipation capacity led to a significant reduction of the displacement ductility. Therefore, the seismic safety index was equal to  $V_{I,X}=0.63$ , having considered the seismic demand equal to 0.22 cm and the corresponding capacity of the structural system equal to 0.14 cm. Vice versa, in Y direction, the structure has presented symmetrical behaviour, moreover, as can be seen in Figure 5.5, a considerable increase in terms of both, displacement (hence in ductility) and resistance, generated by the vertical seismic action, was observed. In this condition, the safety index,  $V_{I,Y}$ , was equal to 1.5.

The results have been summarized in Table 36:

**Table 36:** Results achieved evaluating the mechanical safety index in case of VGM excitation.

Capacity [cm]	Demand [cm]	$F_y^*$ [ $ms^{-2}$ ]	$V_{I,X}$	$V_{I,Y}$
0.14	0.22	0.21	0.63	-
0.33	0.22	0.32	-	1.5

Similarly, considering the scenario generated in case of the absence of vertical seismic action, (H), the same verification was carried out for estimating the mechanical vulnerability index, as shown in Figure 5.6.

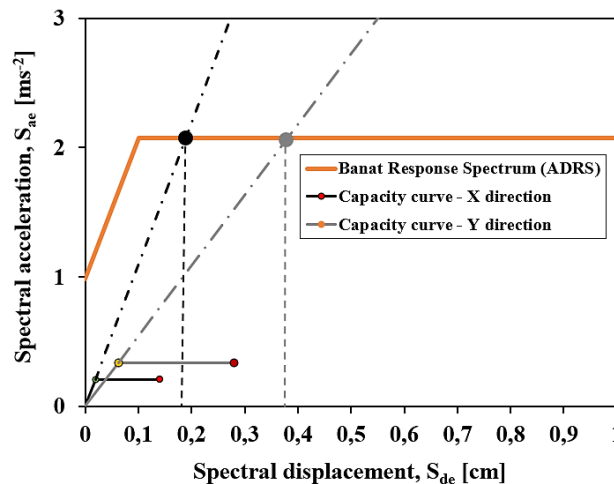


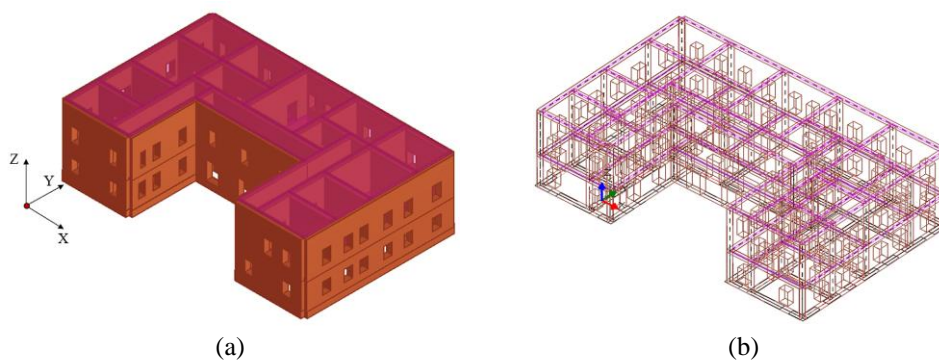
**Figure 5.6:** Evaluation of mechanical vulnerability index in absence of VGM.

From the archived results, it was observed that in both analysis directions, the displacement capacity was less than the corresponding seismic request. This result has been confirmed to what was observed in paragraph § 5.1, in which, in absence of ground motion vertical component, the structure presents a higher vulnerability. This circumstance was supported by the fact that the vertical seismic action, at time step  $t=1.68$  sec, has generated a beneficial effect due to the maximum compression acceleration peak. However, according to the scenario presented in the previous figure, the mechanical safety index was defined, which appears to be equal to 0.77 in X direction and 0.73 in the Y-direction.

Besides, the seismic behaviour of the case study building was implemented using the 3Muri software [226], to identify and quantify the damage caused considering the ground motion horizontal components only. In this sense, a non-linear static analysis was performed.

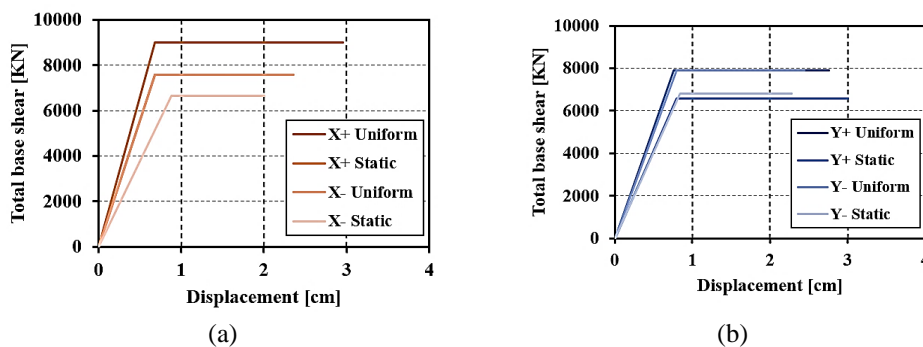
It is worth highlighting how the adoption of the 3Muri software [226] aims to highlight exclusively the damage that occurred in the various structural elements since, in terms of the analysis procedure, the non-linear static is too conservative compared to what has been analysed utilising non-linear dynamic analysis.

Furthermore, the equivalent frame approach brings with it uncertainties regarding the modelling phase related to the effective identification of the typological class of the building. As discussed in Chapter 4, the buildings, belonging to the first typological class, has been characterized by a local seismic behaviour; in this perspective, it appears evident that the equivalent frame modelling (macroelements) erroneously considers the presence of rigid nodes and spandrel beams which should be neglected in the calculation phase. So, following what has been stated, in Figure 5.7 the model elaborated through 3Muri software was shown.



**Figure 5.7:** Structural model elaborated through 3Muri software, (a) solid model, (b) wireframe model.

Consecutively, Figure 5.8, has been presented both, the plotted capacity curves and the global damage obtained by non-linear static analysis considering the two analysis directions, X and Y, respectively.



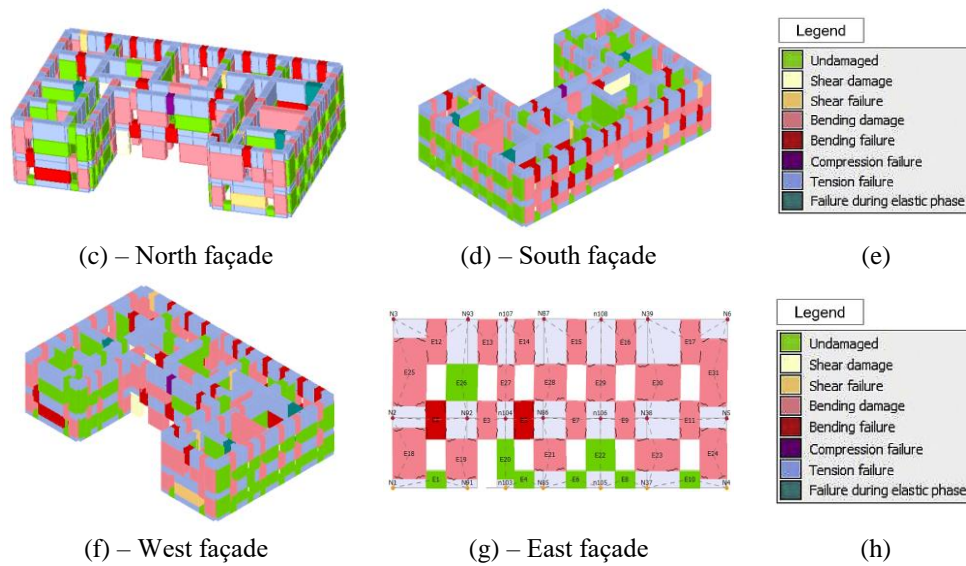


**Figure 5.8:** Non-linear static analysis results, (a-b) capacity curves in X and Y directions, (c-g) damages detected in each façade.

As can be seen, being a pushover analysis, the displacements were greater than those estimated by time history. This discrepancy arises from the fact that using a non-linear static analysis the following limitations were found: (i) it does not simulate the real behaviour of the building without taking into account any local behaviour; (ii) does not take into account the real behaviour of the structure subjected to the real recorded seismic event; (iii) does not take into account possible out-plan mechanisms. However, it can be seen from the damage level reached that a greater number of wall panels tend to crack due to the rocking mechanism (compatibly to what was explained in the time-history analysis) while the spandrel beams collapse due to the bending mechanism at ULS.

The seismic verification was carried out regarding the MDoF system deriving from the two worst analyses in the X and Y direction (static distribution of forces), using the ADRS spectrum [104] as depicted in Figure 5.9.



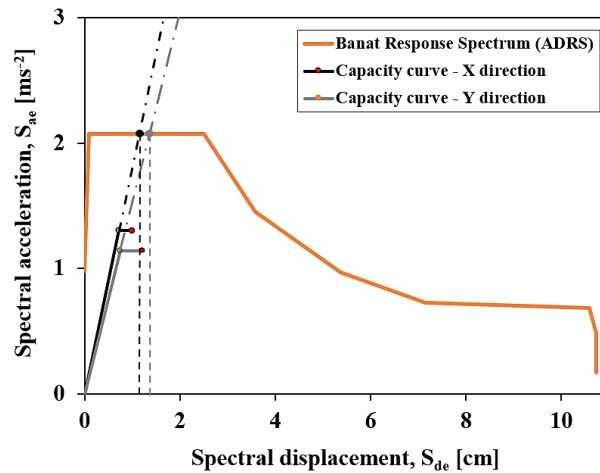


Figure 5.9: Seismic verification adopting the ADRS spectrum.

Therefore, concerning what is shown in the previous figure, it was possible to estimate the seismic safety indexes,  $V_{I, X}$  and  $V_{I, Y}$ , equal to 0.86 and 0.81, respectively.

Another important step regarding the analysis of the hazard in the Banloc area to characterize the seismic intensity occurred due to the event in 1991.

In particular, the seismic event has presented a magnitude,  $M_w$  equal to 5.5 produced considerable damage to the structures located in the study area. Referring to the seismic intensity-magnitude correlation ( $I-M_w$ ) proposed by [60] it was possible to determine the maximum threshold of macroseismic intensity that occurred in the area.

In particular, it was observed that for a shallow earthquake of a moment magnitude,  $M_w=5.5$ , the seismic intensity was equal to VII-VIII which corresponds to damage equal to D3-D4 (many buildings have serious cracks localized in the load-bearing walls. So, based on this consideration a vulnerability curves have been derived according to the original formula proposed by [90], see § 2.1.2.2, considering both scenario (H) and (H+V) performed using both, non-linear static (NLSA) and dynamic analysis (TH) for the two-analysis direction, X and Y, having assumed a ductility factor Q equal to 2.3 [90]. The results have been reported in Figure 5.10.

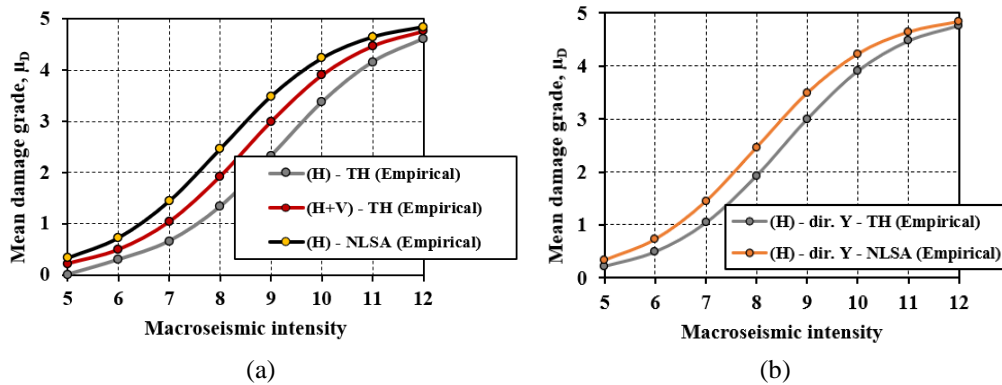


Figure 5.10: Vulnerability curves resumed through the empirical formulation proposed in [90].

First of all, the typical vulnerability curves derived through non-linear dynamic analysis (TH), by employing DIANA FEA software [194] were compatible in the two analysis directions, X and Y.

Referring to the non-linear static analysis (NLSA), developed by using 3Muri software [226], it was deduced how the vulnerability curves in the X and Y direction, providing results in terms of damage greater than those proposed by the TH analysis.

This limiting aspect was one of the intrinsic phenomena of non-linear static analysis, which, being a “push” analysis, did not take into consideration any local behaviour of macroelements.

Secondly, as has been noted, the formulation proposed by [90] did not fully capture the level of damage that occurred for macroseismic intensity equal to VII-VIII, underestimating the real damage detected after the seismic event in 1991.






It should be noted that the vulnerability curve in Y direction for the scenario (H+V) was omitted since the seismic verification was satisfied.

It is quite evident that the earthquake that occurred in Banloc caused significant damage to historic masonry buildings as shown in Chapter 4. For this reason, it is essential to calibrate the empirical methodology based on the results obtained by numerical simulation.

Thus, is necessary to guarantee a mathematical formulation that correlates the observed damage that occurred in the epicentre, equal to D3-D4, to the macroseismic intensity of VII-VIII according to the EMS-98 scale [60].

In particular, Table 37 has been summarized the correlation between expected damage and macroseismic intensity level [60].

**Table 37:** Correlation between damage and macroseismic intensity for masonry buildings.

D0-D1	D2	D3	D4	D5
				
Negligible damage	Moderate damage	Substantial damage	Severe damage	Collapse
Macroseismic intensity -EMS-98				
I-V	V-VII	VII-VIII		VIII-IX-X <sup>+</sup>

So, the mathematical expression of the proposed law is given by the following Equation (5.8):

$$\mu_D = 2.5 \cdot \left[ 1 + \tanh \left( \frac{I_{\text{EMS-98}} + \psi \times V_1 - \lambda}{Q} \right) \right] \quad (5.8)$$

having assumed the  $\psi = 12.10$ ,  $\lambda = 14.00$ , and the  $Q = 1.50$ .

Thus, a representation of the damage-intensity curve has been provided, as illustrated in Figure 5.11.

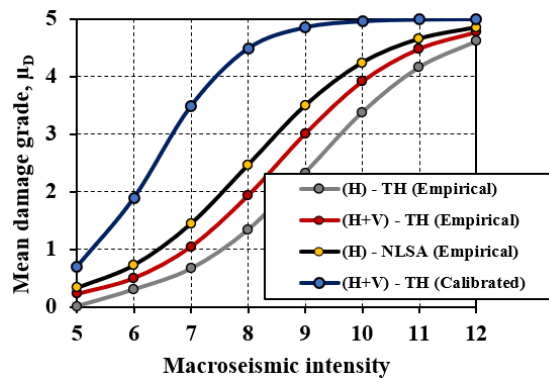


**Figure 5.11:** Calibrated typical vulnerability curves in the case of VGM.

From the results depicted in Figure 5.11, it has been possible to notice that the original empirical formulation proposed in [90], is too conservative for predicting the expected damage and cannot be adapted to the Banat Seismic Region in case of a near-field earthquake.

In contrast, the new formula, even if it requires further development, allowed to predict a damage level (equal to D3 and D4, as shown in Table 38), compatible

with the post-earthquake damage (see Chapter 4), obtained through numerical analyses simulation in a non-linear dynamic field.

Subsequently, in [15] the calibration of the typological vulnerability curves derived based on the seismic event that occurred in Banloc in 1991 was reported considering the effects that were produced at a distance of 20-25 km from the city of Timisoara. The formula was calibrated through non-linear static analysis, proposing a slight variation of the original formulation, having assumed a  $\psi$ -factor equal to 12.50 and a ductility factor,  $Q$ , equal to 2.3.

Based on these considerations, the formulation calibrated in [15] and [192] was suitably compared to what has been derived employing TH analysis previously proposed (see Equation 5.8) to provide a forecast of the expected damage among the applied methodologies.

However, the maximum expected acceleration for the Banat Seismic Region, prescribed by the Romanian design code [39], is equal to 0.2 g which corresponds to a maximum macroseismic intensity equal to IX according to the empirical correlation law proposed by [231] as explained in Equation 5.9:

$$\log(a_g) = C_1 \cdot I_{EMS-98} - C_2 \quad [g] \quad (5.9)$$

having assumed the correlation coefficients,  $C_1$  and  $C_2$  equal 0.602 and 7.073, respectively.

The proposed correlation has been plotted as shown in Figure 5.12.

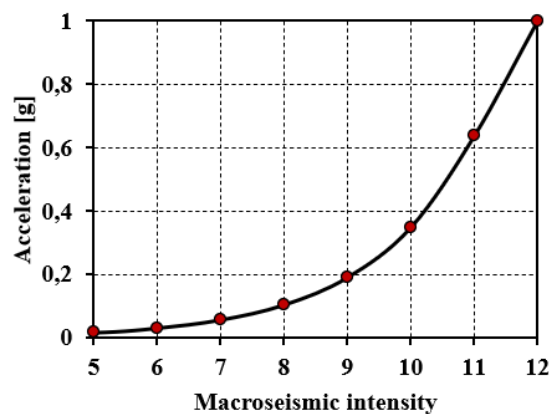
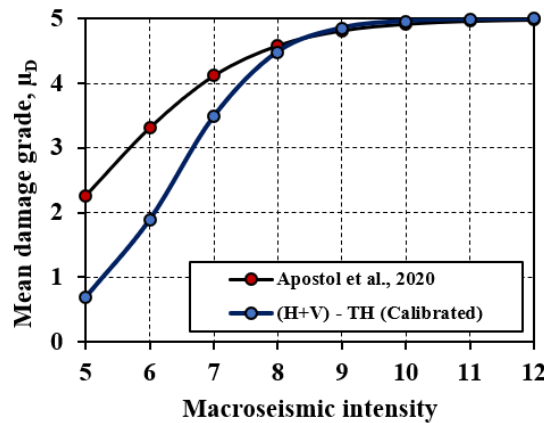


Figure 5.12: Correlation between macroseismic intensity  $I_{EMS-98}$  and  $a_g$ .

So, the comparison between the methodologies applied has been presented in Figure 5.13 having fixed a safety seismic index,  $V_I$ , equal to 0.63.



**Figure 5.13:** Comparison between typological vulnerability curves for the near-field event.

It can be seen how the curve proposed by [15] and [192] provides expected damage values higher than the ones derived from the calibrated method proposed, which was based on the TH analysis procedure developed carefully for the case study building. In particular, the proposed calibrated-formula have provided, for macroseismic intensities VII, VIII, a damage percentage decrement equal to -18%, -2%, and for intensity IX, an increment of +1%, in comparison to what has been expected by [15], [192]. The results have been depicted in Table 38:

**Table 38:** Damage comparison for the investigated area.

Numerical Procedure	Damage assessment		
	VII	VIII	IX
Apostol et al., 2020 (NLSA) [192], [15]	4.11	4.58	4.81
Calibrated curve (TH)	3.48	4.48	4.85
Damage difference	-18%	-2.0%	1.0%

From the comparison of the results, it emerged that the formulation proposed by [15], [192] has provided higher damage levels than those appropriately calibrated through TH analysis. Substantial increases in terms of damage were found for the macroseismic intensity VII and VIII (+18% and +2.0%, respectively) but a moderate difference for intensity IX (1.0%).

However, what has been proposed in [15], [192] represents the upper limit of a vulnerability analysis conducted for a class of buildings located at 20-25 km from the epicentre using a non-linear static analysis procedure (very restrictive) compared to what was appropriately calibrated through non-linear dynamic analysis for buildings located at 7 km far from the epicentre. Therefore, certainly, from the aforementioned Table 47, it appears that the proposed formulation, if

compared with the method proposed by [15],[192] provides safe and appreciable results in predicting the possible expected damage in the case of a near-field event.

The calibration of the typological vulnerability curves highlighted important aspects concerning the behaviour of buildings subjected to near-field events. In particular, from the estimates made it was possible to note the following indications:

- i. by adopting the non-linear dynamic analysis, it was noted that the scenario (H+V) in X-direction had a lower seismic safety index (-42%) than the orthogonal direction, Y, which presented a safety index equal to 1.50;
- ii. the damage was assessed using 3Muri software [226]. The non-linear static analysis provided an increase of the damage compared to TH analysis. This phenomenon was desirable due to the unrefined methodology. However, it was found that the damage level estimated by the macroelements approach was compatible with the estimated one by adopting the DIANA FEA [194] software regarding the rocking mechanisms (post elastic phase);
- iii. the proposed formulation of the mean damage grade,  $\mu_D$ , has been appropriately calibrated based on the damage that occurred in the epicentral area which was compatible with the damage thresholds D3-D4 according to the EMS-98 scale [60]. In this regard, a value of 12.10 was associated with the coefficient  $\psi$ , which affects the slope of the curve, 14.0 with the factor that affects the concavity of the vulnerability curve and finally assigning a ductility factor,  $Q$ , equal to 1.50;
- iv. the proposed formulation has been compared to the relationship proposed by [15] and [192]. From the results acquired, it emerged that the formulation proposed by [15] and [192] has provided higher damage levels than those appropriately calibrated employing TH since the empirical formulation has been calibrated, in a safe side condition, condition utilising a non-linear static analysis procedure for a building class located at 20-25 km from the epicentre;
- v. in terms of damage, it has been estimated that the proposed formulation provides satisfactory results deriving from the calibration of the damage level that occurred in the epicentral area.

In general, the methodology proposed in this thesis could be further used for the evaluation of the seismic vulnerability of other historic masonry buildings characterized by the same typological and structural peculiarities located in the epicentral area. The seismic vertical component especially for shallow earthquakes is undoubtedly a high-risk factor to be taken into account in the analysis of seismic damage since it would guarantee a profitable forecasting activity for the protection of structures and mitigate possible disastrous effects. It has been noted that for shallow earthquakes the probability of having significant structural damage induced by the vertical seismic component is greater than 50%. Therefore, the methodology described represents a simplified approach for the prediction of seismic damage based on numerical simulations and is also useful for professional purposes.



## 6 Conclusion

The presented Ph.D. thesis aims to continue with particular attention the research topic started years ago by late lamented Prof. Eng. V. Gioncu and Prof. Eng. F. M. Mazzolani as part of the Prohitech European Research Contract concerning the seismic behaviour of buildings located in the epicentral area. In particular, studies over the years have provided, for the entire scientific community, an important starting point related to the assessment of the seismic vulnerability of historic masonry buildings subject to the near-field earthquake, providing a comprehensive overview regarding phenomenological aspects correlated to the induced effects on engineering structures.

These prerogatives have been the basis for developing a systematic procedure for assessing the seismic performance level of a load-bearing capacity structure located in the Banat Seismic Region, mainly conditioned by medium-high seismicity. This research has been started back in 2017 at the Faculty of Architecture and Urban Planning of Timisoara to provide an accurate methodology regarding the seismic assessment of historic masonry buildings concerning the seismic vertical component.

Starting from the knowledge of seismicity of the Banat Region, typically similar to both, buildings construction techniques and seismic activity of the northern part of Italy, and analysis of the damage that occurred it has been possible to plan an organic procedure for assessing the seismic vulnerability by extending the main engineering parameters, internationally recognized, to near-field earthquake characterizing the Banloc area.

In this doctoral dissertation, the proposal of a methodology for assessing seismic vulnerability is presented, with the primary objective of providing a comprehensive overview for the implementation of analytical procedures for estimating the effects induced by the ground motion vertical component on historical masonry structures. The proposed methodology provides an accurate treatment of the main vulnerability factors that can be "altered" in the case of a seismic vertical component. In this sense, it has been underlined the importance of conducting specific numerical analyses that take into account this phenomenology to reduce the expected risk, safeguard historical and cultural heritage and providing appropriate evaluation procedures for different technical purposes, i.e. researchers and professional activity.

Finally, the proposed seismic vulnerability assessment methodology is characterized by an appropriate calibration between the results of the non-linear numerical analysis and the real response of the case study building subjected to shallow earthquakes as occurred in the Banat Region.

## 6.1 Personal contributions

Historic masonry buildings represent the weakest part of the historical-artistic heritage of a given region, therefore, they need to be safeguarded through appropriate conservation and risk mitigation strategies. The basis of any seismic risk mitigation strategy is the level of detail achieved that can be improved by adopting an “ad-hoc” methodologies for assessing seismic vulnerability.

However, the existing methodologies must be adapted to the hazard level of the site by providing basic knowledge which is used as a link between the numerical analyses and the effects induced by past earthquakes.

Therefore, the personal contributions developed on the assessment of the seismic vulnerability of historic building in the case of a near-field earthquake can be summarised below:

- i. The proposed methodology can be used to evaluate the seismic response of other historic masonry buildings (with similar construction techniques of the buildings sample located in the Banat region) in Europe subjected to shallow earthquakes with a medium-high intensity. This work has been developed in compliance with the impulsive phenomenon that occurred in the Municipality of Banloc located 7 km away from the epicentre;
- ii. Technical indications were provided regarding the typological and structural identification for the case study historical masonry building located in the Banat Region based on the typical seismic behaviour;
- iii. For the first time, indications were provided on the dynamic characterization of the simulated seismic event focusing on the frequency contribution and the V/H ratio in case of near-field conditions. The maximum amplification ratio, V/H, was estimated equal to 2.2 for short period,  $T=0.2$  sec;
- iv. The seismic vulnerability assessment of a historic masonry building located in the Banat Region has been estimated for the first time considering the effects of ground motion vertical component;

- v. A systematic methodology was proposed that foresees the global and local seismic behaviour of the analysed case study building;
- vi. The research has shown that the ductility demand estimated in the longitudinal direction is reduced by about 4 times compared to the other direction since torsional phenomena, triggered by the ground motion horizontal components, limit the global capacity of the structure;
- vii. For the first time, the effects induced by the vertical seismic component were estimated on the behaviour factor, the stiffness degradation, respectively;
- viii. The thesis showed how the ground motion vertical component negatively affects the global behaviour of the structure by increasing the expected vulnerability in the case of the maximum decompression phase estimated at 1.68 sec. Conversely, at the time step 3.00 sec, the horizontal seismic actions trigger the structural damage assisted by the maximum compression produced by the vertical component. However, the vertical seismic decompression component reduces the capacity of the structure;
- ix. The failure hierarchy induced by the ground motion vertical component was estimated for the first time to identify the expected in-plane mechanisms;
- x. A simplified procedure has been proposed for the calculation of the possible out-of-plane mechanisms in the case of a vertical earthquake;
- xi. For the first time, damage indices were estimated that take into account the influence of the ground motion vertical excitation on the failure hierarchy of wall panels;
- xii. The thesis provided a clear and precise indication regarding the damage resulting from the effect of the vertical component of the earthquake. In particular, these damages are induced by the asynchronous movement of (more or less) extended portions of masonry which favour the formation of vertical shear planes especially near the spandrel beams;
- xiii. For the first time the analytical fragility curves have been calibrated based on the real damage observed after the Banloc earthquake in case of a near-field earthquake;

- xiv. For the first time, the typological vulnerability curves for the impulsive simulated seismic scenario has been proposed, providing a satisfactory correlation between the empirical and mechanical methodology, respectively.

In conclusion, the proposed research has provided a careful and scrupulous analysis of the seismic behaviour of a historic masonry building in the epicentre area, developing an innovative methodology that can contribute to raising awareness of future research works regarding the effects of the ground motion vertical component on the historical constructions.

## **6.2 Future developments**

Future research is aimed at developing a wider and more reliable methodology for estimating the seismic vulnerability of historic masonry buildings concerning near-field phenomena, focusing mainly on:

- i. Simulating seismic scenarios characterized by different epicentre distances, frequency contents, epicentral depths, type of signals (vibratory and impulsive), soil amplification effects;
- ii. Simulating a possible ground-structure interaction, to take into account any asynchronous movements generated by the ground motion vertical component for the prediction of the damages;
- iii. Extending the typological DB to a wider range of masonry structures located in the Banat Seismic Region;
- iv. Estimating appropriately the ductility and behaviour factors for different masonry structural typologies;
- v. Parameterizing the mechanical parameters of the masonry to grasp the possible failure hierarchies;
- vi. Studying the possibility of considering complex structural systems of buildings arranged in aggregate conditions;
- vii. Analytically estimation of the fragility and vulnerability curves for different typological classes and seismic scenarios for the Banat Region;
- viii. Estimate possible strengthening interventions;
- ix. Providing design indications to be adopted for professional and/or research purposes;

### 6.3 Published papers

<b>Total citations and H-index</b>				
<b>Articles in *Web of Sciences</b>				
<b>Publications in WOS</b>	<b>Sum of times cited</b>	<b>H-index</b>	<b>Average citation per item</b>	<b>Average citation per year</b>
14	92	5	5.4	15.2
<i>*Web of Science Researcher ID - AAN-1583-2020</i>				
<b>Articles in *Scopus</b>				
<b>Publications in Scopus</b>		<b>Sum of times cited</b>	<b>H-index</b>	
17		170	6	
<i>*ORCID profile: <a href="https://orcid.org/0000-0001-5714-3334">https://orcid.org/0000-0001-5714-3334</a></i>				
<b>*Google Scholar</b>				
<b>Citation</b>	<b>i10-Index</b>		<b>H-index</b>	
235	7		8	
<i>*Profile: <a href="https://scholar.google.com/citationshl=it&amp;user=vjl_mTkAAAAJ">https://scholar.google.com/citationshl=it&amp;user=vjl_mTkAAAAJ</a></i>				

#### Attended conferences

1. 17<sup>th</sup> National Technical-Scientific Conference on Modern Technologies for the 3<sup>rd</sup> Millennium, 22-23 March 2018, Oradea, Romania;
2. World Multidisciplinary Civil Engineering-Architecture-Urban Planning Symposium, 18-22 June 2018, Prague, Czech Republic;
3. 8<sup>th</sup> International Conference on Engineering Failure Analysis ICEFA, 8-11 July 2018, Budapest, Hungary;
4. XI International Conference on Structural Dynamics, EURO DYN, 23-26 November 2020, Athens, Greece;
5. 19<sup>th</sup> International Conference of Numerical Analysis and Applied Mathematics. ICNAAM2020, 17-23 September 2020, Rhodes, Greece.

### Research grants

Official member of the research unit RU31 in the **\*ReLUIS 2019-2021 project "Development of a systematic methodology for the assessment of exposure on a territorial scale based on the typological/structural characteristics of buildings"** in collaboration with the **Italian Civil Protection Department (DPC)**. Ref. Code: E66C19000190005.

RU31 - Scientific Coordinator: Prof. Eng. A. Formisano – University of Naples “Federico II” – Activities conducted:

- 2.3.2: Seismic vulnerability of masonry structures;
- 2.3.4: Seismic vulnerability of industrial building typologies;
- 2.3.6: Seismic risk analysis on a territorial scale.

\*acronym of “*Network of University Laboratories in Earthquake Engineering*”

---

---

## **APPENDIX**



**List of articles published in ISI Journals: 6, cited in 68 papers**

1. Mosoarca, M., Onescu, I., Onescu, E., Azap, B., **Chieffo, N.**, Szitar-Sirbu, M. *Seismic vulnerability assessment for the historical areas of the Timisoara city, Romania*. Engineering Failure Analysis. Vol. 101 Pages: 86-112, (**Impact factor 2.897** on 10.04.2020), Vol. 101, pp. 86-112, 2019, WOS:000464960500007, **cited by:**
  - S. Garcia-Ayllon, A. Tomas, J. Luis Rodenas, The spatial perspective in post-earthquake evaluation to improve mitigation strategies: Geostatistical analysis of the seismic damage applied to a real case study, APPLIED SCIENCES-BASEL (**Impact factor 2.217** on 10.04.2021), volume 9, issue 15, article number 3182, 2019;
  - Wang P., Qiao W., Wang Y., Cao S., Zhang Y., Urban drought vulnerability assessment–A framework to integrate socio-economic, physical, and policy index in a vulnerability contribution analysis, Sustainable Cities and Society (**Impact factor 4.624** on 10.04.2021), volume 54, article ID: 102004, 2020;
  - Kassem M.M., Nazri F.M., Farsangi E.N., The efficiency of an improved seismic vulnerability index under strong ground motions, STRUCTURES (**Impact factor 1.646** on 10.04.2021), volume 23, pp. 366-382;
  - S. Liu, J. Ge, W. Li, & M. Bai, Historic environmental vulnerability evaluation of traditional villages under geological hazards and influencing factors of adaptive capacity: a district-level analysis of Lishui, China, Sustainability (**Impact factor 2.592** on 10.04.2021), volume 12, issue 6, article number 2223, 2020;
  - Brando G., Pagliaroli A., Cocco G., & Buccio. F., Site effects and damage scenarios: The case study of two historic centers following the 2016 Central Italy earthquake, Engineering Geology (**Impact factor 3.909** on 10.04.2021), 2020;
  - M.M Kassem, F.M. Nazri, E.N. Farsangi, The seismic vulnerability assessment methodologies: A state-of-the-art review, Ain Shams Engineering Journal (**Impact factor 3.091** on 10.04.2021), 2020;
  - Yazdani, M., Jahangiri, V, Intensity measure-based probabilistic seismic evaluation and vulnerability assessment of ageing bridges, Earthquakes and Structures, Volume: 19 Issue: 5 (**Impact factor 1.714** on 10.04.2021), 2020;

- Mosoarca, M., ; Onescu, I., Onescu, E., Anastasiadis, A, Seismic vulnerability assessment methodology for historic masonry buildings in the near-field areas, Engineering Failure Analysis (**Impact factor 2.897** on 10.04.2021), Volume: 115, Article Number: 104662, 2020;
- Li, SQ.; Chen, YS, Analysis of the probability matrix model for the seismic damage vulnerability of empirical structures, Natural Hazard, (**Impact factor 2.427** on 10.04.2021), Volume: 104, Issue: 1 Pages: 705-730, 2020;
- Biglari M., Formisano A., Damage Probability Matrices and Empirical Fragility Curves From Damage Data on Masonry Buildings After Sarpol-e-zahab and Bam Earthquakes of Iran Front, Built Environ., 2020;
- Keller A.I., Parisi M.A., Tsakanika E., Mosoarca M., Influence of historic roof structures on the seismic behaviour of masonry structures, Proceedings of the Institution of Civil Engineering – Structures and Buildings, ISSN 0965-0911, 2019;

2. **Chieffo, N., Formisano, A. *Induced Seismic-Site Effects on the Vulnerability Assessment of a Historical Centre in the Molise Region of Italy: Analysis Method and Real Behaviour Calibration Based on 2002 Earthquake.* Geosciences 2020, 10(1), 21; <https://doi.org/10.3390/geosciences10010021>, cited by:**

- Scacco, J., Milani, G., Lourenco, PB, Automatic mesh generator for the non-linear homogenized analysis of double curvature masonry structures, Advances in Engineering Software (**Impact factor 3.884** on 10.04.2021), Volume: 150, Article Number: 102919, 2020;
- Ramaglia, G., Fabbrocino, F., Lignola, GP., Prota, A, Impact of FRP and FRCM on the ductility of strengthened masonry members, Structures (**Impact factor 1.839** on 10.04.2021), Volume: 28 Pages: 1229-1243, 2020;
- Crisci, G., Ramaglia, G., Lignola, GP., Fabbrocino, F., Prota, A, Effects of the Mortar Matrix on the Flexural Capacity of Masonry Cross Sections Strengthened with FRCM Materials, Applied Sciences (**Impact factor 2.474**, on 10.04.2021), Volume: 10, Issue: 21, Article Number: 7908, 2020;

- Fathi, A., Sadeghi, A., Azadi, MRE., Hoveidae, N, Assessing the soil-structure interaction effects by direct method on the out-of-plane behavior of masonry structures (case study: Arge-Tabriz), *Bulletin of Earthquake Engineering* (**Impact factor 2.474**, on 10.04.2021), Volume: 18 Issue: 14 Pages: 6429-6443, 2020;

3. **Chieffo, N., Formisano, A., Ferreira, T.M.** *Damage scenario-based approach and retrofitting strategies for seismic risk mitigation: an application to the historical Centre of Sant'Antimo (Italy)*. *European Journal of Environmental and Civil Engineering*, 2019, doi.org/10.1080/19648189.2019.1596164, **cited by:**

- Ramaglia, G., Fabbrocino, F., Lignola, GP., Prota, A, Impact of FRP and FRCM on the ductility of strengthened masonry members, *Structures* (**Impact factor 1.839** on 10.04.2021), Volume: 28 Pages: 1229-1243, 2020;
- Crisci, G., Ramaglia, G., Lignola, GP., Fabbrocino, F., Prota, A, Effects of the Mortar Matrix on the Flexural Capacity of Masonry Cross Sections Strengthened with FRCM Materials, *Applied Sciences* (**Impact factor 2.474**, on 10.04.2021), Volume: 10, Issue: 21, Article Number: 7908, 2020;
- Miano, A., de Silva, D., Compagnone, A., Chiumiento, G., Probabilistic seismic and fire assessment of an existing reinforced concrete building and retrofit design, *Structural Engineering and Mechanics*, Volume: 6, 2020;
- Miano, A., de Silva, D., Compagnone, A., Chiumiento, G., Seismic and Fire Assessment and Upgrading Process for Historical Buildings: The Case Study of Palazzo Colonna in Caggiano, *Frontiers in Built Environment*, 2020;
- Kassem M.M., Nazri F.M., Farsangi E.N., The efficiency of an improved seismic vulnerability index under strong ground motions, *STRUCTURES* (**Impact factor 1.646** on 10.04.2021), volume 23, pp 366-382;
- Biglari M., Formisano A., *Damage Probability Matrices and Empirical Fragility Curves From Damage Data on Masonry Buildings After Sarpol-e-zahab and Bam Earthquakes of Iran Front, Built Environ.*, 2020;

4. **Chieffo, N., Formisano, A.** *Geo-hazard-based approach for the estimation of seismic vulnerability and damage scenarios of the old city of Senerchia (Avellino, Italy)*. *Geosciences*, 9(2), 59, 2019, doi.org/10.3390/geosciences9020059, **cited by:**
- Lazzali, F, Seismic Vulnerability Analysis of RC Buildings: Case Study of Ibn Khaldoun Area in Boumerdes City, Algeria, *JORDAN JOURNAL OF CIVIL ENGINEERING*, Volume: 15, Issue: 1, Pages: 52-63, 2021;
  - Basaglia, A., Aprile, A., Spacone, E., Pela, L, Assessing community resilience, housing recovery and impact of mitigation strategies at the urban scale: a case study after the 2012 Northern Italy Earthquake, *Bulletin of Earthquake Engineering* (**Impact factor 2.602** on 10.04.2021), Volume: 18 Issue: 13 Pages: 6039-6074, 2021;
  - Grillanda, N., Valente, M., Milani, G., Chiozzi, A., Tralli, A, Advanced numerical strategies for seismic assessment of historical masonry aggregates, *Engineering Structures* (**Impact factor 3.548** on 10.04.2021), Volume: 212, Article Number: 110441, 2020;
  - Pavic, G., Hadzima-Nyarko, M., Bulajic, B, A Contribution to a UHS-Based Seismic Risk Assessment in Croatia-A Case Study for the City of Osijek, *SUSTAINABILITY* (**Impact factor 2.576** on 10.04.2021), Volume: 12, Issue: 5, Article Number: 1796, 2020;
  - M. Biglari, Formisano A., *Damage Probability Matrices and Empirical Fragility Curves From Damage Data on Masonry Buildings After Sarpol-e-zahab and Bam Earthquakes of Iran Front*, *Built Environ.*, 2020;
  - Kassem M.M., Nazri F.M., Farsangi E.N., The efficiency of an improved seismic vulnerability index under strong ground motions, *STRUCTURES* (**Impact factor 1.646** on 10.04.2021), volume 23, pp 366-382;
  - Tapete, D, *Key Topics and Future Perspectives in Natural Hazards Research*, *GEOSCIENCES*, Volume: 10 Issue: 1, Article Number: 22, 2020;
  - Giuffrida, S., Trovato, MR., Circo, C., Ventura, V., Giuffre, M., Macca, V., *Seismic Vulnerability and Old Towns. A Cost-Based Programming Mode*, *GEOSCIENCES*, Volume: 9 Issue: 10, Article Number: 427, 2019;

- Bernardini, C., Maio, R., Boschi, S., Ferreira, TM., Vicente, R., Vignoli, A., The seismic performance-based assessment of a masonry building enclosed in aggregate in Faro (Portugal) by means of a new target structural unit approach, *Engineering Structures* (**Impact factor 3.548** on 10.04.2021) Volume: 191 Pages: 386-400, 2019;
- Onescu I., Onescu E., Mosoarca M., The impact of the cultural value to the seismic vulnerability of a historical building, *IOP Conference Series: Materials Science and Engineering*, Volume: 603, Article Number: 042031, 2019.

5. **Chieffo, N., Formisano, A.** *The influence of geo-hazard effects on the physical vulnerability assessment of the built heritage: An application in a district of Naples.* *Buildings*, 9(1), 26, 2019, doi.org/10.3390/buildings9010026, **cited by:**

- Lazzali, F, Seismic Vulnerability Analysis of RC Buildings: Case Study of Ibn Khaldoun Area in Boumerdes City, Algeria, *JORDAN JOURNAL OF CIVIL ENGINEERING*, Volume: 15, Issue: 1, Pages: 52-63, 2021;
- Singha, P., Das, P., Talukdar, S., Pal, S., Modeling livelihood vulnerability in erosion and flooding induced river island in Ganges riparian corridor, India, *Ecological Indicators* ( **Impact factor 4.229** on 10.04.2021), Volume: 119, Article Number: 106825, 2020;
- Mosoarca, M., Onescu, I., Onescu, E., Anastasiadis, A, Seismic vulnerability assessment methodology for historic masonry buildings in the near-field areas, *Engineering Failure Analysis* (**Impact factor 2.897** on 10.04.2021), Volume: 115, Article Number: 104662, 2020;
- Grillanda, N., Valente, M., Milani, G., Chiozzi, A., Tralli, A, Advanced numerical strategies for seismic assessment of historical masonry aggregates, *Engineering Structures* (**Impact factor 3.548** on 10.04.2021), Volume: 212, Article Number: 110441, 2020;
- Miano, A., de Silva, D., Compagnone, A., Chiumiento, G., Probabilistic seismic and fire assessment of an existing reinforced concrete building and retrofit design, *Structural Engineering and Mechanics*, Volume: 6, 2020;
- Biglari M., Formisano A., *Damage Probability Matrices and Empirical Fragility Curves From Damage Data on Masonry Buildings After Sarpol-e-zahab and Bam Earthquakes of Iran Front, Built Environ.*, 2020;

- Kassem M.M., Nazri F.M., Farsangi E.N., The efficiency of an improved seismic vulnerability index under strong ground motions, *STRUCTURES* (**Impact factor 1.646** on 10.04.2021), volume 23, pp 366-382;
  - Brando, G., Cocco, G., Mazzanti, C., Peruch, M., Spacone, E., Alfaro, C., Sovero, K., Tarque, N., Structural Survey and Empirical Seismic Vulnerability Assessment of Dwellings in the Historical Centre of Cusco, Peru, *INTERNATIONAL JOURNAL OF ARCHITECTURAL HERITAGE* (**Impact factor 1.853** on 10.04.2021), DOI: 10.1080/15583058.2019.1685022, 2019;
  - Ferreira, TM., Mendes, N., Silva, R., Reducing the Seismic Vulnerability of Existing Buildings: Assessment and Retrofit, *Buildings*, Volume: 9 Issue: 6, Article Number: 148, 2019;
  - Onescu E., Onescu I., Mosoarca M., Seismic vulnerability assessment of historical group of buildings in Timisoara city, Proceedings of 18th National TechnicalScientific Conference on Modern Technologies for the 3rd Millennium, Oradea, Romania, Edited by: Nistor, S., Popoviciu, GA., 2020, Pages: 259-264;
6. **Chieffo, N.**, Clementi, F., Formisano, A., Lenci, S. *Comparative fragility methods for seismic assessment of masonry buildings located in Muccia (Italy)*. *Journal of Building Engineering*, Vol. 25, 2019, 100813, doi.org/10.1016/j.job.2019.100813, **cited by:**
- D'Altri, AM., Lo Presti, N., Grillanda, N., Castellazzi, G., de Miranda, S., Milani, G., A two-step automated procedure based on adaptive limit and pushover analyses for the seismic assessment of masonry structures, *Computer & Structures* (**Impact factor 4.578** on 03.07.2021), Volume: 252, n. 106561, 2021;
  - Anelli, A., Mori, F., Moscatelli, M., Seismic fragility and vulnerability curves for the Italian residential building stock, *Structure and Infrastructure Engineering*, DOI:10.1080/15732479.2021.1936568, 2021;
  - Domeneschi, M., Noori, AZ., Pietropinto, MV., Cimellaro, GP., Seismic vulnerability assessment of existing school buildings, *Computer & Structures* (**Impact factor 2.955** on 03.07.2021), Volume: 48, n. 106522, 2021;

- Quagliarini, E., Lucesoli, M., Bernardini, G., How to create seismic risk scenarios in historic built environment using rapid data collection and managing, *Journal of Cultural HeritageComputer & Structures* (**Impact factor 4.578** on 03.07.2021), Volume: 248, Pages: 93-105, 2021;
- Nakipoglu, A., Unal, A., Kamanli, M., Damage analysis of Golyazi Apartments building failed under axial loads: A case study in Konya, Turkey, *STRUCTURES* (**Impact factor 1.839** on 10.04.2021), Volume: 30, Pages: 409-417, 2021;
- Yousfi, N., Bensaibi, M., Guessoum, N., Boukri, M., Seismic Scenario of Algiers City: Case Study of Strengthened Masonry Buildings, *STRUCTURAL ENGINEERING INTERNATIONAL* (**Impact factor 0.672** on 10.04.2021), DOI: 10.1080/10168664.2021.1872465, 2021;
- Shehu, R., Implementation of Pushover Analysis for Seismic Assessment of Masonry Towers: Issues and Practical Recommendations, *BUILDINGS*, Volume: 11, Issue: 2, Article Number: 71, 2021;
- Mosoarca, M., Onescu, I., Onescu, E., Anastasiadis, A, Seismic vulnerability assessment methodology for historic masonry buildings in the near-field areas, *Engineering Failure Analysis* (**Impact factor 2.897** on 10.04.2021), Volume: 115, Article Number: 104662, 2020;
- Fathi, A., Sadeghi, A., Azadi, MRE., Hoveidae, N, Assessing the soil-structure interaction effects by direct method on the out-of-plane behavior of masonry structures (case study: Arge-Tabriz), *Bulletin of Earthquake Engineering* (**Impact factor 2.474**, on 10.04.2021), Volume: 18 Issue: 14 Pages: 6429-6443, 2020;
- Hoang, DV., Shin, J., Lee, K., Seismic Fragility Assessment of Columns in a Piloti-Type Building Retrofitted with Additional Shear Walls, *SUSTAINABILITY* (**Impact factor 2.576** on 10.04.2021), Volume: 12, Issue: 16, Article Number: 6530, 2020;
- Forcellini, D., Probabilistic-based assessment of liquefaction-induced damage with analytical fragility curves, *Geosciences (Switzerland)*, Volume 10, Issue 8, Article number 315, Pages 1-16, 2020;
- Li, SQ.; Chen, YS, Analysis of the probability matrix model for the seismic damage vulnerability of empirical structures, *Natural Hazard*, (**Impact factor 2.427** on 10.04.2021), Volume: 104, Issue: 1 Pages: 705-730, 2020;



- Maio, R., Estevao, JMC., Ferreira, TM., Vicente, R., Casting a new light on the seismic risk assessment of stone masonry buildings located within historic centres, *STRUCTURES (Impact factor 1.839 on 10.04.2021)* Volume: 25, Pages: 578-592, 2020;
- Miano, A., de Silva, D., Compagnone, A., Chiumiento, G., Probabilistic seismic and fire assessment of an existing reinforced concrete building and retrofit design, *Structural Engineering and Mechanics*, Volume: 6, 2020;
- Sumerente, G., Lovon, H., Tarque, N., Chacara, C., Assessment of Combined In-Plane and Out-of-Plane Fragility Functions for Adobe Masonry Buildings in the Peruvian Andes, *FRONTIERS IN BUILT ENVIRONMENT*, Volume: 6, DOI: 10.3389/fbuil.2020.00052, 2020;
- Miano, A., de Silva, D., Compagnone, A., Chiumiento, G., Seismic and Fire Assessment and Upgrading Process for Historical Buildings: The Case Study of Palazzo Colonna in Caggiano, *Frontiers in Built Environment*, 2020;
- Wang, W., Wu, FY., Wang, ZY., Revising Seismic Vulnerability of Bridges Based on Bayesian Updating Method to Evaluate Traffic Capacity of Bridges, *SUSTAINABILITY (Impact factor 2.576 on 10.04.2021)*, Volume: 12, Issue: 5, Article Number: 1898, 2020;
- Tiberti, S., Milani, G., 3D voxel homogenized limit analysis of single-leaf non-periodic masonry, *COMPUTERS & STRUCTURES (Impact factor 3.664 on 10.04.2021)*, Volume: 229, Article Number: 106186, 2020;
- Anelli, A., Mori, F., Vona, M., Fragility Curves of the Urban Road Network Based on the Debris Distributions of Interfering Buildings, *APPLIED SCIENCES (Impact factor 2.474 on 10.04.2021)*, Volume: 10, Issue: 4, Article Number: 1289, 2020;
- Kassem M.M., Nazri F.M., Farsangi E.N., The efficiency of an improved seismic vulnerability index under strong ground motions, *STRUCTURES (Impact factor 1.646 on 10.04.2021)*, volume 23, pp 366-382;
- Giuffrida, S., Trovato, MR., Circo, C., Ventura, V., Giuffre, M., Macca, V., Seismic Vulnerability and Old Towns. A Cost-Based Programming Mode, *GEOSCIENCES*, Volume: 9 Issue: 10, Article Number: 427, 2019;

**List of articles published in ISI Proceedings: 6, cited in 10 papers**

1. Apostol, I., Mosoarca, M., **Chieffo, N.**, Keller, A., Bocan, D., Bocan, C.; Bradeanu, R. *Solutions for improving seismic vulnerability of historic masonry buildings*. Proceedings of 17<sup>th</sup> National Technical-Scientific Conference on Modern Technologies for the 3<sup>rd</sup> Millennium, Oradea, Romania, pp 131-136, 2019;
2. Azap, B., Apostol, I., Mosoarca, M., **Chieffo, N.**, Formisano, A. *Seismic vulnerability scenarios for historical areas of Timisoara*. Proceedings of 17<sup>th</sup> National Technical-Scientific Conference on Modern Technologies for the 3<sup>rd</sup> Millennium, Oradea, Romania, pp 149-154, 2019, **cited by:**
  - Mosoarca, M., Onescu, I., Onescu, E., Anastasiadis, A, Seismic vulnerability assessment methodology for historic masonry buildings in the near-field areas, Engineering Failure Analysis (**Impact factor 2.897** on 10.04.2021), Volume: 115, Article Number: 104662, 2020;
  - Onescu E., Onescu I., Mosoarca M., The impact of timber roof framework over historical masonry structures”, IOP Conference Series: Materials Science and Engineering, 2020, in indexation process;
  - Onescu E., Onescu I., Mosoarca M., Seismic vulnerability assessment of historical group of buildings in Timisoara city, Proceedings of 18<sup>th</sup> National Technical-Scientific Conference on Modern Technologies for the 3<sup>rd</sup> Millennium, Oradea, Romania, 2020, in indexation process
3. Keller, A., Mosoarca, M., **Chieffo, N.**, Formisano, A. *Resilience of historic cities and adaptation to climate change*. Urbanism, Arhitectură, Construcții, 1, pp.15-26, 2017, **cited by:**
  - Habibi, K., Hoseini, SM., Dehshti, M., Khanian, M., Mosavi, A., The Impact of Natural Elements on Environmental Comfort in the Iranian-Islamic Historical City of Isfahan, International Journal of Environmental Research and Public Health (**Impact factor 2.849** on 10.04.2021), Volume: 17, Issue: 16, Article Number: 5776, 2020;

4. Formisano, A., **Chieffo, N.**, Fabbrocino, F., Landolfo, R. *Seismic vulnerability and damage of Italian historical centres: A case study in the Campania Region*. AIP Conference Proceedings, Vol. 1863, 2017, **cited by:**
  - Mosoarca, M., Onescu, I., Onescu, E., Anastasiadis, A, Seismic vulnerability assessment methodology for historic masonry buildings in the near-field areas, Engineering Failure Analysis (**Impact factor 2.897** on 10.04.2021), Volume: 115, Article Number: 104662, 2020;
  - Fumo, M., Formisano, A., Sibilio, G., Violano, A., Energy and Seismic Recovering of Ancient Hamlets: the Case of Baia e Latina, SUSTAINABILITY (**Impact factor 2.576** on 10.04.2021), Volume: 10, Issue: 8, Article Number: 2831, 2018;
  - Bossio, A., Fabbrocino, F., Lignola, GP., Prota, A., Manfredi, G., Design Oriented Model for the Assessment of T-Shaped Beam-Column Joints in Reinforced Concrete Frames, BUILDINGS, Volume: 7, Issue: 4, Article Number: 118, 2017.
5. Formisano, A., Fabbrocino, F., **Chieffo, N.**, *Seismic investigation on a masonry building compound in the historical centre of Bacoli (Naples)*. Proceedings of 14th International Forum of Studies World Heritage and Degradation: Smart Design, Planning and Technologies, pp. 412-419, Naples, ITALY, 2016;
6. Formisano, A., **Chieffo, N.**, Milo, B., Fabbrocino, F. *The influence of Local Mechanisms on Large Scale Seismic Vulnerability Estimation of Masonry Building Aggregates*. Proceedings of the International Conference of Computational Methods in Sciences and Engineering 2016 (ICCMSE 2016), Vol. 1790, n. 130010, Athens, GREECE.

#### List of articles published in Scopus Journals: 10, cited in 56 papers

1. **Chieffo, N.**, Formisano, A., Clementi, F., Mosoarca, M. *Influence of local site effects on the typological fragility curves for class-oriented masonry buildings in aggregate condition*. Open Civil Engineering Journal, 2021, 12(Specialissue1), pp. 149–164, **cited by:**

- Formisano, A., D’Amato, M. *Large scale seismic vulnerability and risk evaluation of historical centres and cultural heritage constructions*. *Open Civil Engineering Journal*, 2021, 15(Specialissue1), pp. 115–116, 2021.
2. **Chieffo, N.**, Onescu, I., Formisano, A., Mosoarca, M., Palade, M. *Integrated empirical-mechanical seismic vulnerability analysis method for masonry buildings in Timișoara: Validation based on the 2009 Italian Earthquake*. *Open Civil Engineering Journal*, 2020, 14(1), pp. 314–333;
  3. **Chieffo, N.**, Formisano, A. *Comparative Seismic Assessment Methods for Masonry Building Aggregates: A Case Study*. *Frontiers in Built Environment*, 2019, 5, 123, **cited by:**
    - Grillanda, N., Valente, M., Milani, G., Chiozzi, A., Tralli, A., Advanced numerical strategies for seismic assessment of historical masonry aggregates, *Engineering Structures* (**Impact factor 3.548** on 10.04.2021), Volume: 212, Article Number: 110441, 2020;
    - Sumerente, G., Lovon, H., Tarque, N., Chacara, C., Assessment of Combined In-Plane and Out-of-Plane Fragility Functions for Adobe Masonry Buildings in the Peruvian Andes, *FRONTIERS IN BUILT ENVIRONMENT*, Volume: 6, DOI: 10.3389/fbuil.2020.00052, 2020;
    - Anelli, A., Mori, F., Vona, M., Fragility Curves of the Urban Road Network Based on the Debris Distributions of Interfering Buildings, *APPLIED SCIENCES* (**Impact factor 2.474** on 10.04.2021), Volume: 10, Issue: 4, Article Number: 1289, 2020;
  4. **Chieffo, N.**, Formisano, A. *Induced Seismic-Site Effects on the Vulnerability Assessment of a Historical Centre in the Molise Region of Italy: Analysis Method and Real Behaviour Calibration Based on 2002 Earthquake*. *Geosciences* 2020, 10(1), 21; <https://doi.org/10.3390/geosciences10010021>.

5. **Chieffo, N., Clementi, F., Formisano, A., Lenci, S.** *Comparative fragility methods for seismic assessment of masonry buildings located in Muccia (Italy)*. *Journal of Building Engineering*, Vol. 25, 2019, 100813, [doi.org/10.1016/j.jobbe.2019.100813](https://doi.org/10.1016/j.jobbe.2019.100813), **cited by:**

- Domaneschi, M., Zamani Noori, A., Pietropinto, M.V., Cimellaro, G.P., Seismic vulnerability assessment of existing school buildings, *Computers and Structures*, Volume 248, Article number 106522, 2021;
- Quagliarini, E., Lucesoli, M., Bernardini, G., How to create seismic risk scenarios in historic built environment using rapid data collection and managing, *Journal of Cultural Heritage*, Volume 48, Pages 93-105, 2021;
- Habieb, A.B., Valente, M., Milani, G., Seismic performance of a masonry house prototype retrofitted using FRP, *AIP Conference Proceedings*, International Conference on Numerical Analysis and Applied Mathematics 2019, ICNAAM 2019; Sheraton Rhodes ResortRhodes; Greece; 23 September 2019 through 28 September 2019; Code 165330;
- Giordano, E., Ferrante, A., Ribilotta, E., Clementi, F., Lenci, S., Damage assessment of san francesco church in amandola hit by central Italy 2016-2017 seismic event, *AIP Conference Proceedings*, International Conference on Numerical Analysis and Applied Mathematics 2019, ICNAAM 2019; Sheraton Rhodes ResortRhodes; Greece; 23 September 2019 through 28 September 2019; Code 165330, Volume 2293, 24 November 2020, Article number 380011;
- Ivanov, R.I., Seismic behaviour of brickwork chimneys in buildings, *IOP Conference Series: Materials Science and Engineering*, 11th International Conference on Civil Engineering Design and Construction, DCB 2020; Varna; Bulgaria; 10 September 2020 through 12 September 2020; Code 164563, Volume 951, Issue 1, 2 November 2020, Article number 012017.
- Li, S., Yu, T., Zhang, M., Comparative Study of the Vulnerability of Canonical Structures in Different Intensity Regions, *Huanan Ligong Daxue Xuebao/Journal of South China University of Technology (Natural Science)* Volume 48, Issue 3, Pages 67-75 and 90, 2020;
- Rezaei Ranjbar, P., Naderpour, H., Probabilistic evaluation of seismic resilience for typical vital buildings in terms of vulnerability curves, *Structures*, Volume 23, Pages 314-323, 2020;

- Iacovino, C., Flora, A., Cardone, D., Vona, M., Defining a Masonry Building Inventory for the City of Potenza, Lecture Notes in Computer Science (including subseries Lecture Notes in Artificial Intelligence and Lecture Notes in Bioinformatics) Volume 12250 LNCS, 2020, Pages 914-927, 20th International Conference on Computational Science and Its Applications, ICCSA 2020; Cagliari; Italy; 1 July 2020 through 4 July 2020; Code 249529.

6. **Chieffo, N., Formisano, A. *Geo-hazard-based approach for the estimation of seismic vulnerability and damage scenarios of the old city of Senerchia (Avellino, Italy)*. Geosciences, 9(2), 59, 2019, doi.org/10.3390/geosciences9020059, cited by:**

- Quagliarini, E., Lucesoli, M., Bernardini, G., How to create seismic risk scenarios in historic built environment using rapid data collection and managing, Journal of Cultural Heritage, Volume 48, Pages 93-105, 2021;
- Taibi, H.r, Ait Youcef, M., Khellafi, M., Seismic vulnerability assessment using the macroseismic method proposed in the framework of Risk-UE project based on the recommendations of the Algerian seismic code RPA99/Version 2003, Asian Journal of Civil Engineering Volume 21, Issue 1, Pages 59-66, 2020;
- Rezaei Ranjbar, P., Naderpour, H., Probabilistic evaluation of seismic resilience for typical vital buildings in terms of vulnerability curves, Structures, Volume 23, Pages 314-323, 2020;
- Olivito, R.S., Porzio, S. Codispoti, R., Scuro, C., A case study on seismic vulnerability assessment of masonry buildings by using Cartis database, REHABEND2020, Pages 2677-2684, 8th Euro-American Congress on Construction Pathology, Rehabilitation Technology and Heritage Management, REHABEND 2020; Granada; Spain; 24 March 2020 through 27 March 2020; Code 253609;
- Onescu I., Onescu E., Mosoarca M., The impact of the cultural value to the seismic vulnerability of a historical building, IOP Conference Series: Materials Science and Engineering, Volume 603, Issue 4, 18 September 2019, Article number 042031, 4th World Multidisciplinary Civil Engineering-Architecture-Urban Planning Symposium, WMCAUS 2019; Prague; Czech Republic; 17 June 2019 through 21 June 2019; Code 152111;

7. **Chieffo, N., Formisano, A.** *The influence of geo-hazard effects on the physical vulnerability assessment of the built heritage: An application in a district of Naples.* Buildings, 9(1), 26, 2019, doi.org/10.3390/buildings9010026, **cited by:**
- Taibi, H.r, Ait Youcef, M., Khellafi, M., Seismic vulnerability assessment using the macroseismic method proposed in the framework of Risk-UE project based on the recommendations of the Algerian seismic code RPA99/Version 2003, Asian Journal of Civil Engineering Volume 21, Issue 1, Pages 59-66, 2020;
  - Uva, G., Ciampoli, P.L., Leggieri, V., Nettis, A., Ruggieri, S., A mechanical approach for estimating regional fragility curves of existing RC buildings stock in Puglia, COMPDYN Proceedings, Volume 1, 2019, Pages 1664-1676, 7th International Conference on Computational Methods in Structural Dynamics and Earthquake Engineering, COMPDYN 2019; Crete; Greece; 24 June 2019 through 26 June 2019; Code 157145;
8. Apostol, I., Mosoarca, M., **Chieffo, N.**, Onescu, E. *Seismic Vulnerability Scenarios for Timisoara, Romania.* RILEM Bookseries, 2019, 18, pp. 1191-1200, **cited by:**
- Mosoarca M., Keller A.I., Bocan C., Failure analysis of church towers and roof structures due to high wind velocities, Engineering Failure Analysis (**Impact factor 2.203** on 10.04.2021), Vol. 100, pp. 76-87, 2019;
  - Onescu I., Onescu E., Mosoarca M., Multi-criterial vulnerability assessment for Timisoara city, Romania, Structures and Architecture: Bridging the Gap and Crossing Borders - Proceedings of the 4th International Conference on Structures and Architecture, ICSA 2019, 2019, Pages 923-930 4th International Conference on Structures and Architecture, ICSA 2019; Lisbon; Portugal; 24 July 2019 through 26 July 2019; Code 244909.



9. Mosoarca, M., Onescu, I., Onescu, E., Azap, B., **Chieffo, N.**, Szitar-Sirbu, M. *Seismic vulnerability assessment for the historical areas of the Timisoara city, Romania*. Engineering Failure Analysis. Vol. 101 Pages: 86-112, **cited by:**
- Quezada, R., Jiménez, J., García, H., Calderón, J., Characterization of the building stock heritage oriented to studies of seismic vulnerability at urban scale: Case study historic centre of cuenca, ecuador, REHABEND 2020, Pages 240-251, 8th Euro-American Congress on Construction Pathology, Rehabilitation Technology and Heritage Management, REHABEND 2020; Granada; Spain; 24 March 2020 through 27 March 2020; Code 253609;
  - Onescu, I., Onescu, E. Mosoarca, M., The impact of the cultural value on the seismic vulnerability of a historical building, IOP Conference Series: Materials Science and Engineering, Volume 603, Issue 4, 18 September 2019, Article number 042031, 4th World Multidisciplinary Civil Engineering-Architecture-Urban Planning Symposium, WMCAUS 2019; Prague; Czech Republic; 17 June 2019 through 21 June 2019; Code 152111;
  - Onescu E., Onescu I., Mosoarca M., The impact of timber roof framework over historical masonry structures”, IOP Conference Series: Materials Science and Engineering, 2020, in indexation process;
  - Chiumiento, G., Formisano, A., Simplified and refined analyses for seismic investigation of historical masonry clusters: Comparison of results and influence of the structural units position, Front. Built Environ., 2019.
10. Formisano, A., **Chieffo, N.**, Mosoarca, M. *Seismic vulnerability and damage speedy estimation of an urban sector within the municipality of San Potito Sannitico (Caserta, Italy)*. Open Civil Engineering Journal, 2017, 11, pp. 1106-1121, **cited by:**
- Quagliarini, E., Lucesoli, M., Bernardini, G., How to create seismic risk scenarios in historic built environment using rapid data collection and managing, Journal of Cultural Heritage, Volume 48, Pages 93-105, 2021;

- Stefanini, S., Rovero, L. Tonietti, U., Seismic vulnerability assessment of fes medina in Morocco, International Archives of the Photogrammetry, Remote Sensing and Spatial Information Sciences - ISPRS Archives, Volume 54, Issue M-1, 20 July 2020, Pages 699-706, 2020 International Conference on Vernacular Architecture in World Heritage Sites. Risks and New Technologies, HERITAGE 2020 (3DPast | RISK-Terra); Valencia, Virtual; Spain; 9 September 2020 through 12 September 2020; Code 162105;
- Grillanda, N., Valente, M., Milani, G., Chiozzi, A., Tralli, A., Advanced numerical strategies for seismic assessment of historical masonry aggregates, Engineering Structures (**Impact factor 3.548** on 10.04.2021), Volume: 212, Article Number: 110441, 2020;
- Sumerente, G., Lovon, H., Tarque, N., Chacara, C., Assessment of Combined In-Plane and Out-of-Plane Fragility Functions for Adobe Masonry Buildings in the Peruvian Andes, FRONTIERS IN BUILT ENVIRONMENT, Volume: 6, DOI: 10.3389/fbuil.2020.00052, 2020;
- M. Biglari, Formisano A., Damage Probability Matrices and Empirical Fragility Curves From Damage Data on Masonry Buildings After Sarpol-e-zahab and Bam Earthquakes of Iran Front, Built Environ., 2020;
- Taibi, H.r, Ait Youcef, M., Khellafi, M., Seismic vulnerability assessment using the macroseismic method proposed in the framework of Risk-UE project based on the recommendations of the Algerian seismic code RPA99/Version 2003, Asian Journal of Civil Engineering Volume 21, Issue 1, Pages 59-66, 2020;
- Kassem M.M., Nazri F.M., Farsangi E.N., The efficiency of an improved seismic vulnerability index under strong ground motions, STRUCTURES (**Impact factor 1.646** on 10.04.2021), volume 23, pp 366-382;
- Grillanda, N., Valente, M., Milani, G., Automatic assessment of partial failure mechanisms in retrofitted historical masonry aggregates through adaptive nurbs limit analysis, Proceedings of the International Conference on Structural Dynamic , EURODYN, volume 2, 2020, Pages 4282-4291, 11th International Conference on Structural Dynamics, EURODYN 2020; Virtual, Athens; Greece; 23 November 2020 through 26 November 2020; Code 165382;

- Zarrella, M., Scuro, C., Carnì, D.L., Olivito, R.S., Lamonaca, F., Overview of structural health monitoring systems for the foundations of historic buildings, 2020 IMEKO TC-4 International Conference on Metrology for Archaeology and Cultural Heritage 2020, Pages 106-111, 2020 IMEKO TC-4 International Conference on Metrology for Archaeology and Cultural Heritage, Metro Archaeo 2020; Trento, Virtual; Italy; 22 October 2020 through 24 October 2020; Code 165450;
- Quagliarini, E., Lucesoli, M., Bernardini, G., Rapid tools for assessing building heritage's seismic vulnerability: a preliminary reliability analysis, Journal of Cultural Heritage, Volume 39, Pages 130-139, 2019;
- Olivito, R.S., Scuro, C., Porzio, S., Codispoti, R., Demarco, F., Seismic vulnerability of ancient masonry buildings: The case study of low-rise towers, AIP Conference Proceedings, Volume 2116, 24 July 2019, Article number 420007, International Conference on Numerical Analysis and Applied Mathematics 2018, ICNAAM 2018; Sheraton Rhodes Resort Rhodes; Greece; 13 September 2018 through 18 September 2018; Code 149843;
- Chiumiento, G., Formisano, A., Simplified and refined analyses for seismic investigation of historical masonry clusters: Comparison of results and influence of the structural units position, Front. Built Environ., 2019;
- Onescu, I., Mosoarca, M., Azap, B., Onescu, E., Seismic losses scenario for cultural promenade in Timisoara Capital of Culture 2021, Romania, IOP Conference 241, Series: Materials Science and Engineering, Vol. 471, Session 9, 2019;
- Fumo, M., Formisano, A., Sibilio, G., Violano, A., Energy and Seismic Recovering of Ancient Hamlets: the Case of Baia e Latina, SUSTAINABILITY (Impact factor 2.576 on 10.04.2021), Volume: 10, Issue: 8, Article Number: 2831, 2018;
- Olivito, R.S., Scuro, C., Codispoti, R., Porzio, S., A seismic analysis for ancient trentacapilli palace with different schematization methods of masonry walls, Proceedings of the International Masonry Society Conferences, Volume 0, Issue 222279, 2018, Pages 2555-2562, 10th International Masonry Conference, IMC 2018; Milan; Italy; 9 July 2018 through 11 July 2018; Code 222279;

- Milani, G., Formisano, A., Clementi, F., Open challenges in seismic design of new structures and vulnerability reduction of existing buildings, *Open Civil Engineering Journal*, Volume 11, Pages 1024-1025, 2017.

**List of articles published in Scopus Proceedings: 3, cited in 6 papers**

1. Formisano, A., **Chieffo, N.**, Mosoarca, M. *Probabilistic earthquake scenarios of a historical area in the town of Amatrice*. AIP Conference Proceedings, 2293, art. no. 240006, 2020;
2. **Chieffo, N.**, Mosoarca, M., Formisano, A., Apostol, I. *Seismic vulnerability assessment and loss estimation of an urban district of Timisoara*. IOP Conference Series: Materials Science and Engineering, Vol. 471, Session 9, 2019, **cited by:**
  - Grillanda N., Valente M., Milani G., Chiozzi A., Tralli A., Advanced numerical strategies for seismic assessment of historical masonry aggregates, *Engineering Structures* (**Impact factor 3.084** on 10.04.2021), volume 212, article ID 110441, 2020;
  - Brando G., Cocco G., Mazzanti C. et.al., Structural survey and empirical seismic vulnerability assessment of dwellings in the historical centre of Cusco, Peru, *International Journal of Architectural Heritage* (**Impact factor 1.440** on 10.04.2021), 2019;
  - Biglari M., Formisano A., *Damage Probability Matrices and Empirical Fragility Curves From Damage Data on Masonry Buildings After Sarpol-e-zahab and Bam Earthquakes of Iran* *Front, Built Environ.*, 2020;
  - Taibi, H.r, Ait Youcef, M., Khellafi, M., *Seismic vulnerability assessment using the macroseismic method proposed in the framework of Risk-UE project based on the recommendations of the Algerian seismic code RPA99/Version 2003*, *Asian Journal of Civil Engineering* Volume 21, Issue 1, Pages 59-66, 2020;
  - Chiumiento, G., Formisano, A., *Simplified and refined analyses for seismic investigation of historical masonry clusters: Comparison of results and influence of the structural units position*, *Front. Built Environ.*, 2019;

- Delavar, M.R., Sadrykia, M., Assessment of Enhanced Dempster-Shafer Theory for Uncertainty Modeling in a GIS-Based Seismic Vulnerability Assessment Model, Case Study Tabriz City, ISPRS International Journal of Geo-Information, volume 9, issue 4, article number 195, 2020.
3. **Chieffo, N.**, Formisano, A., Mosoarca, M., Lourenço, P.B. *Seismic vulnerability assessment of a romanian historical masonry building under near-source earthquake*. Proceedings of the International Conference on Structural Dynamic , EUROODYN, 2, pp. 4957-4971, 2020.

**List of articles in other international Proceedings: 5, cited in 1 paper**

1. **Chieffo, N.**, Apostol, I., Keller A., Mosoarca, M., Marzo, A. *Global behavior of historical masonry structures and timber roof framework*. Prohitech 2017, Lisabona, Portugalia, **cited by:**
  - Mosoarca M., Keller A.I., A complex assessment methodology and procedure for historic roof structures, International Journal of Architectural heritage (**Impact factor 1.440** on 10.04.2021), Vol. 12, Issue 4, pp. 578-898, 2018;
2. Formisano, A., **Chieffo, N.**, Mosoarca, M. *Probabilistic damage scenario: a case study in Amatrice affected by the 2016 seismic sequence*. Prohitech 2017, Lisabona, Portugalia;
3. Formisano, A., **Chieffo, N.**, Mosoarca, M. *Urban resilience of built-up area in the Municipality of Marigliano (Naples, Italy)*. Prohitech 2017, Lisabona, Portugalia;
4. Formisano, A., **Chieffo, N.**, Mosoarca, M. *Seismic vulnerability and damage of historical centre in the district of Caserta (Italy)*. Prohitech 2017, Lisabona, Portugalia;
5. **Chieffo, N.**, Formisano, A., Mosoarca, M. *The impact of local hazard effects on the vulnerability assessment of an urban area in Timisoara*. Vol. 2, Journal of Arch. Urbanism and Heritage, 2018, ISSN: 1224-6024.

## Bibliography

- [1] G.M. Calvi, R. Pinho, G. Magenes, J.J. Bommer, L.F. Restrepo-Vélez, H. Crowley, Development of seismic vulnerability assessment methodologies over the past 30 years, *ISET Journal of Earthquake Technology*, 43, 75–104, 2006.
- [2] P.G. Asteris, M.P. Chronopoulos, C.Z. Chrysostomou, H. Varum, V. Plevris, N. Kyriakides, V. Silva, Seismic vulnerability assessment of historical masonry structural systems, *Engineering Structures*, 62-63, 118-134, 2014.
- [3] L.F. Ramos, P.B. Lourenço, Modeling and vulnerability of historical city centers in seismic areas: A case study in Lisbon, *Engineering Structures*, 26, 1295–1310, 2004.
- [4] P.B. Lourenço, J.A. Roque, Simplified indexes for the seismic vulnerability of ancient masonry buildings, *Construction and Building Materials*, 20, 200-208, 2006.
- [5] L.E. Yamin, A. Hurtado, R. Rincon, J.F. Dorado, J.C. Reyes, Probabilistic seismic vulnerability assessment of buildings in terms of economic losses, *Engineering Structures*, 138, 308-323, 2017.
- [6] G. Castori, A. Borri, A. De Maria, M. Corradi, R. Sisti, Seismic vulnerability assessment of a monumental masonry building, *Engineering Structures*, 136, 454-465, 2017.
- [7] M. Mosoarca, V. Gioncu, Assessment and mitigation procedures for historical buildings situated in seismic areas, in: *Proceedings of the International Conference on Risk Management, Assessment and Mitigation, RIMA'10*, 27-32, 2010.
- [8] F. Clementi, V. Gazzani, M. Poiani, S. Lenci, Assessment of seismic behaviour of heritage masonry buildings using numerical modelling, *Journal of Building Engineering*, 8, 29–47, 2016.
- [9] A. Formisano, Local-and global-scale seismic analyses of historical masonry compounds in San Pio delle Camere (L'Aquila, Italy), *Natural Hazards*, 86, 465–487, 2017.
- [10] M. Valente, G. Milani, E. Grande, A. Formisano, Historical masonry building aggregates: advanced numerical insight for an effective seismic assessment on two row housing compounds, *Engineering Structures*, 190, 360-379, 2019.
- [11] M. Biglari, A. Formisano, Damage Probability Matrices and Empirical Fragility Curves From Damage Data on Masonry Buildings After Sarpol-e-zahab and Bam Earthquakes of Iran, *Frontiers in Built Environment*, 6:2, 2020. doi: 10.3389/fbuil.2020.00002.
- [12] M. Mosoarca, G. Victor, Structural safety of historical buildings made of reinforced concrete, from Banat region - Romania, *Journal of Cultural Heritage*, 14, e29-e34, 2013.

- [13] F.M. Mazzolani, Urban habitat constructions under catastrophic events: The cost C26 action, 1<sup>st</sup> Edition CRC Press, in F.M. Mazzolani (Ed.), 1068 pages, 2010, ISBN 9780415606851.
- [14] M. Mosoarca, V. Gioncu, Failure mechanisms for historical religious buildings in Romanian seismic areas, *Journal of Cultural Heritage*, 14, e29-e34, 2013.
- [15] M. Mosoarca, I. Onescu, E. Onescu, A. Anastasiadis, Seismic vulnerability assessment methodology for historic masonry buildings in the near-field areas, *Engineering Failure Analysis*, 115, 104662, 2020.
- [16] M. Mosoarca, A.I. Keller, C. Petrus, A. Racolta, Failure analysis of historical buildings due to climate change, *Engineering Failure Analysis*, 82, 666-680, 2017.
- [17] C.J. Collier, A.S. Elnashai, A Procedure for Combining Vertical and Horizontal Seismic Action Effects, *Journal of Earthquake Engineering*, 5, 521-539, 2002.
- [18] A.J. Papazoglou, A.S. Elnashai, Analytical and field evidence of the damaging effect of vertical earthquake ground motion, *Earthquake Engineering and Structural Dynamics*, 25, 1109–1137, 1996.
- [19] V. Gioncu, F.M. Mazzolani, *Earthquake Engineering for Structural Design*, Spon Press (imprint of the Taylor & Francis Group), 581 pages, 2011, ISBN 0-203-84889-6.
- [20] N.A. Abrahamson, J.J. Litcher, Attenuation of vertical peak acceleration, *Bulletin - Seismological Society of America*, 79, 549–580, 1989.
- [21] N. Newmark, W. Hall, *Earthquake Spectra and Design*, EERI Monographs, 103 pages, 1982.
- [22] V. Gioncu, G. Mateescu, Comparative studies of Banat and Vrancea earthquakes, INCERC Report, 1998 (n.d).
- [23] P.G. Carydis, The effects of the vertical earthquake motion in near field, *Earthquake Engineering, in the 21<sup>st</sup> Century*, EE-21C, Skopje-Ohrid, 2005.
- [24] A.S. Elnashai, K. Pilakoutas, The Kalamata (Greece) earthquake of 13 September 1986, Research Report ESEE-86/9, Imperial College, 1986.
- [25] B.M. Broderick, A.S. Elnashai, N.N. Ambraseys, J.J. Barr, R.J. Goodfellow, E.M. Higazy, The Northridge (California) earthquake of 17 January 1994: Observations, strong-motion and correlative response analyses, Research Report ESEE-Y4/4, Imperial College, 1994.
- [26] P.K. Malhotra, Response of buildings to near-field pulse-like ground motions, *Earthquake Engineering and Structural Dynamics*, 28, 1309-1326, 1999.
- [27] M. Ouyed, M. Meghraoui, A. Cisternas, A. Deschamps, J. Dorel, J. Frechet, R. Gaulon, D. Hatzfeld, H. Philip, Seismotectonics of the El Asnam earthquake, *Nature*, 292, 26-31, 1981.



- [28] R.J. Walters, J.R. Elliott, N. D'Agostino, P.C. England, I. Hunstad, J.A. Jackson, B. Parsons, R.J. Phillips, G. Roberts Edinburgh, The 2009 L'Aquila earthquake (central Italy): A source mechanism and implications for seismic hazard, *Geophysical Research Letters*, 36, 2009.
- [29] N. Augenti, F. Parisi, Learning from Construction Failures due to the 2009 L'Aquila, Italy, Earthquake, *Journal of Performance of Constructed Facilities*, 24, 2010.
- [30] L. Sorrentino, A.S. Elnashai, G. Manfredi, Assessment of RC columns subjected to horizontal and vertical ground motions recorded during the 2009 L'Aquila (Italy) earthquake, *Engineering Structures*, 33, 1514-1535, 2011.
- [31] F. Comodini, G. Fagotti, M. Mezzi, V.R. Vecchia, Effects of the earthquake vertical component in masonry buildings: vertical collapse mechanisms?, in: *Proceedings of the 17<sup>th</sup> International Brick/Block Masonry Conference (17thIB2MaC 2020)*, July 5-8, Kraków, Poland, 2020.
- [32] F. Di Michele, C. Cantagallo, E. Spacone, Effects of the vertical seismic component on seismic performance of an unreinforced masonry structures, *Bulletin of Earthquake Engineering*, 18,1635–1656, 2020.
- [33] P.P. Diotallevi, L. Landi, Response of RC structures subjected to horizontal and vertical ground motions, in: *8<sup>th</sup> US National Conference on Earthquake Engineering*, 2006.
- [34] G. Rinaldin, M. Fasan, S. Noé, C. Amadio, The influence of earthquake vertical component on the seismic response of masonry structures, *Engineering Structures*, 185,184–193, 2019.
- [35] M. Acito, M. Bocciarelli, C. Chesi, G. Milani, Collapse of the clock tower in Finale Emilia after the May 2012 Emilia Romagna earthquake sequence: Numerical insight, *Engineering Structures*, 72, 70-91, 2014.
- [36] N. Chieffo, A. Formisano, M. Mosoarca, P.B. Lourenço, Seismic vulnerability assessment of a romanian historical masonry building under near-source earthquake, in: *XI International Conference on Structural Dynamic, EURODYN20*, 23-26 November, Athens, Greece, 4957-4971, 2020.
- [37] DM LL. PP. 14 Gennaio 2008. Norme Tecniche per le Costruzioni, in: *Gazzetta Ufficiale (in Italian)*, n.d.
- [38] Eurocode 8, European Standard EN 1998-3:2005: Design of structures for earthquake resistance - Part 3: Assessment and retrofitting of buildings, *Comite Europeen de Normalisation*, Brussels, 2005.
- [39] P100-1/2013 Cod de proiectare seismică – Partea I–Prevederi de proiectare pentru clădiri, O.M.D.R.A.P. nr. 2.956/18.11.2019, *Monitorul Oficial al României*Nr./dată M.Of., p I, nr.928/18.11.2019.
- [40] DM 17/01/2018, Aggiornamento delle “Norme Tecniche per le Costruzioni” - NTC 2018, 1–198, 2018 (in Italian).
- [41] M. Mariani, F. Pugi, A. Francioso, Vertical component of the seismic action: amplified vulnerability of existing masonry buildings, in: *Multibody Dynamics Conference ECCOMAS19*, July 15-18, Duisburg, Germany, 3807–3835, 2019.

- [42] I. Andreescu, V. Gaivoronsch, M. Mosoarca, Old and New - The Complex Problem of Integrating New Functions into Old Building, in: *Procedia Engineering*, 161, 1103-1108, 2016.
- [43] F. Ceroni, M. Pecce, S. Sica, A. Garofano, Assessment of Seismic Vulnerability of a Historical Masonry Building, *Buildings*, 2, 332-358, 2012.
- [44] M. Mosoarca, A.I. Keller, A complex assessment methodology and procedure for historic roof structures, *International Journal of Architectural Heritage*, 12, 578-598, 2018.
- [45] V. Gioncu, M. Mosoarca, Ultimate limit state of masonry historical buildings using collapse mechanism methodology: application for Orthodox churches, in: F.M. Mazzolani (Ed.), *Proceedings of the International Conference on Protection of Historical Buildings, PROHITECH 09, Rome, Italy, 21-24 June*, CRC Press, Inc., Boca Raton, 1153–1158, 2009.
- [46] A. Borri, G. Castori, M. Corradi, E. Speranzini, Shear behavior of unreinforced and reinforced masonry panels subjected to in situ diagonal compression tests, *Construction and Building Materials*, 25, 4403-4414, 2011.
- [47] G. de Felice, S. De Santis, P.B. Lourenço, N. Mendes, Methods and Challenges for the Seismic Assessment of Historic Masonry Structures, *International Journal of Architectural Heritage*, 11, 143-160, 2017.
- [48] N. Mendes, P.B. Lourenço, Seismic vulnerability of existing masonry buildings: Nonlinear parametric analysis, *Computational Methods in Applied Sciences*, 37, 139-164, 2015.
- [49] G. Fiorentino, A. Forte, E. Pagano, F. Sabetta, C. Baggio, D. Lavorato, C. Nuti, S. Santini, Damage patterns in the town of Amatrice after August 24th 2016 Central Italy earthquakes, *Bulletin of Earthquake Engineering*, 16, 1399-1423, 2018.
- [50] L. Sorrentino, S. Cattari, F. da Porto, G. Magenes, A. Penna, Seismic behaviour of ordinary masonry buildings during the 2016 central Italy earthquakes, *Bulletin of Earthquake Engineering*, 17, 5583-5607, 2019.
- [51] A. Formisano, N. Chieffo, M. Mosoarca, Probabilistic earthquake scenarios of a historical area in the town of Amatrice, in: *AIP Conference Proceedings*, 2293, 240006, 2020.
- [52] I.S. Borcia, I. Craifaleanu, E.N. Tanase, E.I. Praun, Example of use of the SM-ROM-GL DataBase, in: *1<sup>st</sup> National Conference on Earthquake Engineering and Seismology 1CNISS, Bucharest, Romania*, 1, 165-172, 2014.
- [53] E. Oros, Seismological DataBase for Banat Seismic Region (Romania)-Part 1: The Parametric Earthquake Catalogue, *Romanian Journal of Physics*, 53 955–964, 2008.
- [54] O.D. Cardona, M.G. Ordaz, L.E. Yamin, M.C. Marulanda, A.H. Barbat, Earthquake loss assessment for integrated disaster risk management, *Journal of Earthquake Engineering*, 12, 48–59, 2008.

- [55] A.H. Barbat, M.L. Carreño, L.G. Pujades, N. Lantada, O.D. Cardona, M.C. Marulanda, Seismic vulnerability and risk evaluation methods for urban areas. A review with application to a pilot area, *Structure and Infrastructure Engineering*, 6, 17–38, 2010.
- [56] A.J. Kappos, K.C. Stylianidis, K. Pitilakis, Development of seismic risk scenarios based on a hybrid method of vulnerability assessment, *Natural Hazards*, 17, 177–192, 1998.
- [57] V. Comerçi, Mercalli Giuseppe (1850–1914), *Encyclopedia of Earth Sciences Series*, Springer Netherlands, in Bobrowsky, P.T. (Ed.), 671–672, 2013.
- [58] F. Neumann, *Engineering seismology*, GSA Reviews, *Engineering Geology*, 1, 161–186, 1962.
- [59] H.O. Wood, F. Neumann, Modified Mercalli Intensity Scale of 1931, *Bulletin of the Seismological Society of America*, 21, 277–283, 1931.
- [60] G. Grünthal, European Macroseismic Scale 1998 (EMS-98), *Cahiers du Centre Européen de Géodynamique et de Séismologie* 15, Centre Européen de Géodynamique et de Séismologie, Luxembourg, 99, 1998.
- [61] H. Kuramoto, *Seismic Design Codes for Buildings in Japan*, *Journal of Disaster Research*, 2006.
- [62] C.R. Allen, Charles F. Richter: a personal tribute, *Earthquakes & Volcanoes (USGS)*, 19, 146–149, 1987.
- [63] G.F. Panza, F. Romanelli and F. Vaccari, Seismic wave propagation in laterally heterogeneous anelastic media: Theory and applications to seismic zonation, *Advances in Geophysics*, 43, 1–95, 2001.
- [64] P. Bazzurro, C.A. Cornell, Disaggregation of seismic hazard, *Bulletin of the Seismological Society of America*, 89, 501–520, 1999.
- [65] J.W. Baker, C.A. Cornell, Uncertainty propagation in probabilistic seismic loss estimation, *Structural Safety*, 30, 236–252, 2008.
- [66] G.P. Cimellaro, S. Marasco, *Seismic hazard analysis*, Geotechnical, Geological and Earthquake Engineering, Springer Netherlands, 251–261, 2018.
- [67] S.L. Kramer, R.A. Mitchell, Ground motion intensity measures for liquefaction hazard evaluation, *Earthquake Spectra*, 22, 413–438, 2006.
- [68] J.P. Wang, D. Huang, Deterministic seismic hazard assessments for Taiwan considering non-controlling seismic sources, *Bulletin of Engineering Geology and the Environment*, 73, 635–641, 2014.
- [69] R.K. McGuire, W.J. Arabasz, 12. An Introduction to Probabilistic Seismic Hazard Analysis, *Geotechnical and Environmental Geophysics Society of Exploration Geophysicists*, 333–354, 1990.
- [70] R.K. McGuire, Probabilistic seismic hazard analysis: Early history, *Earthquake Engineering and Structural Dynamics*, 37, 329–338, 2008.
- [71] D. Somette, A. Somette, General Theory of the Modified Gutenberg-Richter Law for Large Seismic Moments, *Bulletin of the Seismological Society of America*, 89, 1121–1130, 1999.

- [72] P. Mouroux, B. Le Brun, Risk-Ue Project: An Advanced Approach to Earthquake Risk Scenarios With Application to Different European Towns, *Assessing and Managing Earthquake Risk*, Springer Netherlands, 2, 479–508, 2007.
- [73] S.T. Algermissen, K. V Steinbrugge, Seismic Hazard and Risk Assessment: Some Case Studies, *The Geneva Papers on Risk and Insurance - Issues and Practice*, 9, 8–26, 1984.
- [74] F. E. M. Agency, FEMA Mitigation Division, HAZUS-MH MR3: Multi-Hazard Loss Estimation Methodology: Technical Manual, Washington DC, 2003.
- [75] S. Lagomarsino, S. Giovinazzi, Macroseismic and mechanical models for the vulnerability and damage assessment of current buildings, *Bulletin of Earthquake Engineering*, 4, 415–443, 2006.
- [76] G. Augusti, M. Ciampoli, Performance-Based Design in risk assessment and reduction, *Probabilistic Engineering Mechanics*, 23, 496–508, 2008.
- [77] N. Alam, M.S. Alam, S. Tesfamariam, Buildings' seismic vulnerability assessment methods: A comparative study, *Natural Hazards*, 62, 405-424, 2012.
- [78] R. V. Whitman, J.W. Reed, S.-T. Hong, Earthquake Damage Probability Matrices, *Proceedings of the Fifth World Conference on Earthquake Engineering*, Rome, Italy, 2, 2531–2540, 1974.
- [79] F. Braga, D. Liberatore, M. Dolce, Fast and reliable damage estimation for optimal relief operations, in: *International Symposium on Earthquake Relief in Less Industrialized Areas (Zurich)*, 145–151, 1984.
- [80] G. Di Pasquale, G. Orsini, R.W. Romeo, New developments in seismic risk assessment in Italy, *Bulletin of Earthquake Engineering*, 3, 101-128, 2005.
- [81] M. Dolce, A. Kappos, A. Masi, G. Penelis, M. Vona, Vulnerability assessment and earthquake damage scenarios of the building stock of Potenza (Southern Italy) using Italian and Greek methodologies, *Engineering Structures*, 28, 357–371, 2006.
- [82] S. Giovinazzi, S. Lagomarsino, A Macroseismic Method for the Vulnerability Assessment of Buildings, in: *Proceedings of 13<sup>th</sup> World Conference on Earthquake Engineering*, 1–6, 2004.
- [83] D. Benedetti, V. Petrini, Sulla vulnerabilita sismica di edifici in muratura: Proposta su un metodo di valutazione, *L'industria Delle Costruzioni*, 149, 66–74, 1984 (in Italian).
- [84] R. Vicente, T. Ferreira, R. Maio, Seismic Risk at the Urban Scale: Assessment, Mapping and Planning, *Procedia Economics and Finance*, 18, 71–80, 2014.
- [85] A. Formisano, G. Florio, R. Landolfo, F.M. Mazzolani, Numerical calibration of an easy method for seismic behaviour assessment on large scale of masonry building aggregates, *Advances in Engineering Software*, 80, 116–138, 2015.

- [86] A. Formisano, N. Chieffo, M. Mosoarca, Seismic Vulnerability and Damage Speedy Estimation of an Urban Sector within the Municipality of San Potito Sannitico (Caserta, Italy), *The Open Civil Engineering Journal*, 11, 1106–1121, 2018.
- [87] N. Chieffo, A. Formisano, T. Miguel Ferreira, Damage scenario-based approach and retrofitting strategies for seismic risk mitigation: an application to the historical Centre of Sant’Antimo (Italy), *European Journal of Environmental and Civil Engineering*, 2019, doi:10.1080/19648189.2019.1596164.
- [88] N. Chieffo, F. Clementi, A. Formisano, S. Lenci, Comparative fragility methods for seismic assessment of masonry buildings located in Muccia (Italy), *Journal of Building Engineering*, 25, 100813, 2019.
- [89] M. Mosoarca, I. Onescu, E. Onescu, B. Azap, N. Chieffo, M. Szitar-Sirbu, Seismic vulnerability assessment for the historical areas of the Timisoara city, Romania, *Engineering Failure Analysis*, 101, 86–112, 2019.
- [90] S. Lagomarsino, On the vulnerability assessment of monumental buildings, *Bulletin of Earthquake Engineering*, 4, 445–463, 2006.
- [91] R.J.S. Spence, A.W. Coburn, A. Pomonis, S. Sakai, Correlation of ground motion with building damage: The definition of a new damage-based seismic intensity scale, in: *Proceedings of 10th World Conference on Earthquake Engineering*, Madrid, Spain, 551–556, 1992.
- [92] G. Orsini, A model for buildings’ vulnerability assessment using the parameterless scale of seismic intensity (PSI), *Earthquake Spectra*, 15, 463–483, 1999.
- [93] F. Sabetta, a Pugliese, Attenuation of peak horizontal acceleration and velocity from Italian strong-motion records, *Bulletin of the Seismological Society*, 77, 1491–1513, 1987.
- [94] F. Sabetta, A. Pugliese, Estimation of response spectra and simulation of nonstationary earthquake ground motions, *Bulletin of the Seismological Society of America*, 86, 337–352, 1996.
- [95] A. Singhal, A.S. Kiremidjian, Method for Probabilistic Evaluation of Seismic Structural Damage, *Journal of Structural Engineering*, 122, 1459–1467, 2002.
- [96] Y.J. Park, A.H.S. Ang, Y.K. Wen, Damage limiting a seismic design of buildings, *Earthquake Spectra*, 3, 1–26, 1987.
- [97] T. Rossetto, A. Elnashai, A new analytical procedure for the derivation of displacement-based vulnerability curves for populations of RC structures, *Engineering Structures*, 27, 397–409, 2005.
- [98] A.J. Kappos, V. Lekidis, G. Panagopoulos, I. Sous, N. Theodulidis, C. Karakostas, T. Anastasiadis, T. Salonikios, B. Margaris, Analytical estimation of economic loss for buildings in the area struck by the 1999 Athens earthquake and comparison with statistical repair costs, *Earthquake Spectra*, 23, 333–355, 2007.

- [99] A. Bernardini, M.R. Valluzzi, C. Modena, D. D'Ayala, E. Speranza, Vulnerability assessment of the historical masonry building typologies of Vittorio Veneto (NE Italy), *Bollettino Di Geofisica Teorica Ed Applicata*, 49, 463–483, 2008.
- [100] A. Bernardini, R. Gori, C. Modena, Application of Coupled Analytical Models and Experiential Knowledge to Seismic Vulnerability Analyses of Masonry Buildings: Earthquake Damage Evaluation and Vulnerability Analysis of Buildings Structures, In: Koridze A. (ed), *Earthquake Damage Evaluation and Vulnerability Analysis of Buildings Structures*, INEEC, Omega Scientific, Ozon, 161-180, 1990.
- [101] D. D'Ayala, E. Speranza, Definition of Collapse Mechanisms and Seismic Vulnerability of Historic Masonry Buildings, *Earthquake Spectra*, 19, 479–509, 2003.
- [102] F. E. M. Agency, FEMA Mitigation Division, Hazus, Hazus–MH 2.1: Technical Manual, Washington DC, 2003.
- [103] ATC 40, *Seismic Evaluation and Retrofit of Concrete Building Volume 1*, Applied Technology Council, California, USA, 1996.
- [104] P. Fajfar, Capacity spectrum method based on inelastic demand spectra, *Earthquake Engineering and Structural Dynamics*, 28, 979–993, 1999.
- [105] S. Lagomarsino, S. Cattari, PERPETUATE guidelines for seismic performance-based assessment of cultural heritage masonry structures, *Bulletin of Earthquake Engineering*, 13, 13–47, 2015.
- [106] S. Lagomarsino, S. Cattari, Seismic Vulnerability of Existing Buildings, in: *Seismic Vulnerability of Structures*, John Wiley & Sons, Inc., 1–62, 2013.
- [107] Z. V Milutinovic, G.S. Trendafiloski, WP4: Vulnerability of Current Buildings, in: *RISK-UE Project Handbook*, 111 pages, 2003.
- [108] A.S. Elnashai, L. Di Sarno, *Fundamentals of Earthquake Engineering*, 2<sup>nd</sup> Edition, John Wiley and Sons, 494 pages, 2015.
- [109] D.M. Boore, W.B. Joyner, Site amplifications for generic rock sites, *Bulletin of the Seismological Society of America*, 87, 327–341, 1997.
- [110] S. Grimaz, P. Malisan, How could cumulative damage affect the macroseismic assessment?, *Bulletin of Earthquake Engineering*, 15, 2465–2481, 2017.
- [111] N.N. Ambraseys, J. Douglas, Near-field horizontal and vertical earthquake ground motions, *Soil Dynamics and Earthquake Engineering*, 23, 1–18, 2003.
- [112] M. Davoodi, M. Sagjadi, P. Goljahani, M. Kamalian, Effects of Near-Field and Far-Field Earthquakes on Seismic Response of SDOF System Considering Soil Structure Interaction, in: *Proceedings of 15th World Conference on Earthquake Engineering*, Lisbon, Portugal, 2012.
- [113] S. Grimaz, P. Malisan, Near field domain effects and their consideration in the international and Italian seismic codes, *Bollettino Di Geofisica Teorica Ed Applicata*, 55, 717–738, 2014.



- [114] S. V. Medvedev, W. Sponheuer, Scale of Seismic Intensity, in: Proc. IV World Conference of the Earthquake Engineering, Santiago, Chile, 143–153, 1969.
- [115] S. Midorikawa, H. Kobayashi, Ioseismal map in ner-field with regard to fault rupture and site geological conditions, in: Turk Natl Comm on Earthquake Eng, Ankara, 259–262, 1980.
- [116] E. Faccioli, Seismic hazard assessment for derivation of earthquake scenarios in Risk-UE, *Bulletin of Earthquake Engineering*, 4, 341–364, 2006.
- [117] S. Giovinazzi, Geotechnical hazard representation for seismic risk analysis, *Bulletin of the New Zealand Society for Earthquake Engineering*, 42, 308, 2009.
- [118] N. Chieffo, A. Formisano, The influence of geo-hazard effects on the physical vulnerability assessment of the built heritage: An application in a district of Naples, *Buildings*, 9, 2019.
- [119] N. Chieffo, A. Formisano, Geo-hazard-based approach for the estimation of seismic vulnerability and damage scenarios of the old city of senerchia (Avellino, Italy), *Geosciences (Switzerland)*, 9, 2019.
- [120] V. Gioncu, F.M. Mazzolani, Influence of earthquake types on the design of seismic-resistant steel structures. Part 1: Challenges for new design approaches. Part 2: Structural response for different earthquake types. *Behavior of Steel Structures in Seismic Areas, STESSA 2006* (eds. F.M. Mazzolani and A. Wada), Taylor & Francis, London, 113-120, 121-127, 2006.
- [121] J.D. Bray, A. Rodriguez-Marek, Characterization of forward-directivity ground motions in the near-fault region, *Soil Dynamics and Earthquake Engineering*, 24, 815–828, 2004.
- [122] V. Gioncu, F.M. Mazzolani, *Seismic design of steel structures*, CRC Press, 525 pages, 2014.
- [123] F. Mollaioli, S. Bruno, L.D. Decanini, G.F. Panza, Characterization of the dynamic response of structures to damaging pulse-type near-fault ground motions, *Meccanica*, 41, 23–46, 2006.
- [124] J. Györgyi, Analysis of the Application of the Near-Fault Ground Motion Functions, *Transactions, SMiRT 21*, 6-11 November, New Delhi, India, 1–8, 2011.
- [125] J.J. Kempton, J.P. Stewart, Prediction equations for significant duration of earthquake ground motions considering site and near-source effects, *Earthquake Spectra*, 22, 985–1013, 2006.
- [126] P.G. Somerville, Magnitude scaling of the near fault rupture directivity pulse, *Physics of the Earth and Planetary Interiors*, 137, 201–212, 2003.
- [127] G.W. Housner, M.D. Trifunac, Analysis of accelerograms--Parkfield earthquake, *Bulletin of the Seismological Society of America*, 57, 1193–1220, 1967.
- [128] N.M. Newmark, Method of computation for structural dynamics, *Pressure Vessels Piping Design Anal.*, 2, 1235–1264, 1972



- [129] N.N. Ambraseys, K.A. Simpson, Prediction of vertical response spectra in Europe, *Earthquake Engineering and Structural Dynamics*, 25, 401–412, 1996.
- [130] N.N. Ambraseys, The prediction of earthquake peak ground acceleration in Europe, *Earthquake Engineering & Structural Dynamics*, 24, 467–490, 1995.
- [131] E. Kalkan, P. Gülkan, Empirical attenuation equations for vertical ground motion in Turkey, *Earthquake Spectra*, 20, 853–882, 2004.
- [132] G.M. Atkinson, Ground-motion prediction equation for small-to-moderate events at short hypocentral distances, with application to induced-seismicity hazards, *Bulletin of the Seismological Society of America*, 105, 981–992, 2015.
- [133] M. Çelebi, P. Bazzurro, L. Chiaraluce, P. Clemente, L. Decanini, A. Desortis, W. Ellsworth, A. Gorini, E. Kalkan, S. Marcucci, G. Milana, F. Mollaioli, M. Olivieri, R. Paolucci, D. Rinaldis, A. Rovelli, F. Sabetta, C. Stephens, Recorded motions of the 6 April 2009 Mw 6.3 L’Aquila, Italy, earthquake and implications for building structural damage: Overview, *Earthquake Spectra*, 26, 651–684, 2010.
- [134] A. Masi, L. Chiauzy, G. Santarsiero, M. Liuzzi, V. Tramutoli, Seismic damage recognition based on field survey and remote sensing: general remarks and examples from the 2016 Central Italy earthquake, *Natural Hazards*, 86, 193–195, 2017.
- [135] M. Indirli, L.A.S. Kouris, A. Formisano, R.P. Borg, F.M. Mazzolani, Seismic damage assessment of unreinforced masonry structures after the Abruzzo 2009 earthquake: The case study of the historical centers of L’Aquila and Castelvecchio Subequo, *International Journal of Architectural Heritage*, 7, 536–578, 2013.
- [136] D. Bindi, L. Luzi, M. Massa, F. Pacor, Horizontal and vertical ground motion prediction equations derived from the Italian Accelerometric Archive (ITACA), *Bulletin of Earthquake Engineering*, 8, 1209–1230, 2010.
- [137] D. D’Ayala, J. F. Walker, Z. Mildon, D. Lombardi, C. Galasso, D. Pedicone, V. Putrino, P. Perugini, F. De Luca, G. Del Gobbo, T. Lloyd, E. C. Morgan, A. Torato, D. Alexander, S. Tagliacozzo, The Mw 6.2 Amatrice, Italy Earthquake of 24th August 2016, *EEFIT Technical Report*, 2019.
- [138] J. Batt, Reinventing Banat, *Regional and Federal Studies*, 12, 178–202, 2002.
- [139] A. Drace-Francis, Empires and Peninsulas: Southeastern Europe between Karlowitz and the Peace of Adrianople, 1699-1829, ed. Plamen Mitev, Ivan Parvev, Maria Baramova and Vania Racheva, *The English Historical Review*, 128, 439–440, 2013.
- [140] C. Thomas, The Anatomy of a Colonization Frontier: The Banat of Temešvar, *Austrian History Yearbook*, 19, 2–22, 1984.
- [141] V. Spinei, The Romanians and the Turkic nomads north of the Danube delta from the tenth to the mid-thirteenth century, *East Central and Eastern Europe in the Middle Ages 450-1450*, 6, 1-562, 2009.

- [142] The City of Banloc, Wikipedia, [https://Ro.Wikipedia.org/Wiki/Castelul Banloc](https://Ro.Wikipedia.org/Wiki/Castelul_Banloc) (accessed September 25, 2020).
- [143] M. Sandulescu, Cenozoic Tectonic History of the Carpathians, in: F. Royden, L.H., Horvath (Ed.), *The Pannonian Basin: A Study in Basin Evolution*, AAPG Memoir, 17–25, 1998.
- [144] M.C. Oncescu, V.I. Marza, M. Rizescu, M. Popa, *The Romanian Earthquake Catalogue Between 984–1997*, 43–47, 1999.
- [145] A. Bala, D. Toma-Danila, M. Radulian, Focal mechanisms in Romania: statistical features representative for earthquake-prone areas and spatial correlations with tectonic provinces, *Acta Geodaetica et Geophysica*, 54, 263–286, 2019.
- [146] L. Ardeleanu, G. Leydecker, K.P. Bonjer, H. Busche, D. Kaiser, T. Schmitt, Probabilistic seismic hazard map for Romania as a basis for a new building code, *Natural Hazards and Earth System Science*, 5, 679–684, 2005.
- [147] F. Pavel, R. Vacareanu, J. Douglas, M. Radulian, C. Cioflan, A. Barbat, *An Updated Probabilistic Seismic Hazard Assessment for Romania and Comparison with the Approach and Outcomes of the SHARE Project*, *Pure and Applied Geophysics*, 173, 1881–1905, 2016.
- [148] Earthquake Selection WebGIS App (BIGSEES), available at: <https://infp.maps.arcgis.com> (accessed October 20, 2020).
- [149] A. Der Kiureghian, P. Keshishian, Effect of Site Response on Spatial Variability of Ground Motion, in: *11<sup>th</sup> World Conference on Earthquake Engineering*, 1996.
- [150] IPROTIM, *Expertiza cu principii de consolidare* (In Romanian), 1990.
- [151] Castelul Banloc, Wikiwand, available at: [wikiwand.com](http://wikiwand.com) (accessed September 25, 2020).
- [152] Bommer JJ, Ruggeri C, The Specification of Acceleration Time-histories in Seismic Design Codes, *European Earthquake Engineering*, 16, 3–16, 2003.
- [153] J.J. Bommer, A.B. Acevedo, The use of real earthquake accelerograms as input to dynamic analysis, *Journal of Earthquake Engineering*, 8, 43–91, 2004.
- [154] I. Iervolino, C.A. Cornell, Record selection for nonlinear seismic analysis of structures, *Earthquake Spectra*, 21, 2005.
- [155] T. Paulay, P.J. Loeber, A.H. Mattock, H.P.J. Taylor, A.C. Scordelis, D. Ngo, H.A. Franklin, J. Houde, M.S. Mirza, R.N. Swamy, A.D. Andriopoulos, J. Ruhnau, M. Moayer, P.E. Regan, *Shear in reinforced concrete*, Volumes 1 and 2, in: *Shear in Reinf Concr*, Am. Concr. Inst. (Publ SP-42), 1974.
- [156] P.B. Lourenço, *A user/programmer guide for the micro-modelling of masonry structures*, report no. 03.21.1.31.35, 1996.
- [157] J. Lopez, S. Oller, E. Oñate, J. Lubliner, A homogeneous constitutive model for masonry, *International Journal for Numerical Methods in Engineering*, 46, 1651–1671, 1999.
- [158] A.W. Page, Finite element model for masonry, *Journal of the Structural Division*, 104, 1267–1285, 1978.

- [159] A.W. Page, P.W. Kleeman, M. Dhanasekar, An in-plane finite element model for masonry, in: *New Analysis Techniques for Structural Masonry*, in: *Proceedings of a Session Held in Conjunction with Structures Congress*, Chicago, Illinois, September 18, 1985.
- [160] S. Pietruszczak, X. Niu, A mathematical description of macroscopic behaviour of brick masonry, *International Journal of Solids and Structures*, 29, 531–546, 1992.
- [161] A. Anthoine, Derivation of the in-plane elastic characteristics of masonry through homogenization theory, *International Journal of Solids and Structures*, 32, 137–163, 1995.
- [162] A. Zucchini, P.B. Lourenço, A micro-mechanical model for the homogenisation of masonry, *International Journal of Solids and Structures*, 39, 3233–3255, 2002.
- [163] G. Milani, P.B. Lourenço, A discontinuous quasi-upper bound limit analysis approach with sequential linear programming mesh adaptation, *International Journal of Mechanical Sciences*, 51, 89–104, 2009.
- [164] EC-6-P-3, Eurocode 6 - Design of masonry structures - Simplified calculation methods for unreinforced masonry structures, Part 1-1: General Rules for Reinforced and Unreinforced Masonry Structures, 2005.
- [165] EN 771-1, Specification for masonry units - Part 1: Clay masonry units, European Standard, 32 Suppl. 8, 1–4, 2003.
- [166] BS EN 772-1, Methods of Test for Masonry Units Part 1 : Determination of Compressive Strength, BSI Standards Publication, 1–18 2011.
- [167] BS:EN:771-6:2005, Specification for masonry units — Part 6: Natural stone masonry units, BSI Standards Publication, 3, 1–34, 2005.
- [168] BS EN 1992-1-1, Eurocode 2: Design of concrete structures - Part 1-1 : General rules and rules for buildings, British Standards Institution, 1, 230, 2004.
- [169] G. Magenes, P. Morandi, Valutazione della risposta sismica di edifici in muratura: modelli e normative, Dipartimento Di Meccanica Strutturale, Università Di Pavia, 2006 (in Italian).
- [170] Uni En, BS EN 1996-2:2006 - Eurocode 6: Design of masonry structures - Part 2: Design considerations, selection of materials and execution of masonry, Eurocode 6, 2, 2006.
- [171] N. Augenti, Il calcolo sismico degli edifici in muratura, 1st ed., Turin, Italy, 2004 (in Italian).
- [172] G. Florio, Vulnerability of historical masonry buildings under exceptional actions, PhD Thesis, University of Naples “Federico II”, 2010.
- [173] M. Tomaževič, Shear resistance of masonry walls and Eurocode 6: Shear versus tensile strength of masonry, *Materials and Structures/Materiaux et Constructions*, 42, 889–907, 2009.
- [174] BS EN 1052-3, Methods of test for masonry - Part 3: Determination of initial shear strength, BSi - British Standards, 18, 2002.
- [175] P.B. Lourenço, Computational strategies for masonry structures, PhD-Thesis, Delft University of Technology, 1996.

- [176] M. Angelillo, P.B. Lourenço, G. Milani, Masonry behaviour and modelling, in: CISM International Centre for Mechanical Sciences, Courses and Lectures, 2014.
- [177] D.C. Jansen, S.P. Shah, Effect of Length on Compressive Strain Softening of Concrete, *Journal of Engineering Mechanics*, 123, 25–35, 2002.
- [178] P.B. Lourenço, Experimental and numerical issues in the modelling of the mechanical behaviour of masonry, *Structural Analysis of Historical Constructions*, 57–91 1998.
- [179] P.B. Lourenço, J. Barros, J.C. Almeida, Characterization of masonry under uniaxial tension, Report 02-DEC/E-12, 24, 2002.
- [180] R. Van Der Pluijm, Non-linear behaviour of masonry under tension, *Heron*, 42, 25–48, 1997.
- [181] CEB-FIP, Model Code 1990, Comite Euro-International Du Beton, Paris, 87–109, 1991.
- [182] P.B. Lourenço, Structural Masonry Analysis: Recent Developments and Prospects, *Journal of Chemical Information and Modeling*, 53, 160, 2008.
- [183] S. Lagomarsino, A. Penna, A. Galasco, S. Cattari, TREMURI program: An equivalent frame model for the nonlinear seismic analysis of masonry buildings, *Engineering Structures*, 56, 1787–1799, 2013.
- [184] A. Brencich, L. Gambarotta, S. Lagomarsino, A macroelement approach to the three-dimensional seismic analysis of masonry buildings, 11<sup>th</sup> European Conference on Earthquake Engineering, 90, 1–10, 1998.
- [185] C. Calderini, S. Cattari, S. Lagomarsino, The use of the diagonal compression test to identify the shear mechanical parameters of masonry, *Construction and Building Materials*, 24, 677-685, 2010.
- [186] D.F. D’Ayala, S. Paganoni, Assessment and analysis of damage in L’Aquila historic city centre after 6th April 2009, *Bulletin of Earthquake Engineering*, 9, 81–104, 2011.
- [187] G. Magenes, Masonry Building Design in Seismic Areas: recent experiences and prospects from a European standpoint, in: 1<sup>st</sup> European Conference on Earthquake Engineering and Seismology, Geneva, Switzerland, Keynote 9, 2006.
- [188] Eurocode, 8: Design of structures for earthquake resistance—Part 1: General rules, seismic actions and rules for buildings (EN 1998-1: 2004), European Committee for Normalization, Brussels, 1, 2004.
- [189] V. Turnšek, F. Čačovič, Some experimental results on the strength of brick masonry walls, in: Proceedings of the 2<sup>nd</sup> International Brick Masonry Conference, 149–156, 1971.
- [190] F. Cannizzaro, B. Pantò, M. Lepidi, S. Caddemi and I. Calì, Multi-Directional Seismic Assessment of Historical Masonry Buildings by Means of Macro-Element Modelling: Application to a Building Damaged during L’Aquila Earthquake (Italy), *Buildings*, 7, 106, 2017 .

- [191] K. Campbell, Near-source attenuation of peak horizontal acceleration, *Bulletin of the Seismological Society of America*, 71, 1981.
- [192] I. Apostol, Seismic vulnerability assessment of historical urban centres, PhD Thesis, Politehnica University of Timisoara, 2020.
- [193] Major Earthquakes, Wikipedia, Available at: [wikipedia.org](http://wikipedia.org) (accessed October 20, 2020).
- [194] DIANA FEA, Diana User's Manual, Release 10.2, 2017.
- [195] N. Mendes, P.B. Lourenço, A. Campos-Costa, Seismic vulnerability assessment of ancient masonry building: An experimental method, in: *Advanced Materials Research*, 133-134, 635-640, 2010.
- [196] P.B. Lourenço, J.M. Pereira, Seismic Retrofitting Project Recommendations for Advanced Modeling of Historic Earthen Sites, 2018.
- [197] S. Rajadurai, M.G. Prasad, R. Kavin, M. Sundaravadivelu, FEA Best Practices Approach, *International Journal of Recent Development in Engineering and Technology*, 2014.
- [198] T.E. Boothby, H.S. Atamturktur, A guide for finite element analyses of historic load-bearing masonry structures, North American Masonry Conference, 2007.
- [199] F.J. Vecchio, M.P. Collins, Modified compression field theory for reinforced concrete elements subject to shear, *Journal of the American Concrete Institute*, 83, 219-231, 1986.
- [200] D. Diaconu, V. Stoian, Experimental Test Report No. 580.2, 2015.
- [201] N. Ademović, D. V Oliveira, Seismic Assessment of a Typical Masonry Residential Building in Bosnia and Herzegovina, in: *15<sup>th</sup> World Conference on Earthquake Engineering - WCEE*, Lison (Portugal), 2012.
- [202] C. Ferrero, P.B. Lourenço, C. Calderini, Nonlinear modeling of unreinforced masonry structures under seismic actions: Validation using a building hit by the 2016 central Italy earthquake, *Frattura ed Integrità Strutturale*, 14, 2020.
- [203] Seismosoft, SeismoSignal, User's Manual, 2016.
- [204] W.J. Hall, *Dynamics of Structures - Theory and Applications to Earthquake Engineering*, Earthquake Spectra, 1996.
- [205] E.H. Vanmarcke, D.A. Gasparini, Simulated earthquake ground motions, Report no. K-Seismic Response Analysis of Nuclear Power Plant Systems K1-Ground Motion and Design Criteria, SMiRT 4 - San Francisco, USA, 1977.
- [206] I. Iervolino, C. Galasso, E. Cosenza, REXEL: Computer aided record selection for code-based seismic structural analysis, *Bulletin of Earthquake Engineering*, 8, 339-362, 2010.
- [207] I. Apostol, M. Mosoarca, N. Chieffo, E. Onescu, Seismic Vulnerability Scenarios for Timisoara, Romania, in: *RILEM Bookseries*, Springer Netherlands, 191-1200, 2019.
- [208] B. Calderoni, E.A. Cordasco, P. Lenza, Il comportamento strutturale delle fasce di piano degli edifici in muratura soggetti ad azioni orizzontali: Indagine sperimentale, *Ingegneria Sismica*, 2010 (in Italian).

- [209] D. Liberatore, C. Doglioni, O. AlShawa, S. Atzori, L. Sorrentino, Effects of coseismic ground vertical motion on masonry constructions damage during the 2016 Amatrice-Norcia (Central Italy) earthquakes, *Soil Dynamics and Earthquake Engineering*, 120, 423-435, 2019.
- [210] T. Paulay, M.J.N. Priestly, *Seismic Design of Reinforced Concrete and Masonry Buildings*, Ed. Wiley-Interscience, 768 pages, 1992, ISBN-10: 0471549150.
- [211] J. Ben Gu, Y. Tao, R. Xin, Z. Yang, Q.X. Shi, Seismic Performance of Multistorey Masonry Structure with Openings Repaired with CFRP Grid, *Advances in Civil Engineering*, Article ID 4374876, 11, 2018.
- [212] M. Tomažević, P. Weiss, Displacement capacity of masonry buildings as a basis for the assessment of behavior factor: An experimental study, *Bulletin of Earthquake Engineering*, 8, 1267-1294, 2010.
- [213] M. Tomažević, V. Bosiljkov, P. Weiss, Structural Behavior Factor for Masonry Structures, in: *Proceedings of 13th World Conference on Earthquake Engineering*, Vancouver, B.C., Canada, Paper No. 2642, 2004.
- [214] M.D. Llanes-Tizoc, A. Reyes-Salazar, E. Bojorquez, J. Bojorquez, A. Lopez-Barraza, J.L. Rivera-Salas, J.R. Gaxiola-Camacho, Local, story, and global ductility evaluation for complex 2D steel buildings: Pushover and dynamic analysis, *Applied Sciences (Switzerland)*, 2019.
- [215] D. Zonta, G. Zanardo, C. Modena, Experimental evaluation of the ductility of a reduced-scale reinforced masonry building, *Materials and Structures*, 34, 636-644, 2001.
- [216] A. Formisano, G. De Matteis, F.M. Mazzolani, Numerical and experimental behaviour of a full-scale RC structure upgraded with steel and aluminium shear panels, *Computers and Structures*, 88, 1348-1360, 2010.
- [217] M. Dolce, A. Goretti, Building damage assessment after the 2009 Abruzzi earthquake, *Bulletin of Earthquake Engineering*, 13, 2241-2264, 2015.
- [218] P.B. Lourenço, Computations on historic masonry structures, *Prog. Struct. Eng. Mater.*, 4, 301-319, 2002.
- [219] N. Chieffo, I. Onescu, A. Formisano, M. Marius, Empirical-mechanical Seismic Vulnerability Analysis Method for Masonry Buildings in Timișoara: Validation based on the 2009 Italian Earthquake, *The Open Civil Engineering Journal*, 314-333, 2020.
- [220] F. Parisi, N. Augenti, Nonlinear seismic behaviour of irregular URM walls with openings, in: *Proceedings of 14<sup>th</sup> Italian Conference on Earthquake Engineering (ANIDIS 2011)*, Bari, Italy, 18-22 September, Paper No. 752, 2011.
- [221] Q. Su, G. Cai, A.S. Larbi, Seismic Damage Assessment Indexes for Masonry Structures, *Journal of Structural Engineering*, 145, 2019.
- [222] A. Colombo, P. Negro, A damage index of generalised applicability, *Engineering Structures*, 27, 1164-1174, 2005.



- [223] B. Fitzner, K. Heinrichs, D. La Bouchardiere, D. La Bouchardiere, E. Galan, F.P.O. Zezza, Damage index for stone monuments, Protection and Conservation of the Cultural Heritage of the Mediterranean Cities, in: Proceedings of the 5th International Symposium on the Conservation of Monuments in the Mediterranean Basin, Sevilla, Spain, 5-8 April, 2002.
- [224] G. Milani, S. Russo, M. Pizzolato, A. Tralli, Seismic Behavior of the San Pietro di Coppito Church Bell Tower in L'Aquila, Italy, The Open Civil Engineering Journal, 6, 131-147, 2012.
- [225] A. Formisano, G. Milani, Seismic vulnerability analysis and retrofitting of the SS. Rosario church bell tower in finale emilia (Modena, Italy), Frontiers in Built Environment, 5, 70, 2019.
- [226] S.T.A data srl, 3Muri 10.9.0 - User Manual, (n.d.).
- [227] F. Sabetta, A. Goretti, A. Lucantoni, Empirical Fragility Curves from Damage Surveys and Estimated Strong Ground Motion, 11th European Conference on Earthquake Engineering, Paris, France, 1-11, 1998.
- [228] S. Cattari, E. Curti, S. Giovinazzi, S. Parodi, S. Lagomarsino, A. Penna, Un modello meccanico per l'analisi di vulnerabilità del costruito in muratura a scala urbana, in: Proceedings of XI Congresso Nazionale "L'Ingegneria Sismica in Italia"- ANIDIS, 2004 (in Italian).
- [229] H. Azizi-Bondarabadi, N. Mendes, P.B. Lourenço, N.H. Sadeghi, Empirical seismic vulnerability analysis for masonry buildings based on school buildings survey in Iran, Bulletin of Earthquake Engineering, 14, 3195-3229, 2016.
- [230] T.M. Ferreira, R. Maio, R. Vicente, Seismic vulnerability assessment of the old city centre of Horta, Azores: calibration and application of a seismic vulnerability index method, Bulletin of Earthquake Engineering, 15, 2879-2899, 2017.
- [231] C. Margottini, D. Molin, L. Serva, Intensity versus ground motion: A new approach using Italian data, Engineering Geology, 33, 45-58, 1992.